The Large-Scale Structure of the Deep Earth as Constrained by Free Oscillation Observations

by

Rudolf Widmer

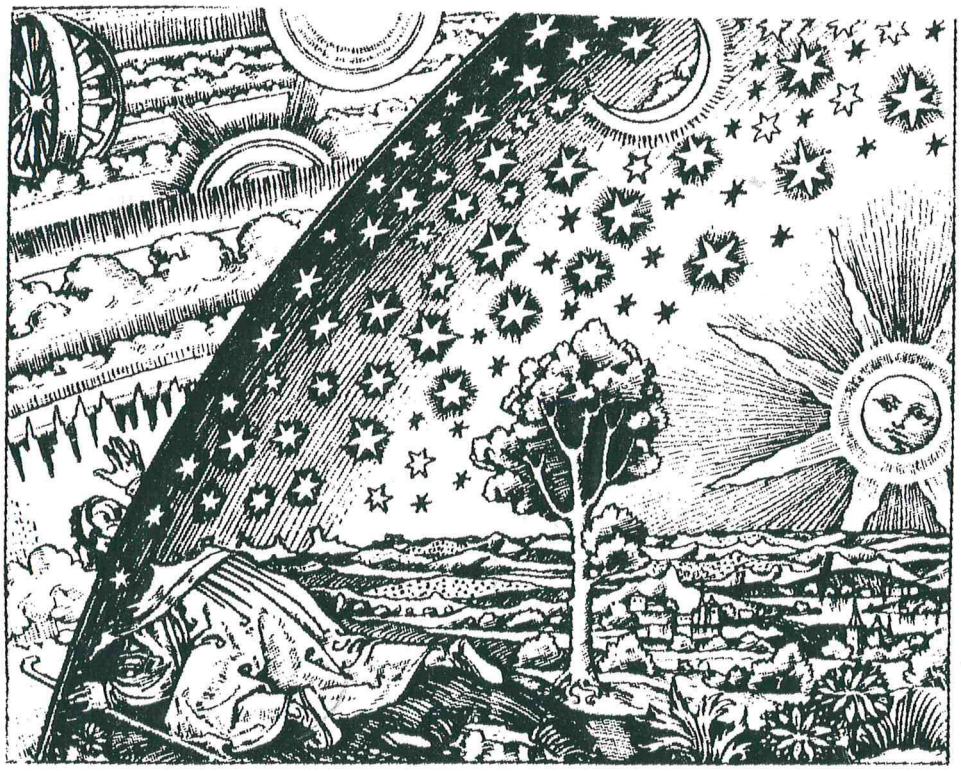

UNIVERSITY OF CALIFORNIA, SAN DIEGO

SCRIPPS INSTITUTION OF OCEANOGRAPHY

1991

UNIVERSITY OF CALIFORNIA, SAN DIEGO

The Large-Scale Structure of the Deep Earth as Constrained by Free Oscillation Observations

A dissertation submitted in partial satisfaction of the
requirements for the degree Doctor of Philosophy
in Earth Sciences

by

Rudolf Widmer

Committee in charge:

Professor T. Guy Masters, Chairperson
Professor J. Freeman Gilbert
Professor Jean-Bernard H. Minster
Professor Richard L. Salmon
Professor John A. Rice

1991

To Jela

LE LOUP ET L'AGNEAU

La raison du plus fort est toujours la meilleure;
Nous l'allons montrer tout à l'heure.

Un Agneau se désaltérait
Dans le courant d'une onde pure.
Un Loup survient à jeun, qui cherchait aventure,
Et que la faim en ces lieux attirait.
"Qui te rend si hardi de troubler mon breuvage?
Dit cet animal plain de rage:
Tu seras châtié de ta témérité.
— Sire, répond l'Agneau, que Votre Majesté
Ne se mette pas en colère;
Mais plutôt considère
Que je me vas désaltérant
Dans le courant,
Plus de vingt pas au-dessous d'Elle;
Et que par conséquent, en aucune façon,
Je ne puis troubler sa boisson.
— Tu la troubles, reprit cette bête cruelle;
Et je sais que de moi tu médis l'an passé.
— Comment l'aurais-je fait si je n'étais pas né?
Reprit l'Agneau; je tette encore ma mère.
— Si ce n'est toi, c'est donc ton frère.
— Je n'en ai point. — C'est donc quelqu'un des tiens;
Car vous ne m'épargnez guère,
Vous, vos bergers, et vos chiens.
On me l'a dit: il faut que je me venge."
Là-dessus, au fonds des forêts
Le Loup l'emporte, et puis le mange,
Sans autre forme de procès.

La Fontaine, 1621 – 1695

Table of Contents

List of Figures

Chapter 3

Chapter 4

Chapter 5

List of Tables

Chapter 4

Chapter 5

Acknowledgments

Attending graduate school at Scripps is a privilege for a number of reasons and many people deserve credit for my being able to say that the last six years have been a period of learning, of personal growth, and of enjoyment.

My advisor, Guy Masters, has guided me through all my research, and his shared enthusiasm for normal modes has allowed our collaboration to become fruitful and enjoyable. Guy has taught me how to use low-frequency seismic data to learn about the structure of the Earth's interior in a quantitative fashion. The scepticism and integrity of his approach to science will serve me as a shining example. More than once, Guy came to my rescue when I was stuck with some program. He was also very supportive when it came to writing up the thesis. He patiently rearranged many of my awkward sentences so that they now read like English. I am grateful to Guy for his support and loyalty – he spared me much of the anxieties involved with writing NSF proposals. I know only too well that I will soon miss the days when I didn't have to worry about funding.

Freeman Gilbert has shown continued interest in my research and discussions with him have been elucidating. Matters may have appeared to be complex, but Freeman always found a way to explain them to me in a clear and concise way. I am also indepted to Freeman for his long-term commitment to low-frequency seismology, and I think it is fair to say that he and George Backus have made IGPP the "Home of Modes". I would have never been able to do my research had I not been able to build on the know-how which has accumulated at IGPP over the last three decades of continued research in the field of normal modes.

I would like to thank Bernard Minster, Rick Salmon and John Rice for serving on my thesis committee. The IGPP faculty has a number of excellent teachers and I would like to thank specifically Bob Parker for teaching the courses "Essentials in Geophysics" and "Inverse Theory". The rigor of Bob's solutions to geophysical problems gave me a standard to aim for early on in graduate school.

All the work in this thesis is based on recordings of large earthquakes, and it is only thanks to the efforts by network managers and station operators of the IDA, GDSN, GEOSCOPE and, most recently, IRIS networks, that mode studies such as presented in this thesis are possible. Special thanks go to Trung Nguyen who does a meticulous job writing the bimonthly IDA data tapes and never became tired of my special data requests.

Upon the invitation of Walter Zürn I worked for three months at the Black Forest Observatory

(BFO) in Germany. During my stay there the Macquarie rise earthquake occurred and Walter generously provided me with the recordings from all the instruments at BFO. Walter also pointed out to me that the mode ${}_0T_2$ had been recorded by the Invar strain meters, and he stimulated much of the work presented in Chapter 4.

I have benefited much from my fellow graduate students with whom I've shared an office, a computer room and many long working hours. Discussions with Mike Ritzwoller, Bob Woodward and Mark Smith have helped me understand low-frequency seismology and in several places of this thesis I was able to build on analytical techniques and results described in their these. The contact with non-mode students has helped me broaden my scientific horizons. I would like to thank Kristine Larson, Dahlia Lahav, Jennifer Scott, Michael Hedlin and Mary Kappus for their comradeship. The many questions from the new generation of global seismology students, Harold Bolton and Joydeep Bhattacharyya, have helped me rethink many concepts of which I had only a loose idea.

I've had the pleasure to know many graduate students outside of IGPP and together we've explored much of the southwestern United States and Baja California. These trips were certainly the highlights of my stay in San Diego. In particular I have enjoyed the company of John, Alessandra, Dan, Montse, Walter, Ashley, Robin and Mark.

When I needed it, my family and friends back home have not shied away from any effort to support me. I am grateful for that, and hope I will be able return many favours once I am back in Europe.

Finally, I would like to thank Jela for her love. Jela also reminded me that there is more than one way to look at the world, and that the scientific method is only one of them.

Vita

October 16, 1958 – Born – Basel, Switzerland

1985	Dipl. Natw., Eidgenössische Technische Hochschule, Zürich, Switzerland.
1983–1984	Research Assistant, Department of Geology, Arizona State University, Tempe, Arizona.
1985–1991	Research Assistant, Institute of Geophysics and Planetary Physics, University of California, San Diego.
1991	Ph.D., Earth Sciences, University of California, San Diego.

Publications

Buland, R., D. A. Yuen, K. Konstanty and R. Widmer, Source Phase Shift: A New Phenomenon in Wave Propagation due to Anelasticity. *Geophys. Res. Lett.* ,**12**, 569-572, 1985.

Sabadini R., D. A. Yuen and R. Widmer, Constraints on short-term mantle rheology from $\dot{J}_2$ observations and the dispersion of the 18.6 y tidal Love number. *Phys. Earth. Planet. Inter.* , **38**, 235-249, 1985.

Widmer R., G. Masters and F. Gilbert, Spherically Symmetric Attenuation within the Earth from Normal Mode Data. *Geophys. J. Int.*, **104**, 541–553, 1991.

Abstracts

R. Widmer, G. Masters and F. Gilbert, The Spherical Earth Revisited, *TERRA cognita*, **8**, 1988.

R. Widmer, G. Masters and F. Gilbert, The Spherically Symmetric Earth: Observational Aspects and Constraints on new Models, *EOS Trans. AGU*, **69**, 1310, 1988.

R. Widmer and G. Masters, The long-period moment tensor of the Loma Prieta earthquake from IRIS/IDA data, *EOS Trans. AGU*, **71**, 290, 1990.

R. Widmer, G. Masters and F. Gilbert, Anomalously Split Modes: New Observations and Possible Causes, *EOS Trans. AGU*, **71**, 1479, 1990.

Fields of Study

Major Field: Geophysics

Studies in Geophysics	Professor R. L. Parker
Studies in Seismology	Professor J. F. Gilbert
Studies in Earth Structure	Professor T. G. Masters
Inverse Theory	Professor R. L. Parker

ABSTRACT OF THE DISSERTATION

The Large-Scale Structure of the Deep Earth as Constrained by
Free-Oscillation Observations

by

Rudolf Widmer

Doctor of Philosophy in Earth Sciences
University of California, San Diego, 1991
Professor T. Guy Masters, Chairperson

Large earthquakes are capable of exciting the elasto-gravitational free oscillations of the Earth to a detectable level. In this thesis, recordings of such earthquakes from the last 16 years are used to observe the resonance frequencies of the Earth. Given that the deviations from spherical symmetry are small, the determination of the large-scale mechanical structure of the Earth separates into two problems. Observations of the complex multiplet degenerate frequencies allow us to constrain the spherically symmetric elastic and anelastic structure and deviations from spherical symmetry can be constrained by observations of mode splitting.

Chapter two reports observations of the degenerate frequencies of 600 spheroidal and toroidal multiplets with frequencies less than 10 mHz. We pay particular attention to the assessment of bias in these observations caused by the effects of large-scale aspherical structure. Current Earth models do not predict correctly our observations and we present a new model, CORE11, which goes a long way to fitting the new dataset. We are unable to find models which adequately fit the frequencies of modes sensitive to core structure.

In chapter three, we use two techniques, which explicitly take the effect of large-scale aspherical structure into account to estimate degenerate frequency and axisymmetric degree 2 structure coefficients of 10 core-sensitive multiplets in the frequency band 5-10 mHz. We show that axisymmetric structure in the inner core cannot explain the anomalous splitting of core-sensitive multiplets. Our analysis of the data leads us to suggest that the cause of anomalous splitting is in the outer core. In chapter four we use recordings of the 1989 Macquarie rise earthquake to analyze the lowest order fundamental toroidal modes and we report the first unambiguous observation of the gravest toroidal mode ${}_0T_2$. Chapter five discusses the use of observations of the attenuation of free oscillations to infer the depth dependence of the intrinsic attenuation. We find that models with only five homogeneous layers can explain the data.

Observations of PKIKP equivalent modes lead to a shear Q of $110 \pm 25\%$ in the inner core. Chapter six critically summarizes the data set constraining spherically symmetric Earth structure.

Chapter 1

Introduction

For a geophysicist, the fact that we know so little about the interior of the Earth is motivation enough to try and learn more about it. For those readers who do not settle for this motivation – geophysicists or not – we might add that the phenomena which shape the Earth's surface over millions of years are driven by processes which are rooted in the Earth's mantle and core.

This thesis deals with the large-scale structure of the Earth as revealed by seismic observations. There are several reasons for doing this kind of research. First and foremost is the fact that seismology, of all the geophysical disciplines, gives the most detailed view of the one-dimensional (1-D) and three-dimensional (3-D) structure of the Earth. The resulting maps of velocity variations can, in principle, tell us about the way the Earth is convecting and evolving. A secondary issue is that 3-D structure can mask the signature of rupture propagation in seismograms and better structural models lead to better understanding of the earthquake source.

The study of global-scale Earth structure by seismological methods is a well developed field. The study of the traveltimes of high frequency seismic pulses which penetrate deep into the Earth's interior allowed early seismologists to map the major internal discontinuities which have led to the division into crust, upper and lower mantle and inner and outer core. The arrival time of a short period body wave is easy to measure accurately but the uneven distribution of the Earths natural seismicity and the seismic observatories means that large parts of the Earth's interior are not well-sampled by travel-time data sets and hence models of the Earth's large-scale structure based on such data sets may be severely biased.

Large earthquakes are capable of exciting terrestrial free oscillations to an observable level and this thesis focuses on the observation of the resonance frequencies of the Earth and their interpretation in terms of the large scale mechanical structure. The study of the Earth's free oscillations largely alleviates the sampling problem of the travel time dataset because such oscillations have long lateral wavelengths.

There are other advantages to studying free oscillation frequencies. For example, such data are insensitive to errors in earthquake location which is a problem that bedevils the study of travel times. Furthermore, free oscillation frequencies are the only data that can tell us about details of the density distribution inside the Earth.

A single mode of oscillation (singlet) of a spherically symmetric Earth model can be completely specified with 3 integer numbers: the radial order or overtone number n, the harmonic degree l and the azimuthal order m. n identifies a particular displacement pattern in the radial direction, l and m are the degree and order of the spherical harmonic describing the angular dependence of the displacement field over spherical shells. Associated with every pair of n and l are $2l+1$ azimuthal orders. The ensemble of $2l+1$ singlets is termed a multiplet and on a spherically symmetric Earth model the singlets are degenerate and oscillate with the same frequency, the degenerate frequency of the multiplet. Deviations from spherical symmetry such as the diurnal rotation, ellipticity of figure and general aspherical structure, remove the degeneracy and lead to splitting of the spectrum of individual multiplets.

The interpretation of free oscillation frequencies separates naturally into two parts. Observations of multiplet degenerate frequencies can be used to constrain the spherically averaged Earth structure. Observations of the fine structure of split multiplets can be used to constrain the aspherical structure of the Earth.

In chapter 2 we set out to estimate the degenerate frequencies of the Earth's free oscillations. We analyze recordings of large earthquakes produced by the IDA (*Agnew et al. 1976*), GDSN (*Peterson et al. 1980*) and GEOSCOPE (*Romanowicz et al. 1984*) seismic networks. When spectra are computed from recordings which are typically several days long, the resonances of the Earth stand out as tall peaks over the background noise (Figure 1.1). While the single peaks are generally well separated at frequencies below 2 mHz, the line spectrum becomes increasingly dense toward higher frequencies and identification of single peaks becomes problematic. We use the technique called "Multiplet stacking and stripping" which allows us to observe individual multiplets up to a frequency of 10 mHz. We arrive at a dataset of 620 multiplet degenerate frequencies with which we can constrain the spherically symmetric mechanical structure of the Earth. We find that recent models do not fit our observations. While we are able to find new mantle models which fit the modes sensitive to structure in the mantle we are unable to find a model for the core which, on average, fits the degenerate frequencies of the modes sensitive to structure in the core to better than 2.5 times the observational uncertainty. Our inability to fit the degenerate frequencies of core-sensitive modes leads us to reexamine and expand our data set of degenerate frequencies, using techniques which take explicit account of the effect of three-dimensional structure. We are specifically

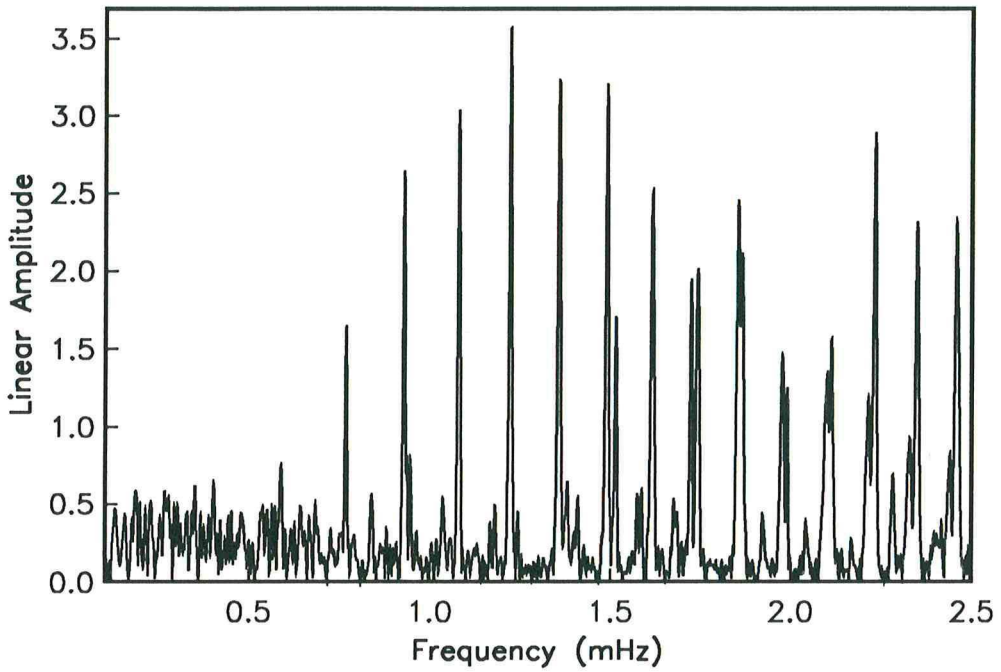

Figure 1.1 Linear amplitude spectrum a recording of the Macquarie rise earthquake (May 23, 1989). The recording was made with an Askania pandulum oriented in the E-W direction and located at the Black Forest Observatory. The timeseries used to compute this spectrum starts 2 hours after the event and is 79 hours long. A Hanning taper was used to reduce spectral leakage. The regularly spaced peaks are the fundamental toroidal modes starting with ${}_0T_3$ at a frequency of 0.59 mHz.

concerned with the question of whether our difficulties with modeling the core stems from unidentified bias in the data set or whether it is an indication of a structural complication in the core which our parameterization of the model does not allow.

The modes which place the strongest constraints on the structure of the core generally have a high Q value and are of low harmonic degree. There are two well established techniques which lend themselves to the analysis of this type of mode: "Singlet stripping" and "Iterative spectral fitting". In chapter 3 we use both techniques to identify and resolve the fine structure of several previously unobserved core-sensitive multiplets. Such multiplets are commonly very broadly split and are thus termed "anomalously split". From our dataset of 20 anomalously split multiplets, we find that there is no correlation between the degree of splitting and the amount of elastic energy these multiplets have in the inner core. This leads us to the conclusion that aspherical structure or axisymmetric anisotropy in the inner core, both of which have been invoked to explain anomalous splitting (*Poupinet et al. 1983*; *Morelli et al. 1986*; *Woodhouse et al. 1986*; *Shearer et al. 1988*; *Li et al. 1991*), cannot be the sole cause of anomalous splitting. We are thus led to reevaluate potential causes for anomalous splitting located in

the outer core.

While the approximations made in the singlet stripping technique are very restrictive, it can be used to analyze multiplets with relatively low signal-to-noise ratio. In iterative spectral fitting on the other hand, the effect of aspherical structure on the spectrum of a multiplet is fully specified through a set of "structure coefficients". The objective of the method is to match the observed data spectra with synthetic spectra by varying the structure coefficients. The method requires that the individual data spectra have a relatively high signal to noise ratio for the algorithm to converge. We find it to work best if we use only recordings from the 5 earthquakes which have most efficiently excited PKIKP equivalent modes in the last 15 years.

To determine the aspherical structure of the Earth from a set of structure coefficients we have to solve a linear inverse problem. In general, aspherical structure of a single harmonic degree and order is parameterized using three functions of radius: the perturbation in density, bulk modulus and shear modulus plus the height of topography on all first order discontinuities. In order to stabilize the inversion, we reduce the degrees of freedom to a single function of radius by requiring a constant scaling between perturbations in density on the one hand and perturbations in shear and bulk modulus on the other hand. The scaling between these different perturbations can be constrained both with seismic observations and laboratory experiments. To further stabilize the inversion and reduce the tradeoff between perturbations of the boundaries and volumetric perturbations in adjacent regions, we require that the perturbation of the core-mantle boundary be dynamically consistent with the geoid and current viscosity models of the mantle. The inversion experiments show that the only structure coefficients which cannot be explained with structure in the mantle alone are the c_2^0 estimates. The interpretation of the c_2^0 structure coefficients of anomalously split multiplets requires large amounts of structure in the core and we perform several experiments to identify the structure responsible for this splitting.

In chapter 4 we employ the machinery established in chapters 2 and 3 to analyze the previously neglected low order fundamental toroidal modes. There are several reasons for the difficulties involved in observing low order toroidal modes: toroidal modes are highly attenuated so that their signal decays rapidly into the noise; toroidal modes are horizontally polarized so that only recordings of horizontal seismic sensors can be used – this is unfortunate since ambient noise levels on horizontal sensors are at least an order of magnitude larger than on vertical sensors. Furthermore, seismic sensors with a transfer function suitable for the detection of horizontally polarized modes below 1.5 mHz have only been deployed routinely since 1986.

We use the recordings of the Macquarie rise earthquake to resolve the splitting of some of

the low order toroidal modes and simultaneously obtain estimates of the multiplet degenerate frequency and Q. We also believe that this work provides the first unambiguous detection of the mode ${}_0T_2$. We use the multitaper spectral analysis technique (*Thomson, 1982*; *Park et al. 1987*; *Lindberg et al. 1987*) which has been proven to have superior detection capabilities over conventional periodogram/spectral estimates in low signal-to-noise environments to demonstrate that previously reported detections based on the Isabella strain meter record of the 1960 great Chilean earthquake are unreliable at best.

Singlet stripping not only allows us to estimate the singlet frequencies but we can also obtain an estimate of the singlet Q. It is consistent with the assumptions of singlet stripping to estimate the multiplet Q by averaging the singlet Q values. In chapter 5, we use these newly observed Q values together with Q observations of fundamental modes derived from single record measurements (*Smith and Masters, 1989*), to infer the distribution of attenuation of seismic energy within the Earth. Singlet stripping has allowed us to expand the Q data set of core-sensitive modes. We now have a sufficient number of multiplet Q values of PKIKP equivalent modes to allow us to constrain inner core shear attenuation without having to use unreliable observations of inner core shear modes. We solve a linear inverse problem and seek models of the spherically symmetric attenuation within the Earth which are smoothly varying functions of depth. We find that the resolving power of the data is very poor and that simple models with only six layers can satisfy our observations. The results of this work have now been published (*Widmer et al. 1991*).

The last chapter summarizes the progress made in the research and assesses the outlook for the interpretation of the degenerate frequency dataset in terms of new 1-D models.

References

Agnew, D.C., J. Berger, R. Buland, W. Farrell, and F. Gilbert, International deployment of accelerometers: A network for very long period seismology. *EOS Trans. AGU*, **57**, 180–188, 1976.

Lindberg, C.R., and J. Park, Multiple-taper spectral analysis of terrestrial free oscillations: Part II. *Geophys. J. R. Astron. Soc.*, **91**, 795–836, 1987.

Li, X.-D., and D. Giardini J. H. Woodhouse, Large-Scale Three -Dimensional Even -Degree Structure of the Earth from Splitting of Long-Period Normal Modes. *J. Geophys. Res.*, **96**, 551–577, 1991.

Morelli, A., A.M. Dziewonski, and J.H. Woodhouse, Anisotropy of the inner core inferred from $PKIKP$ travel times. *Geophys. Res. Lett.*, **13**, 1545–1548, 1986.

Park, J., C.R. Lindberg, and D. Thomson, Multiple-taper spectral analysis of terrestrial free oscillations: Part I. *Geophys. J. R. Astron. Soc.*, **91**, 755–794, 1987.

Peterson, J., C.R. Hutt, and L.G. Holcomb, *Test and calibration of the SRO observatories.* U.S.G.S. Report, 1980.

Poupinet, G., R. Pillet, and A. Souriau, Possible heterogeneity of the earth's core deduced from $PKIKP$ travel times. *Nature*, **305**, 204–206, 1983.

Romanowicz, B., M. Cara, J.F. Fels, and G. Roult, GEOSCOPE; a French initiative in long period three component global seismic networks. *EOS Trans. AGU*, **65**, 753–756, 1984.

Shearer, P.M., K.M. Toy, and J.A. Orcutt, Axi-symmetric earth models and inner core anisotropy. *Nature*, **333**, 228–232, 1988.

Smith, M.F., and G. Masters, Aspherical structure constraints from free oscillation frequency and attenuation measurements. *J. Geophys. Res.*, **94**, 1953–1976, 1989.

Thomson, D.J., Spectrum estimation and harmonic analysis. *IEEE Proc.*, **70**, 1055–1096, 1982.

Widmer, R., G. Masters, and F. Gilbert, Spherically symmetric attenuation within the Earth from normal mode data. *Geophys. J. Int.*, **104**, 541–553, 1991.

Woodhouse, J.H., D. Giardini, and X.-D. Li, Evidence for inner core anisotropy from free oscillations. *Geophys. Res. Lett.*, **13**, 1549–1552, 1986.

Chapter 2

Observational Constraints on the Spherically Averaged Earth Structure

Abstract

Spherical models of the Earth play an important role in geophysics but many aspects of the structure of spherical models are uncertain. A better "terrestrial monopole" is needed for many different kinds of problems. In low frequency seismology, the study of strongly coupled modes and the interpretation of strongly split multiplets requires a model which predicts extremely accurate eigenfrequencies and eigenfunctions. Furthermore, spherical models are the starting point for many investigations of aspherical structure and source mechanisms and so they must be as precise as possible. The spherically averaged structure can also tell us about the thermal and chemical structure of the Earth but the resolution we can currently achieve is less than what is needed.

In this chapter we demonstrate that we are able to improve the quality of the existing constraints on the spherically-averaged structure by removing systematic errors and reducing standard deviations (by as much as a factor of ten). We have constructed a new dataset of 620 multiplet degenerate frequencies with periods longer than 100 seconds and demonstrate that relatively small perturbations to existing Earth models allow the fit to the data to be greatly improved. The availability of supercomputer facilities has allowed us to search model space for different classes of models which fit the data. Many of these models go a long way to fitting the new data but we have had a persistent difficulty in finding a model which gives an acceptable fit to all the data.

2.1 Introduction

Several years have elapsed since the last effort to produce a model of the spherically averaged Earth structure (*Dziewonski and Anderson, 1981*). Since that time, attention has turned to the evaluation of the large-scale aspherical structure of the Earth which in turn has improved our understanding of the effect of aspherical structure on seismic spectra. These effects can be very large (particularly in the case of anomalously split multiplets discussed in the next chapter) and it is clear that some of the mode frequencies used to construct spherically averaged Earth models are systematically biased. Assessment of this bias allows the reduction of the observational errors of some of the degenerate frequencies by as much as a factor of ten. We then find that existing spherically averaged models do not provide an adequate fit to the data.

An accurate spherical Earth model is essential for several problems in low-frequency seismology. For example, strong coupling between free oscillations depends critically on the frequency separation of modes. Obvious examples of predicted strong coupling occur between spheroidal and toroidal fundamental modes, *e.g.*, ${}_0S_{11} - {}_0T_{12}$, ${}_0S_{19} - {}_0T_{20}$ and ${}_0S_{32} - {}_0T_{31}$. The latter of these is very poorly predicted by current spherically averaged models. Variations of a few microhertz between the degenerate frequencies of potentially coupled modes can radically affect the nature of the coupling and it is clearly important to have a better model to study this effect.

A subset of modes have characteristics which are very strongly model dependent. These are modes which have classical turning points close to a discontinuity in structure. A small change in Earth properties near this discontinuity can cause strong changes in mode eigenfrequency and eigenfunction. There are a few instances where a core mode is very close in frequency to a $PKIKP$ equivalent mode or shear mode with the same harmonic degree, l. Some examples are ${}_6S_2 - {}_7S_2$, ${}_{10}S_2 - {}_{11}S_2$, ${}_5S_{10} - {}_6S_{10}$ and ${}_{11}S_8 - {}_{12}S_8$. Small changes in properties near the inner core boundary or within the inner core lead to large changes in the eigenfunctions with the mode pairs sometimes exchanging identities. For example, model 1066B has ${}_{10}S_2$ as a core mode and ${}_{11}S_2$ as a $PKIKP$ mode, but the identities are exchanged for model 1066A. Even some of the most recent models are incorrect in this respect, and there is a clear need for improvement now that unambiguous observations show that ${}_{10}S_2$, the $PKIKP$ mode, is also anomalously split.

Source mechanism retrieval over large frequency bands is also sensitive to the spherically averaged structure. For example, many models do not accurately predict the average group velocity of

surface waves, particularly Love waves. This leads to spurious variations in the inferred source duration and complexity. Little is known about attenuation at periods shorter than 150 – 200 seconds and a poor attenuation model can again lead to spurious source parameters.

Finally, we note that an accurate spherically averaged structure is of general interest to the geophysical community. Existing models have been used to help infer the chemistry and mineralogy of the mantle, the thermal state of the mantle and core, the existence of energy sources for the geodynamo and much more. Often it is the radial gradient of the model parameters (*e.g.*, density) which is the parameter of interest and it is perhaps true that some of the features of current models have been over-interpreted. Thus, for the model to be of use, we must have a clear idea of its precision and the resolution of its features.

Clearly, a model will only be as good as the data which goes into its construction. Current Earth models are constructed using a large dataset of free oscillation degenerate frequencies together with some travel-time information to aid resolution of fine-scale structure. There is bias in this dataset caused by coupling between free oscillations, mode misidentification and inadequate geographical coverage of the primary dataset which is now over 20 years old. In the last decade, several thousand digital long-period recordings of large earthquakes have been accumulated and it is now possible to assess (and sometimes remove) the bias in the existing dataset. Most of this chapter is devoted to the construction of an improved free oscillation dataset. We will close the chapter by presenting one model, CORE11, which was obtained by looking for the smallest and smoothest perturbation to PREM, necessary to fit the new observations.

2.2 Estimating Degenerate Frequencies

One single method cannot give accurate degenerate frequencies for all modes and, in fact, we have used four methods of degenerate frequency estimation:

1) Histogram analysis of peak-frequency measurements from single recordings. The measurements must be corrected for the signal from 3-D structure (*Silver and Jordan, 1981*; *Masters and Gilbert, 1983*; *Roult and Romanowicz, 1984*; *Romanowicz et al. 1987*, *Davis, 1987*; *Smith and Masters, 1989*; *Roult et al. 1990*).
2) Multiple-record analysis to isolate the individual singlets of a multiplet so that a reliable mean can be estimated (*Buland et al. 1979*; *Ritzwoller et al. 1986*)
3) Fitting of the spectra of split multiplets including the effects of aspherical structure as well as

a perturbation to the degenerate frequency (*Giardini et al. 1987, 1988*; *Ritzwoller et al. 1986, 1988*; *Li et al. 1991*).

4) Multiple-record analysis ignoring 3-D structure (this technique is called "multiplet stripping", see *Gilbert and Dziewonski, 1975*).

Many of our measurements have been determined using more than one of these techniques allowing some sources of bias to be estimated. The first three methods have recently been applied to large datasets and are described elsewhere. In this chapter we shall concentrate on multiplet stripping. This is the technique which was used to estimate most of the degenerate frequencies used to construct current spherically-averaged Earth models though it can give biased results unless great care is taken. We are encouraged to try it because spherical Earth synthetic seismograms usually fit the observations quite well suggesting that aspherical structure effects can be treated as noise (albeit with a large variance). To make multiplet stripping work we require a good geographical coverage of high quality three-component seismic recordings, reasonably accurate source mechanisms, a reasonably accurate spherically averaged structure, and a good knowledge of the instrument responses. As we shall show below, even with all these conditions satisfied, multiplet stripping can fail for some modes.

Our data sources are the IDA network, the SRO, ASRO and CDSN networks of the GDSN and the GEOSCOPE network. The IDA network records only vertical component data while the other networks record three components of ground motion. The IDA, GEOSCOPE and CDSN data are intended for normal mode work and are consequently well-calibrated and easy to use. The SRO and ASRO instruments have a poorer low-frequency response but for relatively large events, have a usable signal down to a frequency of about 1mHz. Figure 2.1 shows amplitude spectra of recordings of a typical event (moment $\sim 10^{20}$Nm). The ASRO recordings are typically of similar quality to the IDA recordings in this frequency band while the SRO response is poorer below about 3mHz. We have found that the original DWWSSN and RSTN recordings are presently too noisy at long periods to justify the considerable effort required to use them, however the upgraded DWWSSN are similar in quality to the GEOSCOPE and CDSN arrays.

We have edited 50 hours of data for all recordings of events with a moment in excess of 5×10^{19}Nm. The editing procedure involves the removal of Earth tides, the interpolation of short lengths of "bad" data caused by instrumental malfunction, and the zeroing of large panels of bad data. Nearly all time-series have some panel structure after editing and it is not feasible to account correctly for this in the stripping procedure. We therefore discard records which have more than 25% of their length zeroed or which start with a gap longer than 10% of the entire record.

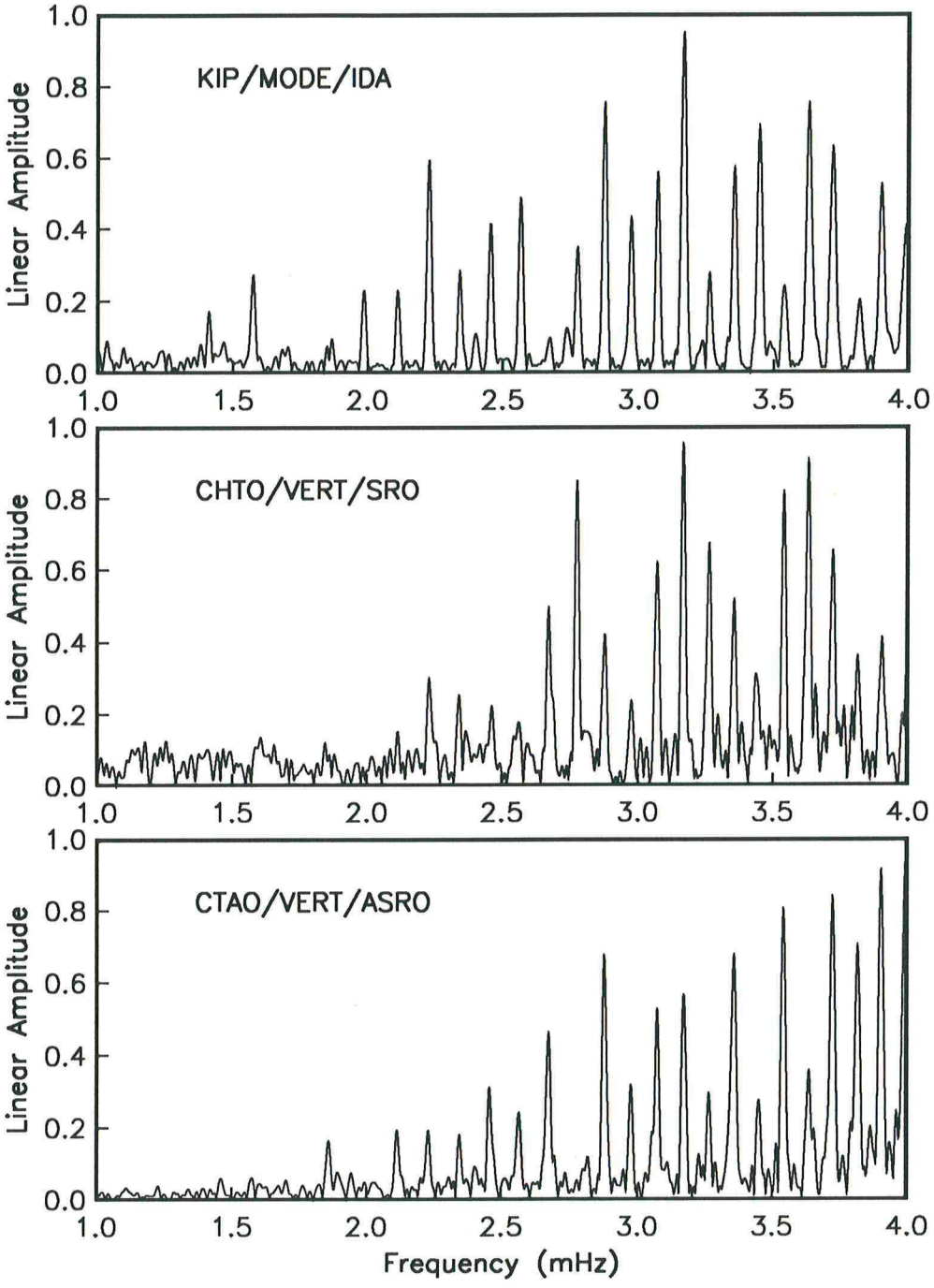

Figure 2.1 Spectra of 30 hour Hanning tapered recordings from an IDA instrument (KIP), the vertical component of an SRO instrument (CHTO) and the vertical component of an ASRO instrument (CTAO). The SRO instruments are generally of slightly inferior quality in this frequency band. All three records are from the Iranian event (September 16, 1978) which had a source depth of 7 km and a scalar moment of 1×10^{20} Nm.

More subtle problems in the data (*e.g.*, timing errors, polarity errors, multiplexing errors and gross calibration errors) only become obvious after comparison with synthetic seismograms and so we routinely estimate source mechanisms for all large events. At frequencies lower than about 8mHz, existing spherically averaged models of elastic structure (*e.g.*, 1066A, *Gilbert and Dziewonski, 1975*; PREM, *Dziewonski and Anderson, 1981*), and attenuation structure (*Masters et al. 1983*; *Widmer et al. 1991*) are sufficiently accurate to allow retrieval of a reliable source mechanism. We have found that, at these frequencies, the source can be adequately characterized by the six elements of the zeroeth order seismic moment rate tensor and a source time function. This latter feature is necessary to account for the fact that the low frequency centroid time of the event is not necessarily the same as the origin time deduced from body wave arrivals (*Backus, 1977*; *Dziewonski and Woodhouse, 1983*). We use a triangle function for the source time function though the exact form is not important as far as the quality of the fit to the data in this frequency band is concerned. We have also found that mislocation of the spatial centroid of the event does not significantly degrade the fit to the data in this frequency band though it is possible to find an optimum location (*Dziewonski et al. 1981*). Source retrieval is, in principle, a straightforward operation (*e.g.*, *Buland and Gilbert, 1976*) though linear fitting for the elements of the seismic moment tensor does not always succeed. The main problem is phase mismatching due to the presence of aspherical structure leading to a bias toward low moment. This can be overcome by modifying the source orientation to give, as best as possible, the observed distribution of power at all stations recording the event. We demonstrate the results of this technique with three events. The first is a deep event in the Banda Sea ($h = 450$ km). Linear fitting works extremely well for deep events ($h > 400$ km) and both the frequency and time domain fits look extremely good (Figure 2.2). The second event is a shallow earthquake in Iran ($h = 7$ km) and overall the fit is acceptable (Figure 2.3). The final event is an intermediate depth earthquake in the Kuriles ($h = 91$ km). For reasons which we do not fully understand, we are unable to find a source which produces good waveforms at all stations (Figure 2.4). This happens in about 30% of shallow and intermediate earthquakes and appears to be independent of source size.

In general, the fit to the SRO and ASRO recordings is poorer than the fit to the IDA records. In part this is due to the fact that horizontal recordings are somewhat noisier than vertical recordings and in part it is due to the poorer long period calibrations of the GDSN instruments. (These fits include the improved sensitivity calibrations of *Woodward and Masters, 1989*.) If we exclude events which are not modeled well by our chosen source parameterization and spherical Earth Green's functions we are still left with a very large dataset with which we can perform multiplet stacking and stripping (*Gilbert and*

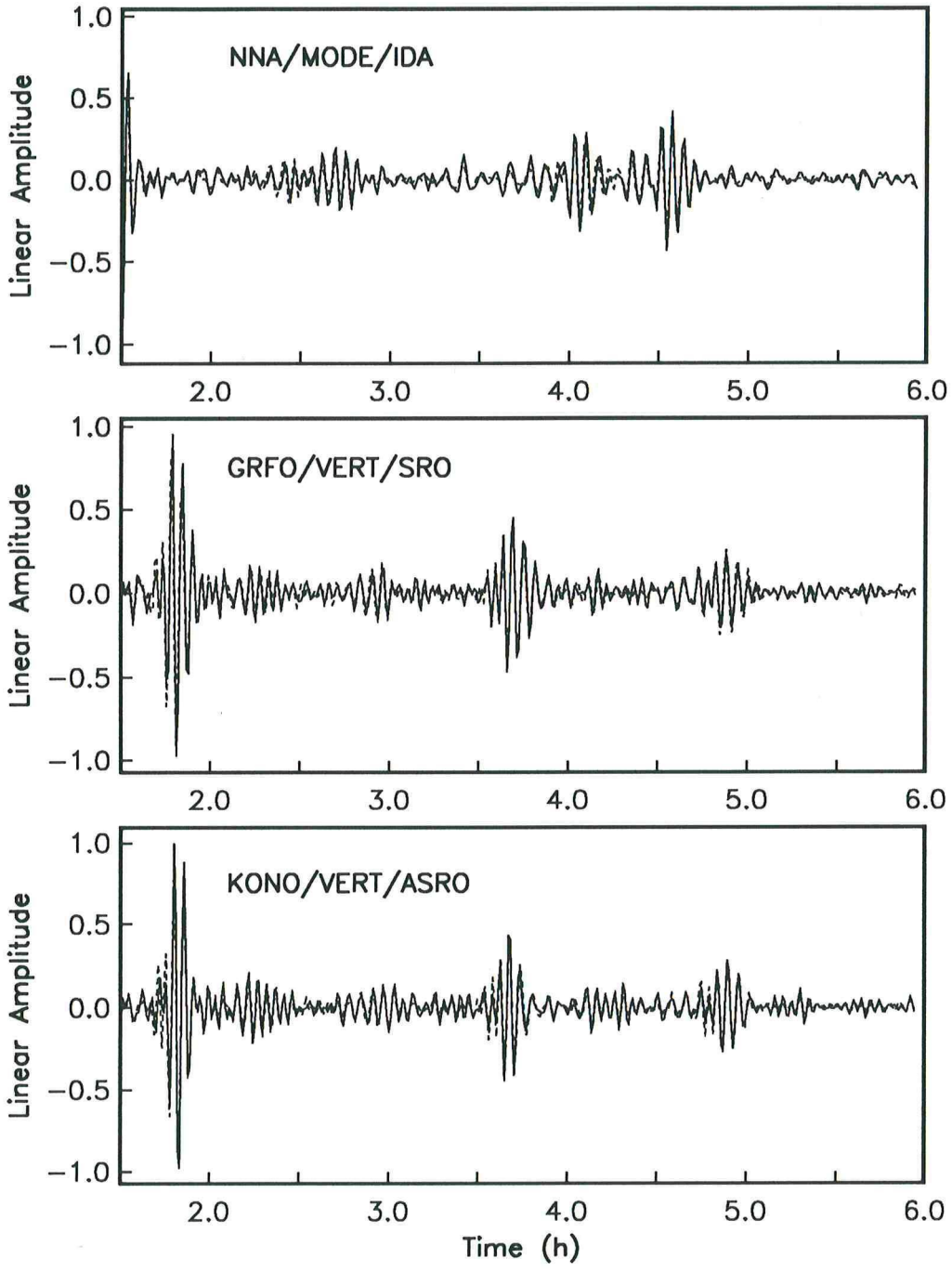

Figure 2.2 Comparisons of spherical Earth synthetic seismograms (dashed lines) with data (solid lines) for an IDA instrument (NNA), an SRO vertical component (GRFO) and an ASRO vertical component (KONO). These recordings are from a large deep event in Banda Sea (June 22 1982, depth: 450km, scalar moment: 1.4×10^{20} Nm) and have been low passed with a filter corner at 6.5 mHz.

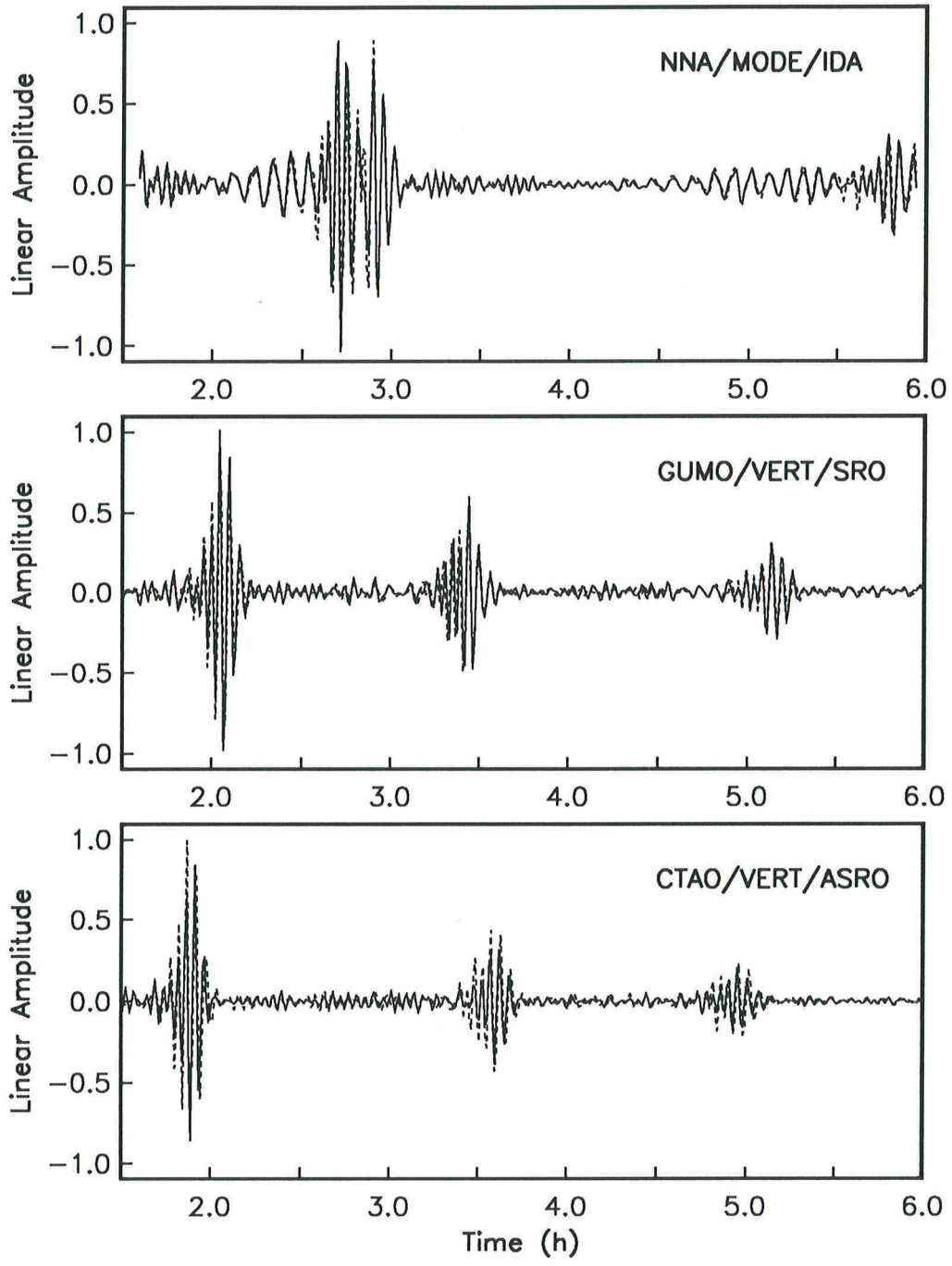

Figure 2.3 Comparisons of synthetic seismograms with data for an IDA instrument (NNA), and SRO vertical component (GUMO) and an ASRO vertical component (CTAO). These recordings are from a large shallow event and the fits are acceptable. The records are from the same event as in Figure 2.1.

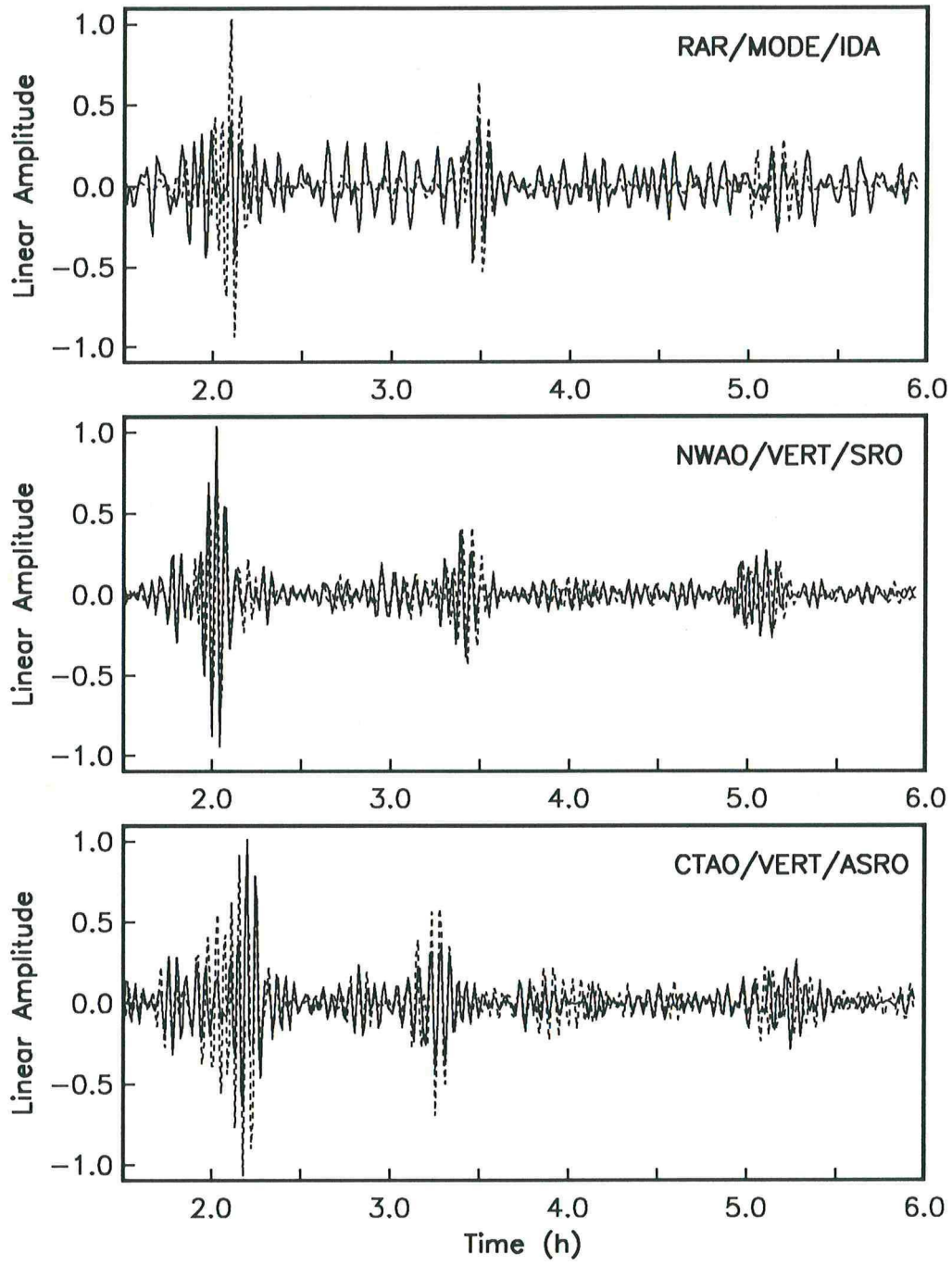

Figure 2.4 Comparisons of synthetic seismograms with data for recordings from a large, intermediate depth event in Kuriles (December 6 1978, depth: 175 km, scalar moment: 4.2×10^{20} Nm). Several recordings from this event are very badly fit (*e.g.*, RAR).

Dziewonski, 1975). The dataset used in the experiments reported in this paper consists of roughly 3500 recordings from 120 well-distributed large events.

We consider small frequency bands in which a known number of multiplets lie. The object of stacking and stripping is to retrieve the multiplet resonance functions and then measure their center frequencies (the spectral widths of the resonance functions also provide estimates of the attenuation rates of the multiplets). The basic problem to be solved is described by a simple linear system

$$\mathbf{u}(\omega) = \mathbf{A}\,\mathbf{c}(\omega) \tag{2.1}$$

$\mathbf{u}(\omega)$ is a vector consisting of the observed complex spectra corrected for instrument response and source phase, $\mathbf{c}(\omega)$ is a vector of the complex spectra of the multiplet resonance functions and $\mathbf{A}$ is a matrix of computed multiplet excitation factors. For small frequency bands, $\mathbf{A}$ may be regarded as being independent of frequency so the linear system can be solved for each frequency independently. This leads to very fast algorithms for stripping which is symbolically represented by the equation

$$\hat{\mathbf{c}}(\omega) = \mathbf{A}^{-1}\mathbf{u}(\omega) \tag{2.2}$$

where $\mathbf{A}^{-1}$ is a generalized inverse of the matrix $\mathbf{A}$. The resulting $\hat{\mathbf{c}}(\omega)$ are termed "strips." We use an SVD algorithm to form the generalized inverse. This process is described in several excellent references (*e.g., Lawson and Hanson, 1974*).

Stacking generally works less well than stripping and is represented by the operation

$$\hat{\mathbf{s}}(\omega) = \mathbf{A}^{T}\mathbf{u}(\omega) = \mathbf{A}^{T}\mathbf{A}\,\mathbf{c}(\omega) \tag{2.3}$$

With a good geographical coverage, $\mathbf{A}^{T}\mathbf{A}$ tends to become diagonal so the "stacks," $\hat{\mathbf{s}}(\omega)$, become proportional to the multiplet resonance functions $\hat{\mathbf{c}}(\omega)$.

A naive implementation of the above algorithms gives extremely poor results. For example, to reduce spectral leakage, we must work with tapered spectra. The taper must be identical for all recordings so we align records in time to account for the source time constant and for the different sampling of time series relative to the effective origin time of the event. Stacking and stripping now results in tapered resonance functions which are easier to evaluate than untapered ones (see below). The application of a taper also complicates the removal of the instrument phase. Simple division of the vector $\mathbf{u}(\omega)$ by the appropriate instrument response effectively changes the taper that we have applied and results in resonance functions which are abnormally broad. We circumvent this problem by band-passing the data

before tapering so that all records appear to come from the instrument with the narrowest pass band which is, in our case, the SRO. This filtering can be accomplished with a short convolution filter.

Even now, for stacking and stripping to work, we must employ a relative weighting scheme for different recordings. Several factors must be considered. First, we are using a spherical Earth approximation to model the excitation of split multiplets, *i.e.*, we are treating them as perfectly collapsed multiplets. The error incurred by doing this increases proportionally with the size of the event so it makes sense to normalize the records by the moment of the event. This weighting also has the advantage of improving the effective geographical coverage because the resulting strips are not dominated by a few records from the largest events. The disadvantage of this weighting scheme is that the signal-to-noise ratio of the strip is less than optimum. One way to desensitize the results to noisy records is to weight each record with the mean amplitude of the signal in the frequency band being analyzed. Such a scheme is essential when mixing GDSN and IDA recordings as the GDSN low frequency response appears to be poorly determined. One weighting scheme which we have found useful is

$$w_p = \bar{u}_p^{-1} \left(1 - \frac{\bar{u}_p}{u_{max}} \right) \tag{2.4}$$

where $\bar{u}_p$ and u_{max} are the mean and peak values respectively of the amplitude spectrum of the pth record in a small frequency band surrounding the target multiplet. This has the advantage of rewarding "peaky" spectra while crudely accounting for both variability in source size and noise level. For a representative set of 3000 spectra the mean amplitude $\bar{u}_p$ varies by more than two orders of magnitude and exhibits the same distribution as a histogram of earthquake magnitudes. The second factor in (2.4) only varies between 0.5 and 0.8.

A final consideration is uniformity of geographical coverage. To assess this, we use the asymptotic result that a seismogram is dominantly sensitive to structure under the great circle path joining the source and receiver (*e.g.*, *Jordan, 1978*). The density of poles of great circles of our recordings as a function of position on the surface of the Earth is then a measure of geographical coverage. We estimate the pole density at any point on the surface of the Earth by counting the number of poles in a spherical cap of radius 15° about that point. A contour map of pole density for a typical experiment is shown in Figure 2.5. If we compare this map with a map of peak shifts as a function of pole position for fundamental spheroidal modes (Figure 2.6), we find that we have a slight preponderance of fast great circles and our estimated degenerate frequencies will be slightly high for these modes.

Ideally, we would like to weight each record by the local pole density so as to achieve uniform

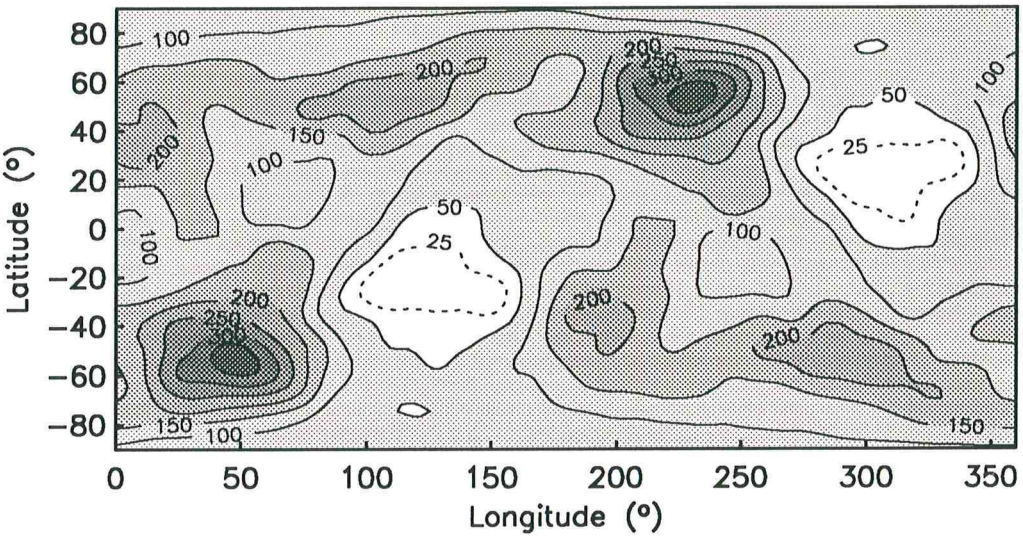

Figure 2.5 Contour map of the great circle pole density for a set of 3800 records. To bin the data we used a circular cap with a 15° radius. Both vertical and horizontal recordings of events with a scalar moment larger than 10^{19} Nm are included.

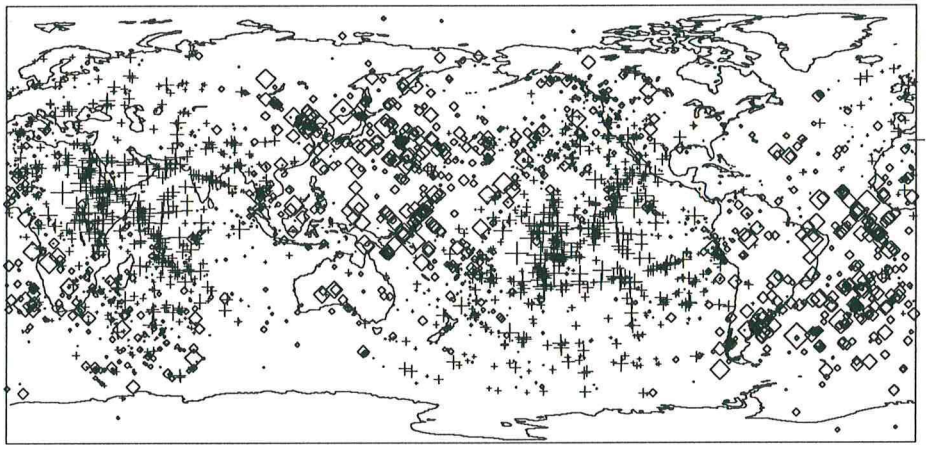

Figure 2.6 Fundamental mode peak shifts for the mode ${}_0S_{23}$ from *Smith and Masters (1989)*. Plus symbols (+) indicate fast great circles and diamonds (◇) slow ones. The size of the symbols reflects the magnitude of the frequency shift and varies by $\pm 10\mu$Hz. Note the coherent degree 2 pattern.

coverage of the globe. We have opted not to do this since a few records would be very strongly weighted and the resulting variance of the strips would be increased. In an attempt to compromise between bias and variance we have limited the maximum weight that a record can get.

The ability of stripping to separate multiplets is demonstrated in Figure 2.7. Note that overtones (*e.g.*, ${}_3S_{14}$) appear to be completely separated from highly excited nearby fundamental modes (*e.g.*, ${}_0S_{28}$).

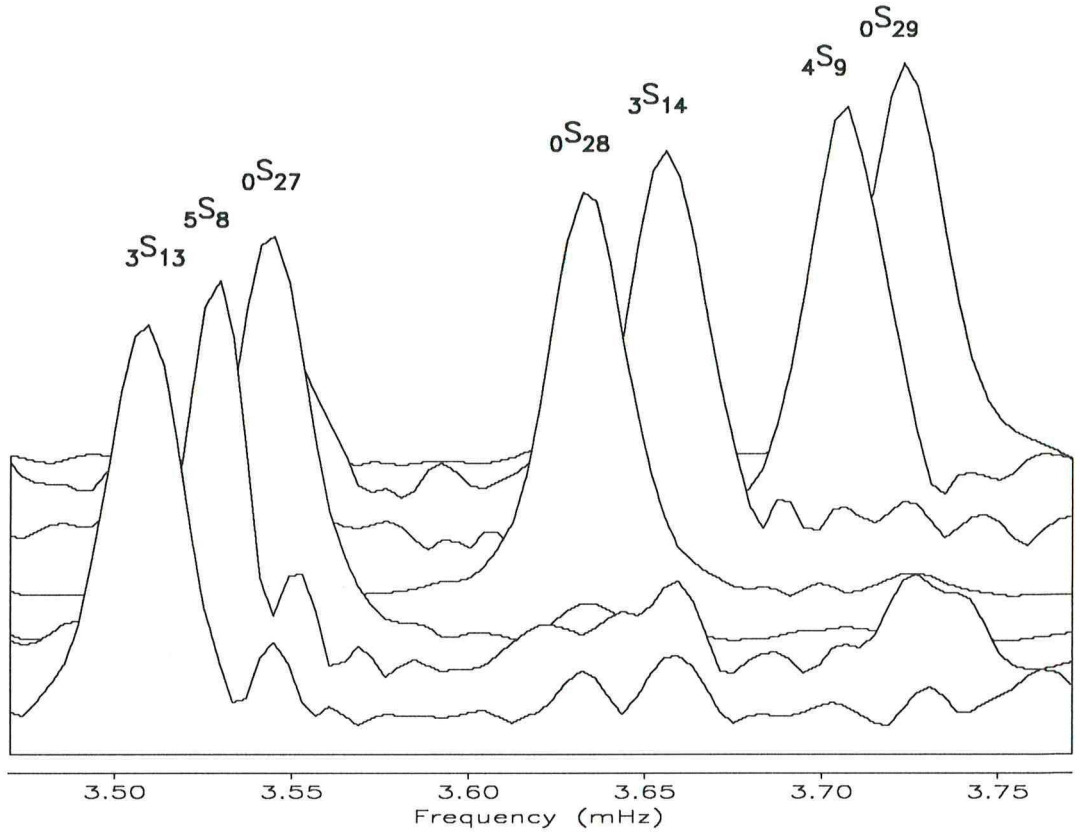

Figure 2.7 The results of multiplet stripping in a small frequency band which includes the fundamental spheroidal modes ${}_0S_{27}$ and ${}_0S_{28}$. The target multiplets are (front to back) ${}_3S_{13}$, ${}_5S_8$, ${}_0S_{27}$, ${}_0S_{28}$, ${}_3S_{14}$, ${}_4S_9$ and ${}_0S_{29}$. Note that overtones such as ${}_3S_{14}$ are clearly separated from the highly excited fundamental modes.

Both the fundamental toroidal and spheroidal modes are extremely well recovered with this technique. Figure 2.8 shows the resonance function for ${}_0S_l$ ($l = 8 \rightarrow 30$) plotted on a frequency axis relative to the predicted frequency of model PREM. Figure 2.9 is the corresponding plot for ${}_0T_l$ ($l = 8 \rightarrow 30$). These figures illustrate the biasing effects of mode-mode coupling. The distinctive kinks in the ω/l curves are due to Coriolis coupling between the two mode types and whole sequences of observations can be systematically shifted (*Masters et al. 1983*). Coriolis coupling is well understood and the apparent degenerate frequency can be reasonably accurately calculated except for very strongly coupled pairs. Most of our observations can therefore be corrected for Coriolis coupling effects. Strong coupling (*e.g.*, ${}_0S_{11} - {}_0T_{12}$, ${}_0S_{19} - {}_0T_{20}$) cannot be reliably predicted at present due to the sensitivity of the computation to the frequency spacing of the coupling multiplets and the lack of a separation into distinct lumps of energy. The dominant effect of coupling is a repelling of the coupling multiplets in real part frequency. Thus we can deduce from Figures 2.8 and 2.9 that the frequency of ${}_0S_{11}$ must be slightly greater than the

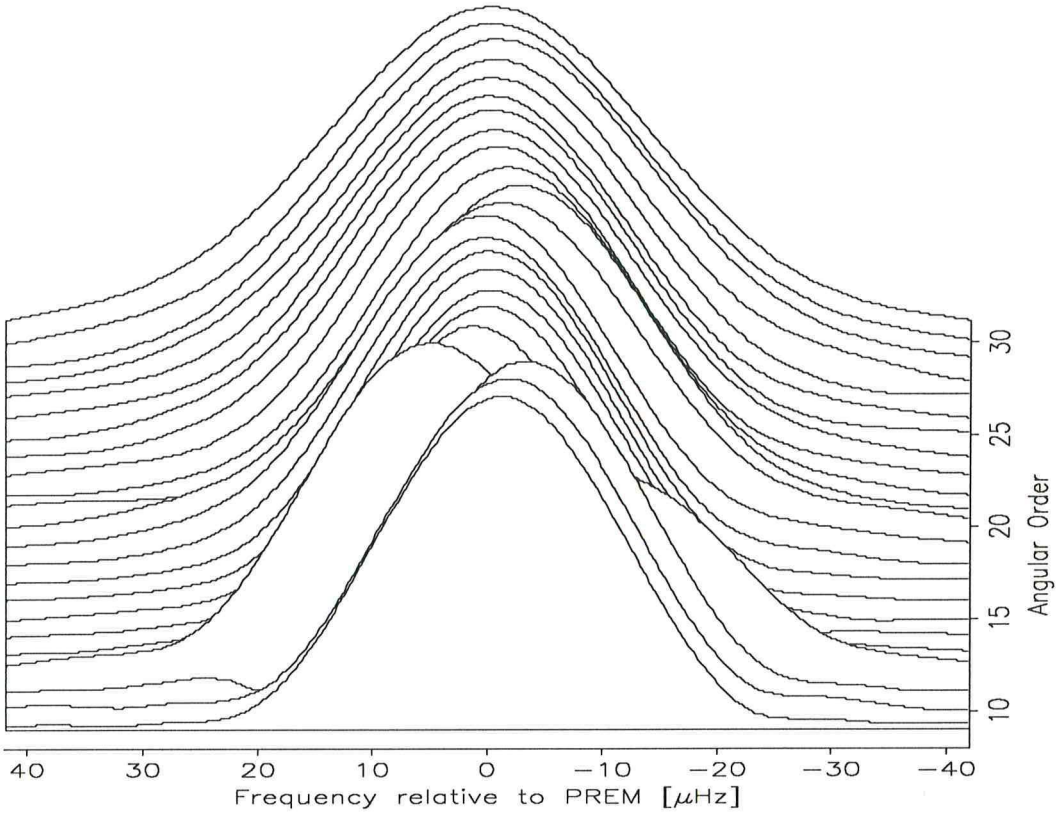

Figure 2.8 The results of stripping fundamental spheroidal modes ${}_0S_8 - {}_0S_{30}$. The strips are centered at the frequency predicted for each mode by model PREM. Note the "tears" in the peak shifts caused by Coriolis coupling to nearby toroidal modes.

frequency of ${}_0T_{12}$ for the spherically averaged Earth (similarly the frequency of ${}_0S_{19}$ must be slightly greater than the frequency of ${}_0T_{20}$). Such observational constraints can be incorporated into the inversion scheme.

The major potential source of bias in our mode measurements is caused by inadequate geographical sampling of the Earth. We wish to emphasize that, while stripping often produces excellent spectral peaks, it is difficult to assign an error to the resulting frequency measurement which realistically represents the uncertainty of the degenerate frequency. Our approach to this problem has been to compare the results of stripping with analyses which explicitly account for aspherical structure. Such an analysis was given by *Masters et al. (1982)* and has been extended with more data to give very accurate center frequencies for fundamental spheroidal modes (*Smith and Masters, 1989*). We compare these measurements with estimates of complex frequencies made from strips using the nonlinear least squares fitting technique described by *Masters and Gilbert (1983)*. Errors are assigned using the analysis of *Dahlen (1982)*. The comparison in Figure 2.10 shows that the stripping results are a little less precise

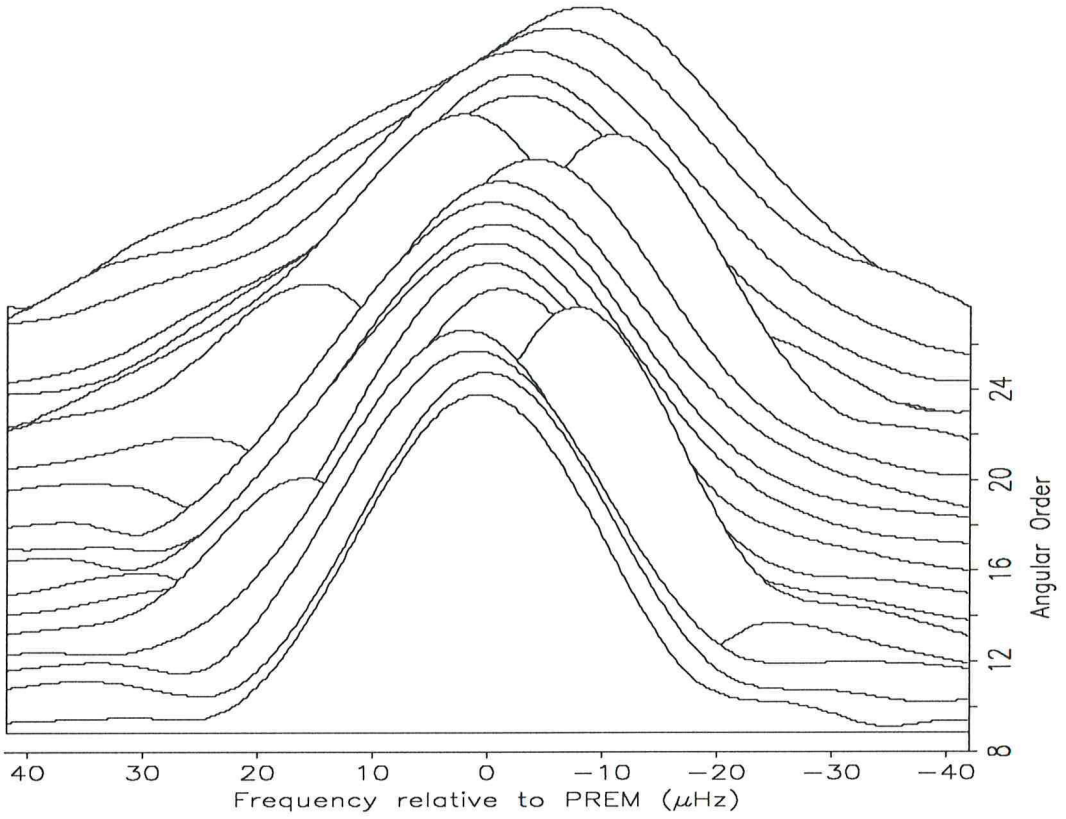

Figure 2.9 As for Figure 2.8 but for the fundamental toroidal modes ${}_0T_8 - {}_0T_{26}$. Again the "tears" in the peak shifts caused by Coriolis coupling to nearby spheroidal modes are very obvious.

and show a slight systematic deviation (at about the 1 σ level) from the results which explicitly account for 3-D structure. Experimentation with the pole-density weighting scheme shows that the fundamental spheroidal modes are, in a sense, a worst-case scenario. We found that the estimated fundamental mode degenerate frequencies are more strongly affected by changes in the weighting scheme than spheroidal overtones. This is fortunate since fundamental modes can be observed with techniques which take explicitly account of the effect of 3-D structure whereas the large majority of spheroidal overtones can only be observed with the multiplet stripping technique. The reason why fundamental modes are more affected by a change in the weighting scheme is likely to be related to the fact that the power of 3-D structure falls off rapidly with depth as suggested by recent models of the shear velocity in the mantle.

Multiplet stacking and stripping only gives unbiased degenerate frequencies when the multiplet in question has a relatively uniform frequency distribution of singlets. When a multiplet has a highly non-uniform distribution of singlets, stripping fails by giving a peak at a subset of the singlets which may have a very different frequency from the true degenerate frequency. Diagnosis of such a failure may

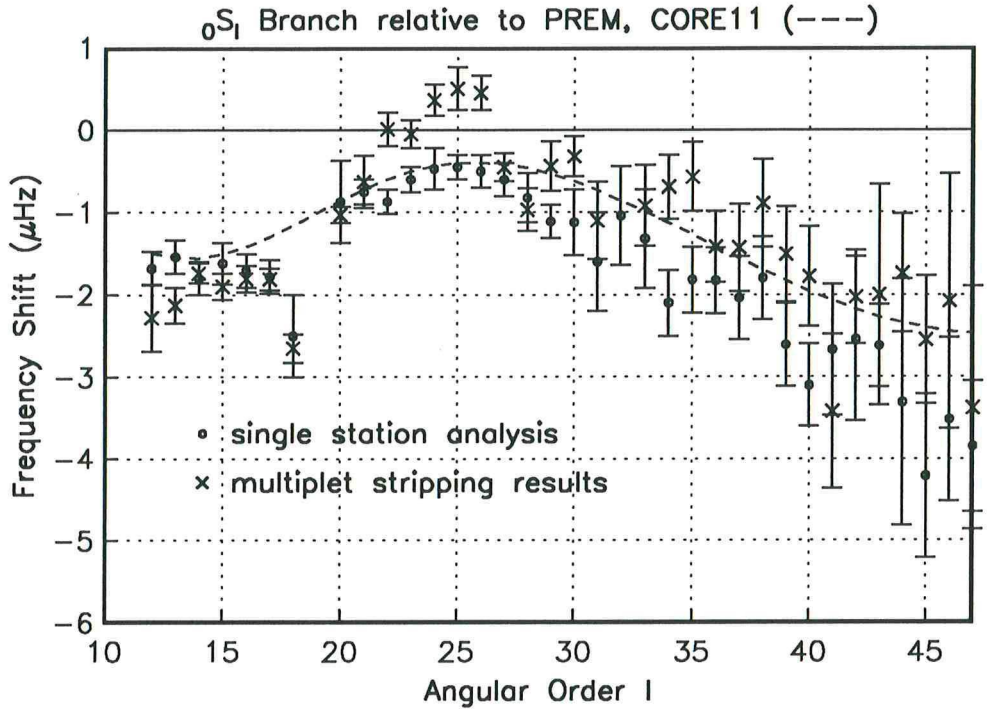

Figure 2.10 Observed fundamental spheroidal mode peak frequencies plotted relative to the predictions of PREM obtained by histogram analysis of single record measurements (o) (*Smith and Masters, 1989*) and multiplet stripping (×). The frequencies estimates based on the multiplet stripping technique are biased low but generally agree at the 1 σ level.

be difficult but a common symptom is for the strip to have multiple peaks. In Figure 2.11 we show the results of stripping for ${}_1S_4$. A double peak is produced and it is difficult to assign a center frequency. Synthetic experiments show that this kind of result is to be expected. For example, a multiplet strip of 19 synthetic seismograms which include the effects of ellipticity and rotation is also shown in Figure 2.11 and is very similar to the result obtained from the data. Clearly, multiplet stacking and stripping is incapable of producing accurate results for broadly split modes such as ${}_1S_4$ which have a nonuniform distribution of singlets. The situation is even worse for anomalously split, low l, high Q modes such as ${}_{10}S_2$ where multiplet stripping produces a single peak at an extreme end of the multiplet leading to systematically biased degenerate frequencies. As a consequence of these observations, we have discarded all the multiplet stripping results for modes with harmonic degree l less than 8.

Ritzwoller et al. (1986, 1988) demonstrate that accurate degenerate frequencies for broadly split multiplets can be found by either stripping for individual singlets or by directly modeling the effect of aspherical structure on the data spectra. Their results along with the results from multiplet stripping and results from later chapters give 620 precise multiplet degenerate frequencies (Appendix A). Note

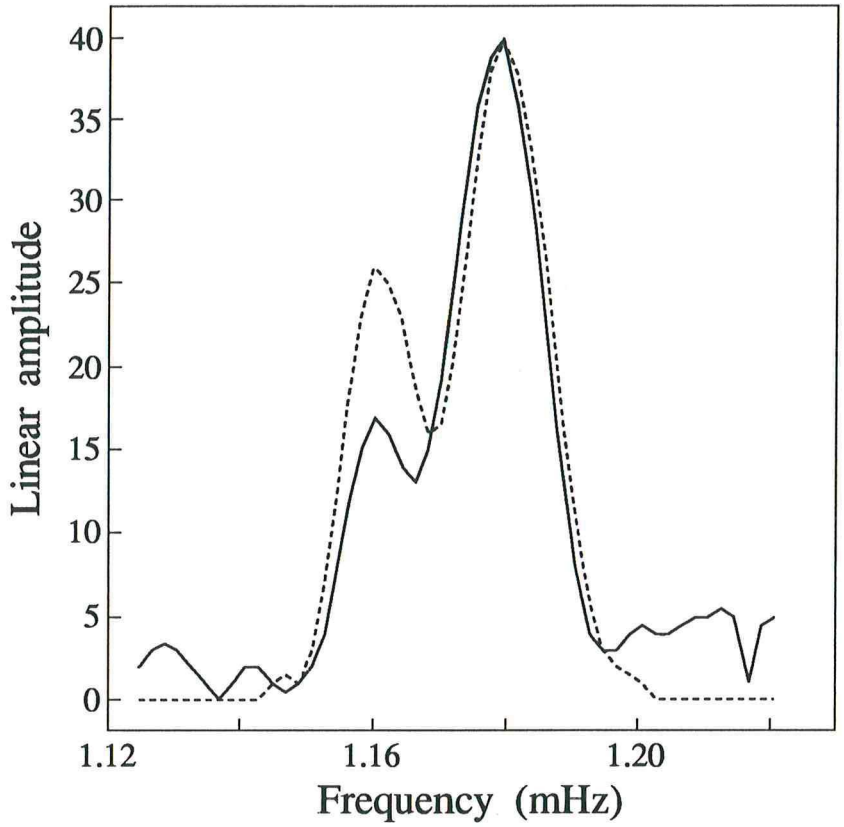

Figure 2.11 Multiplet strip for ${}_1S_4$. Solid line is a strip of data and the dashed line is a strip of synthetic data. This demonstrates that multiplet stripping is incapable of giving good degenerate frequencies for broadly split multiplets with a nonuniform distribution of singlets.

that second order rotational effects and the spherical part of the rotational potential must be taken into account for very low frequency multiplets and we use the results of *Dahlen and Sailor (1979)* to perform the appropriate corrections. The analysis so far has only been applied to multiplets with periods longer than 100 sec and the observed multiplets are shown in the ω/l plots of Figure 2.12. Most of the remaining unmeasured multiplets in this frequency range are Stoneley modes, core modes and poorly excited ScS-equivalent toroidal modes.

The estimates of frequencies from the strips also give estimates of the apparent attenuation of the multiplets. Our expectation was that the attenuation measurements would be biased as suggested by the results of *Dahlen, (1979)* for stacked spectra and, in fact, we find that for the fundamental modes the observed Q values are systematically low compared to the results from the histogram analysis (Figure 2.13). In order to confirm that this discrepancy stems solely from the effect of 3-D structure and is not related to panel structure in the data we have performed a synthetic experiment in which we have used

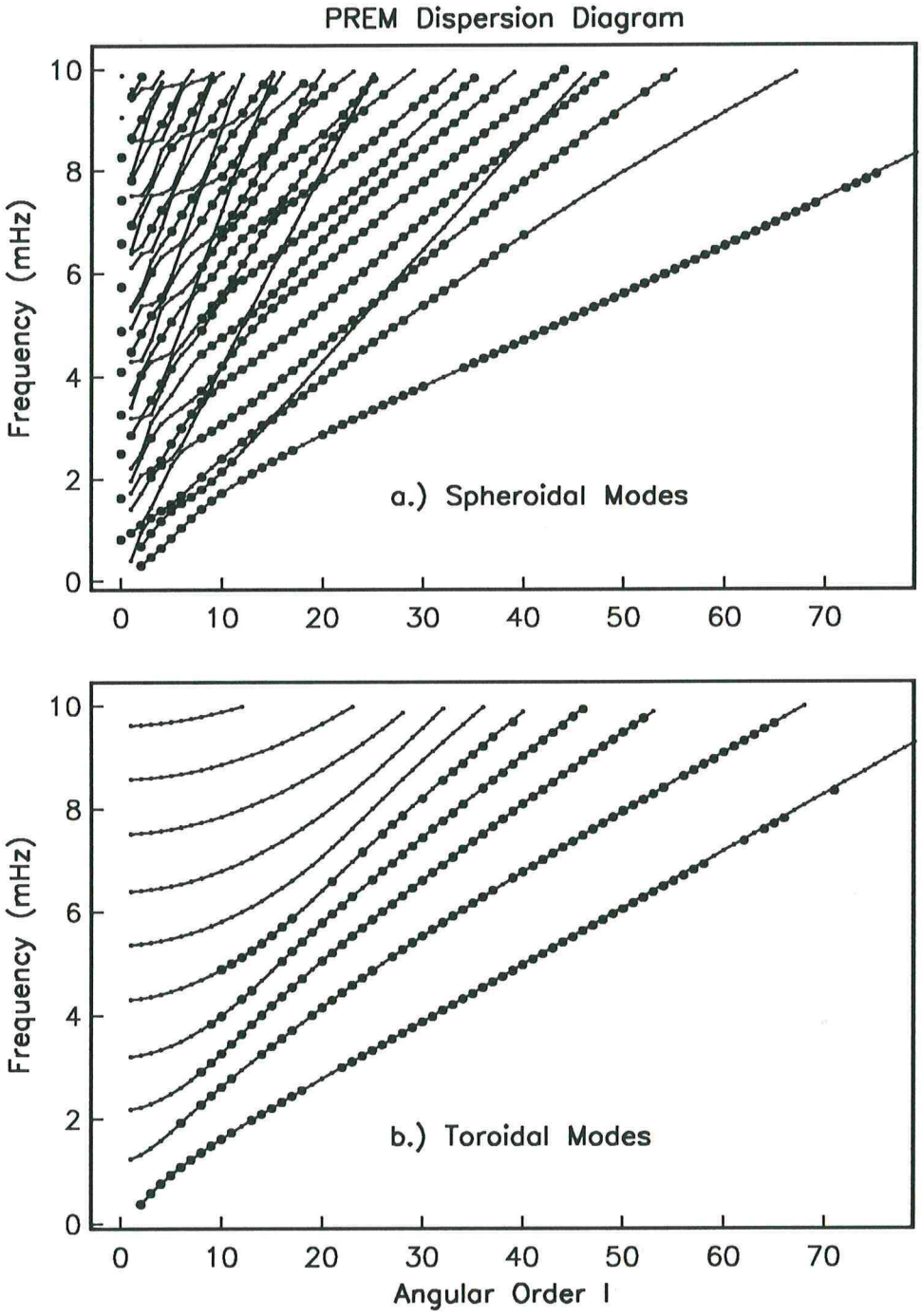

Figure 2.12 ω/l plots for a) spheroidal modes and b) toroidal modes. The large dots indicate the modes for which a reliable degenerate frequency could be assigned and that were used in the inversions (see Appendix A).

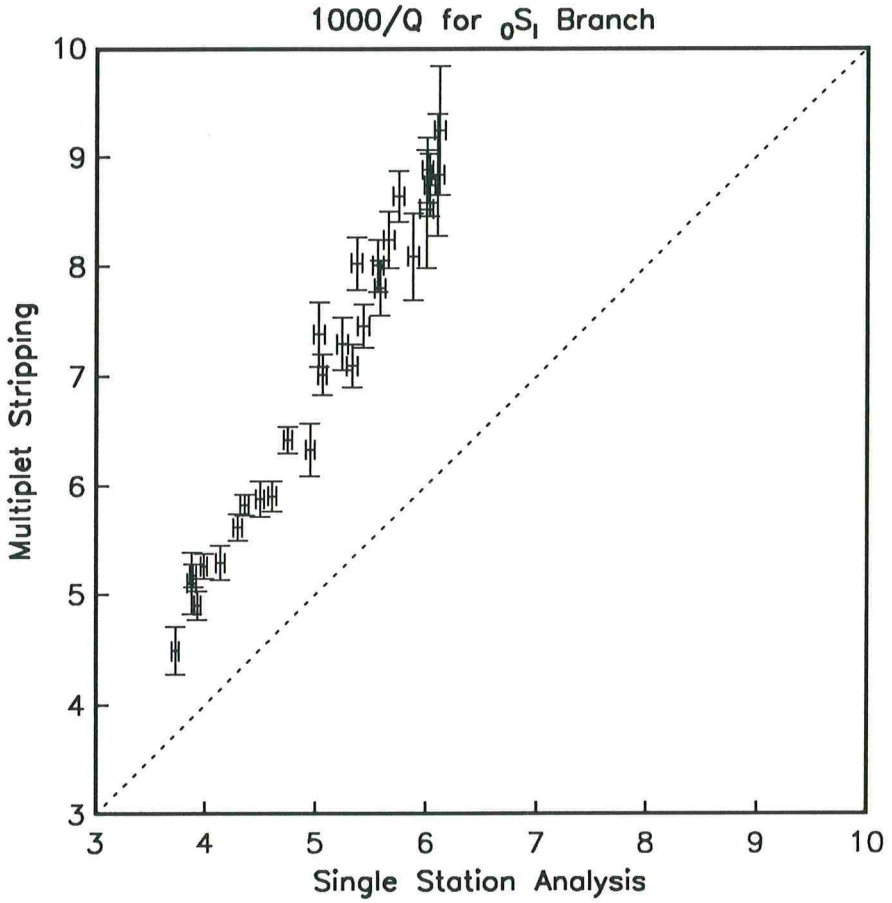

Figure 2.13 Scatter plot of Q measurements for fundamental spheroidal modes ${}_0S_l$ obtained by a.) averages of many single station measurements and b.) multiplet stripping. While the former are expected to be unbiased the latter are biased to low Q as suggested by the results of *Dahlen (1979)*.

the two techniques (histogram analysis and multiplet stripping) on four sets of synthetic seismograms. The seismograms were computed both with and without aspherical structure (M84A of *Woodhouse and Dziewonski, 1984*) and were free of panel structure in one case and contained realistic gaps in the other case. We found that the histogram analysis yields unbiased results in all four cases whereas multiplet stripping of the aspherical synthetics produces systematically low Q values. Stripping the spherical synthetics yields unbiased Q values. The only effect of the panel structure is to slightly degrade the signal to noise ratio of the multiplet strips. These results suggest that Q estimates from strips provide lower bounds on anelastic structure and can be used as inequality constraints in an inversion for the Q structure.

Figures 2.14–2.18 illustrate the fit of model PREM to our data and to the data used in the construction of PREM. Some of the PREM dataset is a product of a traveling wave analysis so the errors

are almost certainly correlated from mode to mode along a dispersion branch. There is a tendency for our data to be slightly lower in frequency than the PREM dataset which we believe to represent bias in the PREM dataset. Most of the new data are consistent with the old data at the 1σ level though there are some exceptions (particularly among the low l, high Q modes which sample deep Earth structure). Tables 2.1 and 2.2 summarize the fit of PREM to the old and new datasets.

Neither PREM nor any other model fits the new data adequately and the next section outlines some preliminary experiments in modeling.

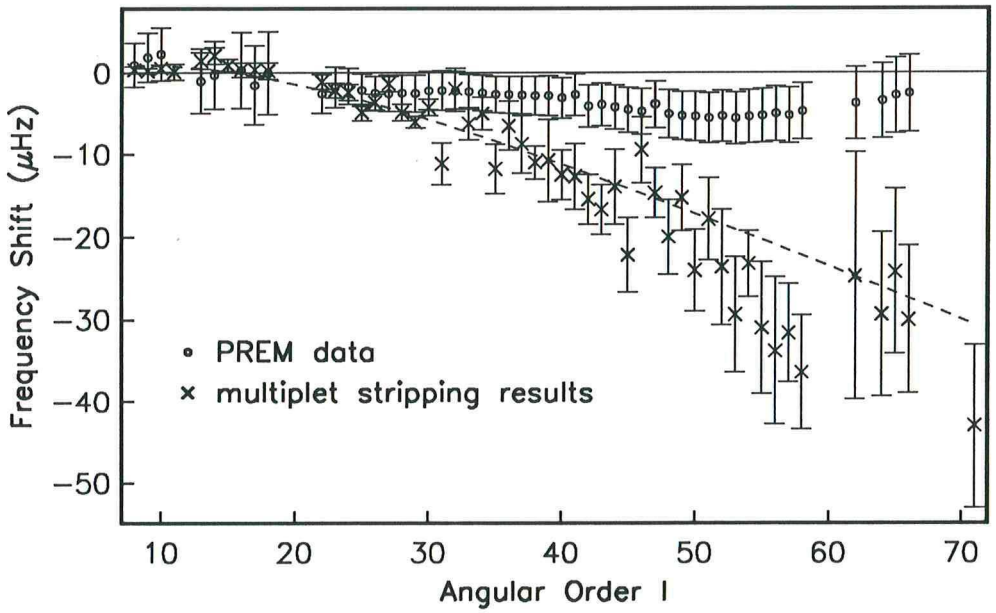

Figure 2.14 A comparison of our data (×) with the data used in the construction of PREM (○). The data are plotted as frequency shifts away from those predicted by that model and this example is for fundamental toroidal modes. The smoothness of the PREM data suggests that they come from a traveling wave analysis and are therefore unlikely to be independent. The dashed line shows the predictions of model CORE11.

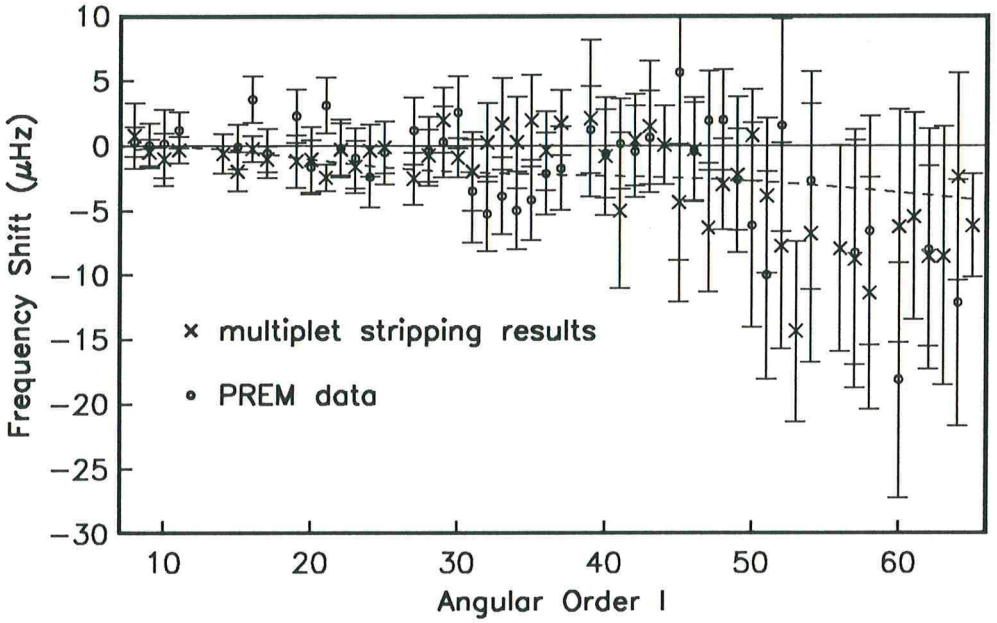

Figure 2.15 As for Figure 2.14 but for ${}_1T_l$ modes. On average the new observations are slightly lower in frequency than the older data.

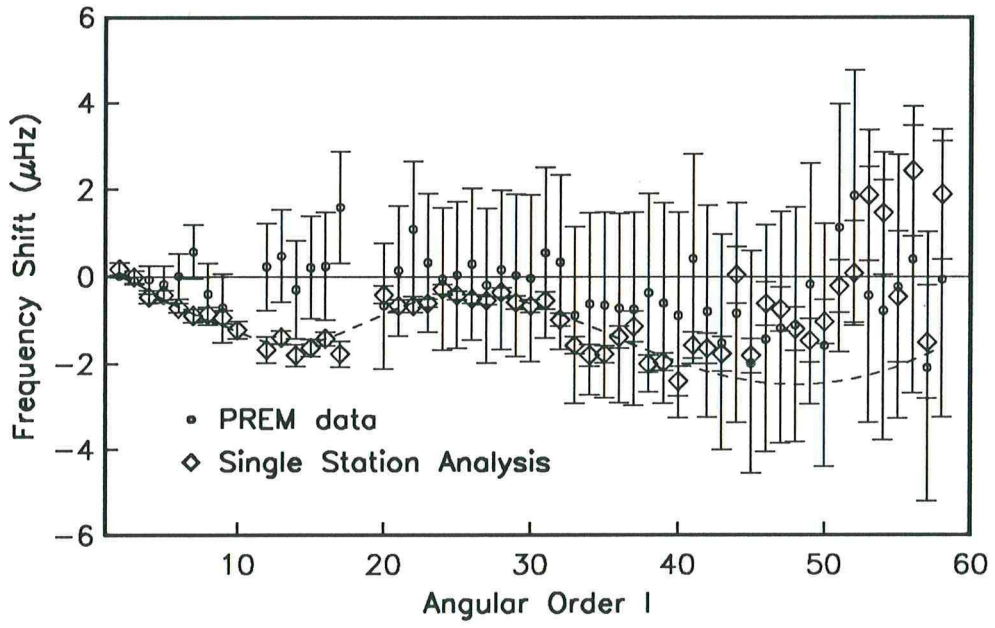

Figure 2.16 As for Figure 2.14 but for ${}_0S_l$ modes. Note the large systematic deviation in the Coriolis band.

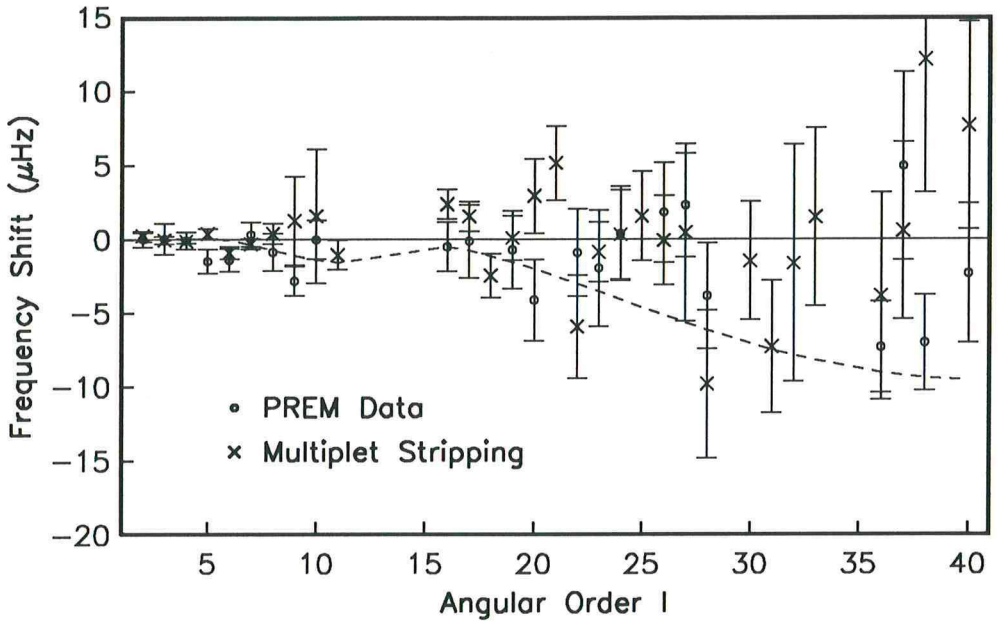

Figure 2.17 As for Figure 2.14 but for ${}_1S_l$ modes.

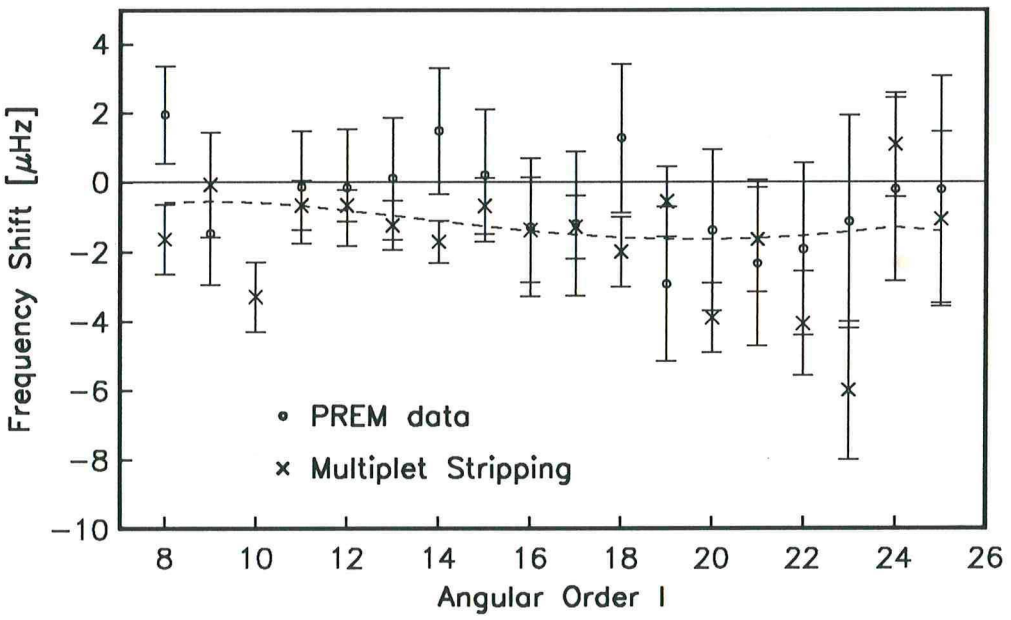

Figure 2.18 As for Figure 2.14 but for ${}_3S_l$ modes.

Table 2.1 Fit of PREM to old dataset.

mode type	n	χ^2	χ^2/n
radial	7	22	3.1
toroidal	214	277	1.3
spheroidal	492	836	1.7
all	713	1134	1.6

Table 2.2 Fit of PREM to new dataset.

mode type	n	χ^2	χ^2/n
radial	10	486	48.7
toroidal	204	1388	6.8
spheroidal	412	9533	23.1
all	626	11408	18.2

2.3 Modeling of the Dataset

The 620 multiplet frequencies, described in the previous section, together with the mean density (5515.0±2.5 kgm^{-3}) and moment of inertia factor (.33083±.00003) are the 622 gross Earth data used in our modeling. The precision of this dataset means that we must be careful in the way we specify Earth structure. For example, it is quite likely that when averaged over spherical shells, the solid regions of the Earth are slightly transversely isotropic so we allow this possibility throughout the inner core and mantle. From a physical point of view, it is harder to see how a fluid region could depart significantly from an isotropic state but, mathematically, it is possible that the average velocity in the radial direction is different from the average velocity tangential to a spherical surface. Because of some difficulties in fitting the data, we have performed some experiments allowing this kind of behavior in the outer core. Our models include physical dispersion using the assumption that attenuation is weak and that Q is a slowly varying function of frequency between 0.3 and 10 mHz. Given a model of Q structure, we can then correct the mode measurements to a reference frequency (see *e.g., Liu et al. 1976*). The reference frequency that we use is 4mHz so that the Q correction is quite small over the whole band and errors in our assumptions probably do not have a significant effect on the models. An extreme example is the fundamental toroidal mode branch (Figure 2.19). If a 1 second reference period is chosen, the Q correction in our frequency band is several tens of standard deviations while a 250 second reference period results in corrections which are of the same order as the observational errors.

We are dealing with a typical ill-posed inverse problem and we choose to use the method of regularization to obtain solutions. In particular we begin with a starting model $m_0(r)$ whose shells contain smooth functions of density and elastic moduli. These smooth functions are represented by cubic splines. Sharp transitions are allowed at the interfaces between shells and the radii of these interfaces are allowed to vary in the inversion. We have experimented with the number of shells in our models, particularly in the upper mantle and in the vicinity of the boundaries of the outer core. We prefer this kind of model specification to the polynomials of PREM because fine scale structure is allowed to develop if it is necessary to fit the data. From a numerical point of view, the chosen procedure involves the decomposition of an $n \times n$ real, symmetric matrix where n is the number of data at each iteration. This is not a particularly onerous task for a supercomputer.

We seek perturbations $\delta m(r)$ that minimize $||\delta \ddot{m}(r)||$ and that provide acceptable fits to the data. The chosen norm is a roughness penalty or smoothness criterion and its choice for an inner

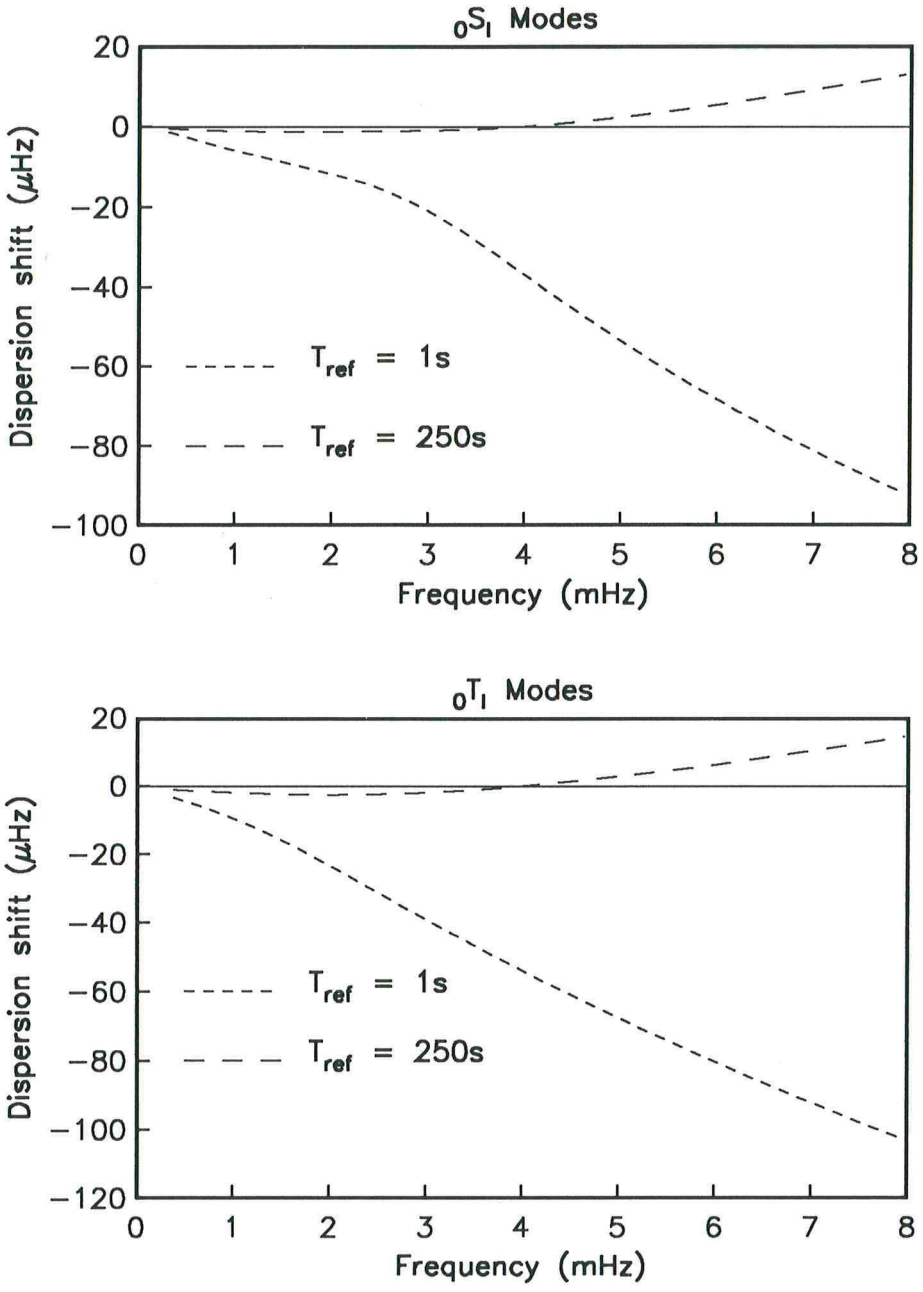

Figure 2.19 Physical dispersion for the fundamental modes in the case of a model that is specified at the reference period T_{ref} of 1s and 250s.

product means that our infinite dimensional Hilbert space is a Sobolev space (*Adams, 1975*; *Debnath and Mikusiński, 1990*) . This is the procedure described by *Johnson and Gilbert (1972)* and *Gilbert et al. (1973)*. Because of the high precision of the data, the model perturbation must be small to stay in the range of linearity about the starting model where the error due to linearisation is smaller than the observational error. We therefore typically require ten iterations from a starting model to achieve convergence to an acceptable model. All the modes contained in our dataset are recomputed at each iteration and it is the computation of the spheroidal modes which is the most computationaly burdensome part of the inversion procedure.

Before we present the modeling results, we wish to emphasize that we have been conservative in assigning errors to the data. For example, the degenerate frequency of ${}_{13}S_3$, obtained by singlet stripping and the diagonal sum rule, has a formal error of 0.1 μHz, a relative error of 2.0×10^{-5} or 20 ppm. Conservatively, we increase the error to 0.35 μHz to account for possible biases introduced by the assumptions inherent in the singlet stripping technique.. For many of the 620 multiplet frequencies, the assigned errors used in the modeling are 2–3 times larger than is indicated by a formal analysis.

As a measure of goodness-of-fit, we use

$$\chi^2 = \sum_{j=1}^{n} \left((\gamma_j^o - \gamma_j^c)/\sigma_j \right)^2 \tag{2.5}$$

where σ_j is the standard deviation of the jth datum γ_j, γ^o is the observed and γ^c the computed value of γ. χ^2 has the form of a chi-square distribution if the γ_j^o are independent, normally distributed variables with means γ_j^c and variances σ_j^2. For large values of n, χ is approximately normally distributed about $\sqrt{n}$. The variance of $\sqrt{2}\chi$ is approximately unity so a successful inversion should have χ^2 near n ($n = 620$ in our modeling experiments).

As an example of a modeling experiment we seek the smallest, smoothest perturbation to PREM required to fit the data. This, and other experiments show that we are not yet able to find a model which truly "fit" the data. In order to gain a better understanding of the misfit of the modal dataset we present an analysis of goodness of fit. We also consider a new function which we call the sensitivity and which is defined below. Our modeling equation can be written

$$\gamma_j = \sum_{k=1}^{6} \int_{r=0}^{a} F_{jk}(r) h_k(r) dr + \sum_{l=1}^{d} f_{jl} x_l \tag{2.6}$$

where:

γ_j jth datum

$h_k(r)$	kth model function (*e.g.*, density, velocity,...)
$F_{jk}(r)$	jth representer for the kth model function
x_l	radial perturbation of the lth interface
f_{jl}	jth partial derivative w.r.t. r_l
d	number of discontinuities
a	radius of the Earth.

Based on the modeling equation we define the following function

$$p_j(r) = \Big[\int_{\xi=0}^{r} \sum_{k=1}^{6} F_{jk}^2(\xi)d\xi + \sum_{\substack{l \\ r_l<r}} f_{jl}^2\Big]^{1/2}. \tag{2.7}$$

This is a monotonically non-decreasing function of r with step discontinuities at the interfaces. We define

$$S_j(r) = p_j(r)/p_j(a); \quad \big(p_j(a) \text{ is a 2-norm}\big) \tag{2.8}$$

to be the sensitivity function for the jth datum. The sensitivity function $S(r)$ defined this way is a measure of how much a mode is sensitive to structure below radius r.

The fit of the model (CORE11) which is the smoothest and smallest perturbation to PREM and provides the best fit to the data is shown in Table 2.3. Note, that only modes with frequencies less than 8 mHz are included in this table.

Table 2.3 Fit of CORE11 to the new dataset.

mode type	n	χ^2	χ^2/n
radial	7	38	5.4
toroidal	161	165	1.0
spheroidal	269	785	2.9
all	437	988	2.3

Tables 2.4 and 2.5 show how the relative χ^2 increases as one concentrates more on modes with the greatest sensitivity to the core. The pattern is strongest in Table 2.5 which ignores the effect of the core-mantle boundary indicating that the cause of the misfit lies *below* this boundary. The modes which have less than 5% sensitivity to the core have a χ^2 ratio of 2.2 for model CORE11 which verifies that the core sensitive modes are the main cause of data misfit.

This analysis of variance and other experiments indicate that the mantle modes are well fit by several of our spherically averaged models, but that a subset of modes sensitive to the structure of the

Table 2.4 Fit of core-sensitive modes

sensitivity[a]	n	χ^2	χ^2/n
10	121	379	3.1
20	69	289	4.2
30	39	175	4.5

[a] Minimum percentage sensitivity to the core and CMB

Table 2.5 Fit of core-sensitive modes but excluding the CMB

sensitivity	n	χ^2	χ^2/n
5	65	321	4.9
10	40	269	6.7
15	31	251	8.1

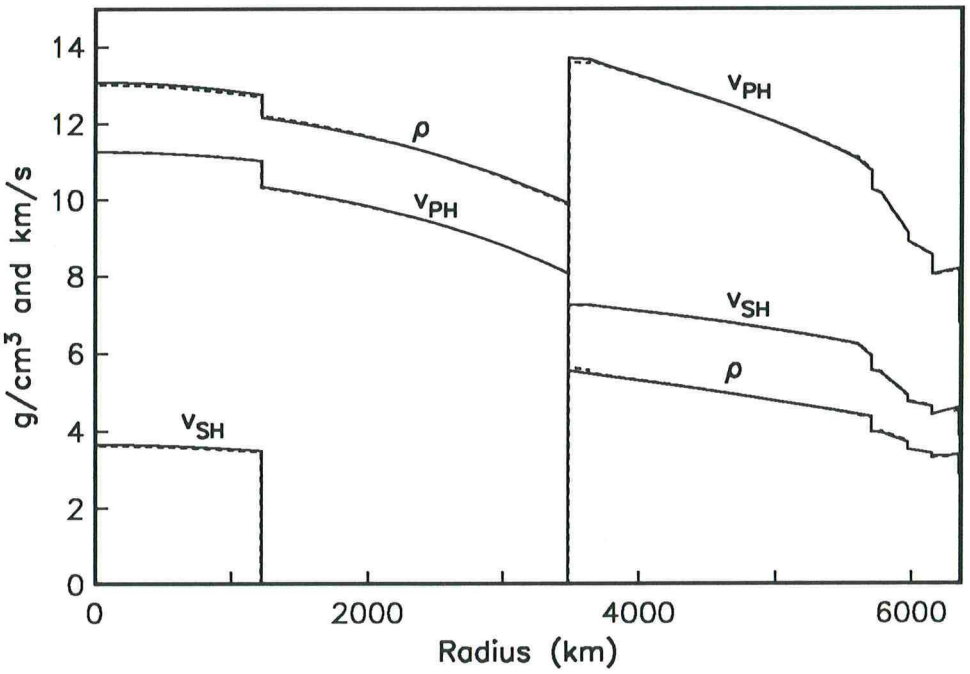

Figure 2.20 Comparison of model PREM (solid line) and CORE11 (dashed line).

inner and outer core are poorly fit. Either they are systematically biased in such a way that a monopole model cannot fit them, or they are good monopole data and the structure of the model is wrong. That is, our parameterization of the model may not contain the right degrees of freedom for the core-sensitive modes.

Mode degenerate frequencies in the datasets have been measured in several ways. The majority

of the measurements were obtained by multiplet stripping. The rest were processed by singlet stripping and nonlinear analysis of structure coefficients. The former tend to have larger assigned errors than the latter. To see whether the two sets of modes have different misfits we have divided the modes into two sets, one with assigned errors greater than 1.0 μHz and the other less than 1.0 μHz. We find that both sets are fit equally well so there is no obvious bias between the methods of measuring degenerate eigenfrequencies, nor is the misfit caused by those modes with small assigned errors.

2.4 Conclusions

We have constructed an accurate free-oscillation degenerate frequency dataset with most of the sources of bias identified and corrected for. Many of these new observations are significantly different from the data used in the construction of PREM. The size of our database (over 3500 long-period recordings) leads us to believe that our observations are superior to previous ones.

Our modeling indicates that we can find models which are dispersive and transversely isotropic which satisfy the data that are dominantly sensitive to the mantle. We present one model (CORE11) which is the smallest and smoothest perturbation to PREM required to give the best fit to the data. Note that all solid regions of this model (including the inner core) were allowed to be transversely isotropic. Modes which are sensitive to structure below the core-mantle boundary are the worst fit suggesting that either we do not have the correct degrees of freedom in our model or that bias still remains in the center frequencies of modes which sample the core. In passing, we note that most of these modes are also extremely anomalously split. An experiment with a transversely isotropic *outer* core gave almost no improvement in the fit to the data. It is our belief that more core-sensitive modes must be analyzed (and accurate degenerate frequencies found for them) before the trends in the observations that we discussed here can be considered proved beyond doubt and new types of core structure devised. In the next chapter we will perform a systematic search for core-sensitive modes in the frequency band between 5 and 10 mHz and the analysis of these modes will provide us with additional constraints on both the spherically symmetric and the aspherical structure of the deep Earth.

References

Adams, R., *Sobolev Spaces* . Academic Press, New York, 1975.

Backus, G.E., Interpreting the seismic glut moments of total degree two or less. *Geophys. J. R. Astron. Soc.*, **51**, 1–25, 1977.

Buland, R., J. Berger, and F. Gilbert, Observations from the IDA network of attenuation and splitting during a recent earthquake. *Nature*, **277**, 358–362, 1979.

Buland, R., and F. Gilbert, Matched filtering for the seismic moment tensor. *Geophys. Res. Lett.*, **3**, 205–206, 1976.

Dahlen, F.A., The spectra of unresolved split normal mode multiplets. *Geophys. J. R. Astron. Soc.*, **58**, 1–33, 1979.

Dahlen, F.A., The effect of data windows on the estimation of free oscillation parameters. *Geophys. J. R. Astron. Soc.*, **69**, 537–549, 1982.

Dahlen, F.A., and R.V. Sailor, Rotational and elliptical splitting of the free oscillations of the earth. *Geophys. J. R. Astron. Soc.*, **58**, 609–623, 1979.

Davis, J.P., Local eigenfrequency and its uncertainty inferred from fundamental spheroidal mode frequency shifts. *Geophys. J. R. Astron. Soc.*, **88**, 693–722, 1987.

Debnath, L., and P. Mikusiński, *Introduction to Hilbert spaces with applications.* Academic Press, 1990.

Dziewonski, A.M., and D.L. Anderson, Preliminary reference Earth model. *Phys. Earth Planet. Inter.*, **25**, 297–356, 1981.

Dziewonski, A.M., and D.L. Anderson, Travel times and station corrections for P-waves at teleseismic distances. *J. Geophys. Res.*, **88**, 3295–3314, 1983.

Dziewonski, A.M., T.A. Chou, and J.H. Woodhouse, Determination of earthquake source parameters from waveform data for studies of global and regional seismicity. *J. Geophys. Res.*, **36**, 2825–2831, 1981.

Giardini, D., X.-D. Li, and J.H. Woodhouse, Three-dimensional structure of the earth from splitting in free oscillation spectra. *Nature*, **325**, 405–411, 1987.

Giardini, D., X.-D. Li, and J.H. Woodhouse, Splitting functions of long period normal modes of the earth. *J. Geophys. Res.*, **93**, 13,716–13,742, 1988.

Gilbert, F., A.M. Dziewonski, and J.N. Brune, An informative solution to a seismological inverse problem. *Proc. Natl. Acad. Sci.*, **70**, 1410–1413, 1973.

Gilbert, F., and A.M. Dziewonski, An application of normal mode theory to the retrieval of structural parameters and source mechanisms from seismic spectra. *Phil. Trans. R. Soc. Lond.*, **A278**, 187–269, 1975.

Johnson, L.E., and F. Gilbert, A new datum for use in the body wave travel time inverse problem. *Geophys. J. R. Astron. Soc.*, **30**, 373–380, 1972.

Jordan, T.H., A procedure for estimating lateral variations from low-frequency eigenspectra data. *Geophys. J. R. Astron. Soc.*, **52**, 441–455, 1978.

Lawson, C.L., and R.J. Hanson, *Solving Least Squares Problems.* Prentice-Hall, Englewood Cliffs, N.J., 1974.

Li, X.-D., and D. Giardini J. H. Woodhouse, Large-Scale Three -Dimensional Even -Degree Structure of

the Earth from Splitting of Long-Period Normal Modes. *J. Geophys. Res.*, **96**, 551–577, 1991.

Liu, H.-P., D.L. Anderson, and H. Kanamori, Velocity dispersion due to anelasticity; implications for seismology and mantle composition. *Geophys. J. R. Astron. Soc.*, **47**, 41–58, 1976.

Masters, G., and F. Gilbert, Attenuation in the earth at low frequencies. *Phil. Trans. R. Soc. Lond.*, **A308**, 479–522, 1983.

Masters, G., T.H. Jordan, P.G. Silver, and F. Gilbert, Aspherical earth structure from fundamental spheroidal-mode data. *Nature*, **298**, 609–613, 1982.

Masters, G., J. Park, and F. Gilbert, Observations of coupled spheroidal and toroidal modes. *J. Geophys. Res.*, **88**, 10,285–10,298, 1983.

Ritzwoller, M., G. Masters, and F. Gilbert, Observations of anomalous splitting and their interpretation in terms of aspherical structure. *J. Geophys. Res.*, **91**, 10,203–10,228, 1986.

Ritzwoller, M., G. Masters, and F. Gilbert, Constraining aspherical structure with low frequency interaction coefficients: Application to uncoupled multiplets. *J. Geophys. Res.*, **93**, 6369–6396, 1988.

Romanowicz, B., G. Roult, and T. Kohl, The upper mantle degree two pattern: constraints from GEOSCOPE fundamental spheroidal mode eigenfrequency and attenuation measurements. *Geophys. Res. Lett.*, **14**, 1219–1222, 1987.

Roult, G., and B. Romanowicz J. P. Montagner, 3-D upper mantle shear velocity and attenuation from fundamental mode free oscillation data. *Geophys. J. Int.*, **101**, 61–80, 1990.

Roult, G., and B. Romanowicz, Very long-period data from the geoscope network: Preliminary results on great circle averages of fundamental and higher Rayleigh and Love modes. *Bull. Seismol. Soc. Am.*, **74**, 2221–2243, 1984.

Silver, P.G., and T.H. Jordan, Fundamental spheroidal mode observations of aspherical heterogeneity. *Geophys. J. R. Astron. Soc.*, **64**, 605–634, 1981.

Smith, M.F., and G. Masters, The effect of Coriolis coupling of free oscillation multiplets on the determination of aspherical earth structure. *Geophys. Res. Lett.*, **16**, 263–266, 1989.

Smith, M.F., and G. Masters, Aspherical structure constraints from free oscillation frequency and attenuation measurements. *J. Geophys. Res.*, **94**, 1953–1976, 1989.

Widmer, R., G. Masters, and F. Gilbert, Spherically symmetric attenuation within the Earth from normal mode data. *Geophys. J. Int.*, **104**, 541–553, 1991.

Woodhouse, J.H., and A.M. Dziewonski, Mapping of the upper mantle: three-dimensional modeling of earth structure by inversion of seismic waveforms. *J. Geophys. Res.*, **89**, 5953–5986, 1984.

Woodward, R.L., and G. Masters, Calibration and data quality of the long period SRO/ASRO networks, 1977 – 1980. *Bull. Seismol. Soc. Am.*, **79**, 1972–1983, 1989.

Appendix A

mode	f [mHz]	df [μHz]	mode	f [mHz]	df [μHz]	mode	f [mHz]	df [μHz]
${}_0S_0$	0.81439	0.01	${}_0S_{45}$	5.15720	0.40	${}_1S_{23}$	4.37900	2.00
${}_1S_0$	1.63136	0.05	${}_0S_{46}$	5.24850	0.50	${}_1S_{24}$	4.52500	3.00
${}_2S_0$	2.50790	0.20	${}_0S_{47}$	5.33860	0.50	${}_1S_{25}$	4.67050	3.00
${}_3S_0$	3.27270	0.60	${}_0S_{48}$	5.42850	0.50	${}_1S_{26}$	4.81250	3.00
${}_4S_0$	4.10620	0.10	${}_0S_{49}$	5.51870	0.50	${}_1S_{27}$	4.95600	6.00
${}_5S_0$	4.88910	0.50	${}_0S_{50}$	5.60970	0.50	${}_1S_{28}$	5.08800	5.00
${}_6S_0$	5.74200	0.20	${}_0S_{51}$	5.70120	0.60	${}_1S_{30}$	5.37850	4.00
${}_7S_0$	6.58420	1.10	${}_0S_{52}$	5.79230	1.20	${}_1S_{31}$	5.51250	4.50
${}_8S_0$	7.42800	2.00	${}_0S_{53}$	5.88500	1.50	${}_1S_{32}$	5.65700	8.00
${}_9S_0$	8.26950	1.00	${}_0S_{54}$	5.97560	1.40	${}_1S_{33}$	5.79800	6.00
			${}_0S_{55}$	6.06480	1.50	${}_1S_{36}$	6.20000	7.00
${}_0S_2$	0.30945	0.15	${}_0S_{56}$	6.15890	1.50	${}_1S_{37}$	6.33800	6.00
${}_0S_3$	0.46855	0.15	${}_0S_{57}$	6.24630	1.30	${}_1S_{38}$	6.48200	9.00
${}_0S_4$	0.64688	0.10	${}_0S_{58}$	6.34110	1.50	${}_1S_{40}$	6.73900	7.00
${}_0S_5$	0.84008	0.10	${}_0S_{59}$	6.43630	2.50			
${}_0S_6$	1.03758	0.10	${}_0S_{60}$	6.52600	2.00	${}_2S_3$	1.24296	0.10
${}_0S_7$	1.23096	0.20	${}_0S_{61}$	6.61350	2.50	${}_2S_4$	1.37960	0.20
${}_0S_8$	1.41273	0.09	${}_0S_{62}$	6.70450	3.00	${}_2S_5$	1.51527	0.30
${}_0S_9$	1.57735	0.06	${}_0S_{63}$	6.79550	2.50	${}_2S_6$	1.68117	0.20
${}_0S_{10}$	1.72521	0.09	${}_0S_{64}$	6.89000	3.00	${}_2S_8$	2.04935	0.20
${}_0S_{12}$	1.98859	0.06	${}_0S_{65}$	6.97900	3.50	${}_2S_{10}$	2.40400	0.70
${}_0S_{13}$	2.11135	0.06	${}_0S_{66}$	7.07350	3.50	${}_2S_{12}$	2.73660	0.50
${}_0S_{14}$	2.22964	0.06	${}_0S_{67}$	7.16450	3.50	${}_2S_{13}$	2.90350	2.00
${}_0S_{15}$	2.34471	0.06	${}_0S_{68}$	7.25400	3.00	${}_2S_{14}$	3.06200	1.50
${}_0S_{16}$	2.45669	0.06	${}_0S_{69}$	7.34850	2.00	${}_2S_{26}$	5.57900	2.00
${}_0S_{17}$	2.56545	0.06	${}_0S_{72}$	7.63100	4.50	${}_2S_{27}$	5.73650	2.50
${}_0S_{20}$	2.87795	0.20	${}_0S_{73}$	7.71900	3.00	${}_2S_{28}$	5.90400	2.00
${}_0S_{21}$	2.97705	0.15	${}_0S_{74}$	7.81350	3.00	${}_2S_{29}$	6.06850	2.50
${}_0S_{22}$	3.07460	0.15	${}_0S_{75}$	7.91000	4.00	${}_2S_{30}$	6.23050	2.50
${}_0S_{23}$	3.17065	0.10				${}_2S_{31}$	6.38850	2.00
${}_0S_{24}$	3.26560	0.10	${}_1S_2$	0.68010	0.25	${}_2S_{32}$	6.54850	4.00
${}_0S_{25}$	3.35895	0.10	${}_1S_3$	0.93996	0.10	${}_2S_{35}$	7.01500	3.50
${}_0S_{26}$	3.45140	0.10	${}_1S_4$	1.17277	0.10	${}_2S_{36}$	7.16650	3.00
${}_0S_{27}$	3.54310	0.10	${}_1S_5$	1.37001	0.20	${}_2S_{37}$	7.31450	3.50
${}_0S_{28}$	3.63440	0.10	${}_1S_6$	1.52136	0.40	${}_2S_{38}$	7.47600	4.00
${}_0S_{29}$	3.72475	0.15	${}_1S_7$	1.65448	0.20	${}_2S_{39}$	7.62700	4.00
${}_0S_{30}$	3.81485	0.15	${}_1S_8$	1.79776	0.10	${}_2S_{40}$	7.77600	4.00
${}_0S_{34}$	4.17210	0.25	${}_1S_9$	1.96172	0.60	${}_2S_{41}$	7.91750	6.00
${}_0S_{35}$	4.26145	0.20	${}_1S_{10}$	2.15000	4.50	${}_2S_{42}$	8.06500	8.00
${}_0S_{36}$	4.35115	0.25	${}_1S_{11}$	2.34650	1.00	${}_2S_{43}$	8.21300	7.00
${}_0S_{37}$	4.44070	0.35	${}_1S_{15}$	3.16900	2.50	${}_2S_{44}$	8.36700	6.00
${}_0S_{38}$	4.52920	0.20	${}_1S_{16}$	3.34100	1.00	${}_2S_{45}$	8.51500	8.00
${}_0S_{39}$	4.61865	0.20	${}_1S_{17}$	3.49550	1.00	${}_2S_{46}$	8.68200	6.00
${}_0S_{40}$	4.70770	0.35	${}_1S_{18}$	3.64250	1.50	${}_2S_{48}$	8.95500	10.00
${}_0S_{41}$	4.79810	0.30	${}_1S_{19}$	3.79400	1.50	${}_2S_{49}$	9.09300	9.00
${}_0S_{42}$	4.88770	0.35	${}_1S_{20}$	3.94450	2.50	${}_2S_{52}$	9.53800	8.00
${}_0S_{43}$	4.97735	0.40	${}_1S_{21}$	4.09350	2.50	${}_2S_{54}$	9.82000	10.00
${}_0S_{44}$	5.06905	0.65	${}_1S_{22}$	4.22850	3.50			

mode	f	df	mode	f	df	mode	f	df
	[mHz]	[μHz]		[mHz]	[μHz]		[mHz]	[μHz]
${}_3S_1$	0.94436	0.10	${}_4S_{29}$	6.87000	2.00	${}_5S_{43}$	9.82600	7.00
${}_3S_2$	1.10598	0.40	${}_4S_{30}$	7.03400	2.00	${}_5S_{44}$	9.98600	6.00
${}_3S_8$	2.81902	0.30	${}_4S_{31}$	7.20000	2.00			
${}_3S_9$	2.95150	1.50	${}_4S_{32}$	7.36600	2.00	${}_6S_3$	2.82187	0.10
${}_3S_{10}$	3.08150	1.00	${}_4S_{33}$	7.53200	1.50	${}_6S_8$	3.73750	1.00
${}_3S_{11}$	3.22060	0.70	${}_4S_{34}$	7.69100	1.50	${}_6S_9$	3.96450	2.00
${}_3S_{12}$	3.36140	0.45	${}_4S_{35}$	7.85600	1.50	${}_6S_{13}$	5.23350	2.50
${}_3S_{13}$	3.50620	0.70	${}_4S_{36}$	8.01550	3.50	${}_6S_{14}$	5.40900	2.00
${}_3S_{14}$	3.65540	0.60	${}_4S_{37}$	8.17750	3.00	${}_6S_{15}$	5.60650	2.50
${}_3S_{15}$	3.80980	0.80	${}_4S_{38}$	8.33600	2.00	${}_6S_{16}$	5.81150	2.50
${}_3S_{16}$	3.96550	1.50	${}_4S_{39}$	8.49250	3.00	${}_6S_{17}$	6.02650	2.00
${}_3S_{17}$	4.12430	0.90	${}_4S_{40}$	8.65150	3.00	${}_6S_{18}$	6.24200	2.00
${}_3S_{18}$	4.28400	1.00				${}_6S_{19}$	6.45350	2.50
${}_3S_{19}$	4.44700	1.00	${}_5S_3$	2.16867	0.20	${}_6S_{20}$	6.65950	2.00
${}_3S_{20}$	4.60600	1.00	${}_5S_4$	2.37917	0.20	${}_6S_{21}$	6.85900	2.00
${}_3S_{21}$	4.77100	1.50	${}_5S_5$	2.70367	0.20	${}_6S_{22}$	7.05350	2.50
${}_3S_{22}$	4.93150	1.50	${}_5S_6$	3.01154	0.20	${}_6S_{23}$	7.24100	2.00
${}_3S_{23}$	5.09250	2.00	${}_5S_7$	3.29188	0.30	${}_6S_{24}$	7.41850	2.00
${}_3S_{24}$	5.26250	1.50	${}_5S_8$	3.52643	0.70	${}_6S_{25}$	7.59000	1.50
${}_3S_{25}$	5.42450	2.50	${}_5S_{10}$	4.21400	2.00	${}_6S_{26}$	7.75600	4.00
${}_3S_{41}$	8.81650	2.50	${}_5S_{11}$	4.46400	2.00	${}_6S_{27}$	7.92900	7.00
${}_3S_{42}$	8.96650	2.50	${}_5S_{12}$	4.70000	0.80	${}_6S_{28}$	8.09400	5.00
${}_3S_{43}$	9.12050	2.00	${}_5S_{13}$	4.92750	1.50	${}_6S_{29}$	8.25750	4.00
${}_3S_{44}$	9.27500	3.50	${}_5S_{14}$	5.13800	2.00	${}_6S_{30}$	8.41700	6.00
${}_3S_{45}$	9.42400	4.50	${}_5S_{15}$	5.32800	2.00	${}_6S_{31}$	8.58900	5.00
${}_3S_{46}$	9.57550	4.50	${}_5S_{16}$	5.50700	2.00	${}_6S_{32}$	8.75500	5.00
${}_3S_{47}$	9.72900	6.00	${}_5S_{17}$	5.66900	3.00	${}_6S_{33}$	8.92900	6.00
${}_3S_{48}$	9.87700	6.00	${}_5S_{18}$	5.83100	3.00	${}_6S_{34}$	9.10000	10.00
			${}_5S_{19}$	5.98950	2.00	${}_6S_{36}$	9.42000	6.00
${}_4S_3$	2.04811	0.30	${}_5S_{20}$	6.15200	3.00	${}_6S_{37}$	9.59750	6.50
${}_4S_4$	2.27963	0.45	${}_5S_{21}$	6.31250	2.00			
${}_4S_9$	3.70750	1.50	${}_5S_{22}$	6.48000	6.00	${}_7S_8$	4.44800	1.00
${}_4S_{10}$	3.86450	2.00	${}_5S_{23}$	6.63500	3.50	${}_7S_9$	4.61200	2.50
${}_4S_{11}$	4.00900	2.00	${}_5S_{24}$	6.80200	3.00	${}_7S_{10}$	4.76350	4.50
${}_4S_{12}$	4.15000	2.00	${}_5S_{25}$	6.96450	3.50	${}_7S_{11}$	4.91550	3.00
${}_4S_{13}$	4.29400	2.00	${}_5S_{26}$	7.12900	2.00	${}_7S_{12}$	5.06850	2.50
${}_4S_{14}$	4.43300	1.50	${}_5S_{28}$	7.45050	2.00	${}_7S_{16}$	6.47100	4.50
${}_4S_{15}$	4.58300	1.50	${}_5S_{29}$	7.61600	2.50	${}_7S_{17}$	6.61100	4.50
${}_4S_{16}$	4.73000	2.50	${}_5S_{30}$	7.77650	2.50	${}_7S_{18}$	6.76400	6.00
${}_4S_{17}$	4.88250	2.00	${}_5S_{31}$	7.93900	1.50	${}_7S_{19}$	6.91900	7.00
${}_4S_{18}$	5.04300	2.50	${}_5S_{32}$	8.09800	5.00	${}_7S_{20}$	7.08500	5.00
${}_4S_{19}$	5.20100	2.00	${}_5S_{33}$	8.25350	3.50	${}_7S_{21}$	7.23850	4.50
${}_4S_{20}$	5.36200	2.50	${}_5S_{34}$	8.41000	4.00	${}_7S_{22}$	7.41600	6.00
${}_4S_{21}$	5.52500	2.00	${}_5S_{35}$	8.57050	3.50	${}_7S_{23}$	7.59800	3.50
${}_4S_{22}$	5.69400	2.50	${}_5S_{36}$	8.72650	3.50	${}_7S_{24}$	7.78800	5.00
${}_4S_{23}$	5.85850	2.00	${}_5S_{37}$	8.88250	2.00	${}_7S_{25}$	7.96800	3.50
${}_4S_{24}$	6.02550	3.50	${}_5S_{38}$	9.03550	4.50	${}_7S_{26}$	8.15200	8.00
${}_4S_{25}$	6.19900	3.00	${}_5S_{39}$	9.19500	4.50	${}_7S_{27}$	8.34700	6.00
${}_4S_{26}$	6.36300	3.50	${}_5S_{40}$	9.35350	3.00	${}_7S_{28}$	8.53600	9.00
${}_4S_{27}$	6.53200	2.00	${}_5S_{41}$	9.51250	4.50	${}_7S_{31}$	9.10700	8.00
${}_4S_{28}$	6.70500	1.50	${}_5S_{42}$	9.66600	3.00	${}_7S_{33}$	9.46400	9.00

mode	f [mHz]	df [μHz]	mode	f [mHz]	df [μHz]	mode	f [mHz]	df [μHz]
${}_{7}S_{34}$	9.65100	5.00	${}_{10}S_{16}$	7.42300	2.50	${}_{14}S_{9}$	7.34250	2.00
${}_{7}S_{35}$	9.82700	9.00	${}_{10}S_{17}$	7.67800	1.50	${}_{14}S_{10}$	7.62400	4.00
			${}_{10}S_{18}$	7.94050	2.50	${}_{14}S_{11}$	7.80300	6.00
${}_{8}S_{1}$	2.87284	0.15	${}_{10}S_{19}$	8.20000	3.50	${}_{14}S_{13}$	8.72450	4.00
${}_{8}S_{5}$	4.16571	0.23	${}_{10}S_{20}$	8.45150	2.50	${}_{14}S_{14}$	8.97800	6.00
${}_{8}S_{8}$	4.90450	2.50	${}_{10}S_{21}$	8.66900	4.50	${}_{14}S_{18}$	9.72500	10.00
${}_{8}S_{9}$	5.21100	2.00	${}_{10}S_{22}$	8.86800	7.00			
${}_{8}S_{10}$	5.50600	2.00	${}_{10}S_{25}$	9.81100	5.00	${}_{15}S_{3}$	6.03096	0.35
${}_{8}S_{11}$	5.71550	3.00				${}_{15}S_{10}$	7.89300	6.00
${}_{8}S_{12}$	5.87450	3.50	${}_{11}S_{4}$	4.76579	0.20	${}_{15}S_{11}$	8.13200	6.00
${}_{8}S_{13}$	6.01600	3.50	${}_{11}S_{5}$	5.07264	0.20	${}_{15}S_{12}$	8.43250	3.00
${}_{8}S_{14}$	6.16900	6.00	${}_{11}S_{9}$	6.43750	1.50	${}_{15}S_{15}$	9.59900	7.00
${}_{8}S_{15}$	6.30650	4.50	${}_{11}S_{10}$	6.71250	3.50			
${}_{8}S_{20}$	7.84800	6.00	${}_{11}S_{11}$	6.91500	9.00	${}_{16}S_{5}$	6.82984	1.44
${}_{8}S_{22}$	8.13500	8.00	${}_{11}S_{12}$	7.14400	5.00	${}_{16}S_{6}$	7.14913	0.54
${}_{8}S_{23}$	8.27300	7.00	${}_{11}S_{13}$	7.41150	4.00	${}_{16}S_{7}$	7.47004	1.00
${}_{8}S_{24}$	8.43100	8.00	${}_{11}S_{14}$	7.67900	3.50	${}_{16}S_{9}$	8.11600	2.00
${}_{8}S_{25}$	8.58200	6.00	${}_{11}S_{16}$	8.10000	10.00	${}_{16}S_{10}$	8.43300	3.00
${}_{8}S_{26}$	8.76000	9.00	${}_{11}S_{17}$	8.26500	8.00	${}_{16}S_{11}$	8.72900	5.00
${}_{8}S_{27}$	8.91200	6.00	${}_{11}S_{18}$	8.42400	8.00			
${}_{8}S_{29}$	9.25800	9.00	${}_{11}S_{20}$	8.71500	10.00	${}_{17}S_{12}$	9.14600	5.00
${}_{8}S_{30}$	9.41300	9.00	${}_{11}S_{22}$	9.10150	4.50	${}_{17}S_{13}$	9.43000	6.00
${}_{8}S_{31}$	9.59600	8.00	${}_{11}S_{23}$	9.33300	5.00	${}_{17}S_{14}$	9.70500	6.00
			${}_{11}S_{24}$	9.57650	4.50			
${}_{9}S_{3}$	3.55794	0.50				${}_{18}S_{3}$	6.88800	0.55
${}_{9}S_{4}$	3.88003	1.25	${}_{12}S_{8}$	6.13550	1.00	${}_{18}S_{4}$	7.23825	0.18
${}_{9}S_{8}$	5.13850	3.50	${}_{12}S_{10}$	6.86000	5.00	${}_{18}S_{9}$	8.73500	7.00
${}_{9}S_{9}$	5.37800	3.50	${}_{12}S_{11}$	7.13800	1.50			
${}_{9}S_{10}$	5.60450	2.50	${}_{12}S_{12}$	7.45150	2.00	${}_{19}S_{9}$	9.03800	8.00
${}_{9}S_{11}$	5.88700	7.00	${}_{12}S_{13}$	7.77100	2.50	${}_{19}S_{10}$	9.34300	5.00
${}_{9}S_{12}$	6.18450	2.00	${}_{12}S_{14}$	8.09300	2.50			
${}_{9}S_{13}$	6.48700	1.50	${}_{12}S_{15}$	8.40200	9.00	${}_{20}S_{1}$	6.94850	0.60
${}_{9}S_{14}$	6.77150	1.00	${}_{12}S_{16}$	8.68950	4.00	${}_{20}S_{5}$	8.46465	0.84
${}_{9}S_{15}$	7.02800	2.50	${}_{12}S_{17}$	8.92900	5.00	${}_{20}S_{9}$	9.81000	10.00
${}_{9}S_{16}$	7.23800	3.00	${}_{12}S_{19}$	9.34100	8.00			
${}_{9}S_{17}$	7.39000	5.00	${}_{12}S_{20}$	9.48600	9.00	${}_{21}S_{6}$	8.84853	0.72
${}_{9}S_{18}$	7.55100	5.00	${}_{12}S_{21}$	9.64600	7.00	${}_{21}S_{7}$	9.16782	1.00
${}_{9}S_{19}$	7.69500	4.50				${}_{21}S_{8}$	9.48988	1.20
${}_{9}S_{23}$	9.02500	10.00	${}_{13}S_{1}$	4.49000	0.80			
${}_{9}S_{24}$	9.17500	10.00	${}_{13}S_{2}$	4.84460	0.20	${}_{22}S_{1}$	7.81670	0.40
${}_{9}S_{26}$	9.50200	8.00	${}_{13}S_{3}$	5.19439	0.10			
			${}_{13}S_{12}$	7.95450	5.50	${}_{23}S_{4}$	8.93436	0.70
${}_{10}S_{2}$	4.04100	0.60	${}_{13}S_{14}$	8.26500	8.00	${}_{23}S_{5}$	9.28953	0.30
${}_{10}S_{8}$	5.73500	7.00	${}_{13}S_{15}$	8.46200	9.00			
${}_{10}S_{9}$	5.93900	4.50	${}_{13}S_{16}$	8.74600	5.00	${}_{25}S_{1}$	8.65250	0.40
${}_{10}S_{10}$	6.17650	2.50	${}_{13}S_{17}$	9.05550	4.00	${}_{25}S_{2}$	9.02651	0.69
${}_{10}S_{11}$	6.44600	6.00	${}_{13}S_{18}$	9.36600	6.00			
${}_{10}S_{12}$	6.68250	3.00	${}_{13}S_{19}$	9.66800	7.00	${}_{27}S_{1}$	9.48400	0.50
${}_{10}S_{13}$	6.87100	9.00				${}_{27}S_{2}$	9.86931	1.00
${}_{10}S_{14}$	7.02700	4.50	${}_{14}S_{4}$	5.54494	0.79			
${}_{10}S_{15}$	7.20200	5.00	${}_{14}S_{8}$	7.03900	1.50	${}_{0}T_{2}$	0.37727	0.80

mode	f	df	mode	f	df	mode	f	df
	[mHz]	[μHz]		[mHz]	[μHz]		[mHz]	[μHz]
${}_0T_3$	0.58759	0.66	${}_0T_{66}$	7.80400	9.00	${}_1T_{62}$	9.30700	7.00
${}_0T_4$	0.76691	0.37	${}_0T_{71}$	8.34000	10.00	${}_1T_{63}$	9.42000	10.00
${}_0T_5$	0.92897	0.37				${}_1T_{64}$	9.53900	8.00
${}_0T_6$	1.07951	0.18	${}_1T_6$	1.92551	0.45	${}_1T_{65}$	9.64800	4.00
${}_0T_7$	1.22150	0.30	${}_1T_8$	2.28100	2.50			
${}_0T_8$	1.35668	0.25	${}_1T_9$	2.45200	1.00	${}_2T_8$	2.91300	4.50
${}_0T_9$	1.48731	0.16	${}_1T_{10}$	2.61900	2.00	${}_2T_9$	3.09200	7.00
${}_0T_{10}$	1.61396	0.17	${}_1T_{11}$	2.78300	1.00	${}_2T_{10}$	3.26750	3.50
${}_0T_{11}$	1.73585	0.38	${}_1T_{14}$	3.25500	1.50	${}_2T_{11}$	3.45600	2.50
${}_0T_{13}$	1.97975	0.30	${}_1T_{15}$	3.40700	1.50	${}_2T_{12}$	3.64050	2.50
${}_0T_{14}$	2.09651	0.34	${}_1T_{16}$	3.56050	1.00	${}_2T_{13}$	3.83050	3.50
${}_0T_{15}$	2.21268	0.32	${}_1T_{17}$	3.71000	1.00	${}_2T_{14}$	4.01100	4.50
${}_0T_{16}$	2.32671	0.30	${}_1T_{19}$	4.00600	2.00	${}_2T_{15}$	4.19000	2.00
${}_0T_{17}$	2.44241	0.32	${}_1T_{20}$	4.15200	2.50	${}_2T_{16}$	4.36700	3.50
${}_0T_{18}$	2.55393	0.40	${}_1T_{21}$	4.29500	1.00	${}_2T_{17}$	4.54300	2.00
${}_0T_{21}$	2.88708	0.34	${}_1T_{22}$	4.44000	2.00	${}_2T_{18}$	4.71000	2.50
${}_0T_{22}$	2.99770	0.44	${}_1T_{23}$	4.58000	2.00	${}_2T_{20}$	5.04450	4.00
${}_0T_{23}$	3.10818	0.40	${}_1T_{24}$	4.72100	2.00	${}_2T_{21}$	5.20200	2.50
${}_0T_{24}$	3.22125	0.46	${}_1T_{25}$	4.85950	2.00	${}_2T_{22}$	5.36600	2.50
${}_0T_{25}$	3.33108	0.42	${}_1T_{27}$	5.12900	2.00	${}_2T_{23}$	5.52550	2.50
${}_0T_{26}$	3.44140	0.50	${}_1T_{28}$	5.26450	2.00	${}_2T_{24}$	5.68450	4.00
${}_0T_{28}$	3.65903	0.60	${}_1T_{29}$	5.39950	2.50	${}_2T_{25}$	5.84300	3.50
${}_0T_{29}$	3.76839	0.64	${}_1T_{30}$	5.52750	1.50	${}_2T_{26}$	6.00100	4.50
${}_0T_{33}$	4.20742	0.84	${}_1T_{31}$	5.65600	3.00	${}_2T_{27}$	6.15100	6.00
${}_0T_{34}$	4.31766	0.66	${}_1T_{32}$	5.78650	3.00	${}_2T_{28}$	6.30950	3.50
${}_0T_{35}$	4.42845	0.64	${}_1T_{33}$	5.91500	3.50	${}_2T_{29}$	6.46450	3.00
${}_0T_{37}$	4.64375	0.98	${}_1T_{34}$	6.03950	3.50	${}_2T_{30}$	6.60900	3.50
${}_0T_{38}$	4.74900	2.00	${}_1T_{35}$	6.16600	3.50	${}_2T_{31}$	6.76300	4.50
${}_0T_{39}$	4.85900	5.00	${}_1T_{36}$	6.28750	3.00	${}_2T_{32}$	6.91100	4.50
${}_0T_{40}$	4.96700	3.00	${}_1T_{37}$	6.41250	2.50	${}_2T_{33}$	7.06600	4.00
${}_0T_{41}$	5.07650	4.00	${}_1T_{39}$	6.65600	6.00	${}_2T_{34}$	7.21400	6.00
${}_0T_{42}$	5.18350	3.00	${}_1T_{40}$	6.77350	4.50	${}_2T_{35}$	7.36200	4.00
${}_0T_{43}$	5.29200	3.00	${}_1T_{41}$	6.88900	6.00	${}_2T_{36}$	7.50500	5.00
${}_0T_{44}$	5.40450	4.50	${}_1T_{42}$	7.01350	3.50	${}_2T_{37}$	7.65300	3.00
${}_0T_{45}$	5.50600	4.50	${}_1T_{43}$	7.13300	5.00	${}_2T_{38}$	7.79700	4.00
${}_0T_{46}$	5.62850	4.00	${}_1T_{44}$	7.24950	3.00	${}_2T_{39}$	7.94350	3.00
${}_0T_{47}$	5.73300	3.00	${}_1T_{45}$	7.36250	4.50	${}_2T_{40}$	8.08900	5.00
${}_0T_{48}$	5.83750	4.50	${}_1T_{46}$	7.48350	4.00	${}_2T_{41}$	8.23000	8.00
${}_0T_{49}$	5.95200	4.00	${}_1T_{47}$	7.59400	5.00	${}_2T_{42}$	8.37000	10.00
${}_0T_{50}$	6.05300	5.00	${}_1T_{48}$	7.71350	3.50	${}_2T_{43}$	8.50700	8.00
${}_0T_{51}$	6.16900	5.00	${}_1T_{49}$	7.83000	6.00	${}_2T_{44}$	8.66100	9.00
${}_0T_{52}$	6.27300	7.00	${}_1T_{50}$	7.94850	3.50	${}_2T_{45}$	8.78500	6.00
${}_0T_{53}$	6.37700	7.00	${}_1T_{51}$	8.05900	6.00	${}_2T_{46}$	8.93200	7.00
${}_0T_{54}$	6.49300	4.00	${}_1T_{52}$	8.17000	8.00	${}_2T_{47}$	9.06900	8.00
${}_0T_{55}$	6.59500	8.00	${}_1T_{53}$	8.27800	7.00	${}_2T_{48}$	9.20400	8.00
${}_0T_{56}$	6.70200	9.00	${}_1T_{54}$	8.40000	10.00	${}_2T_{49}$	9.33300	8.00
${}_0T_{57}$	6.81400	6.00	${}_1T_{56}$	8.62700	8.00	${}_2T_{50}$	9.47500	10.00
${}_0T_{58}$	6.91900	7.00	${}_1T_{57}$	8.74000	10.00	${}_2T_{51}$	9.61500	10.00
${}_0T_{62}$	7.37000	15.00	${}_1T_{58}$	8.85100	9.00	${}_2T_{52}$	9.74500	10.00
${}_0T_{64}$	7.58500	10.00	${}_1T_{60}$	9.08300	9.00			
${}_0T_{65}$	7.70000	10.00	${}_1T_{61}$	9.19700	8.00	${}_3T_9$	3.84300	5.00

mode	f	df	mode	f	df	mode	f	df
	[mHz]	[μHz]		[mHz]	[μHz]		[mHz]	[μHz]
${}_3T_{10}$	3.99000	5.00	${}_3T_{32}$	7.75750	4.50	${}_4T_{13}$	5.24300	7.00
${}_3T_{12}$	4.31700	6.00	${}_3T_{33}$	7.91450	4.50	${}_4T_{14}$	5.38450	4.50
${}_3T_{13}$	4.48200	7.00	${}_3T_{34}$	8.08000	5.00	${}_4T_{15}$	5.53800	7.00
${}_3T_{16}$	5.04000	4.50	${}_3T_{36}$	8.39500	10.00	${}_4T_{16}$	5.70900	7.00
${}_3T_{17}$	5.23400	8.00	${}_3T_{37}$	8.54800	5.00	${}_4T_{17}$	5.87000	9.00
${}_3T_{18}$	5.41400	7.00	${}_3T_{38}$	8.69700	8.00	${}_4T_{21}$	6.59400	6.00
${}_3T_{19}$	5.60700	4.50	${}_3T_{39}$	8.85800	8.00	${}_4T_{24}$	7.15900	8.00
${}_3T_{20}$	5.78500	8.00	${}_3T_{40}$	9.02000	10.00	${}_4T_{26}$	7.51200	6.00
${}_3T_{21}$	5.95500	6.00	${}_3T_{41}$	9.16600	8.00	${}_4T_{27}$	7.69400	7.00
${}_3T_{22}$	6.12000	6.00	${}_3T_{42}$	9.32300	8.00	${}_4T_{28}$	7.86300	8.00
${}_3T_{23}$	6.29900	6.00	${}_3T_{43}$	9.47200	7.00	${}_4T_{30}$	8.19500	10.00
${}_3T_{25}$	6.62250	3.50	${}_3T_{44}$	9.61500	7.00	${}_4T_{32}$	8.54800	7.00
${}_3T_{26}$	6.79100	7.00	${}_3T_{45}$	9.78200	9.00	${}_4T_{33}$	8.71800	4.50
${}_3T_{27}$	6.94650	3.50	${}_3T_{46}$	9.92600	7.00	${}_4T_{34}$	8.87300	6.00
${}_3T_{28}$	7.11350	3.50				${}_4T_{35}$	9.05000	5.00
${}_3T_{29}$	7.27300	4.50	${}_4T_{10}$	4.88500	5.00	${}_4T_{36}$	9.21000	8.00
${}_3T_{30}$	7.43900	4.50	${}_4T_{11}$	4.99350	4.50	${}_4T_{37}$	9.39000	7.00
${}_3T_{31}$	7.60500	5.00	${}_4T_{12}$	5.11600	6.00	${}_4T_{39}$	9.67900	9.00

Appendix B : Model CORE11 ($T_{ref} = 1s$)

Radius	Density	v_{PV}	v_{SV}	Q_κ	Q_μ	v_{PH}	v_{SH}	η
[m]	[kgm^{-3}]	[ms^{-1}]	[ms^{-1}]			[ms^{-1}]	[ms^{-1}]	
0	13017.9	11291.5	3568.5	15700	3140	11271.6	3634.3	0.985
38172	13017.5	11291.3	3568.3	15700	3140	11271.3	3634.1	0.985
76344	13016.6	11290.6	3567.7	15700	3140	11270.6	3633.6	0.985
114516	13015.0	11289.5	3566.8	15700	3140	11269.5	3632.8	0.985
152688	13012.7	11287.9	3565.6	15700	3140	11267.8	3631.6	0.985
190859	13009.9	11285.8	3564.0	15700	3140	11265.8	3630.2	0.985
229031	13006.3	11283.3	3562.0	15700	3140	11263.2	3628.3	0.985
267203	13002.2	11280.4	3559.8	15700	3140	11260.2	3626.2	0.985
305375	12997.4	11277.0	3557.2	15700	3140	11256.8	3623.8	0.985
343547	12992.0	11273.1	3554.3	15700	3140	11252.9	3621.0	0.984
381719	12986.0	11268.8	3551.0	15700	3140	11248.5	3617.9	0.984
419891	12979.3	11264.0	3547.4	15700	3140	11243.7	3614.4	0.984
458063	12972.0	11258.7	3543.5	15700	3140	11238.4	3610.7	0.984
496234	12964.0	11253.0	3539.2	15700	3140	11232.7	3606.6	0.984
534406	12955.4	11246.9	3534.6	15700	3140	11226.5	3602.2	0.984
572578	12946.2	11240.2	3529.7	15700	3140	11219.8	3597.4	0.984
610750	12936.4	11233.2	3524.4	15700	3140	11212.7	3592.4	0.984
648922	12925.9	11225.6	3518.8	15700	3140	11205.1	3587.0	0.984
687094	12914.7	11217.7	3512.8	15700	3140	11197.0	3581.3	0.984
725266	12903.0	11209.2	3506.5	15700	3140	11188.5	3575.2	0.984
763438	12890.6	11200.3	3499.9	15700	3140	11179.6	3568.9	0.984
801609	12877.6	11191.0	3492.9	15700	3140	11170.2	3562.2	0.984
839781	12863.9	11181.2	3485.6	15700	3140	11160.3	3555.1	0.984
877953	12849.6	11170.9	3478.0	15700	3140	11150.0	3547.8	0.984
916125	12834.7	11160.2	3470.0	15700	3140	11139.2	3540.1	0.984
954297	12819.1	11149.0	3461.7	15700	3140	11127.9	3532.1	0.984
992469	12802.9	11137.3	3453.0	15700	3140	11116.2	3523.8	0.984
1030641	12786.1	11125.2	3444.0	15700	3140	11104.0	3515.1	0.984
1068813	12768.6	11112.7	3434.7	15700	3140	11091.4	3506.1	0.984
1106984	12750.5	11099.7	3425.0	15700	3140	11078.3	3496.8	0.984
1145156	12731.8	11086.2	3415.0	15700	3140	11064.8	3487.2	0.984
1183328	12712.4	11072.3	3404.6	15700	3140	11050.8	3477.2	0.984
1218767	12692.4	11057.9	3393.9	15700	3140	11036.3	3466.9	0.983
1218767	12217.3	10329.8	0.0	∞	∞	10329.8	0.0	1.000
1292078	12177.6	10289.6	0.0	∞	∞	10289.6	0.0	1.000
1362656	12136.2	10248.5	0.0	∞	∞	10248.5	0.0	1.000
1433234	12093.0	10206.4	0.0	∞	∞	10206.4	0.0	1.000
1503813	12047.9	10163.4	0.0	∞	∞	10163.4	0.0	1.000
1574391	12000.9	10119.1	0.0	∞	∞	10119.1	0.0	1.000
1644969	11952.0	10073.5	0.0	∞	∞	10073.5	0.0	1.000
1715547	11901.2	10026.6	0.0	∞	∞	10026.6	0.0	1.000
1786125	11848.3	9978.1	0.0	∞	∞	9978.1	0.0	1.000
1856703	11793.4	9928.1	0.0	∞	∞	9928.1	0.0	1.000

Radius	Density	v_{PV}	v_{SV}	Q_κ	Q_μ	v_{PH}	v_{SH}	η
[m]	[kgm^{-3}]	[ms^{-1}]	[ms^{-1}]			[ms^{-1}]	[ms^{-1}]	
1927281	11736.3	9876.2	0.0	∞	∞	9876.2	0.0	1.000
1997859	11677.1	9822.6	0.0	∞	∞	9822.6	0.0	1.000
2068438	11615.8	9767.0	0.0	∞	∞	9767.0	0.0	1.000
2139016	11552.2	9709.3	0.0	∞	∞	9709.3	0.0	1.000
2209594	11486.3	9649.5	0.0	∞	∞	9649.5	0.0	1.000
2280172	11418.0	9587.4	0.0	∞	∞	9587.4	0.0	1.000
2350750	11347.5	9522.9	0.0	∞	∞	9522.9	0.0	1.000
2421328	11274.5	9455.8	0.0	∞	∞	9455.8	0.0	1.000
2491906	11199.0	9386.2	0.0	∞	∞	9386.2	0.0	1.000
2562485	11121.1	9313.8	0.0	∞	∞	9313.8	0.0	1.000
2633063	11040.6	9238.5	0.0	∞	∞	9238.5	0.0	1.000
2703641	10957.5	9160.3	0.0	∞	∞	9160.3	0.0	1.000
2774219	10871.9	9079.1	0.0	∞	∞	9079.1	0.0	1.000
2844797	10783.5	8994.6	0.0	∞	∞	8994.6	0.0	1.000
2915375	10692.4	8906.8	0.0	∞	∞	8906.8	0.0	1.000
2985953	10598.6	8815.7	0.0	∞	∞	8815.7	0.0	1.000
3056531	10501.9	8721.0	0.0	∞	∞	8721.0	0.0	1.000
3127110	10402.4	8622.6	0.0	∞	∞	8622.6	0.0	1.000
3197688	10300.0	8520.6	0.0	∞	∞	8520.6	0.0	1.000
3268266	10194.7	8414.7	0.0	∞	∞	8414.7	0.0	1.000
3338844	10086.4	8304.7	0.0	∞	∞	8304.7	0.0	1.000
3409422	9975.1	8190.8	0.0	∞	∞	8190.8	0.0	1.000
3482391	9860.6	8072.6	0.0	∞	∞	8072.6	0.0	1.000
3482391	5653.6	13643.6	7224.2	16600	332	13613.2	7246.0	1.009
3517500	5634.9	13634.2	7224.4	16600	332	13603.8	7246.3	1.009
3555000	5616.1	13625.0	7224.6	16600	332	13594.4	7246.6	1.009
3592500	5597.4	13615.8	7224.8	16600	332	13585.1	7246.8	1.009
3630000	5578.7	13606.7	7224.9	16600	332	13575.9	7247.0	1.009
3630000	5511.1	13671.8	7261.6	16600	332	13658.1	7255.5	1.008
3666482	5492.4	13628.3	7244.9	16600	332	13614.6	7238.9	1.008
3702963	5473.7	13585.1	7228.4	16600	332	13571.4	7222.4	1.008
3739445	5455.0	13542.3	7211.9	16600	332	13528.7	7206.0	1.008
3775926	5436.4	13499.7	7195.5	16600	332	13486.2	7189.6	1.008
3812408	5417.7	13457.4	7179.1	16600	332	13444.0	7173.3	1.008
3848889	5399.0	13415.4	7162.8	16600	332	13402.0	7157.1	1.008
3885371	5380.3	13373.6	7146.5	16600	332	13360.2	7140.9	1.008
3921852	5361.6	13331.9	7130.3	16600	332	13318.7	7124.7	1.008
3958333	5342.9	13290.4	7114.1	16600	332	13277.3	7108.5	1.008
3994815	5324.2	13249.1	7097.9	16600	332	13236.0	7092.4	1.008
4031296	5305.5	13207.8	7081.6	16600	332	13194.8	7076.2	1.008
4067778	5286.7	13166.6	7065.4	16600	332	13153.6	7060.1	1.008
4104259	5267.9	13125.4	7049.2	16600	332	13112.5	7043.9	1.008
4140741	5249.1	13084.2	7032.9	16600	332	13071.5	7027.7	1.007
4177222	5230.2	13043.0	7016.5	16600	332	13030.3	7011.4	1.007
4213704	5211.3	13001.7	7000.1	16600	332	12989.2	6995.1	1.007
4250185	5192.4	12960.4	6983.7	16600	332	12947.9	6978.7	1.007
4286667	5173.4	12918.9	6967.1	16600	332	12906.5	6962.3	1.007

Radius	Density	v_{PV}	v_{SV}	Q_κ	Q_μ	v_{PH}	v_{SH}	η
[m]	[kgm^{-3}]	[ms^{-1}]	[ms^{-1}]			[ms^{-1}]	[ms^{-1}]	
4323148	5154.4	12877.3	6950.5	16600	332	12865.0	6945.7	1.007
4359630	5135.3	12835.5	6933.8	16600	332	12823.3	6929.1	1.007
4396111	5116.2	12793.4	6917.0	16600	332	12781.4	6912.3	1.007
4432593	5097.0	12751.2	6900.0	16600	332	12739.2	6895.5	1.007
4469074	5077.8	12708.7	6883.0	16600	332	12696.8	6878.5	1.006
4505556	5058.4	12665.8	6865.7	16600	332	12654.1	6861.3	1.006
4542037	5039.1	12622.7	6848.4	16600	332	12611.1	6844.0	1.006
4578519	5019.6	12579.2	6830.8	16600	332	12567.7	6826.6	1.006
4615000	5000.1	12535.3	6813.1	16600	332	12523.9	6809.0	1.006
4651482	4980.5	12491.0	6795.3	16600	332	12479.7	6791.2	1.006
4687963	4960.8	12446.2	6777.2	16600	332	12435.0	6773.2	1.006
4724445	4941.1	12401.0	6758.9	16600	332	12389.9	6755.0	1.005
4760926	4921.2	12355.2	6740.4	16600	332	12344.3	6736.6	1.005
4797408	4901.3	12308.9	6721.7	16600	332	12298.1	6717.9	1.005
4833889	4881.2	12262.0	6702.7	16600	332	12251.4	6699.1	1.005
4870371	4861.1	12214.6	6683.5	16600	332	12204.0	6680.0	1.005
4906852	4840.8	12166.5	6664.1	16600	332	12156.1	6660.6	1.004
4943334	4820.5	12117.7	6644.3	16600	332	12107.5	6641.0	1.004
4979815	4800.1	12068.3	6624.3	16600	332	12058.2	6621.0	1.004
5016297	4779.5	12018.1	6604.0	16600	332	12008.1	6600.8	1.004
5052778	4758.8	11967.2	6583.4	16600	332	11957.4	6580.3	1.004
5089260	4738.0	11915.5	6562.5	16600	332	11905.8	6559.5	1.003
5125741	4717.1	11863.0	6541.3	16600	332	11853.4	6538.4	1.003
5162222	4696.1	11809.6	6519.8	16600	332	11800.2	6516.9	1.003
5198704	4674.9	11755.4	6497.9	16600	332	11746.2	6495.1	1.003
5235185	4653.6	11700.3	6475.6	16600	332	11691.2	6473.0	1.002
5271667	4632.1	11644.3	6453.0	16600	332	11635.3	6450.5	1.002
5308148	4610.6	11587.2	6430.0	16600	332	11578.5	6427.6	1.002
5344630	4588.8	11529.2	6406.6	16600	332	11520.6	6404.3	1.002
5381111	4567.0	11470.2	6382.8	16600	332	11461.7	6380.7	1.001
5417593	4545.0	11410.1	6358.7	16600	332	11401.8	6356.6	1.001
5454074	4522.8	11349.0	6334.1	16600	332	11340.8	6332.1	1.001
5490556	4500.5	11286.7	6309.0	16600	332	11278.7	6307.2	1.000
5527037	4478.0	11223.3	6283.6	16600	332	11215.5	6281.8	1.000
5563519	4455.3	11158.7	6257.6	16600	332	11151.1	6256.0	1.000
5600000	4432.5	11092.9	6231.2	16600	332	11085.5	6229.7	0.999
5600000	4418.6	11082.7	6268.6	16600	332	11106.7	6259.5	0.985
5633667	4397.9	10977.7	6170.2	16600	332	11002.0	6160.9	0.985
5667334	4377.1	10872.6	6071.7	16600	332	10897.2	6062.2	0.985
5701000	4356.1	10767.4	5973.3	16600	332	10792.4	5963.6	0.985
5701000	3984.7	10260.9	5590.0	13850	277	10281.9	5585.7	0.994
5771000	3968.4	10152.2	5535.9	13850	277	10173.5	5531.6	0.994
5771000	4004.6	10077.9	5465.1	13850	277	10134.0	5500.6	0.976
5804334	3962.6	9906.3	5367.1	13850	277	9963.9	5403.6	0.975
5837667	3920.6	9734.6	5269.1	13850	277	9793.9	5306.6	0.974
5871000	3878.6	9562.9	5171.0	13850	277	9623.9	5209.7	0.972
5904334	3836.6	9391.1	5072.9	13850	277	9453.9	5112.7	0.971

Radius	Density	v_{PV}	v_{SV}	Q_κ	Q_μ	v_{PH}	v_{SH}	η
[m]	[kgm^{-3}]	[ms^{-1}]	[ms^{-1}]			[ms^{-1}]	[ms^{-1}]	
5937667	3794.6	9219.2	4974.7	13850	277	9283.9	5015.8	0.970
5971000	3752.6	9047.3	4876.5	13850	277	9114.0	4918.9	0.969
5971000	3541.9	8899.1	4769.9	5895	118	8889.8	4790.6	1.021
5993500	3528.4	8855.7	4754.1	5895	118	8846.3	4775.0	1.021
6016000	3515.0	8812.4	4738.4	5895	118	8802.9	4759.4	1.021
6038500	3501.5	8769.0	4722.6	5895	118	8759.5	4743.8	1.022
6061000	3488.1	8725.7	4706.9	5895	118	8716.0	4728.2	1.022
6083500	3474.7	8682.3	4691.1	5895	118	8672.6	4712.6	1.023
6106000	3461.2	8638.9	4675.4	5895	118	8629.1	4697.0	1.023
6128500	3447.8	8595.6	4659.6	5895	118	8585.7	4681.4	1.024
6151000	3434.4	8552.2	4643.9	5895	118	8542.2	4665.8	1.024
6151000	3323.8	7899.9	4445.4	5895	118	8025.2	4433.9	0.994
6179000	3326.8	7931.5	4438.9	5895	118	8045.8	4459.3	0.983
6207000	3329.9	7963.1	4432.4	5895	118	8066.4	4484.7	0.971
6235000	3332.9	7994.6	4425.8	5895	118	8086.9	4510.1	0.960
6263000	3335.9	8026.2	4419.3	5895	118	8107.5	4535.5	0.948
6291000	3339.0	8057.8	4412.8	5895	118	8128.1	4560.9	0.937
6291000	3398.1	7936.1	4343.2	5895	118	8113.2	4480.7	0.897
6318800	3401.2	7967.5	4336.8	5895	118	8133.3	4506.0	0.887
6346600	3404.2	7998.9	4330.4	5895	118	8153.5	4531.3	0.877
6346600	2900.0	6800.0	3900.0	5895	118	6800.0	3900.0	1.000
6356000	2900.0	6800.0	3900.0	5895	118	6800.0	3900.0	1.000
6356000	2600.0	5800.0	3200.0	5895	118	5800.0	3200.0	1.000
6368000	2600.0	5800.0	3200.0	5895	118	5800.0	3200.0	1.000
6368000	1020.0	1450.0	0.0	∞	∞	1450.0	0.0	1.000
6371000	1020.0	1450.0	0.0	∞	∞	1450.0	0.0	1.000

Chapter 3

Observably Split Multiplets – Data Analysis and Interpretation in Terms of Large-scale Aspherical Structure

3.1 Introduction

The aspherical structure of the Earth's deep interior can be studied with a number of different seismological techniques and the past decade has seen a flurry of activity. At the high-frequency end of the spectrum of seismic signals, the tomographic inversion of travel-time residuals of seismic phases catalogued by the International Seismic Center (ISC) has led to the first images of compressional wave velocity perturbations in the lower mantle (*Dziewonski et al. 1977*; *Dziewonski, 1984*; *Hager and Clayton, 1989*). Travel-time residuals of phases which interact with the core-mantle boundary, in conjunction with the models of lower mantle structure, have been used to study the topography of the core-mantle boundary (*Creager and Jordan, 1986*; *Morelli and Dziewonski, 1986*). The ISC data set was also used by *Poupinet et al. (1983)* to infer aspherical inner core structure from a study of PKIKP travel times. More recent studies of core phases, (*Morelli et al. 1986*; *Shearer et al. 1988* and *Shearer and Toy, 1991*) prefer inner core models with axisymmetric anisotropy in compressional wave velocity.

Travel-time residuals of long-period body waves with a characteristic period of 25 seconds recorded primarily by the Global Digital Seismic Network (GDSN) have also been used for studies of mantle and core structure. While the number of observations is considerably smaller than that of the ISC dataset, the GDSN dataset exhibits less scatter and the raw data show large coherent residual patterns indicative of large-scale aspherical structure (*Woodward and Masters, 1991a, 1991b).* The global coverage for the GDSN and ISC datasets is comparable and, while the northern hemisphere is well sampled, coverage is quite sparse in the southern hemisphere where structure cannot be reliably

determined.

An alternative way to interpret the long-period data is to model the waveforms directly. This approach has been applied to surface waves in an effort to model long wavelength upper mantle structure (*e.g., Woodhouse and Dziewonski, 1984*). *Tanimoto (1990)* has applied waveform modeling to the body-wave part of long-period seismograms to retrieve a shear wave velocity model of the whole mantle.

At periods from 20 to 300 seconds, studies of surface wave dispersion have yielded models of the large scale structure of the upper mantle (*e.g., Nakanishi and Anderson, 1984*; *Montagner and Tanimoto, 1990*). While the surface waves constitute the largest signal in most seismic records, their study only reveals information about the structure of the upper mantle and crust and their ability to resolve structural perturbations in the radial direction is very limited.

At periods longer than 100 seconds it is convenient to study aspherical structure by directly analyzing the normal mode splitting which it causes. Since the first observations of normal mode splitting in the wake of the 1960 Great Chilean Earthquake, the theory for the calculation of synthetic spectra for an Earth model with very general aspherical structure has been highly developed (*Dahlen, 1968, 1969*; *Luh, 1973, 1974*; *Woodhouse and Dahlen, 1978*; *Woodhouse, 1980*; *Park and Gilbert, 1986*; *etc.*).

We distinguish two kinds of mode splitting: resolvable and unresolvable splitting. Modes with large harmonic degree are unresolvably split because the close spacing of the singlet resonance functions makes it impossible to observe individual singlets though it is usually true that the observed spectrum still appears like a single resonance function. The effect of large-scale aspherical structure on unresolvably split multiplets manifests itself primarily as an apparent center frequency which varies from record to record. Observations of such frequency shifts of fundamental modes have been used to infer upper mantle structure and lead to models dominated by degree 2 structure in the transition zone (*Masters et al. 1982*; *Romanowicz et al. 1986*; *Davis, 1987*; *Smith and Masters, 1989*; *Roult et al. 1990*). If the spacing between singlets of a multiplet is of the same order as the peak width due to attenuation then the spectrum of a multiplet may consist of multiple peaks and is termed resolvably split. PKIKP equivalent low-l high-Q multiplets generally fall into this category and they are the subject of study in this chapter.

An analysis based on spectra of individual records is generally only possible for fundamental modes because they dominate the amplitude spectra of all but the very deepest earthquakes and mask overtones which tell us about deep Earth structure. Only a few events are very good at exciting high-Q modes which have a large fraction of their elastic energy in the weakly attenuating outer core (see chapter 5). For recordings of such events, we can use the Earth as an attenuation filter to discriminate against the densely spaced, low-Q modes. In practice, this means that we discard the initial few hours of a recording

to give sufficient time for the low-Q modes to decay away.

If we define the splitting width of a multiplet to be the frequency difference between the highest and lowest frequency singlet, we find that, for many modes, the observed splitting width is more than 1.5 times larger than predicted for a rotating earth model in hydrostatic equilibrium. Such multiplets are termed "anomalously" split. The splitting width for the mode ${}_{18}S_4$ for example is 20 μHz while the predicted value for a rotating earth in hydrostatic equilibrium is 10.7 μHz. Anomalous splitting of multiplets is a large signal and we feel that understanding anomalous splitting is the key to understanding the 3-D structure of the inner and outer core.

The first unambiguous observation of an anomalously split multiplet, ${}_{10}S_2$, was given by *Masters and Gilbert (1981)*. Subsequent systematic analyses of observably split high-Q modes below 5 mHz has allowed the construction of degree 2 and 4 mantle models (*e.g., Giardini et al. 1987, 1988*; *Ritzwoller et al. 1986, 1988*; *Li et al. 1991a*) though such models are incapable of explaining the anomalous splitting of core-sensitive modes. Possible explanations for anomalous splitting include 2% non-hydrostatic density perturbation in the outer core (*Ritzwoller et al. 1986*) and 7% axisymmetric anisotropy in compressional velocity in the inner core (*Li et al. 1991a)* but such models are either physically unrealistic or are unable to predict the splitting of modes which are largely confined to the mantle and outer core.

In this chapter we extend the search for observably split multiplets up to a frequency of 10mHz. Analysis of such multiplets allows us to place new constraints on models of both the 1-D and 3-D structure of the lower mantle and core.

3.2 Theory

We use two well-established techniques to analyze the splitting of isolated multiplets: "Singlet stripping" (*Buland et al. 1979*; *Ritzwoller et al. 1986*) and "Iterative spectral fitting" (*Giardini et al. 1987, 1988*; *Ritzwoller et al. 1986, 1988*). Both techniques are based on first order splitting theory and their goal is to estimate the so-called "structure coefficients" from the data spectra. The structure coefficients of a suite of modes can then be used in a linear inverse problem to determine the radial dependence of aspherical structure.

We give a brief summary of the first-order splitting theory for isolated multiplets to the extent needed for the understanding of our observational techniques and refer the interested reader to the original references (*e.g., Woodhouse and Dahlen, 1978).*

3.2.1 First Order Splitting Theory

The largest apparent deviations of the Earth from spherical symmetry are the diurnal rotation and the ellipticity of figure. We may consider the rate of rotation to be known and, under the assumption of hydrostatic equilibrium, the ellipticity of figure is also determined (*Jeffreys, 1976*). The structure of interest to us is the deviation from spherical symmetry beyond rotation and hydrostatic ellipticity and so we find it convenient to refer all observations to the predictions for a rotating earth model in hydrostatic equilibrium. We restrict our attention to multiplets which can be considered uncoupled be it because their frequency or Q differs much from neighboring multiplets or because their eigenfunctions are sufficiently dissimilar. For a rotating earth model in hydrostatic equilibrium, the displacement eigenfunction of the mth singlet of an isolated multiplet is (*e.g., Backus and Gilbert, 1961*)

$$\boldsymbol{\sigma}_k^m(\mathbf{r},t) = \left[\hat{\mathbf{r}}\, U_k(r) Y_l^m(\theta,\phi) + V_k(r)\, \boldsymbol{\nabla}_1 Y_l^m(\theta,\phi) - W_k(r)\, \hat{\mathbf{r}} \times \boldsymbol{\nabla}_1 Y_l^m(\theta,\phi)\right] e^{i\omega_m t} \tag{3.1}$$

where k is the multiplet index, l is the harmonic degree, m is the azimuthal order and ω_m is the frequency of the mth singlet. m takes on the values $-l \leq m \leq l$ so that we get $2l+1$ singlets per multiplet and the multiplet index k is a shorthand for the triplet of indices (n,l,q) with $n \geq 0$ being the overtone number and q taking on the value S or T for spheroidal or toroidal modes. The three scalar functions U_k, V_k and W_k are the radial eigenfunctions of the 1-D reference model for the kth multiplet and are identical for all singlets within a multiplet. Finally $\hat{\mathbf{r}}$ is a unit vector in the radial direction and $\boldsymbol{\nabla}_1$ is the surface gradient $\boldsymbol{\nabla}_1 = r(\boldsymbol{\nabla} - \hat{\mathbf{r}}\partial_r)$. If the Earth were spherically symmetric, all the singlets would oscillate with the same frequency: the so-called multiplet degenerate frequency ω_k. If the spherical symmetry is broken by the diurnal rotation and the Earth model is allowed to deform and reach hydrostatic equilibrium, then the frequencies of the singlets of an isolated multiplet follow a quadratic in m *(Dahlen, 1968)*

$$\omega_m = \omega_k(1 + a + mb + m^2 c) \tag{3.2}$$

For such a model, the displacement field for a particular component of a receiver at $\mathbf{r}$ and a source at $\mathbf{r}_0$ can be written in the form

$$s(\mathbf{r},t) = \mathrm{Re}\left[\sum_k \boldsymbol{\sigma}_k^T(\mathbf{r}) e^{i\mathbf{H}^k t} \mathbf{a}_k(\mathbf{r}_0) e^{i\omega_k t}\right] \tag{3.3}$$

where $\mathbf{a}_k$ and $\boldsymbol{\sigma}_k$ are the source and receiver vectors for the kth multiplet. The $2l+1$ elements of the

receiver vector ($-l \leq m \leq l$) are given by (3.1) The elements of the source vector describe the excitation of the individual singlets by a source with moment rate tensor M and are the contraction of the complex conjugate strain tensor for the mth singlet, evaluated at the source, with the moment rate tensor (*Gilbert and Dziewonski, 1975*): $a_k^m = -\mathbf{E}_k^{m*} : \mathbf{M}$.

The matrix $\mathbf{H}^k$ is termed the splitting matrix. In the case of a rotating earth model in hydrostatic equilibrium, $\mathbf{H}^k$ is diagonal with $H_{mm'}^k = \omega_k(a + mb + m^2c)\delta_{mm'}$. The two parameters a and c are called the ellipticity splitting parameters and b is the rotational splitting parameter. Equation (3.3) is also applicable in the case of a model with small but general aspherical perturbations in which case the splitting matrix is written:

$$H_{mm'}^k = \omega_k(a + mb + m^2c)\delta_{mm'} + \sum_s \gamma_s^{mm'}{}_k c_s^t \tag{3.4}$$

where the ${}_k c_s^t$ are the structure coefficients. We have expanded the aspherical structure specified by perturbations in density $\delta\rho$, bulk modulus $\delta\kappa$ and shear modulus $\delta\mu$ in terms of spherical harmonics:

$$\delta\rho(r,\theta,\phi) = \sum_{s,t} \delta\rho_s^t(r) Y_s^t(\theta,\phi) \tag{3.5}$$

$$\delta\kappa(r,\theta,\phi) = \sum_{s,t} \delta\kappa_s^t(r) Y_s^t(\theta,\phi) \tag{3.6}$$

$$\delta\mu(r,\theta,\phi) = \sum_{s,t} \delta\mu_s^t(r) Y_s^t(\theta,\phi) \tag{3.7}$$

and similarly defined the topography of the ith first order discontinuity

$$h_i(\theta,\phi) = \sum_{s,t} h_{si}^t Y_s^t(\theta,\phi). \tag{3.8}$$

The structure coefficients in (3.4) are then related to aspherical structure by

$${}_k c_s^t = \int_0^a ({}_k R_s(r)\delta\rho_s^t(r) + {}_k K_s(r)\delta\kappa_s^t(r) + {}_k M_s(r)\delta\mu_s^t(r))r^2 dr - \sum_i r_i^2 h_{si}^t {}_k B_{si} \tag{3.9}$$

This expression shows that the structure coefficients are linearly related to the perturbations in aspherical structure. The kernels R_s, K_s, M_s and B_{si} are functions of the spherical earth eigenfunctions and are given by *Woodhouse and Dahlen (1978)*. (3.9) is the basis of the linear inverse problem which we solve in section 3.5: recover the perturbations $\delta\rho_s^t(r)$, $\delta\kappa_s^t(r)$, $\delta\mu_s^t(r)$ and ${}_k B_{si}$ from a finite number of

observations ${}_kc_s^t$. From (3.3), we see that the displacement $s(\mathbf{r},t)$ is nonlinearly related to the splitting matrix and so is nonlinearly related to the structure coefficients. Iterative spectral fitting is based on a linearization of (3.3) and is a procedure in which we attempt to estimate the structure coefficients ${}_kc_s^t$ directly from observed spectra (see section 3.4). $\gamma_s^{mm'}$ in (3.4) is an integral over three spherical harmonics and can be written as

$$\gamma_s^{mm'} = (-1)^m(2l+1)\left[\frac{2s+1}{4\pi}\right]^{1/2}\begin{pmatrix} l & s & l \\ -m & t & m' \end{pmatrix}\begin{pmatrix} l & s & l \\ 0 & 0 & 0 \end{pmatrix}. \tag{3.10}$$

The last two factors in this expression are Wigner 3-j symbols (*Edmonds, 1960*). As a consequence of the orthogonality relations among spherical harmonics, $\gamma_s^{mm'}$ is non-zero only if (i) s, the harmonic degree of the structure, is even, (ii) s obeys the triangle inequality $0 \leq s \leq 2l$ and (iii) $t = m - m'$. These "selection rules" limit severely the kind of aspherical structure to which an isolated multiplet is sensitive. An isolated multiplet is sensitive only to structure of even degree and a mode of degree $l = 2$ for example, is only sensitive to aspherical structure of degrees 2 and 4.

To evaluate the matrix exponential in (3.3), we perform an eigenvalue decomposition of the splitting matrix

$$\mathbf{H}_k\mathbf{U}_k = \mathbf{U}_k\mathbf{\Omega} \tag{3.11}$$

In the absence of three dimensional Q structure the splitting matrix is Hermitean, so, the diagonal matrix of eigenvalues $\mathbf{\Omega}$ is real and the matrix $\mathbf{U}$ is unitary ($\mathbf{U}^{-1} = \mathbf{U}^H$) where the superscript H indicates Hermitean transpose. With this decomposition we can rewrite (3.3)

$$s(\mathbf{r},t) = \mathrm{Re}\left[\sum_k \boldsymbol{\sigma}_k^T(\mathbf{r})\mathbf{U}_k^H e^{i\mathbf{\Omega}^k t}\mathbf{U}_k\mathbf{a}_k(\mathbf{r}_0)e^{i\omega_k t}\right] \tag{3.12}$$

Now consider the case when the splitting matrix $\mathbf{H}$ is diagonal. This can only be the case if all singlets within a multiplet are only sensitive to axisymmetric structure ($t = 0$). Under these circumstances, the matrix $\mathbf{U}$ is the identity matrix and $\mathbf{H} = \mathbf{\Omega}$ so that

$$\mathbf{s}(\mathbf{r},t) = \mathrm{Re}\left[\sum_k \boldsymbol{\sigma}_k^T(\mathbf{r})e^{i\mathbf{\Omega}^k t}\mathbf{a}_k(\mathbf{r}_0)e^{i\omega_k t}\right] \tag{3.13}$$

with

$$\Omega_{mm} = \omega_k(a + mb + m^2c) + \sum_s \gamma_s^{mm}\,{}_kc_s^0 \tag{3.14}$$

Thus, if aspherical structure is dominantly axisymmetric, we know that the geographic shapes of the singlets are given by (3.1) and we can combine recordings to emphasize a particular singlet. This

procedure is called "singlet stripping". Fourier transforming (3.13) we get

$$s_p(\omega) = \sum_k \sum_{m=-l}^{l} A_{kmp} c_{km}(\omega) \tag{3.15}$$

where $s_p(\omega)$ is the pth observed spectrum and $c_{km}(\omega)$ is the resonance function of the mth singlet in the kth multiplet. The matrix A_{kmp} is given by $A_{kmp} = \boldsymbol{\sigma}_{km}^T(\mathbf{r})\mathbf{a}_{km}(\mathbf{r}_0)$. (3.15) states that the pth observed spectrum is a weighted sum of singlet resonance function $c_{km}(\omega)$ with the weights being given by A_{kmp}.

Singlet stripping is performed over narrow frequency bands and we choose a band which covers the width of the target multiplet. Over such narrow frequency bands, A_{kmp} can be considered independent of frequency so that the linear system (3.15) can be solved for each frequency independently. Formally we write the solution to (3.15) as

$$\hat{\mathbf{c}}(\omega) = \mathbf{A}^{-1}\mathbf{s}(\omega) \tag{3.16}$$

where $\mathbf{A}^{-1}$ is the generalized inverse of $\mathbf{A}$ which we obtain using the SVD algorithm. $\mathbf{s}(\omega)$ is a vector of observed complex spectra corrected for instrument response and source phase and $\hat{\mathbf{c}}(\omega)$ are the estimated singlet resonance functions termed "singlet strips".

3.3 Application of Singlet Stripping

3.3.1 The search for candidate multiplets

Having established the mathematical machinery needed for singlet stripping, we need to find suitable target multiplets. The only multiplets which we can hope to analyze at frequencies higher than 5 mHz are PKIKP equivalent modes as they have both a high Q value and are relatively strongly excited by some earthquakes. These modes also tend to have a nearly vertically polarized particle motion in contrast to SKS equivalent modes, so that vertical component seismograms can be used rather than the much noisier horizontal component recordings. To select candidate modes, we have systematically searched our dataset of 3500 long-period recordings of large earthquakes. We compute amplitude spectra of 40h time series and interactively assign the noise level in the frequency band 5-10 mHz. A histogram of all spectral peaks exceeding a signal-to-noise ratio of 2 shows very strong clustering at the frequencies of PKP and PKIKP modes and has allowed us to narrow the class of candidate modes to less than 30 modes (out of a total of 843 spheroidal and toroidal modes between 5 and 10 mHz).

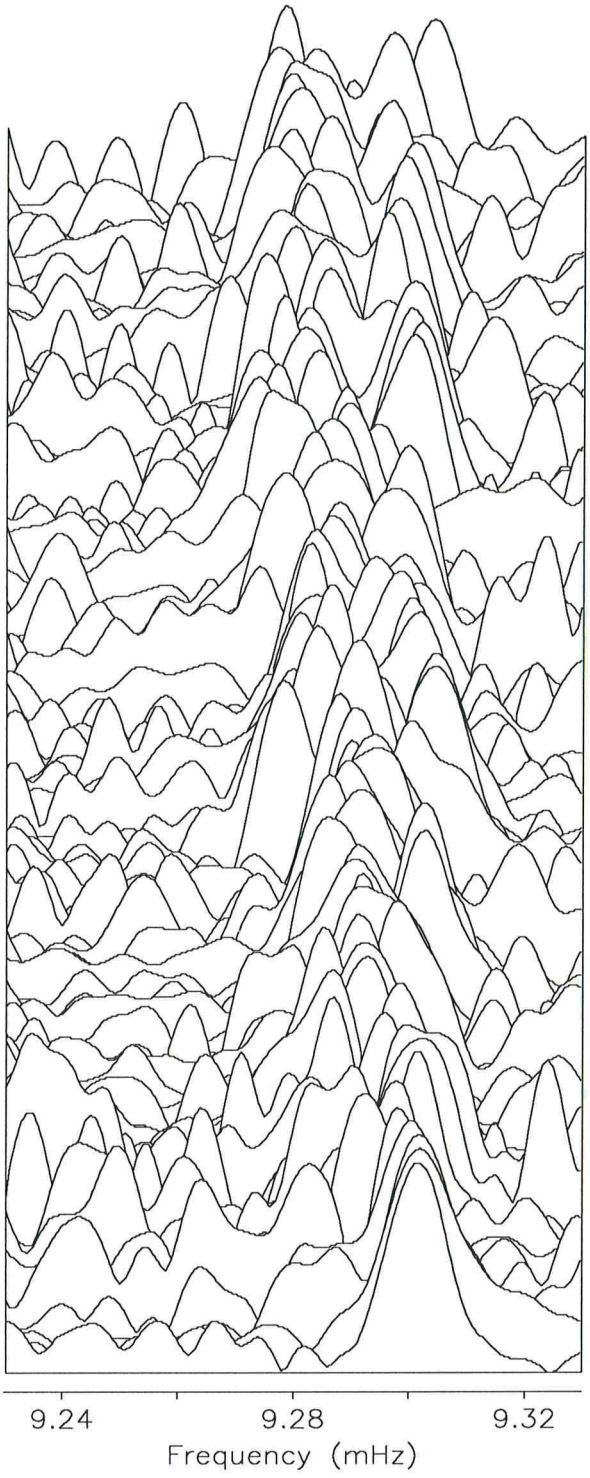

Figure 3.1 Perspective view of 86 vertical component amplitude spectra containing signal for the mode ${}_{23}S_5$. The spectra are sorted according to the latitude of the recording station. Spectra recorded at the South Pole are in front and spectra from equatorial stations are in the back.

Singlet stripping consists of forming a weighted average of observed data spectra with the weights designed to enhance optimally one singlet and suppress all other singlets within a multiplet. The selection of records is critical if such a method is to work. If we require that every record contain a clear peak at the frequency of the target multiplet we end up with too few records. What we need is a criterion which allows us to discriminate between records with a low signal-to-noise ratio and records which are entirely dominated by noise.

From the histogram analysis described above, we find that the most frequently excited PKIKP equivalent multiplet in the frequency band 5-10 mHz is the mode ${}_{18}S_4$. This mode is well isolated from other high Q modes and we have used it to select the records to be used in singlet stripping experiments. From our database of 3500 long-period records we find that only 250 records show a clear peak at the frequency of ${}_{18}S_4$ and we have used this subset of records in all subsequent experiments. The 250 records come typically from events with a source depth greater than 50km though large shallow thrust events are also capable of significantly exciting this mode. From all the earthquakes which have contributed to the 250 records, less than ten are represented with more than five recordings and we will concentrate on these events when using the spectral fitting technique (see below).

3.3.2 Evaluating the results of singlet stripping

The singlet stripping technique is based on the seemingly restrictive assumption that the dominant asphericities sensed by the target multiplet are axisymmetric. While this assumption is certainly valid at frequencies below 1mHz where the splitting of modes is dominated by the effect of rotation, we have to justify its use at higher frequencies. One way to show that our working hypothesis is valid is to inspect vertical component spectra recorded at the South Pole. If a multiplet senses only axisymmetric aspherical structure, the singlet shapes are given by (3.1) and the only non-zero singlet at the pole is the $m = 0$ singlet; hence the spectra should only contain one spectral line. *Ritzwoller et al. (1986)* have shown spectra from both the South Pole and a low latitude station for the multiplets ${}_0S_4$, ${}_1S_4$, ${}_{10}S_2$ and ${}_{11}S_4$ to demonstrate this point. We refer to Figures 3.1 and 5.1 to show that the multiplets ${}_{18}S_4$ and ${}_{23}S_5$ consists only of one spectral line when recorded at a polar station.

A second test of the success of singlet stripping consists in a visual assessment of the resulting strips. If the strips show multiple peaks, the hypothesis has failed or we have insufficient signal in our dataset for the retrieval of a particular singlet.

A further characteristic of anomalously split multiplets is that the singlet distribution obtained

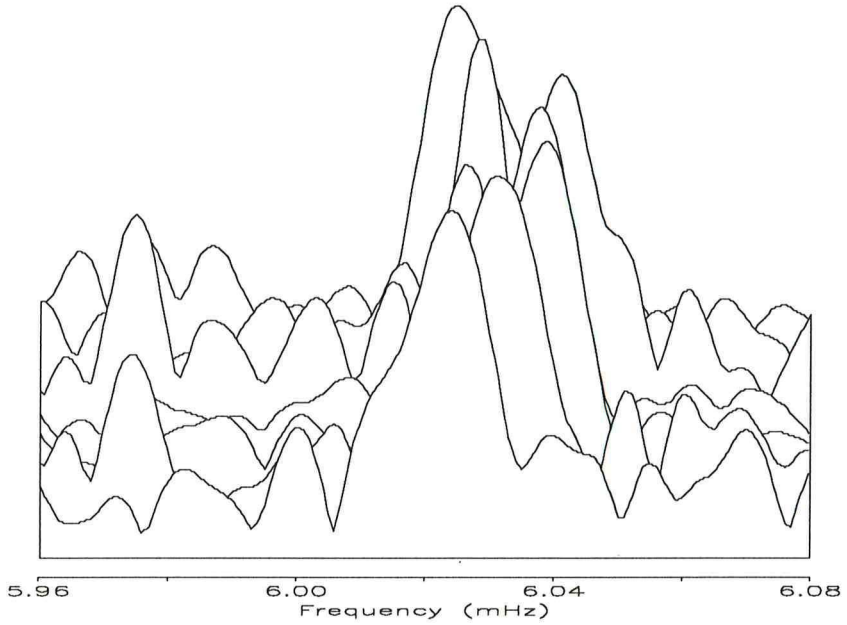

Figure 3.2 Amplitude spectra of singlet strips for the multiplet ${}_{15}S_3$. The strips are arranged in ascending azimuthal order with the one corresponding to the $m = -3$ singlet in front.

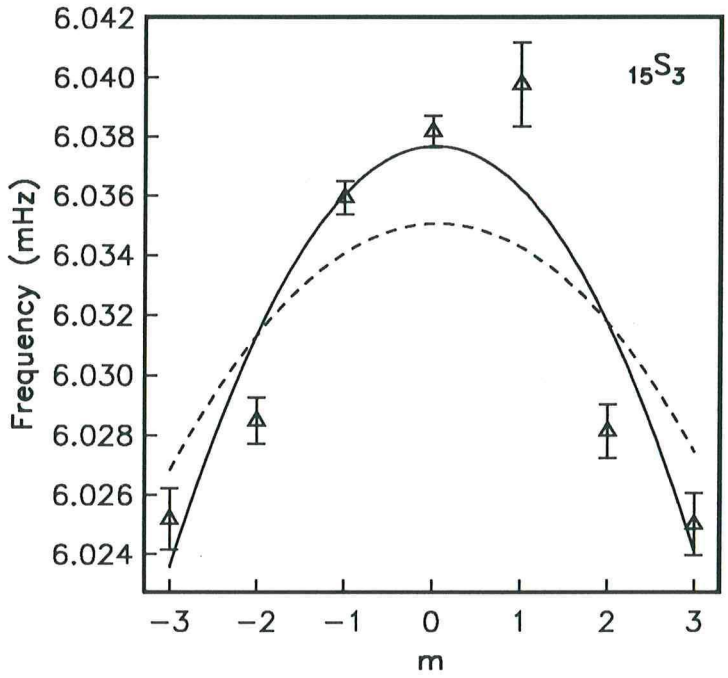

Figure 3.3 Singlet frequency estimates for the multiplet ${}_{15}S_3$ obtained from the strips in Figure 3.2. The solid line is the best fitting quadratic in m and the dashed line follows the singlet frequencies predicted for rotation and ellipticity alone.

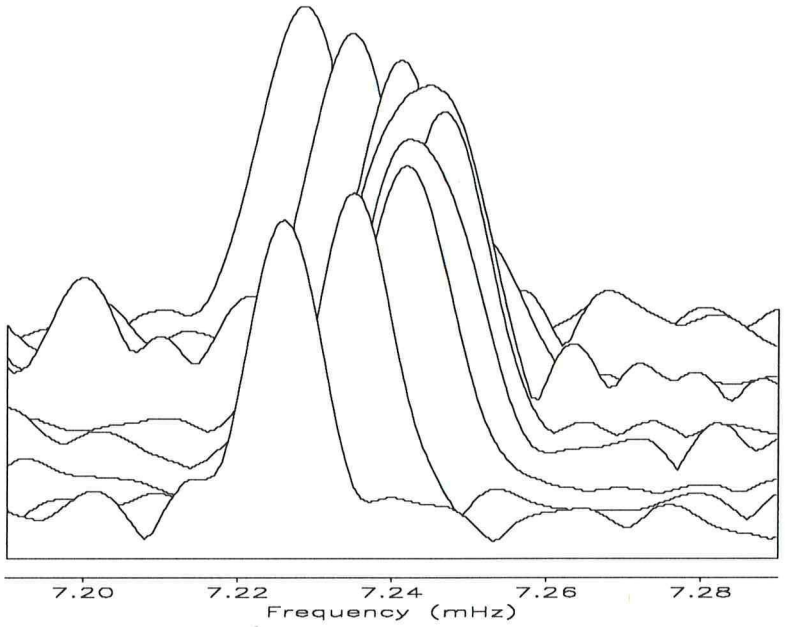

Figure 3.4 Amplitude spectra of singlet strips for the multiplet ${}_{18}S_4$. The strips are arranged in ascending azimuthal order with the one corresponding to the $m = -4$ singlet in front.

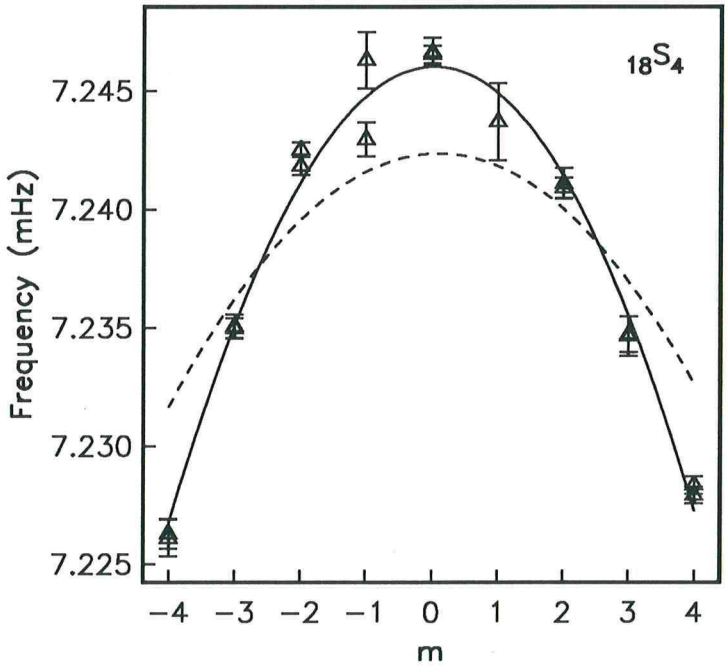

Figure 3.5 Singlet frequency estimates for the multiplet ${}_{18}S_4$ obtained from the strips in Figure 3.4. The solid line is the best fitting quadratic in m and the dashed line follows the singlet frequencies predicted for rotation and ellipticity alone.

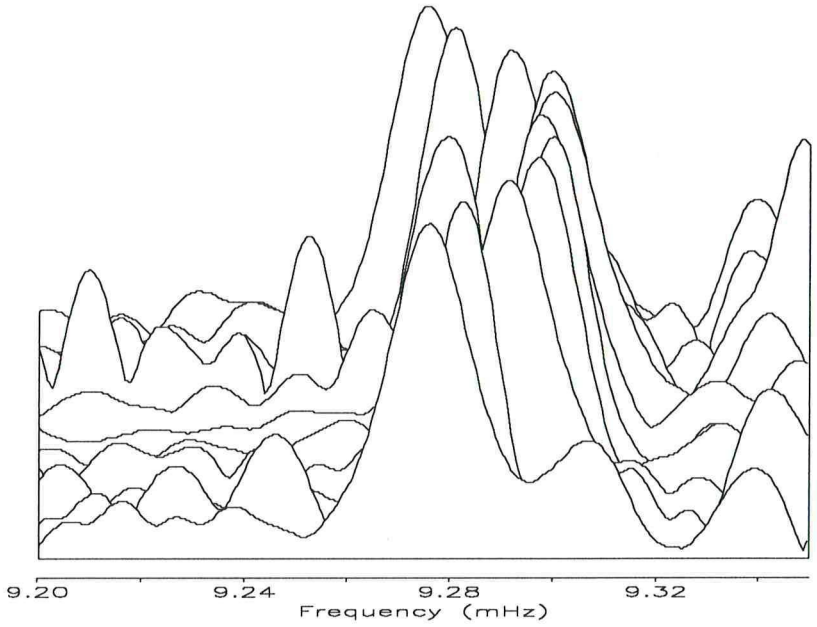

Figure 3.6 Amplitude spectra of singlet strips for the multiplet ${}_{23}S_5$. The strips are arranged in ascending azimuthal order with the one corresponding to the $m = -5$ singlet in front.

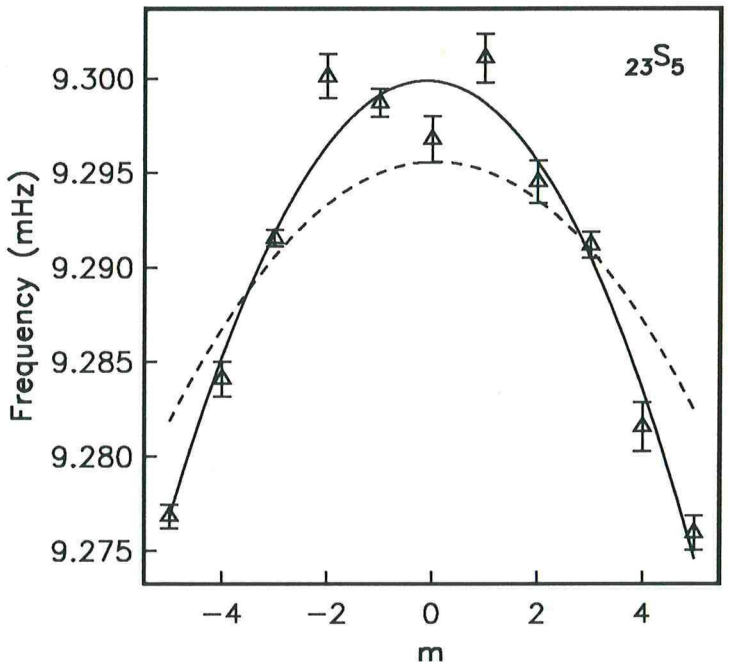

Figure 3.7 Singlet frequency estimates for the multiplet ${}_{23}S_5$ obtained from the strips in Figure 3.6. The solid line is the best fitting quadratic in m and the dashed line follows the singlet frequencies predicted for rotation and ellipticity alone.

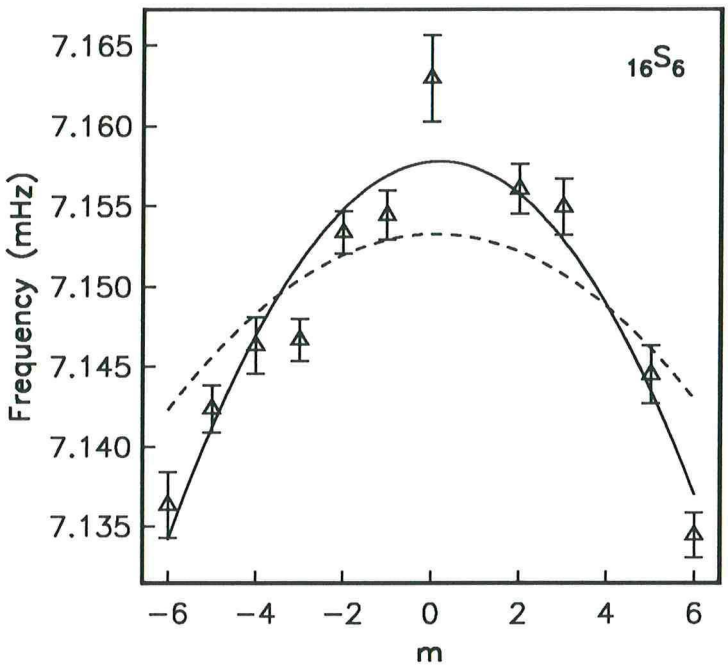

Figure 3.8 Singlet frequency estimates for the multiplet ${}_{16}S_6$. The solid line is the best fitting quadratic in m and the dashed line follows the singlet frequencies predicted for rotation and ellipticity alone.

from singlet stripping is well-approximated by a quadratic in m. Figures 3.2–3.10 demonstrate this feature for the newly analyzed modes ${}_{15}S_3$, ${}_{16}S_6$, ${}_{18}S_4$, ${}_{20}S_5$, ${}_{21}S_6$ and ${}_{23}S_5$. The singlet frequency estimates are obtained by fitting a synthetic resonance function to the singlet strips and the errors are assigned based on an interactively assigned signal-to-noise ratio for every strip (*Dahlen, 1982*). We perform a least-squares fit to find the best fitting parabola and use a bootstrapping procedure (*Effron and Tbshirani, 1986*) to estimate the errors on the parameters of the parabola. The quadratic distribution of the singlets further indicates that the aspherical structure sensed by these modes is dominantly axisymmetric. This can be seen if we evaluate γ_2^{mm} and γ_4^{mm} in (3.14) (*Ritzwoller et al. 1986*)

$$\gamma_2^{mm} = \left(\frac{5}{4\pi}\right)^{1/2} \frac{1}{(2l+3)(2l-1)}\left(l(l+1) - 3m^2\right) \tag{3.17}$$

and

$$\gamma_4^{mm} = \left(\frac{81}{64\pi}\right)^{1/2} \frac{\left(3l(l+1)(l+2)(l-1) + m^2(25 - 30l(l+1)) + 35m^4\right)}{(2l+5)(2l+3)(2l-1)(2l-3)}. \tag{3.18}$$

(3.17) is a quadratic in m, which implies that if the perturbing axisymmetric structure is of degree 2, the singlet frequencies follow a quadratic in m: $\omega_m = \omega_k(1 + a + mb + m^2c)$ with a and c perturbed away from the ellipticity splitting parameters in (3.4). Note also that neither degree 2 nor 4 axisymmetric

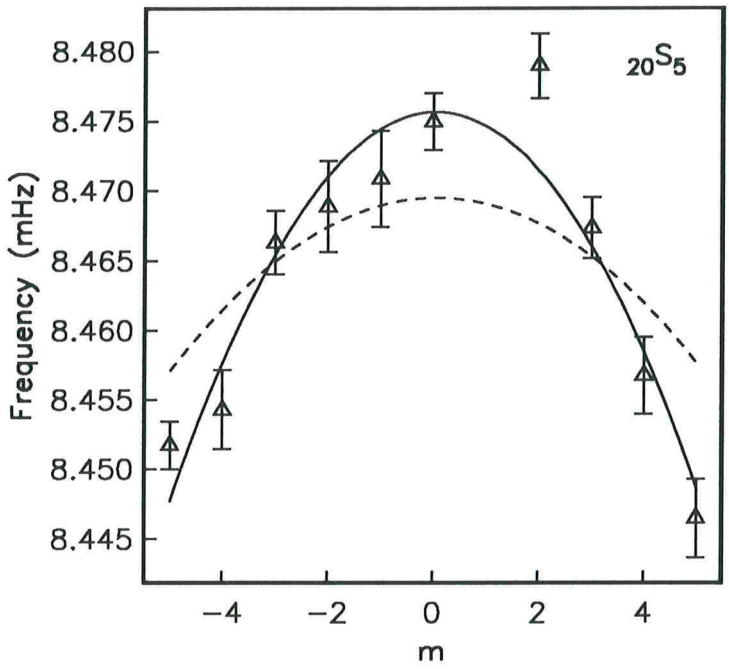

Figure 3.9 Singlet frequency estimates for the multiplet $_{20}S_5$. The solid line is the best fitting quadratic in m and the dashed line follows the singlet frequencies predicted for rotation and ellipticity alone.

structure should affect the infered value of the rotational splitting parameter b, an observation which can also be used to test the validity of our working hypothesis. A last observation about Figures 3.1 and 5.1 is that the spectral peak of the South Pole record in the front row lie at one extreme end of the multiplet. Since the m^2 and the m^4 term in (3.18) have opposite signs, the $m = 0$ singlet would not lie at one extreme end of the multiplet if the dominant axisymmetric structure were of degree 4. This observation encourages us to fit only a quadratic in m to the singlet frequencies and estimate c_2^0 by use of (3.17) and (3.14). Such a procedure is consistent with many other studies of aspherical structure inside the Earth which find that degree 2 structure is much larger in amplitude than degree 4 or higher order structure.

A frequently occurring situation is that we have ample signal to retrieve the large $|m|$ singlets but that low $|m|$ singlets, particularly the $m = 0$ singlet, are poorly resolved. In the asymptotic limit of large l, low $|m|$ singlets are excited on spectra corresponding to near-polar great circle paths whereas high $|m|$ singlets are preferentially excited on near-equatorial paths. Our data set of 250 records contains only a small number of polar or near-polar great circles which explains our difficulties with the retrieval of low $|m|$ singlets.

The situation is particularly vexing in the case of the $l = 1$ modes. While we have on the order of 40 spectra in which we can identify a spectral peak at the frequency of the PKIKP equivalent modes

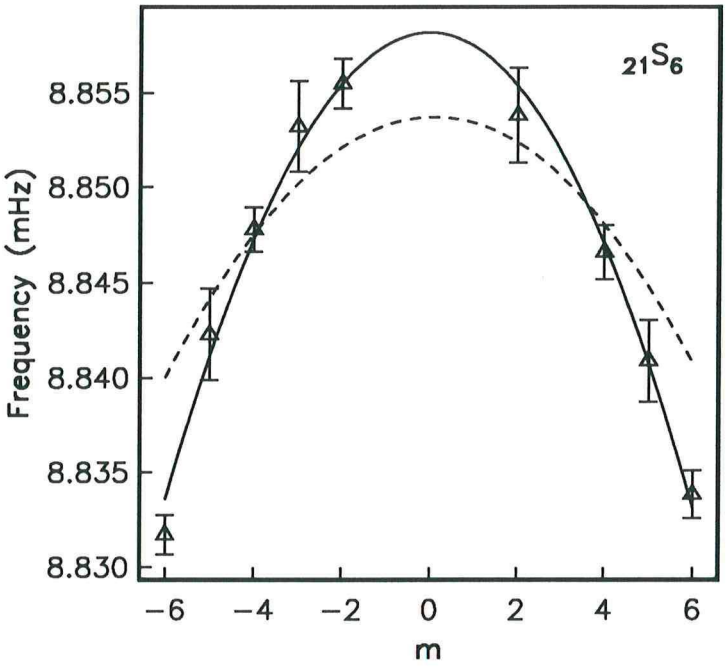

Figure 3.10 Singlet frequency estimates for the multiplet $_{21}S_6$. The solid line is the best fitting quadratic in m and the dashed line follows the singlet frequencies predicted for rotation and ellipticity alone.

$_{20}S_1$, $_{22}S_1$, $_{25}S_1$ and $_{27}S_1$, we have no record from the South Pole or the IDA station at Alert (82.5°N) which contain a spectral peak at the frequency of these modes with a signal-to-noise ratio greater than 3. It is therefore not surprising that singlet stripping fails to produce a clear peak for the $m = 0$ singlet for these modes. This is unfortunate since it makes it impossible to use the diagonal sum rule to get a precise estimate of the degenerate frequency or fit a quadratic to the singlet frequencies and estimate the c_2^0 structure coefficient (note that $l = 1$ modes are sensitive only to degree $s = 2$ aspherical structure). The singlet strips of these modes could however be used to measure Q (chapter 5). Q values measured from singlet strips of observably split multiplets exhibit far less scatter than measurements made by fitting synthetic resonance functions to individual data spectra.

Let us now review the singlet stripping results in detail. All anomalously split multiplets share two robust features: a parabolic distribution of the singlet resonance functions and a well determined overall splitting width. We take the parabolic distribution of the singlets as an indication that the multiplets are not significantly coupled to any nearby modes and that the structure is dominantly of degree 2.

Observations of anomalous splitting have been presented by *Masters and Gilbert, (1981)* and subsequently by *Ritzwoller et al. (1986, 1988)*; *Giardini et al. (1987, 1988)* and *Li et al. (1991a)*. While the splitting width is nonlinearly related to aspherical structure, it is still a useful quantity to observe since

mode	R	E_{IC} (%)	E_{OC} (%)
${}_2S_3$	1.7	1.3	17.8
${}_3S_2$	1.8	10.0	22.2
${}_6S_3$	2.5	1.9	48.4
${}_8S_5$	2.0	1.8	38.9
${}_9S_3$	2.1	2.7	43.2
${}_{11}S_4$	2.3	1.5	47.7
${}_{11}S_5$	1.8	0.9	45.5
${}_{13}S_2$	2.3	10.0	43.6
${}_{13}S_3$	2.2	4.7	47.6
${}_{14}S_4$	2.5	6.5	45.7
${}_{15}S_3$	1.7	9.0	47.7
${}_{16}S_6$	2.2	1.5	46.1
${}_{16}S_7$	1.7	1.8	43.8
${}_{18}S_3$	2.1	12.0	42.1
${}_{18}S_4$	1.8	6.3	45.6
${}_{20}S_5$	2.3	5.3	48.0
${}_{21}S_6$	1.8	2.8	45.6
${}_{23}S_5$	1.8	8.4	45.2
${}_{25}S_2$	1.7	15.8	40.7
${}_{27}S_2$	1.7	14.5	42.1

Table 3.1 Splitting width and energy partitioning of observably split high-Q low-l modes. R is the ratio of observed to predicted splitting width with the predicted splitting width referring to a rotating model in hydrostatic equilibrium. The columns labeled E_{IC} and E_{OC} contain the percentage elastic energy these modes have in the inner and outer core respectively. The observations for the modes ${}_{15}S_3$ through ${}_{27}S_2$ are new to this study.

it is the most robustly determined characteristic of a split multiplet. Until recently, only 10 anomalously split multiplets had been fully resolved and they are listed at the beginning of Table 3.1. The lower half of the table consists of the newly observed anomalously split multiplets. The second column shows the ratio of observed to predicted splitting width where the latter refers to a rotating model in hydrostatic equilibrium. The third and fourth columns show the percentage of elastic energy which these modes have in the inner and outer core respectively. Anomalously split modes have typically 45% of their elastic energy in the outer core. The amount of elastic energy in the inner core varies from less than 1% to 16% and there are altogether seven anomalously split modes with less than 2% energy in the inner core. Also note that there does not seem to be any correlation between R and the percentage of elastic energy in the inner core.

The observed splitting width in table 3.1 can be compared against the predicted values for existing models of aspherical core structure. One recent model, which was designed to fit the spectra of anomalously split multiplets is SAT (*Li et al. 1991a*). SAT allows for general aspherical structure

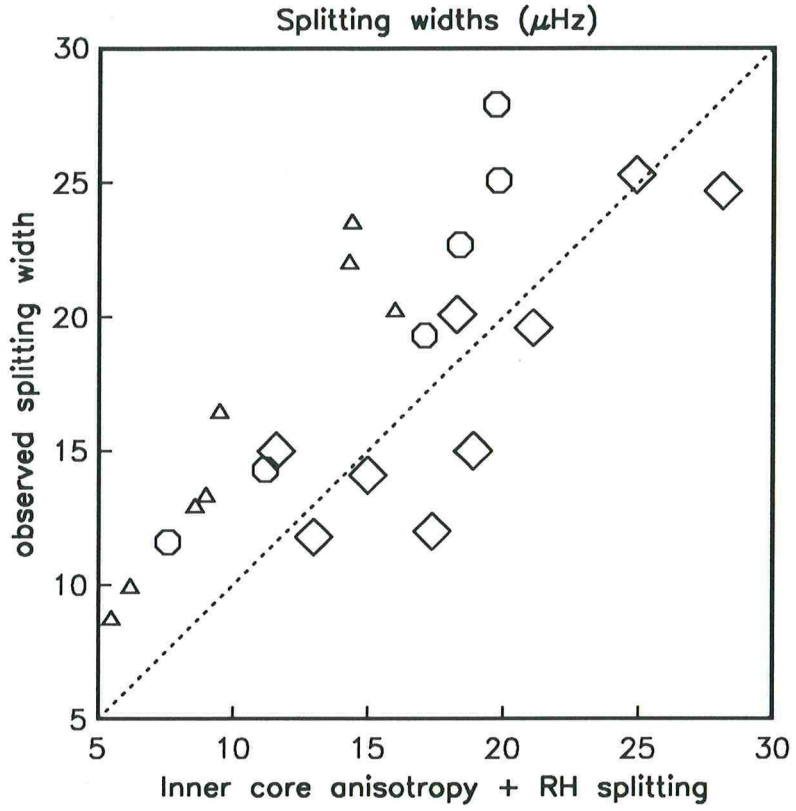

Figure 3.11 Comparison of the total observed splitting width of core-sensitive multiplets with the splitting width predicted for a rotating model in hydrostatic equilibrium and the axisymmetric inner core anisotropy of model SAT (*Li et al. 1991a*). Triangles, octagons and diamonds correspond to modes with less than 2%, 2-7% and more than 7% elastic energy in the inner core, respectively.

of degree 2 and 4 in the mantle and, in the inner core, the parameterization allows for axisymmetric anisotropy of degree 2 and 4. The inner core part of model SAT is also consistent with the observations of PKIKP(AB) - PKIKP(DF) differential travel times which have suggested cylindrical anisotropy in the inner core (*Morelli et al. 1987*; *Shearer et al. 1988*). In Figure 3.11 we have plotted the observed splitting width against the predictions for a rotating Earth model in hydrostatic equilibrium (hereafter called "RH model") with the effect of the inner core part of model SAT included. This figure shows that the splitting width is systematically underpredicted for modes with little energy in the inner core and overpredicted for many modes with more than 7% elastic energy in the inner core. Clearly it will be difficult (if not impossible) to find a model which satisfies all the observations and we may conclude that our observations do not support the proposal that structure in the inner core is the likely cause of the anomalous splitting. In Figure 3.12, we have plotted the observed c_2^0 against the predictions for an RH model with the effect of the inner core part of model SAT included. The situation for c_2^0 is very similar

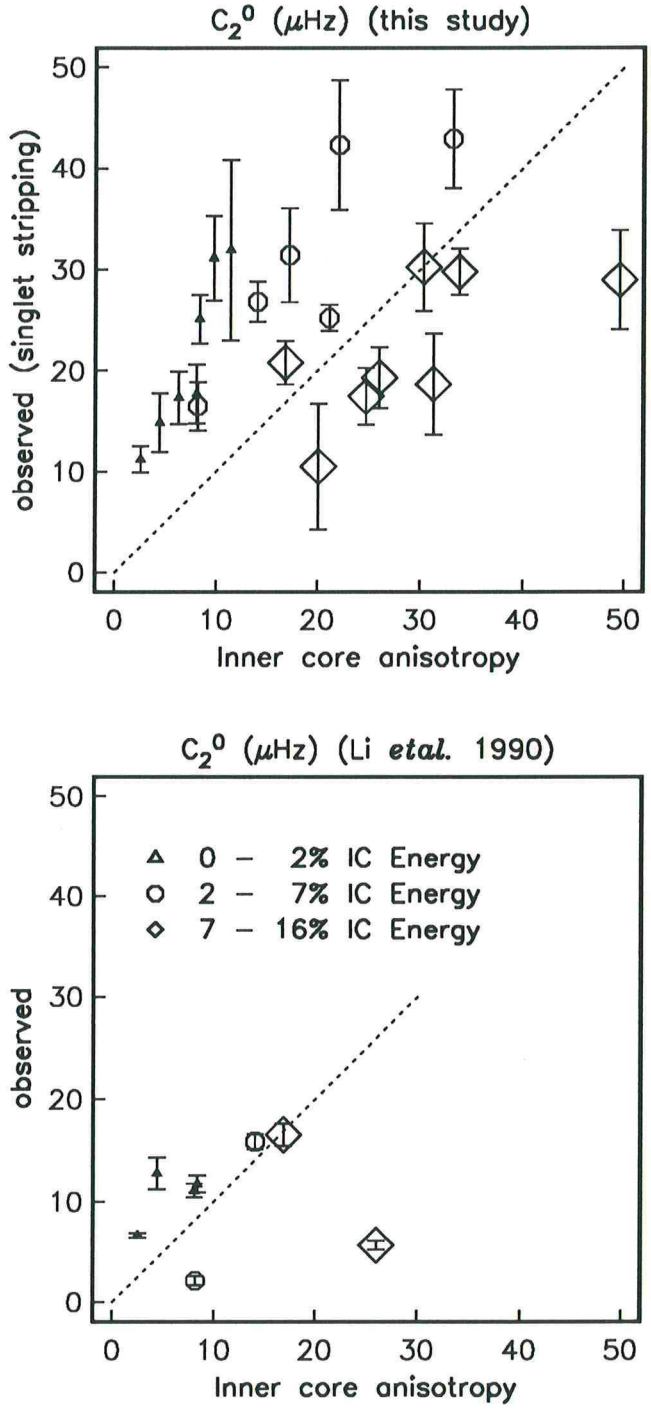

Figure 3.12 Comparison of observed c_2^0 structure coefficients with the predictions for a rotating model in hydrostatic equilibrium with the effect of inner core anisotropy of model SAT included (*Li et al. 1991a*). The top panel shows the data from this study and the bottom panel shows the c_2^0 coefficients observed by *Li et al. (1991a)*. Both panels show the same trend: c_2^0 for modes with little energy in the inner core are under predicted whereas the c_2^0 for modes with more than 7% elastic energy in the inner core are overpredicted.

as for the total splitting width. Increasing the amount of structure in the inner core would result in a model that would over predict c_2^0 even more for the modes with large amounts of energy in the inner core while modes which have little energy in the inner core would still be underpredicted.

3.4 Application of Spectral Fitting

In spectral fitting, we use a linearization of (3.3) to vary the structure coefficients inherent in the splitting matrix so as to minimize the misfit between observed and predicted data. Let s_{obs} be a particular component of the observed displacement field of a receiver at location $\mathbf{r}$ and let s_0 be the predicted displacement for a known model of aspherical structure. We can then write

$$s_{obs}(\mathbf{r},t) \simeq s_0(\mathbf{r},t) + \left(\frac{\partial s_0(\mathbf{r},t)}{\partial \omega_k}\right)\delta\omega_k + \sum_{s,t}\left(\frac{\partial s_0(\mathbf{r},t)}{\partial c_s^t}\right)\delta c_s^t \tag{3.19}$$

We follow *Ritzwoller et al. (1986)* and use a recursion in the time domain to compute the partial derivative seismograms in (3.19). This equation also includes a term for the degenerate frequency which may not be known 'a priori'. The derivative seismograms are then convolved with the instrument response, gaps are inserted to duplicate the panel structure of the original data, and then both data and derivative seismograms are tapered and Fourier transformed: Equation (3.19) can then be written as

$$\Delta s_p = A_{pj}\delta c_j \tag{3.20}$$

where Δs_p is a vector of residual spectra covering a narrow frequency band surrounding the target multiplet: $\Delta s_p = s_{obs} - s_0$. The columns of matrix A_{pj} are spectra of the partial derivative seismograms and δc_j is a vector of unknown structure coefficient perturbations. Only a narrow frequency band around the target multiplet is included in (3.20) which we solve using an SVD. Since the records come from both the IDA and GDSN network, and also from different size earthquakes, we weight the individual spectra by their average amplitude in the frequency band of interest. In addition, we interactively assign a signal-to-noise level to the individual spectra and use it as a weight to reward high signal records in the inversion.

Since we are trying to fit spectra of individual records, we only include records which show a clear peak in the frequency band of the target multiplet (Figure 3.13). As we are trying to model both amplitude and phase of the observed spectra, we need a good model of the source and we therefore choose only records from events where the source mechanism is well-constrained. Our source mechanisms are

Event	Location	year	day	time	Colat.	E-Long.	depth
					(°)	(°)	(km)
1	New Ireland Region	1983	77	9:05:50.0	94.88	153.58	70
2	Banda Sea	1983	328	5:30:34.2	97.48	128.16	179
3	New Britain	1984	151	7:49:43.7	94.83	151.57	174
4	Mindanao	1984	325	8:15:16.2	84.84	125.12	202
5	Hindu Kush	1985	210	7:54:44.1	53.81	70.89	99

Table 3.2 List of Events used in the Spectral Fitting Experiment. Source locations and event times are taken from the PDE listings.

Event	m_0	m_{rr}	$m_{\theta\theta}$	$m_{\phi\phi}$	$m_{r\theta}$	$m_{r\phi}$	$m_{\theta\phi}$	τ
								(s)
1	7.84	6.71	−2.32	−4.39	−3.26	0.33	3.99	30.
2	1.83	1.29	−1.79	0.50	−0.36	0.81	−0.09	0.
3	0.59	0.36	−0.11	−0.25	0.07	0.30	−0.19	0.
4	1.74	−0.91	0.46	0.46	0.67	−1.31	−0.53	6.
5	1.87	1.76	−1.66	−0.10	−0.19	0.41	−0.62	35.

Table 3.3 Source mechanisms of the events in table 3.2. The moment tensors have been determined using the procedure described in chapter 2 and 4. Listed are the scalar moment m_0, the six independent moment tensor elements and the rise time. The units of the moment tensor elements are 10^{20}Nm.

based on a least squares fit of spectra of the first ten hours of data and are thus dominated by the fit of surface wave equivalent fundamental modes (chapter 2). Moment tensors obtained in this way may not be good enough representations of the excitation of relatively high-frequency PKIKP equivalent modes and we therefore introduce a complex scaling factor for every event to allow for an adjustment in the size of the source and the rise time. The events used in the spectral fitting experiments together with the corresponding source mechanisms are given in Tables 3.2 and 3.3. There are fewer events in this table than were used in similar experiments by either *Ritzwoller et al. (1986, 1988)*, *Giardini et al. (1987, 1988)* or *Li et al. (1991)*. We have experimented with larger data sets and included several of the events that had been used in similar studies at frequencies below 5 mHz but found that the algorithm (3.19) diverged. Either the added events contain too little signal for our target modes or our model of the source was not good enough at the relatively high frequencies used in this experiment.

In the cases where the algorithm converges, we estimate the errors by repeating the inversion with varying numbers of unknown parameters (including c_s^t's up to the maximum of $s = 2l$) and comparing the structure coefficients for the different inversions. We also find that the final structure coefficients are independent of the starting point of the inversion, indicating that the algorithm has a

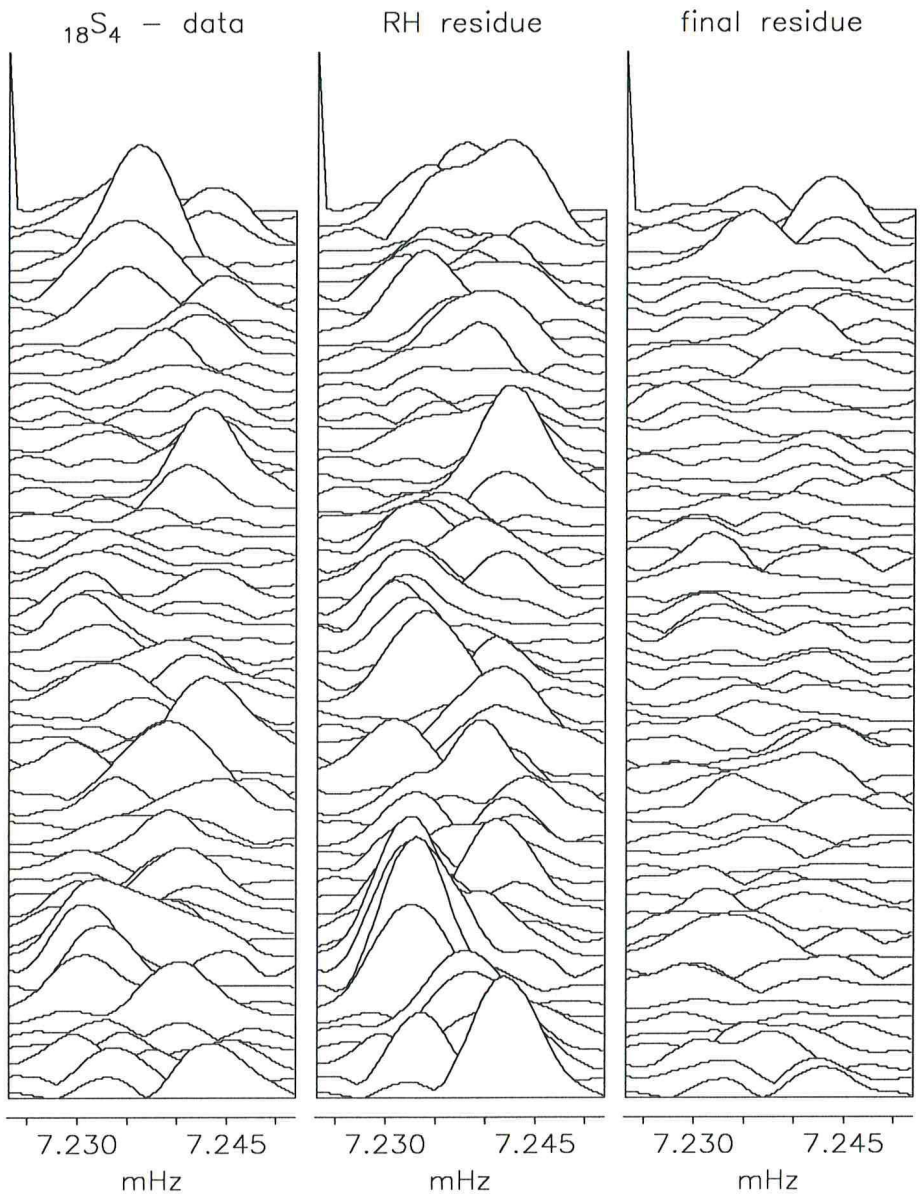

Figure 3.13 Spectral fitting applied to 60 spectra of the mode $_{18}S_4$. The left panel shows the raw data spectra. They are scaled by the averaged power in the displayed frequency band and multiplied by an interactively assigned signal-to-noise ratio (SNR). The middle panel shows the residues if aspherical structure is only modeled by rotation and hydrostatic ellipticity. The left panel shows the residue after the degree 2 structure coefficients have been estimated. All the spectra are plotted with the same vertical scale (the spike in the back row has been introduced to suppress self-scaling by the plotting software). The average SNR of the data spectra is 4.5. For the middle panel the variance reduction is -23% and for the right panel 65%. If we solve simultaneously for structure of degree 2 and 4 the veriance reduction increases to 68%.

large radius of convergence. The only modes for which the spectral fitting procedure has allowed us to estimate the degree 2 structure coefficients are ${}_{15}S_3$, ${}_{18}S_4$, ${}_{23}S_5$ and the estimated coefficients are given in table 3.7.

3.5 Inversion of structure coefficients

The structure coefficient c_s^t of the kth multiplet is linearly related to aspherical structure $\rho_s^t(r)$, $\kappa_s^t(r)$, $\mu_s^t(r)$ and the boundary perturbation h_{si}^t of the same degree s and order t:

$$ {}_kc_s^t = \int_0^a ({}_kR_s(r)\delta\rho_s^t(r) + {}_kK_s(r)\delta\kappa_s^t(r) + {}_kM_s(r)\delta\mu_s^t(r))r^2dr - \sum_i r_i^2 h_{si}^t \, {}_kB_{si} \qquad (3.21) $$

The number and precision of the data at our disposal are insufficient to constrain $\delta\mu_s^t$, $\delta\kappa_s^t$ and $\delta\rho_s^t$ independently so we do not solve (3.21) directly but use additional constraints to reduce the degrees of freedom in the inversion. For example, variations in temperature inside the Earth will change ρ, κ and μ in the same sense and we shall assume that it is possible to assign scale factors between these properties in the mantle. If we assume that the outer core is in hydrostatic equilibrium the only permissible density perturbations in that region are induced by gravitational forcing of structures in the inner core and the mantle and so the density perturbations in the outer core can be removed from the inversion. The next four sections describe in detail the additional constraints that we have chosen to apply.

3.5.1 Scalings between perturbations in density, shear- and bulk modulus

If variations in structure are thermal in origin, it may be that variations in density and elastic moduli can be related to one another by a simple scaling factor. We can appeal to laboratory data on the effects of temperature on the elastic moduli of many materials, as summarized by *Anderson (1987a, 1987b)*. We characterize the scalings by using logarithmic ratios which show little change between materials. Thus

$$ \left(\frac{\partial \ln \mu}{\partial \ln \rho}\right)_p \simeq 6 \qquad (3.22) $$

and, since $\mu = \rho v_s^2$

$$ \left(\frac{\partial \ln v_s}{\partial \ln \rho}\right)_p \simeq 2.5 \qquad (3.23) $$

The temperature dependence of κ is specified by the Anderson–Grüneisen parameter, δ_s, which is

$$\delta_s = \left(\frac{\partial \ln \kappa}{\partial \ln \rho}\right)_p \equiv \left(\frac{\partial \kappa}{\partial p}\right)_s - \left(\frac{\partial \kappa}{\partial p}\right)_\rho \tag{3.24}$$

Experimentally, $\left(\partial\kappa/\partial p\right)_\rho$ is usually slightly positive so $\delta_s \sim\leq \left(\partial\kappa/\partial p\right)_s$. Note that $\left(\partial\kappa/\partial p\right)_s$ is known from the spherically averaged Earth structure so δ_s can be estimated if the experimental data are pertinent to the Earth's interior. The results suggest that

$$\delta_s \simeq 3 \tag{3.25}$$

so, since $\kappa = \rho(v_p^2 - \frac{4}{3}v_s^2)$,

$$\left(\frac{\partial \ln v_p}{\partial \ln \rho}\right)_p \simeq 1.6 \tag{3.26}$$

which is very similar to the value suggested by *Hager et al. (1985)* found by fitting the observed geoid to that derived from a lower mantle P-wave velocity model. Equations (3.23) and (3.26) give:

$$\xi = \left(\frac{\partial \ln v_s}{\partial \ln v_p}\right) \simeq 1.6 \tag{3.27}$$

though a direct assessment of the laboratory data indicates a slightly smaller value ($\xi = 1.3$). This ratio has been the subject of some controversy (*Anderson, 1987*; *Li et al. 1991b*) and, based on the results of seismic inversions, it has been suggested that a much higher value is appropriate for the lower mantle. For example, *Li et al. (1991b)* find that an inversion of the mode data requires that ξ be in the range $1.7 \rightarrow 2.6$ with 75% confidence. A direct assessment of the ratio can be made comparing PcP-P and ScS-S traveltime residuals for the same source-receiver pairs (*Jordan and Lynn, 1974*; *Pulver and Masters, 1990*). This kind of analysis indicates that ξ is about 1.8 which is consistent with the lower end of the range given by *Li et al. (1991b)* and is reasonably close to the experimental values.

We would also like to have an idea of what a reasonable scaling between perturbations in κ and ρ is for the outer core. Experimental data for liquid iron at room pressure are summarized in *Gubbins and Masters (1979)* and give a value of δ_s of about 2.4. Other evidence comes from shock wave studies which can be used to constrain the volume dependence of Grüneisen's ratio (*e.g., Jeanloz, 1979*; *Brown and McQueen, 1986*). Under isentropic compression

$$\left(\frac{\partial \ln \gamma}{\partial \ln \rho}\right)_s = -\left(1 + \gamma - \left(\frac{\partial K_s}{\partial p}\right)_s + \delta_s\right) = -n \tag{3.28}$$

where n would be the exponent in a power-law relation for γ. For the results of *Jeanloz (1979)*, we estimate that δ_s is again about 2.5 although this result must be regarded as being very uncertain.

Estimating scalings for the inner core proves to be even more of a problem since several lines of evidence suggest that the upper part of the inner core has anomalous properties. In particular, the relative attenuation of PKP(BC) and PKP(DF) indicates a highly attenuating upper inner core (*Dornboos, 1983)* which may be indicative of a partially molten state. We might then expect that v_s would be much more variable than v_p in this region.

In the mantle and inner core we adopt the values of

$$\frac{\partial \ln \mu}{\partial \ln \rho} = 6.0 \qquad \text{and} \qquad \frac{\partial \ln \kappa}{\partial \ln \rho} = 3.0 \tag{3.29}$$

and in the outer core

$$\frac{\partial \ln \kappa}{\partial \ln \rho} = 2.5 \tag{3.30}$$

3.5.2 Boundary response kernels

Most kinds of seismic data are sensitive to both volume and boundary perturbations. It turns out that, in a convecting Earth, boundary perturbations and volume perturbations may be related to one another. Suppose we are given a density perturbation $\delta\rho(r, \theta, \phi)$. This density perturbation acts as a forcing term in the equation of conservation of linear momentum and allows us to calculate the convective velocity (if a viscosity structure is given). For mantle convection a good approximation to the conservation equation for linear momentum is

$$\nabla \cdot \boldsymbol{\sigma} - \nabla p + \rho \mathbf{g} = 0 \tag{3.31}$$

where $\boldsymbol{\sigma}$ is the stress tensor and is related to the strain rate by

$$\boldsymbol{\sigma} = 2\eta \partial_t \boldsymbol{\epsilon} \tag{3.32}$$

where η is the viscosity. The equation is solved subject to certain boundary conditions on the velocity field and the traction. For example, it is reasonable to suppose that the traction vector at the surface and the CMB must vanish since the viscosities of the atmosphere and the core are much lower than the viscosity of the mantle. This boundary condition is satisfied on the actual boundary which has been deformed by the convection. Linearization of the boundary conditions (*Richards and Hager, 1984*; *Daly*

and Parsons, 1983) then allows the associated perturbations of the boundaries to be determined. If the viscosity structure can be assumed to be spherically symmetric, a density perturbation of harmonic degree s and order t leads to a boundary perturbation of the same harmonic degree and order. Thus it makes sense to think of the response of the convective system in terms of a kernel which maps $\delta\rho_s^t$ into h_s^t. Once $\delta\rho_s^t$ and h_s^t are known, it is possible to compute the perturbation in gravitational potential at the surface and hence the geoid.

The one-to-one correspondence between harmonic degrees of the forcing density field and the resulting boundary and geoid perturbations breaks down if the viscosity structure is not spherically symmetric. This problem has been investigated by *Richards and Hager (1989)* who conclude that the assumption of spherical symmetry is adequate for the interpretation of the longest harmonics of the geoid (degrees 2 and 3). Here we are mainly concerned with harmonic degree 2 structure so use of the theory may be justified.

With this as introduction, we write the topography kernels

$$h_{si}^t = \int_{r_c}^{r_a} A_{si}(r)\delta\rho_s^t dr \tag{3.33}$$

and

$$\delta N_s^t = \int_{r_c}^{r_a} G_s(r)\delta\rho_s^t dr \tag{3.34}$$

where A_{si} is the topography kernel associated with the ith boundary and G_s is the geoid kernel. The limits of the integrals are the radius of the CMB (r_c) and the radius of the free surface (r_a). These kernels can be computed for a variety of viscosity structures (*Richards and Hager, 1984*; *Hager and Clayton, 1989*). We have used the kernels of several different viscosity models in our modelling experiments to relate the coefficients describing the perturbation of the CMB to volumetric heterogeneity in the mantle (Figure 3.14, *Scott King, 1991 personal communication*).

Given a viscosity model, these kernels allow us to link the aspherical density perturbation with the dynamically maintained topography of boundaries, but this is useful only if the true topography of the interface is dynamically maintained. This is obviously not true at the surface due to the presence of buoyant continental material and other effects. It may be a better approximation at the CMB provided continental-style features do not exist there.

A separate observational constraint on the size of the h_2^0 component of the CMB topography comes from VLBI (*Gwinn et al. 1986*). Observations of the variation of the amplitude of the terrestrial nutations allows to place bounds on the coupling strength between nutations of the mantle and core. The

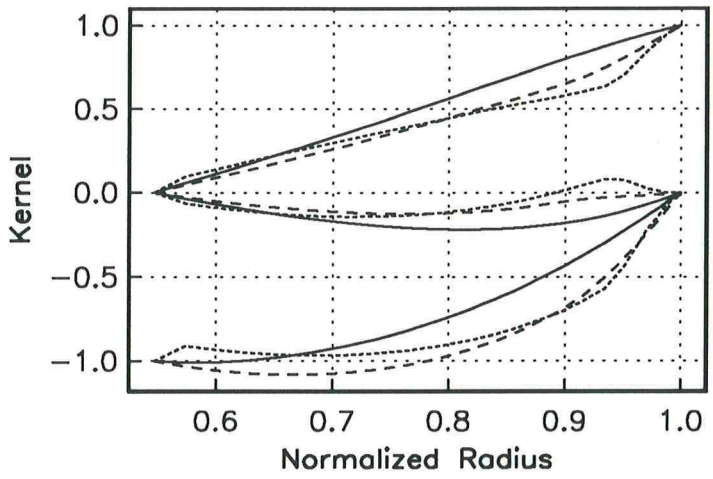

Figure 3.14 Degree 2 boundary and geoid kernels for three different viscosity models. The top three curves increasing from 0 to 1 are the kernels for the free surface, the middle curves are the geoid kernels and the bottom three curves are the CMB kernels. The solid line is for the constant viscosity model, the long dashed lines are for a simple 2-layer viscosity model designed to fit the observed geoid over subducting slabs and the dotted lines are for Hager's preferred 5 layer model (see Table 9.1 in *Hager and Clayton, 1989).* The radial density model is taken from model 1066A. Note that the topography kernel for the free surface has been scaled to be 1 at the free surface and the CMB kernel has been scaled to -1 at the CMB.

coupling strength is related to the amount of topography on the CMB and the peak-to-trough amplitude of the axisymmetric degree 2 structure of the CMB has been estimated as 490 ± 110 m.

3.5.3 Constraining the outer core to be in hydrostatic equilibrium

Several lines of evidence suggest that the outer core has a very low viscosity and departures from hydrostatic equilibrium will therefore be tiny (*Stevenson, 1987*). In our modeling we therefore require that the only density perturbations in the outer core are caused by gravitational forcing from the mantle, from the inner core or from topography on first order discontinuities such as the ICB, CMB, Moho or free surface.

To compute the lateral density variations in the hydrostatic outer core, we use the solution to Poisson's equation (*Dahlen, 1974* Equation 11) and follow very closely the derivation of *Wahr and de Vries (1989).* Let

$$\phi(r,\theta,\varphi) = \sum_{s=0}^{\infty} \sum_{t=-s}^{s} \phi_s^t(r) Y_s^t(\theta,\varphi) \tag{3.35}$$

be the total perturbed potential in the fluid. In a hydrostatic region

$$\delta\rho_s^t \simeq \frac{\partial_r \rho}{g}\phi_s^t \tag{3.36}$$

so Poisson's equation in the outer core reads

$$\partial_r^2\phi_s^t + \frac{2}{r}\partial_r\phi_s^t - \left[\frac{s(s+1)}{r^2} + \frac{4\pi G}{g}\partial_r\rho\right]\phi_s^t = 0 \tag{3.37}$$

and ϕ_s^t must satisfy external boundary conditions at the ICB and CMB.

The density gradient can be estimated numerically for a spherically averaged model or the Adams-Williamson equation can be used *i.e.*, $\partial_r\rho_0 = -\rho_0 g/v_p^2$. The boundary conditions are most easily applied by constructing the following combinations:

$$\partial_r\phi_s^t(r_c) + \frac{(s+1)}{r_c}\phi_s^t(r_c) = -\frac{4\pi G}{2s+1}\left[\frac{2s+1}{r_c}r_c^s\left(\int_{r_c}^{a}\delta\rho_s^t r^{-s+1}dr - \sum_{j>} a_j^{-s+1}h_{js}^t[\rho_0]_-^+\right)\right] \tag{3.38}$$

and

$$\partial_r\phi_s^t(r_i) - \frac{s}{r_i}\phi_s^t(r_i) = -\frac{4\pi G}{2s+1}\left[-\frac{2s+1}{r_i}r_i^{-(s+1)}\left(\int_0^{r_i}\delta\rho_s^t r^{s+2}dr - \sum_{j<} a_j^{s+2}h_{js}^t[\rho_0]_-^+\right)\right] \tag{3.39}$$

The summation in (3.38) is taken over all interfaces j for which $r_j \geq r_c$. Similarly only discontinuities contribute to the sum in (3.39) for which which $r_j \leq r_i$. Note that (3.38) depends only on structure above the CMB and (3.39) on structure below the ICB. The potential perturbation $\phi_s^t(r)$ in the outer core, induced by gravitational forcing from the mantle and inner core, can now be calculated by numerically solving the 2-point boundary value problem (3.37) with the boundary conditions (3.38) and (3.39). We do this using a Runge-Kutta scheme which allows us to predict ϕ_s^t at any point in the outer core. The density perturbation $\delta\rho_s^t$ can then be estimated from (3.36). This procedure allows us to relate $\delta\rho_s^t$ in the outer core to $\delta\rho_s^t$ and h_{js}^t in the rest of the Earth. Some obvious algebraic manipulations therefore enable us to eliminate $\delta\rho_s^t$ in the outer core from the inverse problem.

3.5.4 Crustal correction

One of the largest heterogeneities in the Earth's interior is the variation between continental and oceanic crust. Rather than using observations of normal mode splitting to constrain the large-scale crustal structure, we use more direct observations of crustal composition and thickness. While the crustal structure is locally well known, there are large regions of both oceanic and continental crust where the

depth of the Moho has not been determined. It now seems that variations in oceanic crustal thickness are relatively slight (*Spudich and Orcutt, 1980*) and we can often guess the continental thickness based on isostasy arguments.

We adopt the crustal model of *Smith and Masters (1989)* to compute the correction for the structure coefficients. This model is based on a compilation of data by *Soller et al. (1982)* and consists of a spherical harmonic expansion, truncated at degree $l = 10$, of the height of the three discontinuities Moho, seafloor and free surface and the expansion of the volumetric perturbations in density, bulk modulus and shear modulus. In the case of the fundamental modes, the correction to the structure coefficients can be as large as the observed value itself. We should therefore be very careful before we interpret models of upper mantle structure based on inversions of fundamental mode structure coefficients, and keep in mind that a fair amount of extrapolation has gone into the construction of the crustal model. For low-l high-Q modes, the crustal correction is on the order of the observational uncertainty so that details of the crustal model have little impact on the inferred aspherical structure of the deep Earth.

3.5.5 Inversion of the dataset

We start by using the scale factors discussed in section 3.5.1 and define the combined sensitivity kernel in (3.21)

$$ {}_kG_s(r) = \kappa_o(r)\,{}_kK_s(r)\frac{\delta \ln \kappa}{\delta \ln \rho} + \mu_o(r)\,{}_kM_s(r)\frac{\delta \ln \mu}{\delta \ln \rho} + \rho_o(r)\,{}_kR_s(r) \tag{3.40} $$

Our observed data are ${}_kc_s^t \pm \epsilon_k$. We parameterize the model with a large number of layers (6 in the inner core, 6 in the outer core, 19 in the mantle, and one for the crust). We initially allow for first order discontinuities at the ICB and the CMB. Given the small number of data, our problem is underdetermined as long as we do not impose any additional constraints on the model. If our data are consistent and our error estimates realistic we should be able to fit the observations on average to within one standard deviation or better (assuming our model contains the right degrees of freedom). We discretize the model with J layers and L first order discontinuities and write

$$ \frac{\delta \rho_s^t(r)}{\rho_0(r)} = m_j \qquad \text{for} \qquad r_{j-1} \le r < r_j, \qquad j = 1, \ldots, J \tag{3.41} $$

$$ h_{si}^t / r_i = m_j \quad \text{with} \quad i = 1, \ldots, L \quad \text{and} \quad j = J + i \tag{3.42} $$

$$G_{kj} = \int_{r_{j-1}}^{r_j} {}_kG_s(r)r^2dr \quad \text{with} \quad j = 1, \ldots, J \tag{3.43}$$

$$G_{kj} = {}_kB_{si}r_i^3 \quad \text{with} \quad i = 1, \ldots, L \quad \text{and} \quad j = J + i \tag{3.44}$$

Substituting these definitions into (3.21) leads to the system

$$\sum_{j=1}^{L+J} G_{ij}m_j = c_i \pm \epsilon_i \qquad i = 1, \ldots, N \tag{3.45}$$

With ϵ_i being the observational uncertainty of the structure coefficient c_j. Normalizing every datum c_i and its corresponding row in G by the standard error ϵ_i we have

$$b_i = c_i/\epsilon_i \qquad H_{ij} = G_{ij}/\epsilon_i \tag{3.46}$$

$$\sum_{j=1}^{L+J} H_{ij}m_j = b_i \quad \text{standard deviation} \quad 1 \tag{3.47}$$

In matrix notation, the problem to be solved is then

$$\text{minimize} \quad \|\mathbf{Hm} - \mathbf{b}\| \tag{3.48}$$

We use an SVD algorithm to solve (3.48).

In a first experiment we assume that only the crust is known and see if we can find a model of the mantle which will fit the 63 mantle sensitive multiplets. In a second experiment we include also the 24 core sensitive multiplets and see whether we can find a model of mantle and core structure which will fit the observed structure coefficients. The first two rows of table 3.4 give the χ^2/N values for these experiments. While it is possible to find models which fit the structure coefficients, they are oscillatory and the amplitude of discontinuities is physically unrealistic. Assuming that we have the right degrees of freedom, these first two experiments also suggest that we do not have any gross inconsistencies amongst the c_s^t estimates. The dataset which we use throughout the subsequent modeling is presented in the appendix at the end of this chapter (tables 3.5 – 3.7).

Though we can find models which satisfy the data, these models are very oscillatory so we seek a model construction technique which suppresses such behavior. We choose to achieve radial smoothness by overparameterizing the model and then penalize the solution for roughness. This approach allows the data, rather than the prejudices of the investigator, to dictate where structure is to occur in the model. In

the following derivation, we follow closely the notation of *Constable et al. (1987)* (see also chapter 5). We use the same discretization as in (3.41 – 3.44) and as measures of roughness we choose both first and second differences:

$$R_1 = \sum_{j=2}^{J} (m_j - m_{j-1})^2 \tag{3.49}$$

and

$$R_2 = \sum_{j=2}^{J-1} (m_{j+1} - 2m_j + m_{j-1})^2. \tag{3.50}$$

We modify these two measures of roughness to allow for step discontinuities at the inner core boundary (ICB) core mantle boundary (CMB), 660 and 410 km discontinuities. This is achieved by dropping the terms in (3.49) which straddle the discontinuities. In matrix notation we can write our forward problem as

$$\mathbf{b} = \mathbf{H}\mathbf{m}, \tag{3.51}$$

the misfit to the data as

$$\chi^2 = \|\mathbf{b} - \mathbf{H}\mathbf{m}\|^2 \tag{3.52}$$

where we assume that the data and their associated representers have been normalized to unit variance as in (3.45). The roughness measures can be written as a matrix operation, e.g.

$$R_1 = \mathbf{m}^T \mathbf{D}^T \mathbf{D}\mathbf{m} \tag{3.53}$$

where $\mathbf{D}$ is a matrix which performs first or second differencing of the model vector. Smooth models which fit the data to within a prescribed misfit χ^2 are found by solving

$$\begin{bmatrix} \mathbf{b} \\ \mathbf{0} \end{bmatrix} = \begin{bmatrix} \mathbf{G} \\ \nu\mathbf{D} \end{bmatrix} \mathbf{m} \tag{3.54}$$

The parameter ν determines the amount of smoothing and, by solving (3.54) for a range of ν values, we can explore the trade-off between the norm of the model and the misfit.

We structure the inversions which involve radial smoothing into five experiments: experiments 3 through 7. In experiment 3 we solve for the degree 2 structure in the mantle using the structure coefficients of the 63 mantle sensitive multiplets listed in table 3.5 and 3.6. We assume that the crust

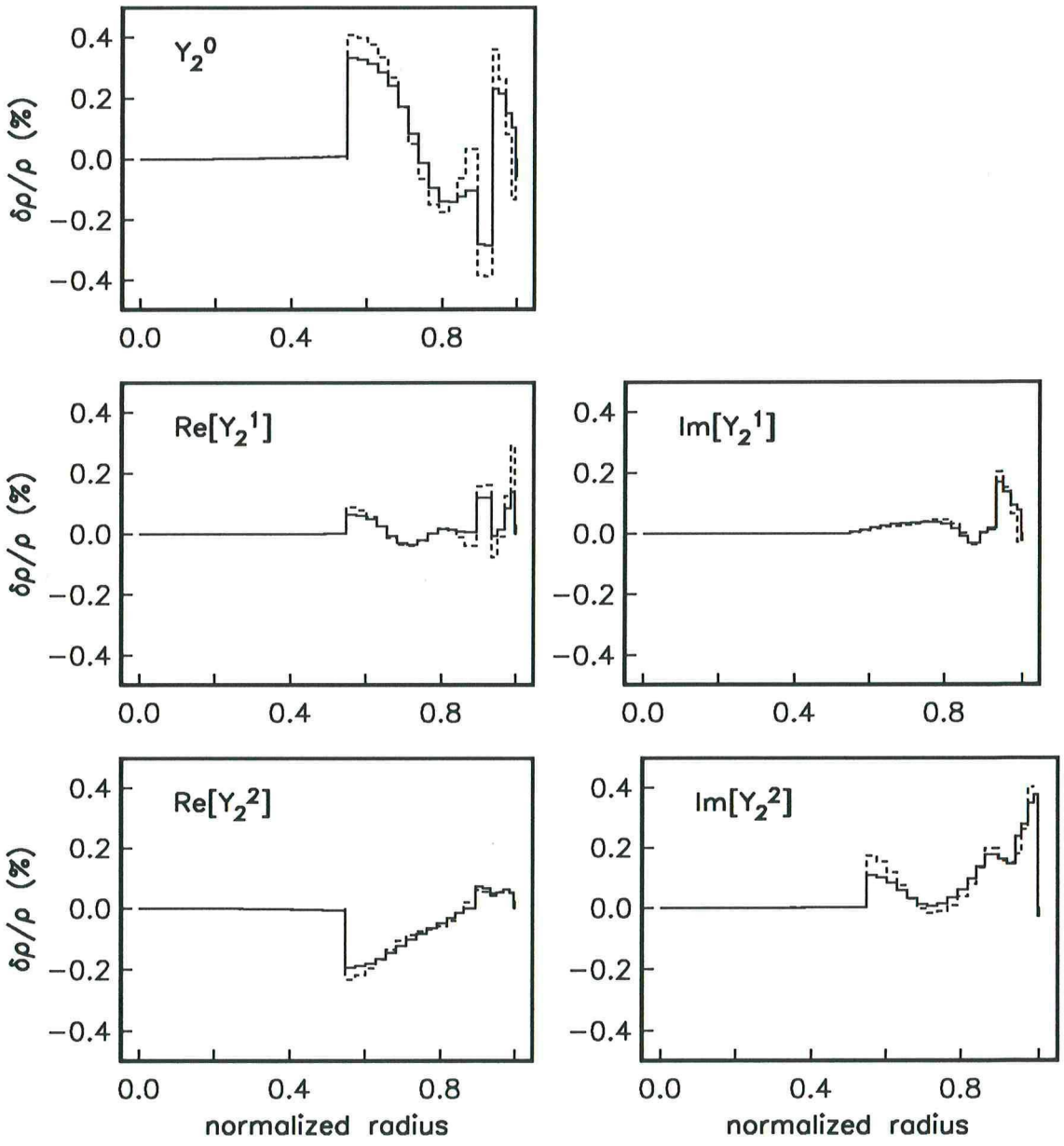

Figure 3.15 Degree 2 mantle models based on the inversion of 63 structure coefficients. The models were penalized for roughness using a first (solid line) and second difference (dashed line) norm.

	N	c_2^0	$\mathrm{Re}c_2^1$	$\mathrm{Im}c_2^1$	$\mathrm{Re}c_2^2$	$\mathrm{Im}c_2^2$
1	63	0.6	0.5	0.4	0.7	1.0
2	87	1.0	0.4	0.4	0.6	0.9
3	63	1.7	0.8	0.6	1.1	1.7
4	87	12.4	1.5	1.2	1.6	1.9
5	87	6.2	—	—	—	—
6	87	4.2	—	—	—	—
7	87	3.2	—	—	—	—

Table 3.4 χ^2/N misfit for the 7 experiments described in the text. The dataset consists of 63 mantle sensitive modes (see appendix, tables 3.5 and 3.6) and modes with high sensitivity to structure in the core (see appendix, table 3.7). Experiments 1 and 2 do not penalize the models for roughness.

is known and use the kernel in (3.32) to constrain the topography of the CMB. We use both first and second difference norms to penalize for roughness and the resulting models are plotted in figure 3.15. The lagrange multiplier ν is the same for all five models and the resulting χ^2/N misfit is listed in the third row of table 3.4. The power in $\delta\rho_2^0$ is largest followed by $\delta\rho_2^2$ and $\delta\rho_2^1$. The topography obtained for the CMB depends on the viscosity model of the mantle but, for the three viscosity models used in figure 3.14, the change in CMB height is less than 25%. The predicted rms height for the models in figure 3.15 is always less than 500 meters.

In experiment 4 we include the 20 core sensitive multiplets in the inversion and allow for the same degrees of freedom as in experiment 3. We find that the χ^2/N misfit (table 3.4) for c_2^1 and c_2^2 remains small but is large for c_2^0. These misfit values suggest that there is no need for Y_2^1 and Y_2^2 structure in the core and we do not pursue this possibility further. Axisymmetric degree 2 mantle structure is incapable of explaining the observed c_2^0 coefficients and the large χ^2/N value suggest that we need structure in the core.

In experiment 5 we allow for volumetric perturbations in the inner core including topography on the ICB while we maintain that perturbations in density be proportional to perturbations in bulk modulus in the outer core (Equation 3.29). The resulting model in this experiment exhibits a 2.5% $\delta\rho_2^0/\rho$ perturbation in the inner core and 80 km topography on the ICB. Constraining the ICB topography to be less than 10km only degrades the fit to the data, χ^2/N increases from 6.2 to 7.5, but leaves the density perturbation in the inner core unchanged.

In experiment 6 we wish to allow for structure in the outer core but, at the same time, keep the region in hydrostatic equilibrium. We do this by decoupling perturbations in density from perturbations in bulk modulus in the outer core. The model resulting from this inversion has a 1.1% $\delta\kappa_2^0/\kappa$ perturbation in

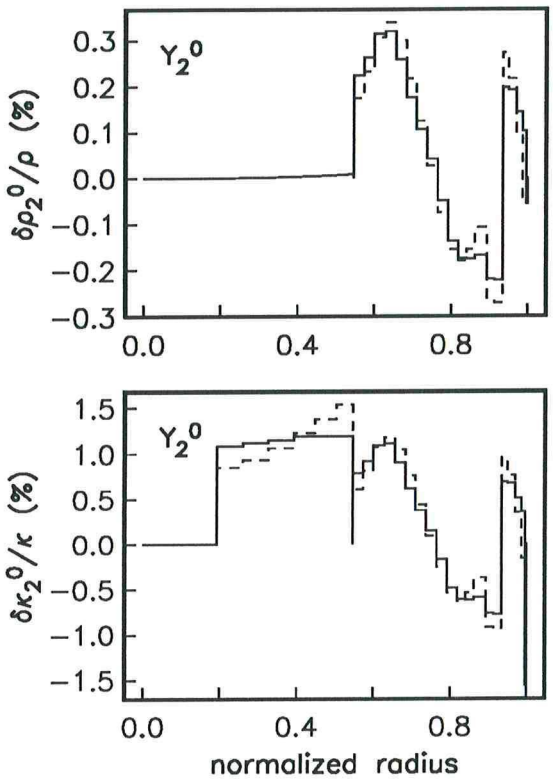

Figure 3.16 Axisymmetric degree 2 models resulting from experiment 5 using 83 c_2^0 structure coefficent estimates. The models were penalized for roughness using a first (solid line) and second difference (dashed line) norm. The CMB topography was constrained to be dynamically consistent with the density perturbations in the mantle and is less than 1 km for all viscosity models used in figure 3.14. The outer core was constrained to be in hydrostatic equilibrium and perturbations of the bulk modulus in that region were not constrained by the scaling (3.30). Inner core and ICB were not allowed to vary.

the outer core (figure 3.16). While it is difficult to supply a physical interpretation for such a perturbation, we look at it as a seismologically simple explanation of anomalous splitting. Such a perturbation in the outer core should also be seen in the travel-times of core phases. We estimate the difference in travel time for a P-wave to cross the outer core in the equatorial plane versus one that travels from pole to pole to be 1.6 seconds. A travel-time residual of this magnitude is not large enough to be seen in the ISC catalogue of travel-times.

In the last experiment we allow both for structure in the inner and outer core and on the ICB. The resulting model has a -0.3% $\delta\rho_2^0/\rho$ perturbation in the inner core and 1.1% $\delta\kappa_2^0/\kappa$ perturbation in the outer core. Again we get a large amount of topography on the ICB (75 km) and if we constrain it to be less than 10 km χ^2/N increases from 3.2 to 3.9 and the volumetric perturbations predicted by the model remain unchanged.

3.6 Discussion and Conclusions

3.6.1 Causes of Anomalous Splitting

Having doubled the number of observations of anomalously split multiplets we can now turn to the question of what causes the anomalous splitting. The data clearly indicate that the structure responsible for anomalous splitting must be dominantly axisymmetric and the nearly quadratic distribution of singlets of most of the anomalously split multiplets suggests that the anomalous structure is of harmonic degree 2. The multiplets confined to the mantle are not anomalously split so that structure in the mantle can be excluded as the cause for anomalous splitting.

We are unable to find a structure which explains the anomalous splitting although a large velocity perturbation in the outer core goes a long way to fitting the data. Other possible explanations for anomalous splitting have been proposed. For example, the observed splitting may be due to the magnetic field in the outer core. *Knopoff and MacDonald (1958)* show that the magnetic field has little effect on seismic waves unless it is extremely large, and, more recently *Tanimoto (1989)* has shown that the magnetic field necessary to produce the observed coupling would lead to a surface heat flow via ohmic heating about 5 orders of magnitude larger than observed. Clearly the B field is not responsible for anomalous splitting.

Another potential candidate responsible for splitting is a steady flow field in the outer core. It is possible to demonstrate that a steady flow field causes symmetrical splitting, odd in m for axisymmetric flow (*Gilbert 1991, personal communication*). Since the observed anomalous splitting is clearly even in m we can also rule out steady flow as the cause for anomalous splitting.

Next, we consider the possibility that our estimates of R, the ratio of observed to predicted splitting width, are too large simply because we underestimate the splitting width for a rotating Earth in hydrostatic equilibrium. Generally, ellipticity splitting is produced by two large phenomena with opposing effects. The first effect is that polar paths are shorter than equatorial paths. The second, opposing effect is that the equatorial bulge of the mantle is filled with 'fast' material, so that the travel time for one orbit of a wave packet on an equatorial path is again made more nearly equal to one on a polar path. To see if this balance can be upset for core-sensitive modes, we have varied v_p and v_s in a 200 km thick region on either side of the CMB by $\pm 100\%$ and found no noticeable effect. We can therefore conclude that perturbations in spherical structure, even near the CMB can not be the cause of anomalous splitting.

Another possibility is that there is an error in the theoretical formulation of the ellipticity splitting. The most likely place that an error could occur is in the treatment of the fluid-solid boundaries which are complicated by the possibility of slip. To check this, we have computed the ellipticity splitting of a mode ($_{13}S_3$) for an Earth model with a fluid core and then for a model with a solid outer core with a very low (500 m/s) shear velocity. The mode frequency and eigenfunction remain almost unchanged (although the radial order changes from 13 to 84) by adding a solid outer core and the ellipticity splitting coefficient is also unchanged. We therefore conclude that there is no error in the treatment of the free-slip boundary conditions.

Another potential candidate for anomalous splitting is topography on the CMB. There are two reasons (at least) which make this unlikely: (i) many of the anomalously split multiplets have very low sensitivity to structure on the CMB and (ii) studies of the Earth's nutation and variation in length of day indicate that structure on the CMB should not exceed 500 m (*Gwinn et al. 1986*). In our inversions we have required that the topography of the CMB be dynamically consistent with the density perturbations in the mantle. For the viscosity models considered here, our inversions have shown that this requirement effectively constrains the degree 2 topography of the CMB to be less than 1 km.

What is apparently left as possible cause for anomalous splitting is a volumetric perturbation – isotropic or anisotropic – in the inner or outer core and/or topography on the ICB. As discussed above, we cannot possibly reconcile all observations with a model of inner core anisotropy. If the power in the model is increased, the splitting of modes with little energy in the inner core is still underpredicted whereas the splitting of modes with more that 7% elastic energy in the inner core is grossly overpredicted. Our modeling experiments also show that no model with volumetric perturbations in the inner core is able to fit the observations of anomalously split modes. We are thus led to the conclusion that the structure responsible for anomalous splitting is an axisymmetric volumetric perturbation in the outer core. This seemingly contradicts the results by *Stevenson (1987)* unless we allow perturbations in bulk modulus to be entirely decoupled from perturbations in density in the outer core. It is easy to find such models which go a long way to explain the observations. In summary, our search for structures responsible for anomalous splitting have allowed us to eliminate (i) volumetric perturbations in the mantle, (ii) CMB topography, (iii) steady flow in the outer core, (iv) B field in the outer core and, (v) volumetric perturbations in the inner core (isotropic or anisotropic). Our current working hypothesis is that the structure responsible for anomalous splitting is a degree 2 velocity perturbation in the outer core. The difficulties associated with this hypothesis are that we arrive at a strange v_p/ρ relationship if the outer core is to be in hydrostatic equilibrium ($\partial \ln v_p / \partial \ln \rho > 75$) .

References

Anderson, D.L., A seismic equation of state, II. Shear properties and thermodynamics of the lower mantle. *Phys. Earth Planet. Inter.*, **45**, 307–323, 1987.

Anderson, D.L., Thermally induced phase changes, lateral heterogeneity of the mantle, continental roots, and deep slab anomalies. *J. Geophys. Res.*, **92**, 13,968–13980, 1987.

Backus, G.E., and J.F. Gilbert, The rotational splitting of the free oscillations of the earth. *Proc. Natl. Acad. Sci.*, **47**, 362–371, 1961.

Brown, J.M., M.D. Furnish, and R.G. McQueen, Thermodynamics for olivine from the Hugoniot. In: *High-Pressure Research in Mineral Physics, eds. M. Manghnani and Y. Syono, AGU, Washington, D.C.*, pp.373–384, 1986.

Buland, R., J. Berger, and F. Gilbert, Observations from the IDA network of attenuation and splitting during a recent earthquake. *Nature*, **277**, 358–362, 1979.

Creager, K.C., and T.H. Jordan, Large scale structure of the outermost core from P'_{DF} and P'_{AB} travel-times. *EOS Trans. AGU*, **67**, 311, 1986.

Dahlen, F.A., The normal modes of a rotating, elliptical earth. *Geophys. J. R. Astron. Soc.*, **16**, 329–367, 1968.

Dahlen, F.A., The normal modes of a rotating, elliptical earth-II, Near-resonance multiplet coupling. *Geophys. J. R. Astron. Soc.*, **18**, 397–436, 1969.

Dahlen, F.A., Inference of the lateral heterogeneity of the Earth from the eigenfrequency spectrum: a linear inverse problem. *Geophys. J. R. Astron. Soc.*, **38**, 143–167, 1974.

Davis, J.P., Local eigenfrequency and its uncertainty inferred from fundamental spheroidal mode frequency shifts. *Geophys. J. R. Astron. Soc.*, **88**, 693–722, 1987.

Dziewonski, A.M., Mapping the lower mantle: determination of lateral heterogeneity in P velocity up to degree and order 6. *J. Geophys. Res.*, **89**, 5929–5952, 1984.

Dziewonski, A.M., B.H. Hager, and R.J. O'Connell, Large-scale heterogeneities in the lower mantle. *J. Geophys. Res.*, **82**, 239–255, 1977.

Edmonds, A.R., *Angular Momentum and Quantum Mechanics*. Princeton University Press, Princeton, N.J., 1960.

Efron, B., and R. Tibshirani, Bootstrap methods for standard errors, confidence intervals, and other measures of statistical accuracy. *Statistical Science*, **1**, 54–77, 1986.

Giardini, D., X.-D. Li, and J.H. Woodhouse, Three-dimensional structure of the earth from splitting in free oscillation spectra. *Nature*, **325**, 405–411, 1987.

Giardini, D., X.-D. Li, and J.H. Woodhouse, Splitting functions of long period normal modes of the earth. *J. Geophys. Res.*, **93**, 13,716–13,742, 1988.

Gilbert, F., and A.M. Dziewonski, An application of normal mode theory to the retrieval of structural parameters and source mechanisms from seismic spectra. *Phil. Trans. R. Soc. Lond.*, **A278**, 187–269, 1975.

Gubbins, D., and T.G. Masters, Driving mechanisms for the Earth's dynamo. In: *Advances in Geophysics, Academic Press*, pp.1–50, 1979.

Gwinn, C.R., T.A. Herring, and I.I. Shapiro, Geodesy by radio interferometry: Studies of the forced

nutations of the Earth. 2. Interpretation. *J. Geophys. Res.*, **91**, 4755–4765, 1986.

Hager, B.H., R.W. Clayton, M.A. Richards, R.P. Comer, and A.M. Dziewonski, Lower mantle heterogeneity, dynamic topography and the geoid. *Nature*, **313**, 541–545, 1985.

Hager, B.H., and R.W. Clayton, Constraints on the structure of mantle convection using seismic observations, flow models, and the geoid. In: *Mantle Convection, ed W.R. Peltier, Gordon and Breach, New York*, pp.657–763, 1989.

Jeffreys, H., *The Earth.* Cambridge University Press, Cambridge, England, 1976.

Li, X.-D., D. Giardini, and J. H. Woodhouse, Large-Scale Three -Dimensional Even -Degree Structure of the Earth from Splitting of Long-Period Normal Modes. *J. Geophys. Res.*, **96**, 551–577, 1991a.

Li, X.-D., D. Giardini, and J.H. Woodhouse, The relative amplitudes of mantle heterogeneity in P-velocity, S-velocity and density from free-oscillation data. *Geophys. J. Int.*, **105**, 649–657, 1991b.

Luh, P.C., Free oscillations of the laterally inhomogeneous earth: Quasi-degenerate multiplet coupling. *Geophys. J. R. Astron. Soc.*, **32**, 187–202, 1973.

Luh, P.C., Normal modes of a rotating, self-gravitating inhomogeneous earth. *Geophys. J. R. Astron. Soc.*, **38**, 187–224, 1974.

Masters, G., and F. Gilbert, Structure of the inner core inferred from observations of its spheroidal shear modes. *Geophys. Res. Lett.*, **8**, 569–571, 1981.

Masters, G., T.H. Jordan, P.G. Silver, and F. Gilbert, Aspherical earth structure from fundamental spheroidal-mode data. *Nature*, **298**, 609–613, 1982.

Montagner, J-P., and T. Tanimoto, Global anisotropy in the upper mantle inferred from the regionalization of phase velocities. *J. Geophys. Res.*, **95**, 4797–4819, 1990.

Morelli, A., A.M. Dziewonski, and J.H. Woodhouse, Anisotropy of the inner core inferred from $PKIKP$ travel times. *Geophys. Res. Lett.*, **13**, 1545–1548, 1986.

Morelli, A., and A.M. Dziewonski, The structure of the earth's core inferred from travel time residuals. *EOS Trans. AGU*, **67**, 311, 1986.

Nakanishi, I., and D.L. Anderson, Measurements of mantle wave velocities and inversion for lateral heterogeneity and anisotropy. II. Analysis by the single station method. *Geophys. J. R. Astron. Soc.*, **78**, 573–617, 1984.

Park, J., and F. Gilbert, Coupled free oscillations of an aspherical dissipative rotating earth: Galerkin theory. *J. Geophys. Res.*, **91**, 7241–7260, 1986.

Poupinet, G., R. Pillet, and A. Souriau, Possible heterogeneity of the earth's core deduced from $PKIKP$ travel times. *Nature*, **305**, 204–206, 1983.

Pulver, S., and G. Masters, $PcP - P$ travel times and the ratio of S to P velocity variations in the lower mantle. *EOS Trans. AGU*, **71**, 1464, 1990.

Richards, M.A., and B.H. Hager, Geoid anomalies in a dynamic earth. *J. Geophys. Res.*, **89**, 5987–6002, 1984.

Richards, M.A., and B.H. Hager, Effects of lateral viscosity variations on long-wavelength geoid anomalies and topography. *J. Geophys. Res.*, **94**, 10,299–10,313, 1989.

Ritzwoller, M., G. Masters, and F. Gilbert, Observations of anomalous splitting and their interpretation in terms of aspherical structure. *J. Geophys. Res.*, **91**, 10,203–10,228, 1986.

Ritzwoller, M., G. Masters, and F. Gilbert, Constraining aspherical structure with low frequency interaction coefficients: Application to uncoupled multiplets. *J. Geophys. Res.*, **93**, 6369–6396, 1988.

Roult, G., and B. Romanowicz J. P. Montagner, 3-D upper mantle shear velocity and attenuation from fundamental mode free oscillation data. *Geophys. J. Int.*, **101**, 61–80, 1990.

Shearer, P.M., K.M. Toy, and J.A. Orcutt, Axi-symmetric earth models and inner core anisotropy. *Nature*, **333**, 228–232, 1988.

Shearer, P. M., and K. M. Toy, PKP(BC) versus PKP(DF) Differential Travel Times and Aspherical Structure in the Earth's Inner Core. *J. Geophys. Res.*, **96**, 2233–2247, 1991.

Smith, M.F., and G. Masters, Aspherical structure constraints from free oscillation frequency and attenuation measurements. *J. Geophys. Res.*, **94**, 1953–1976, 1989.

Soller, D.R., R.D. Ray, and R.D. Brown, A new global crustal thickness model. *Tectonics*, **1**, 125–149, 1982.

Stevenson, D., Limits on lateral density and velocity variations in the earth's core. *Geophys. J. R. Astron. Soc.*, **88**, 311–319, 1987.

Tanimoto, T., Splitting of normal modes and travel time anomalies due to the magnetic field of the Earth. *J. Geophys. Res.*, **94**, 3030–3036, 1989.

Tanimoto, T., Long-wavelength S-velocity structure throughout the mantle. *Geophys. J. Int.*, **100**, 327–336, 1990.

Wahr, J.M., and D. de Vries, The possibility of lateral structure inside the core and its implications for nutation and Earth tide observations. *Geophys. J. Int.*, **99**, 511–519, 1989.

Woodhouse, J.H., The coupling and attenuation of nearly resonant multiplets in the earth's free oscillation spectrum. *Geophys. J. R. Astron. Soc.*, **61**, 261–283, 1980.

Woodhouse, J.H., and F.A. Dahlen, The effect of a general aspherical perturbation on the free oscillations of the earth. *Geophys. J. R. Astron. Soc.*, **53**, 335–354, 1978.

Woodhouse, J.H., and A.M. Dziewonski, Mapping of the upper mantle: three-dimensional modeling of earth structure by inversion of seismic waveforms. *J. Geophys. Res.*, **89**, 5953–5986, 1984.

Woodward, R. L., and G. Masters, Global Upper Mantle Structure From Long-Period Differential Travel Times. *J. Geophys. Res.*, **96**, 6351–6377, 1991.

Appendix

Table 3.5 Degree 2 structure coefficients (in μHz) for spheroidal fundamental modes (*Ritzwoller et al. 1988*; *Smith and Masters, 1989*).

mode	c_2^0	error	Re[c_2^1]	error	Im[c_2^1]	error	Re[c_2^2]	error	Im[c_2^2]	error
${}_0S_3$	0.33	0.60	-0.40	0.80	0.10	0.60	0.50	2.00	0.90	1.60
${}_0S_4$	0.99	0.50	0.40	0.30	0.10	0.50	-0.90	0.60	1.20	0.90
${}_0S_5$	1.72	0.60	0.50	0.30	0.30	0.50	-1.30	0.70	1.60	0.50
${}_0S_6$	2.36	0.60	0.50	0.30	0.20	0.40	-2.10	0.60	2.50	0.50
${}_0S_7$	1.92	0.90	0.90	0.40	0.10	0.50	-2.80	0.70	3.00	0.90
${}_0S_8$	0.87	0.40	0.89	0.25	0.31	0.25	-2.27	0.30	2.38	0.30
${}_0S_9$	-0.81	0.42	1.45	0.30	0.42	0.35	-1.64	0.35	3.08	0.40
${}_0S_{10}$	-1.21	0.70	1.99	0.36	0.32	0.40	-0.58	0.45	3.86	0.52
${}_0S_{12}$	-6.44	0.60	1.33	0.35	-0.03	0.35	0.23	0.35	4.62	0.42
${}_0S_{13}$	-6.74	0.60	2.12	0.35	-0.78	0.30	0.20	0.35	5.38	0.35
${}_0S_{14}$	-8.81	0.60	2.84	0.35	-0.36	0.30	0.25	0.36	5.82	0.36
${}_0S_{15}$	-8.32	0.60	3.05	0.35	-0.95	0.32	1.13	0.36	6.45	0.41
${}_0S_{16}$	-9.21	0.60	3.31	0.35	-1.09	0.40	1.55	0.45	6.68	0.45
${}_0S_{17}$	-9.20	0.70	3.07	0.40	-1.11	0.45	3.20	0.50	6.65	0.50
${}_0S_{21}$	-11.45	0.80	5.66	0.40	-1.01	0.40	4.27	0.40	11.13	0.50
${}_0S_{22}$	-13.17	0.80	6.31	0.40	-0.90	0.40	5.05	0.40	12.13	0.50
${}_0S_{23}$	-12.68	0.80	6.14	0.40	-0.96	0.40	6.09	0.40	12.79	0.50
${}_0S_{24}$	-13.45	0.80	6.97	0.43	-0.95	0.50	6.76	0.55	12.74	0.58
${}_0S_{25}$	-14.97	0.80	6.85	0.39	-1.36	0.48	6.69	0.46	12.15	0.58
${}_0S_{26}$	-12.84	0.82	6.67	0.43	-1.43	0.57	5.92	0.60	12.44	0.66
${}_0S_{27}$	-13.22	0.77	8.20	0.50	-0.90	0.48	7.39	0.55	14.13	0.66
${}_0S_{28}$	-14.60	0.80	8.08	0.50	-0.71	0.44	8.31	0.50	16.40	0.60
${}_0S_{29}$	-13.55	0.80	7.87	0.50	-1.11	0.53	8.63	0.55	14.89	0.71
${}_0S_{30}$	-14.02	1.15	8.94	0.63	-0.07	0.78	8.97	0.88	16.37	1.01
${}_0S_{31}$	-14.70	1.33	9.08	0.73	1.18	0.77	8.45	0.86	13.25	1.11
${}_0S_{34}$	-14.65	1.61	9.96	0.97	0.35	1.01	11.58	1.08	21.11	1.38
${}_0S_{35}$	-14.62	1.76	8.92	1.01	-0.56	1.12	12.28	1.28	19.50	1.45
${}_0S_{36}$	-12.90	1.52	11.08	0.93	0.12	1.13	10.75	1.21	20.74	1.29
${}_0S_{37}$	-10.32	1.43	10.88	0.87	1.16	0.96	13.79	1.05	22.15	1.19
${}_0S_{38}$	-12.62	1.59	12.03	0.98	1.98	1.08	11.32	1.20	22.69	1.38
${}_0S_{39}$	-12.14	1.65	11.86	1.11	2.35	1.17	13.66	1.17	22.01	1.42
${}_0S_{40}$	-12.26	1.81	11.49	1.08	2.26	1.19	13.33	1.29	21.41	1.48
${}_0S_{41}$	-6.87	1.67	10.39	1.07	1.41	1.21	15.05	1.15	20.65	1.47
${}_0S_{42}$	-8.97	1.94	10.84	1.26	1.24	1.35	13.49	1.35	22.22	1.57
${}_0S_{43}$	-7.56	1.99	13.53	1.43	1.84	1.51	13.48	1.48	20.77	1.89
${}_0S_{44}$	-6.57	2.02	13.81	1.19	0.35	1.24	16.60	1.37	22.21	1.53
${}_0S_{45}$	-7.76	2.22	12.29	1.29	0.86	1.43	14.87	1.59	24.66	1.77
${}_0S_{46}$	-7.87	1.95	12.42	1.00	0.69	1.22	12.48	1.30	25.28	1.60
${}_0S_{47}$	-6.99	2.27	12.71	1.31	0.92	1.43	18.35	1.53	23.78	1.90
${}_0S_{48}$	-6.51	1.98	12.30	1.12	-1.25	1.29	14.17	1.40	30.14	1.56
${}_0S_{49}$	-8.06	2.09	11.82	1.17	1.23	1.25	18.58	1.37	26.31	1.59
${}_0S_{50}$	-7.52	2.00	13.61	1.22	-1.38	1.30	19.78	1.49	28.10	1.54
${}_0S_{51}$	-6.79	2.03	14.81	1.19	-1.18	1.43	20.74	1.43	34.23	1.48
${}_0S_{52}$	-7.21	2.09	14.65	1.28	-0.10	1.39	19.50	1.50	34.07	1.63

Table 3.6 Degree 2 structure coefficients (in μHz) for mantle sensitive spheroidal overtones (*Ritzwoller et al. 1988*; *Smith and Masters, 1989*).

mode	c_2^0	error	Re[c_2^1]	error	Im[c_2^1]	error	Re[c_2^2]	error	Im[c_2^2]	error
${}_1S_3$	0.10	0.70	0.60	0.70	0.30	0.70	-1.30	1.70	2.20	1.80
${}_1S_4$	0.60	0.70	0.30	0.50	0.60	0.50	-2.00	1.00	2.00	1.20
${}_1S_5$	2.10	1.40	0.40	0.90	0.80	0.80	-2.80	1.70	3.50	1.30
${}_1S_6$	0.80	2.20	0.10	1.50	-0.30	2.40	-6.10	2.70	3.70	1.70
${}_1S_7$	4.20	1.40	0.30	0.60	1.00	1.00	-4.30	1.60	1.90	1.00
${}_1S_8$	5.30	1.60	0.70	0.60	1.10	1.00	-5.70	1.60	3.10	1.20
${}_1S_9$	6.50	3.60	0.80	0.70	1.40	1.60	-7.00	3.90	4.10	2.50
${}_2S_4$	0.90	1.10	1.60	0.60	1.00	0.70	-3.40	0.90	2.80	0.90
${}_2S_5$	0.70	1.60	2.60	0.80	2.10	1.10	-0.60	1.50	4.80	1.40
${}_2S_6$	-2.00	1.30	3.10	0.60	1.60	1.10	1.60	1.30	5.10	1.30
${}_2S_8$	-4.80	2.00	4.10	0.60	2.10	1.00	0.40	2.10	9.50	1.20
${}_2S_{10}$	-14.73	2.50	2.60	1.50	-1.60	1.50	3.76	1.50	13.44	1.50
${}_2S_{12}$	-7.47	2.50	4.20	1.50	0.40	1.50	7.09	1.50	13.80	1.80
${}_4S_3$	0.10	1.50	0.40	0.80	2.00	1.00	-1.60	1.70	1.50	1.40
${}_5S_4$	-0.30	1.10	0.50	0.60	1.90	1.00	0.50	1.10	5.20	1.00
${}_5S_5$	1.60	1.10	0.20	0.50	1.00	0.70	-0.20	1.10	2.90	1.00
${}_5S_6$	2.60	1.00	0.30	0.50	1.70	0.70	-1.60	1.10	3.80	0.70
${}_5S_7$	2.50	1.30	0.10	0.50	2.40	0.70	-2.60	1.70	3.00	1.00
${}_5S_8$	4.70	4.40	-0.80	1.30	0.70	1.70	-3.00	3.70	5.30	4.00

Table 3.7 Degree 2 structure coefficients of core sensitive multiplets. The observations for the modes ${}_{15}S_3$ through ${}_{27}S_2$ are new, with ${}_{15}S_3$, ${}_{18}S_4$ and ${}_{23}S_5$ estimated with the spectral fitting technique. Multiplets for which only c_2^0 has been estimated were analyzed with the singlet stripping technique.

mode	c_2^0	error	Re[c_2^1]	error	Im[c_2^1]	error	Re[c_2^2]	error	Im[c_2^2]	error
${}_2S_3$	9.00	0.90	1.30	0.70	0.70	0.60	-3.50	0.80	2.60	0.70
${}_3S_1$	0.70	0.70	0.00	0.30	-0.10	0.30	0.00	0.40	1.30	0.40
${}_3S_2$	16.50	1.60	1.10	1.90	0.10	1.20	-2.30	2.40	5.70	2.00
${}_3S_8$	0.70	1.50	3.70	0.80	1.10	1.10	-4.60	1.00	11.50	1.50
${}_5S_3$	-0.50	1.20	-0.40	0.70	0.90	1.10	-5.40	1.30	5.30	0.80
${}_6S_3$	15.70	1.10	0.00	0.90	4.20	1.00	1.80	1.30	4.00	1.20
${}_8S_5$	16.30	1.60	0.60	1.30	-0.20	1.10	-1.10	1.50	4.00	1.80
${}_9S_3$	16.50	2.40	-0.30	2.20	1.80	2.50	4.50	3.10	3.20	3.10
${}_{10}S_2$	21.50	2.20	-2.50	1.70	-1.90	1.70	-2.20	1.90	5.60	1.10
${}_{11}S_4$	15.30	1.50	-1.00	0.80	3.30	0.60	-2.40	1.30	6.20	1.10
${}_{11}S_5$	10.20	1.50	-2.50	0.90	0.70	1.00	-4.70	1.00	4.20	1.30
${}_{13}S_2$	17.50	1.80	-0.60	1.00	0.50	0.90	-3.00	1.40	5.30	1.00
${}_{13}S_3$	17.10	1.70	2.20	1.20	-1.00	1.00	-8.50	1.50	2.80	1.10
${}_{15}S_3$	18.60	2.00	6.40	1.50	4.10	2.00	3.10	2.00	7.40	2.00
${}_{16}S_5$	31.90	9.00								
${}_{16}S_6$	31.10	4.20								
${}_{18}S_3$	30.20	4.30								
${}_{18}S_4$	22.60	0.50	-1.00	1.00	0.10	1.00	-3.60	1.00	7.30	1.00
${}_{20}S_5$	42.20	6.40								
${}_{21}S_6$	31.40	4.60								
${}_{23}S_4$	28.90	4.80								
${}_{23}S_5$	27.50	2.20	-1.80	1.00	4.10	1.00	-4.40	1.00	8.00	1.00
${}_{25}S_2$	18.60	5.00								
${}_{27}S_2$	10.50	6.30								

Chapter 4

The Macquarie Rise Event - A Rare Opportunity for the Observation of Low Order Toroidal Modes

4.1. Introduction

Numerous recent deployments of three component seismometers with improved sensitivity at the low frequency end of the normal mode spectrum have made the Macquarie rise event (May 23, 1989, Moment: 2×10^{21} Nm) a prime candidate for the study of low order toroidal modes. Observations of the degenerate frequency of these modes allows us to constrain average mantle structure. Furthermore, the modes exhibit some sensitivity to structure of the core-mantle boundary and one can use information about the splitting of these modes to constrain the location of the structure responsible for anomalous splitting (see chapter 3).

We inspected all digital long-period (LP) and very long-period (VLP) recordings from the major global networks (IDA, SRO, ASRO, GEOSCOPE, upgraded DWWSSN, CDSN, IRIS) and the Black Forest Observatory (BFO) in SW Germany and retained 116 records with a high signal-to-noise ratio for the study of low order toroidal modes and the determination of the source mechanism. The number of clean recordings available for this earthquake show how much the digital networks have expanded since 1977 when source mechanisms were frequently constrained by data from less than 10 stations. 40 recordings were discarded, sometimes due to obvious problems with either the seismic sensor or the data logger but, in the majority of cases, due to environmental noise at the recording site.

Atmospheric conditions at the recording site and the insulation of seismic sensors from their influence are of prime importance for the observation of free oscillations with periods exceeding 1000 seconds. This is illustrated by the observation that seismic noise at frequencies below 1 mHz due to the

passage of a cold front can easily swamp the signal of all but the largest earthquakes (*Sorrells, 1971*; *Müller and Zürn, 1983*).

In section 4.2 we perform a moment tensor inversion in the frequency band 2-6 mHz and our results confirm the strike slip nature of the event found by earlier studies (*Romanowicz and Ekström, 1989*). In fact, the Macquarie rise event is the largest strike-slip event recorded with modern instruments and its source mechanism is ideal for the excitation of toroidal modes. We have been able to observe fundamental toroidal modes on amplitude spectra of single records down to ${}_0T_2$.

Since all previous reported observations of the gravest toroidal mode ${}_0T_2$ are derived from recordings of the 1960 Chilean earthquake *(Derr, 1969)*, we were curious to see if we can confirm these observations. In section 4.3 we reanalyze the Isabella strain meter record of the 1960 Chilean event (*Benioff et al. 1961)* which, according to *Derr (1969)*, has yielded the best spectra of ${}_0T_2$. This record is also the only recording of the Chilean event which is available to us in digital form. Our search for ${}_0T_2$ in the Isabella strain meter record using the multitaper spectral analysis technique (*Park et al. 1987*; *Lindberg and Park, 1987*) is unsuccessful and we believe that the Macquarie rise event has led to the first unambiguous observation of this mode.

In section 4.4 we estimate multiplet degenerate frequencies and Q of the low order fundamental toroidal modes. We make use of two techniques: we analyze histograms of peak frequency measurements (*Smith and Masters, 1989*) and, for multiplets which have been observed on sufficiently many recordings, we also perform singlet stripping (see chapter 3).

Coriolis coupling between fundamental toroidal and spheroidal modes is strongest for source-receiver configurations with near-polar great circles. It is therefore understandable why the May 25, 1981 Macquarie rise event, located at 52°S, has led to the first observations of Coriolis coupling (*Masters et al. 1983*). The 1989 Macquarie rise event also resulted in numerous recordings corresponding to near-polar great circles and, looking at amplitude spectra of such recordings, we find again ample evidence for Coriolis coupling. We note, however, that, amongst the modes of interest in this chapter, only ${}_0T_9$ and ${}_0T_{10}$ are noticeably affected by Coriolis coupling.

4.2. Moment Tensor Inversion

We adopt the model of a point source in space with a triangular source time function to describe the earthquake rupture. We leave the source location and the event time fixed at the values determined by *NEIC (1989)*: Event time: May 23, 1989, 10h 54:49.5 UT; Latitude: 52.34°S; Longitude: 160.57°E;

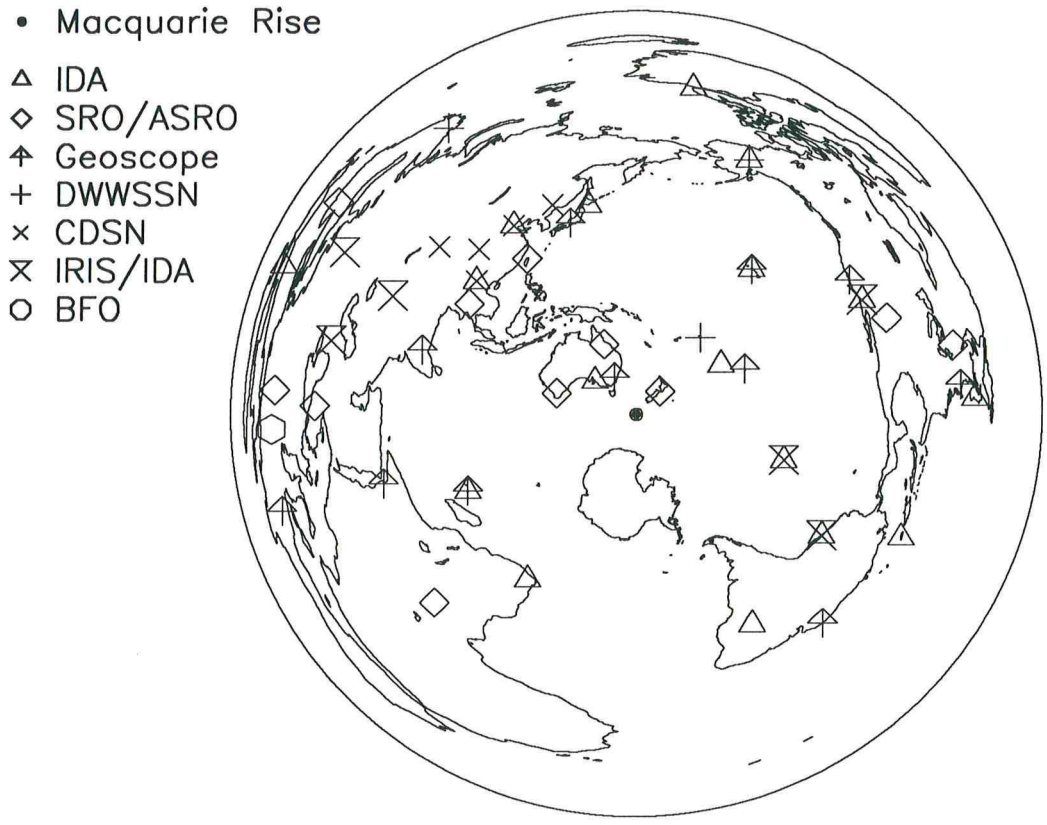

Figure 4.1 Azimuthal projection of the world centered on the Macquarie Rise. Recordings from the stations indicated on the map were used in the moment tensor inversion. Note that great circles through the epicenter appear as straight lines through the center of the map. The azimuthal coverage for this event is excellent.

Depth: 10 km. A quantitative description of the source is needed as part of the singlet stripping technique so that the excitation of individual singlets can be calculated. To justify the use of the point source model in singlet stripping experiments for the modes ${}_0T_5$ through ${}_0T_8$, we show that higher order terms in the moment tensor expansion which account for the spatial extent of the source are negligible compared with the zeroeth order moment tensor describing a point source. *Backus and Mulcahy (1976)* have shown that the magnitude of the higher order terms in the Taylor series expansion of the displacement field in the source volume fall off as $(1/n!)(6\pi\ell/\lambda)^n$ where ℓ is the largest distance of any point in the source volume from the origin and λ is the smallest wavelength of interest. In our case, we find that the mode ${}_0T_8$ has a wavelength $\lambda \simeq 2\pi a/(l+1/2) = 4700$km where a is the radius of the Earth and $l = 8$ is the harmonic degree. The fault length of the Macquarie rise event has been estimated to be $L \simeq 90$km based on a study of broadband body waves and the distribution of aftershocks (*Braunmiller and Nábělek, 1990*). If we asuume that our origin is centered on the fault we have $\ell = L/2$ and we get a ratio of the

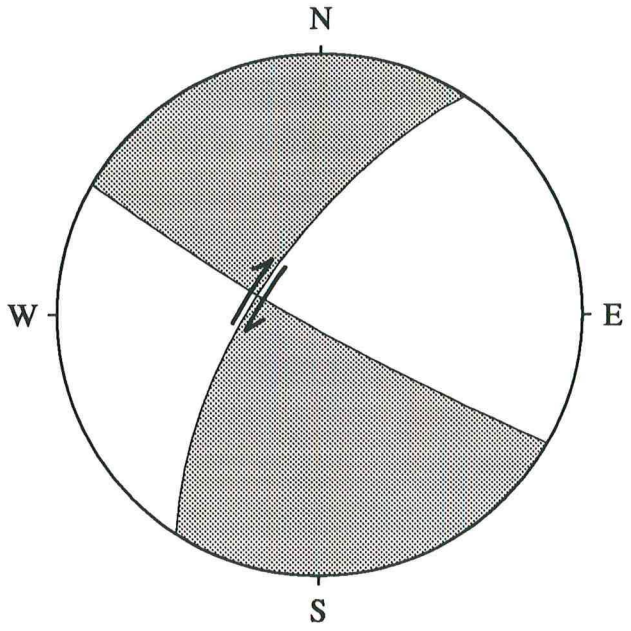

Figure 4.2 Faultplane solution for the Macquarie rise event. We show a stereographic projection of the lower hemisphere. Shaded quadrants indicate compressional first motion, white quadrants indicate dilatation. A comparison with the tectonic setting in which the event occurred suggests that a right lateral rupture occurred on the NE-SW trending fault plane. *(Ekström and Romanowicz, 1990).*

2nd term over the leading term of $(1/2)(6\pi\ell/\lambda) = 0.09$. This error is acceptable for our purpose since all one has to do for singlet stripping to succeed is to predict correctly the sign of the initial amplitude of the target singlet at the receiver.

We calculate the Green's functions associated with the six independent elements of the zeroeth order moment rate tensor by modal summation. For the well-studied fundamental spheroidal and toroidal modes, we also account for the zeroeth order effect of aspherical structure and shift the center frequencies to match the observed great circle average (*Jordan, 1978*; *Smith and Masters, 1989*). The moment tensor inversion is performed by linear fitting in the frequency domain and the rise time is varied until an optimum fit to the data is obtained. Amongst the 160 events in our data base we have not found a single event where the fit to the data was significantly improved by allowing the moment tensor to have an isotropic component. We terefore remove this degree of freedom and constrain the moment tensor to be deviatoric. Decomposing the resulting moment tensor into major and minor double-couples we find that the two differ by more than a factor 20 in size and can therefore conclude that a single double-couple is an adequate representation of the source. Linear fitting tends to give an estimate of moment which is biased low because of a misalignment of the Green's functions with respect to the data caused by aspherical structure. We correct for this effect by rotating and scaling the double-couple until the source

best predicts the observed power at each station. Since noise is included in the power estimate, this latter technique tends to overestimate the true moment of the event. Our estimates of the scalar moment m_0 lie between 12 and 20×10^{20}Nm. The strike of the fault plane is $\sigma = 35° \pm 1°$, the dip is $\delta = 78° \pm 2°$ and the rake is $\gamma = 185° \pm 30°$. For the auxiliary fault plane we get $\sigma = 126° \pm 1°$, $\delta = 83° \pm 2°$ and $\gamma = 349° \pm 30°$. The errors in the fault plane orientation have been estimated from the errors on the moment tensor elements using a bootstrapping technique (*Effron and Tibshirani, 1986*) and by comparing solutions obtained from different subsets of the data. The rise time for this event is well determined and is 45 seconds which is unusually short for this size of event. Figure 4.1 shows the distribution of stations from which data was used in the moment tensor inversion and Figure 4.2 shows the best fitting double couple fault plane solution.

For the final solution we have used $J = 116$ seismic traces: 60 vertical and 56 horizontal component recordings. As a measure of goodness of fit we use the mean variance reduction. Let the jth trace be $x_{ij}, i = 1, \ldots, N_j$ and the synthetic seismogram computed with the final source mechanism be $y_{ij}, i = 1, \ldots, N_j$, then we define the mean variance reduction for the moment tensor solution as

$$V_{red} = \frac{100}{J} \sum_{j=1}^{J} \left(1 - \frac{\sum_{i=1}^{N_j} (x_{ij} - y_{ij})^2}{\sum_{i=1}^{N_j} x_{ij}^2} \right). \tag{4.1}$$

For the Macquarie rise event we obtain a mean variance reduction of only $V_{red} = 43\%$. The cause for this poor fit could be due to three reasons: (1) instrument calibration errors, (2) inadequately modeled 3-D structure and (3) the large spatial extent of the source. Instrument calibration errors can be largely ruled out since we were able to obtain a source mechanism with 77% variance reduction using 66 seismograms for an intermediate size, deep earthquake only three weeks prior to the Macquarie rise event (Peruvian earthquake: May 5, 1989, $m_0 = 0.5 \times 10^{20}$Nm, depth: 593km). The second and third possible reasons are probably equally responsible for the poor variance reduction. As we have already mentioned in chapter 2, we find that shallow and intermediate depth earthquakes are more difficult to model than deep focus events. The Macquarie rise event is shallow and so, the low variance reduction falls within the known pattern. Oddly enough we still lack a plausible explanation as to why spectra from recordings of deep earthquakes can be modeled better than spectra from shallow ones.

The same arguments which we used to show that a double couple point source is an adequate model to predict the singlet excitations for the modes ${}_0T_5$ through ${}_0T_8$ can be used to show the shortcomings of the point source model for synthetic seismograms covering the frequency band 2 – 6 mHz. The mode ${}_0S_{54}$, for example, has a frequency of 5.974 mHz and a wavelength of $\lambda \simeq 735$km which

is just slightly over four times our estimated source dimension. In other words, we would expect our synthetic seismograms to contain phase errors of up to 90° if we were to use a point source model and neglected the source history. Estimating a "source time function" as part of the moment tensor inversion models not only the temporal extent of the source but some of the spatial extent as well. Even so we expect phase errors on the order of a few tens of degrees. Clearly, phase errors of this magnitude will adversely affect our ability to model the data and result in low variance reductions. Models which take the spatial extent of earthquake ruptures into account have been put forward by *Backus and Mulcahy (1976)* and *Backus (1977)* and, in the case of the Macquarie rise event, their use is mandated for studies of all but the gravest modes.

4.3. Searching for ${}_0T_2$ using the Multitaper technique

A systematic search for the excitation of the gravest toroidal mode must concentrate on recordings of the largest events in the last three decades. Earlier events have to be discarded because of the lack of recordings with sufficient dynamic range. The records must be either from a horizontal strain meter or a horizontal seismometer since toroidal motion does not involve any vertical displacement. The largest earthquakes in this time window are, in chronological order, the 1960 Chilean event, the 1964 Alaskan event, the 1977 Indonesian event, the 1987 Alaskan event and the 1989 Macquarie Rise event.

For the first two events, the only horizontal recordings made with an instrument whose passband also contains the frequency of ${}_0T_2$ are the Isabella strain meter records (*Benioff et al. 1961)* and the Trieste tilt meter record (*Bolt and Marussi, 1962*). All the three component seismometers that were deployed following the International Geophysical Year (1957/58) had a passband too narrow to record ${}_0T_2$. Starting in 1969, the first well-calibrated, three component HGLP seismometers were installed. These early instruments together with the subsequent SRO sensors had a rapid fall off at the low-frequency end of the pass band. Even so, the best horizontal recording of the 1977 Indonesian event by an ASRO (a modified HGLP) instrument (ZOBO, E-W) shows a clear peak at the frequency of ${}_0T_4$ and to a lesser extent at the frequency of ${}_0T_3$. No high-quality strain meter recordings of the 1977 Indonesian event are available.

At the beginning of the last decade, major improvements in the design of both the seismic sensors (*Wielandt and Streckeisen, 1982*) and the digital data loggers were achieved so that it became possible to record the entire seismic spectrum relevant to earthquake seismology (from 0.3 mHz to 20 Hz) with a dynamic range of 140dB using a single data stream (*IRIS, 1984*). The wide acceptance of

this new generation of hardware has led to numerous high-quality, three component recordings of both the 1987 Alaskan and 1989 Macquarie rise event.

To search for the presence of the mode ${}_0T_2$ in a time series, we use the multitaper spectral analysis technique developed by *Park et al. (1987)* and *Lindberg and Park (1987)*. This technique is the method of choice as it has been demonstrated to possess superior detection capabilities (*Thomson, 1982*) over single taper estimates.

The main difficulty with detecting a small amplitude harmonic component in a time series of finite length is spectral leakage. When spectra are computed from such time series, the latter are, implicitly or explicitly, being multiplied by a window function (taper). In the frequency domain, this operation is equivalent to convolving the spectrum of the time series with the spectrum of the taper. While the spectrum of any reasonable taper is peaked, the peak must have a finite width and possibly large side lobes. This means that if a time series contains a harmonic, the true spectrum of that time series contains not only energy at the frequency of the harmonic but also at neighboring frequencies. This process is called spectral leakage. The multitaper technique employs a set of tapers that are designed to optimally reduce the spectral leakage of a decaying cosinusoid immersed in white noise. This optimization problem can be cast in terms of a generalized matrix eigenvalue problem with the eigenvectors being the optimal tapers and the eigenvalues being a measure of the efficiency of the tapers to suppress spectral leakage. The tapers are designed to take account of the decay rate of the target mode as well as the variance of the noise and the panel structure of the particular record to be analyzed.

We select the K tapers with the best leakage reduction properties. We multiply the seismogram to be analyzed by these K tapers which results in an equal number of time series. In a least squares procedure, we fit a decaying cosinusoid multiplied by the kth taper to the kth time series. In this way, we obtain K uncorrelated amplitude estimates at every frequency from just one seismogram. We then average the K estimates to obtain a more accurate amplitude estimate than would have been possible with just a single (*e.g.*, Hanning) taper estimate.

A statistical F-test is then performed to test the null hypothesis that the initial amplitude of the decaying cosinusoid vanishes. Conversely, one can use the F-test to measure the likelihood of the presence of a decaying cosinusoid at a given frequency.

In order to compute the optimal tapers, we need an a priori estimate of the decay rate of the target multiplet and the variance of the noise present in the seismic record. The Q value of ${}_0T_2$ can be predicted accurately since this mode samples all parts of the mantle and the average Q value of the mantle is the best constrained property of Q models (*Masters and Gilbert, 1983*; *Widmer et al. 1991*).

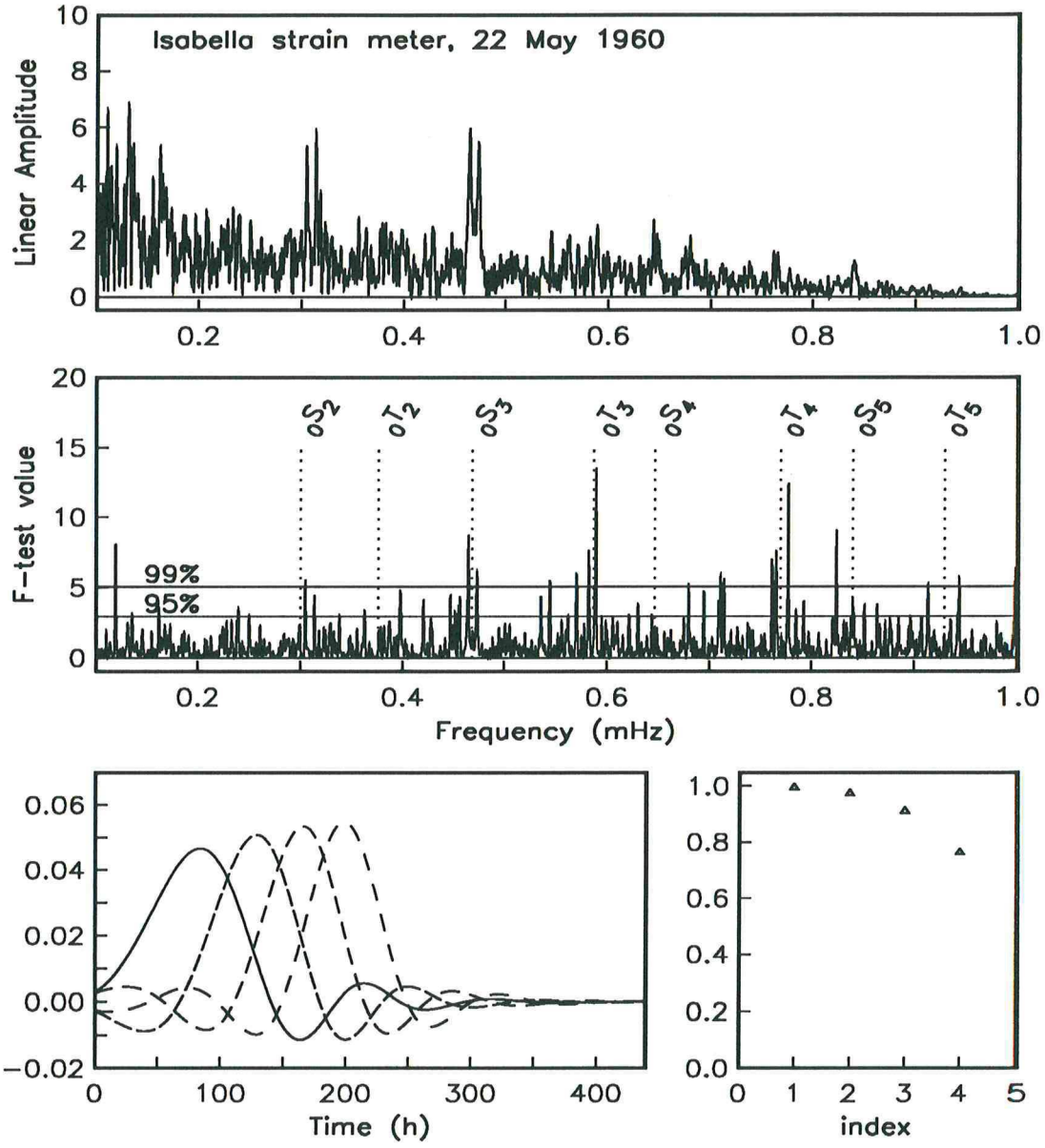

Figure 4.3 Multitaper spectral analysis of the Isabella strain meter record of the 1960 Chilean Earthquake. The multitapers are optimized for the detection of ${}_0T_2$. The top panel shows the estimated amplitude spectrum with ${}_0S_2$ and ${}_0S_3$ forming the largest spectral peaks in the mode band. Both these mutiplets are visibly split due to the Earth's rotation. The middle panel shows the results of the variance ratio F-test. The vertical dashed lines indicate the location of the fundamental mode degenerate frequencies for model 1066A. The two solid horizontal lines indicate the 95 and 99% confidence levels for the presence of a decaying cosinusoid with decay rate $\alpha = 4.3 \times 10^{-6}$ rad/s. While the test is successful for the multiplets ${}_0S_3$, ${}_0T_3$ and ${}_0T_4$, it clearly fails for ${}_0T_2$. The bottom left panel shows the four lowest order eigentapers which were used (design parameters: $\Omega = 8\pi/N$, $\nu = 0.01$). The tapers only sample the first half of the record because of the relatively low quality factor predicted for ${}_0T_2$ ($Q = 275$). The efficiency of the tapers to suppress spectral leakage is measured by the so called bandwidth retention factors shown in the last panel. Only the first four eigentapers were used because the bandwidth retention factor is less than 0.5 for the fifth and all higher order tapers.

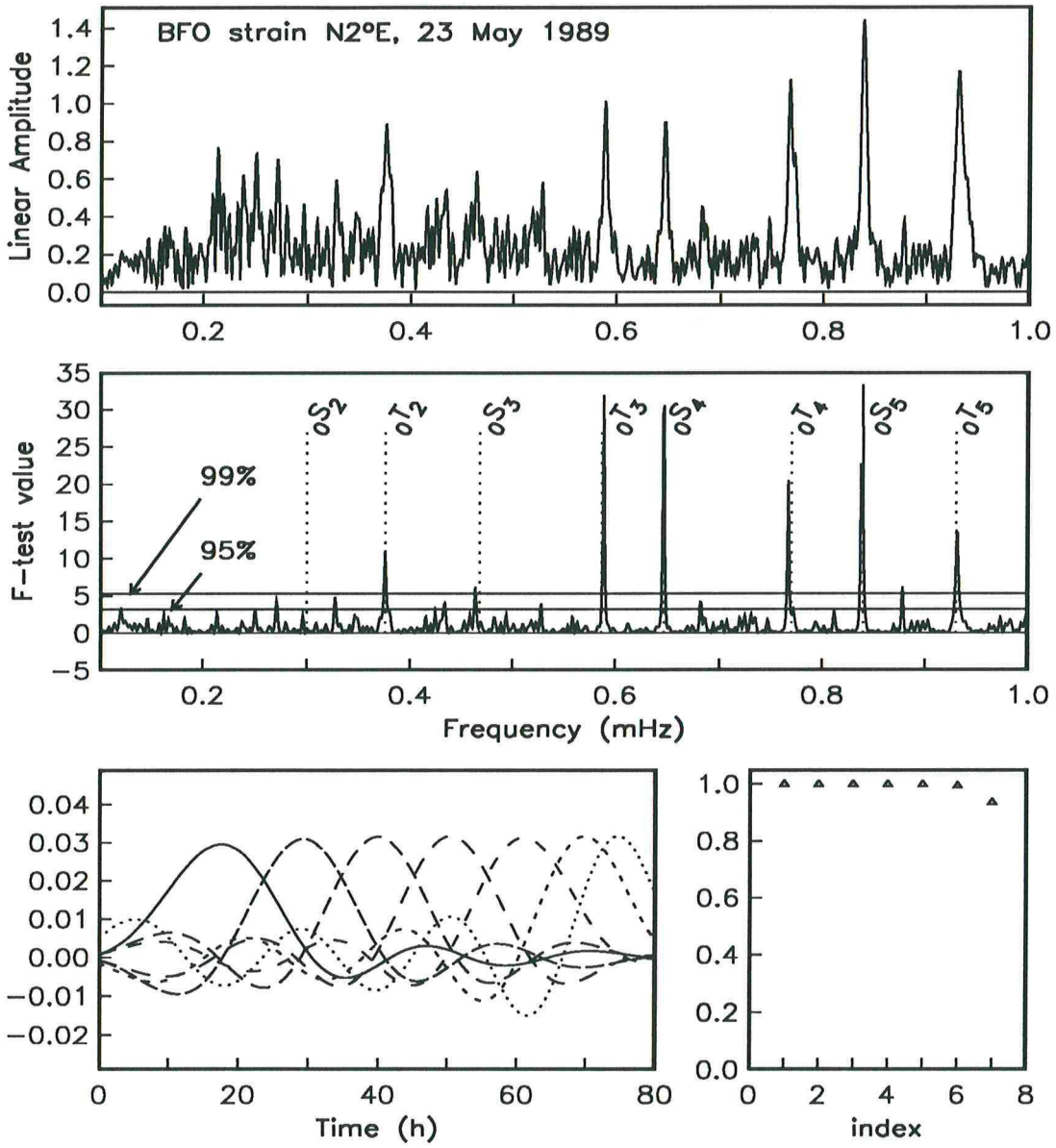

Figure 4.4 Multitaper spectral analysis of the BFO strain meter record of the Macquarie rise earthquake. The multitapers are optimized for the detection of ${}_0T_2$. The top panel shows the estimated amplitude spectrum with ${}_0T_2$, ${}_0T_3$, ${}_0S_4$, ${}_0T_4$ and ${}_0S_5$ forming the largest spectral peaks in the mode band. Mode splitting due to rotation is not visible due to the short record length. The middle panel shows the results of the variance ratio F-test. The vertical dashed lines indicate the location of the fundamental mode degenerate frequencies for model 1066A. The two solid horizontal lines indicate the 95 and 99% confidence levels for the presence of a decaying cosinusoid with decay rate $\alpha = 4.3 \times 10^{-6}$ rad/s. The test fails to detect only ${}_0S_2$. All other fundamental modes have F-test values exceeding the 99% level. The bottom left panel shows the seven lowest order eigentapers which were used (design parameters: $\Omega = 8\pi/N$, $\nu = 0.01$). The tapers sample all parts of the record because the amplitude of ${}_0T_2$ is predicted to decay by only 18% over an 80 hour period. Only the first seven eigentapers were used because the bandwidth retention factor is less than 0.5 for the eighth and all higher order tapers.

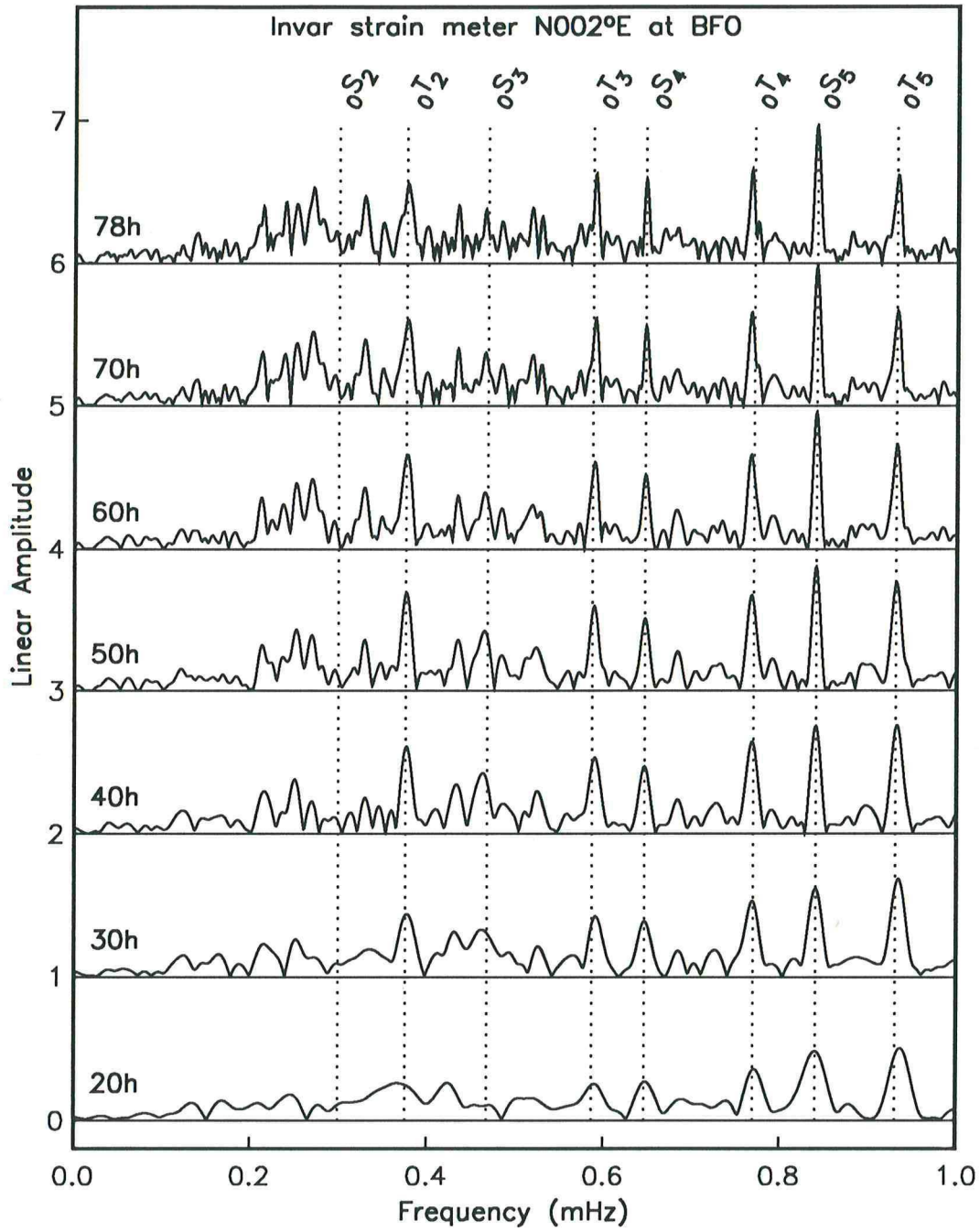

Figure 4.5 Amplitude spectra of the Macquarie rise earthquake recorded with an Invar strain meter at the Black Forest Observatory (BFO). The azimuth of the strain meter is N2°E. The record starts 2 hours after the event and the length of the data segment used to compute the spectra is indicated at the left. A Hanning taper was used and the timeseries was padded with zeroes. The record was truncated at 80 hours due to a severe increase in the ambient noise level caused by atmospheric disturbances at later times. The dashed lines indicate the predicted degenerate frequencies for the fundamental spheroidal and toroidal modes. Note that all fundamental toroidal modes below 1 mHz are excited well above the ambient noise.

mode	n	f [μHz]	$1000/Q$
${}_0T_2$	2	376.60	–
		0.80	–
		0.67	
${}_0T_3$	15	587.26	4.50
		0.66	0.90
		0.33	
${}_0T_4$	35	766.73	3.77
		0.37	0.33
		0.18	
${}_0T_5$	39	928.97	4.92
		0.37	0.30
		0.10	
${}_0T_6$	163	1079.51	4.24
		0.18	0.27
		0.05	
${}_0T_7$	139	1221.50	4.84
		0.30	0.18
		0.01	
${}_0T_8$	193	1356.80	4.82
		0.25	0.16
		0.00	
${}_0T_9$	163	1487.56	5.00
		0.16	0.20
		0.00	
${}_0T_{10}$	182	1614.62	5.42
		0.17	0.26
		0.00	
${}_1T_6$	70	1925.51	3.00
		0.45	0.27
		0.00	

Table 4.1 Multiplet center frequency and Q observations based on the analysis of single record measurements. f and $1000/Q$ are averages of n observations and the errors are obtained by bootstrapping. Note that the center frequencies in this table are not corrected for second order effects of rotation (*Dahlen and Sailor, 1979*). The correction which would have to be added to the center frequency to obtain the degenerate frequency is given in the third row following the error of the center frequency. The center frequency estimates are also uncorrected for the effect of Coriolis coupling and the corrections for the three most strongly coupled modes in this table are given in table 4.2.

Rather than estimating the noise variance ν, we choose to experiment with a range of ν values and base our choice of the final ν on a visual assessment of the estimated amplitude spectra.

Figure 4.3 illustrates the results of the multitaper procedure applied to the 450 hour long Isabella strain meter record of the 1960 Chilean earthquake. In Figure 4.4, the multitaper results are summarized for the much shorter BFO strain meter record of the Macquarie rise event. In Figure 4.5, we use a more conventional method to show the presence of a coherent spectral line at the fundamental mode

mode	f [μHz]	c_2^0	Rec_2^1	Imc_2^1	Rec_2^2	Imc_2^2
${}_0T_8$	1356.56	−6.79	0.1	−2.1	-0.9	2.8
	0.25	1.50	0.7	1.1	0.7	0.9
	0.12	0.49	–	–	–	–
${}_0T_9$	1487.06	−5.26	1.2	−2.5	−0.2	3.6
	0.16	1.30	0.6	0.9	0.7	0.8
	0.25	0.96	–	–	–	–
${}_0T_{10}$	1613.46	−3.04	−1.0	−3.3	0.3	4.3
	0.17	1.30	0.6	0.9	0.7	0.8
	0.50	2.14	–	–	–	–

Table 4.2 Estimated degenerate frequencies and aspherical structure coefficients c_s^t in μHz for selected toroidal modes. To facilitate comparison with the results in table 4.1 and 4.4 we did not correct the degenerate frequency and the c_2^0 coefficients for the effect of Coriolis coupling. For every mode we list in the first row the estimated coefficient followed by the estimated error. The third row contains the Coriolis correction which would have to be added to the values in the first row to get unbiased degenerate frequency and structure coefficient estimates (*Smith and Masters, 1989*).

frequencies by plotting amplitude spectra of variable length, Hanning tapered, data windows.

While we are unable to detect ${}_0T_2$ in the Isabella strain meter record, our test for the presence of a decaying sinusoid in the vicinity of the predicted frequency of ${}_0T_2$ is successful and exceeds the 99% confidence level for the BFO invar strain meter record of the Macquarie rise event. Assuming that our copy of the Isabella strain meter record is a true replica of the original time series and has survived 30 years of storage on computer media unchanged, we conclude that previous claims of ${}_0T_2$ observations were associated with spurious peaks.

To actually measure the degenerate frequency of ${}_0T_2$, we first note that a double-couple source excites the $\pm m$ singlets with equal amplitude. Given the short record length of the BFO strain meter record, we are unable to resolve the splitting of ${}_0T_2$. Since the splitting of this mode is predicted to be entirely dominated by rotation and is thus symmetric about the center frequency, we can expect to get an unbiased estimate of the center frequency if we fit a single resonance function to the data spectrum.

The center frequency estimate for ${}_0T_2$ given in table 4.1 was obtained by fitting synthetic resonance functions to data spectra of variable length and the only traces used are the N2°E and the N300°E BFO invar strain meter records.

As the number of records available per mode increases we can use techniques which make increasingly less restrictive assumptions about the nature of the large-scale aspherical structure.

In table 4.1 we make use of the "Diagonal sum rule" (*Gilbert, 1971*) which states that the average value of the singlet frequencies of a multiplet split by linearly small aspherical perturbations is

the multiplet's degenerate frequency. For the modes ${}_0T_3$ and ${}_0T_4$ the splitting is dominated by rotation and hence the singlets are evenly distributed. Given this condition and a set of records which sample the Earth evenly, the diagonal sum rule implies that peak frequency measurements made from these records average to the degenerate frequency of the multiplet.

For ${}_0T_5$ through ${}_0T_8$, we use the singlet stripping technique which assumes that aspherical structure is dominantly axisymmetric. This technique has already been described in chapter 3 and allows us to estimate the singlet frequencies and from them, by use of the diagonal sum rule, the multiplet degenerate frequency. The distribution of the singlet frequencies can also be compared with the predictions for a rotating Earth model in hydrostatic equilibrium and inferences about non-hydrostatic, axisymmetric structure are possible. We present the results of the singlet stripping experiment in the next section. If we drop the assumption that the large-scale aspherical structure is predominantly axisymmetric, and consider only modes with sufficiently large harmonic degree, we can use *Jordan's (1978)* asymptotic theory and interpret observed center frequency shifts in terms of general aspherical structure along the great circle connecting source and receiver, and obtain for every mode an estimate of both the degenerate frequency and the lowest order aspherical structure coefficients. For the modes ${}_0T_8$, ${}_0T_9$ and ${}_0T_{10}$, we have a sufficient number of peak frequency observations to perform this analysis and the degenerate frequency and the degree $s = 2$ structure coefficients are presented in table 4.2. The dominant heterogeneity sensed by these modes is of degree 2 and in this case, the asymptotic theory works reasonably well for $l \geq 8$.

4.4. Singlet Stripping for ${}_0T_5$ through ${}_0T_8$

The singlet stripping technique was first proposed by *Gilbert (1971)* and successfully applied to a number of spheroidal multiplets by *Buland et al. (1979)*, *Masters and Gilbert (1981)* and *Ritzwoller et al. (1986)*. The goal of singlet stripping is to estimate the resonance functions of all singlets within a multiplet. We call these estimated resonance functions "singlet strips". The singlet frequencies can subsequently be obtained by fitting a synthetic resonance function to the singlet strips (*Masters and Gilbert, 1983)*. Singlet stripping is a phase equalization technique and assumes that we know both the source mechanism and the shape of the singlet eigenfunctions. There exist several procedures to determine the low frequency earthquake source mechanism (*Gilbert and Dziewonski, 1975*; *Dziewonski et al. 1981*; *Romanowicz and Guillemant, 1984*; *Ekström, 1989*) and our prefered solution for the Macquarie Rise event has been presented in section 4.2. Knowledge of the singlet eigenfunctions requires that we know the Earth's aspherical structure. This of course is what we would ultimately like to determine and is

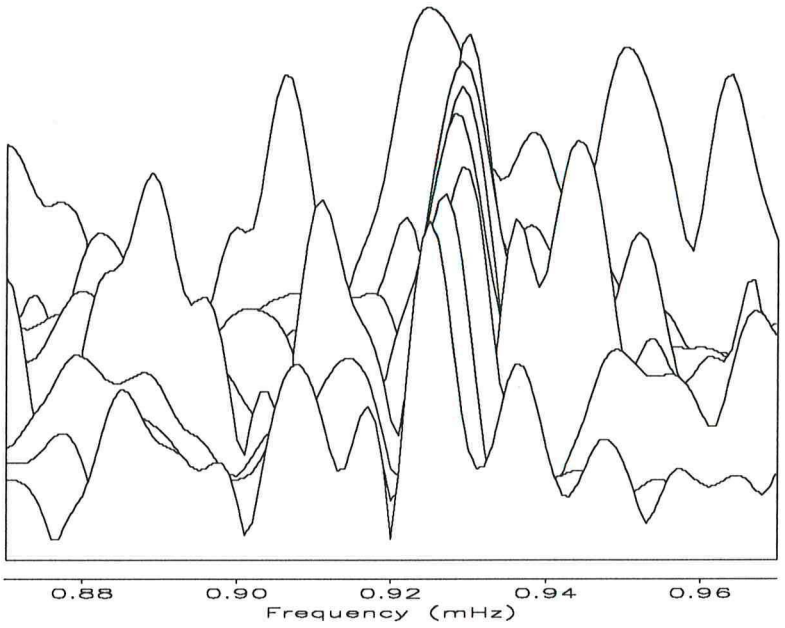

Figure 4.6 Singlet strips for the multiplet ${}_0T_5$. The strips are arranged in ascending order with the one corresponding to the $m = -5$ singlet in front.

not known a priori. In the special case where the deviations from spherical symmetry are dominated by axisymmetric structure such as rotation and ellipticity of figure, the displacement eigenfunction of the mth singlet in the kth multiplet is known and makes singlet stripping possible (Chapter 3). In this case, the ith observed spectrum $u_i(\omega)$, corrected for instrument response and source phase, is a weighted sum of singlet resonance functions $c_j(\omega)$ with the weights A_{ij} being determined by the source and receiver locations, the source mechanism and the singlet eigenfunctions

$$u_i(\omega) = A_{ij}(\omega)c_j(\omega). \tag{4.2}$$

Singlet stripping then consists in solving (4.2) for the unknown resonance functions $c_j(\omega)$. The frequency dependence of the matrix A stems from the finite duration of the earthquake rupture. For a symmetric triangular source time function with the rise time τ as its base length, the frequency dependence of A is proportional to $f(\omega) = sinc^2(\omega\tau/4)$. $f(\omega)$ has a maximum at zero frequency and, if τ = 45 seconds as in the case of the Macquarie rise event, its first zero crossing is at f_o = 44 mHz. This is far beyond the frequency of the modes ${}_0T_5 - {}_0T_8$ so that we are certainly justified in considering A to be frequency independent.

The selection of the records which enter the left-hand side of (4.4) is crucial to the success of the method and we use only records whose amplitude spectra contain a clear peak at the frequency of the

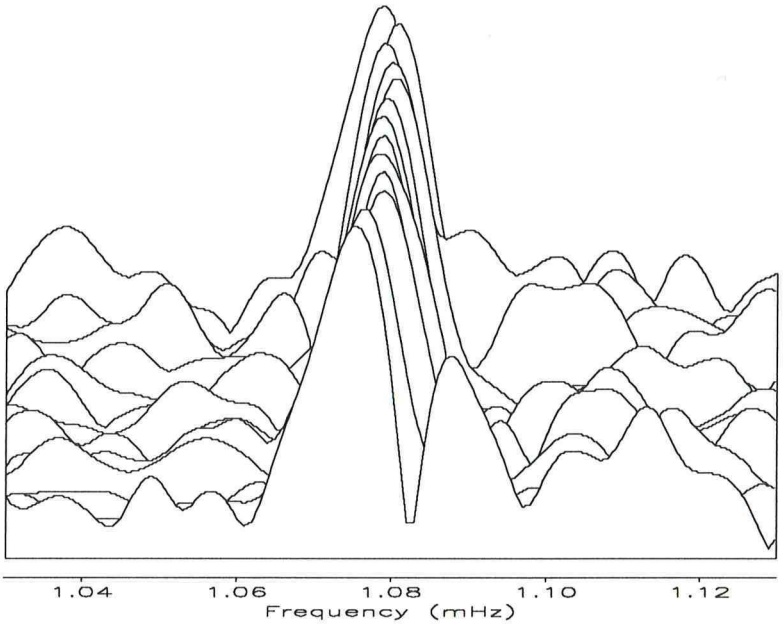

Figure 4.7 Singlet strips for the multiplet ${}_0T_6$. The strips are arranged in ascending order with the one corresponding to the $m = -6$ singlet in front.

target multiplet. Besides the recordings of the Macquarie rise event, we also include any records from our database of digital long-period recordings of large earthquakes since 1977. From the 214 events in this data base we find that the Indonesian event (August 19, 1977) and the Alaskan event (November 30, 1987) were the only other events to excite significantly toroidal modes below ${}_0T_6$.

mode	n	m
${}_0T_2$	2	2
${}_0T_3$	12	17
${}_0T_4$	22	38
${}_0T_5$	28	57
${}_0T_6$	33	175
${}_0T_7$	34	158
${}_0T_8$	41	193

n number of records from Macquarie Rise event

m total number of records

Table 4.3 Composition of the data set. The only records which show ${}_0T_2$ are from two Invar strain meters at the Black Forest Observatory.

Failure of the hypothesis that (3.1) describes the singlet eigenfunctions can be diagnosed based on the outcome of the singlet strips: if the strips have multiple peaks or do not otherwise follow the model of a single resonance function, our assumptions about the singlet eigenfunctions were wrong. The b coefficient in (3.2) results from the first-order effect of the Coriolis force and it can be shown that

it is unaffected by axisymmetric structure (Chapter 3). We can thus compare the b value predicted for a rotating Earth model in hydrostatic equilibrium with the one obtained by fitting a quadratic to the observed singlet frequencies to see whether singlet stripping was successful. The results of fitting a quadradic in m of the form of (3.2) to the singlet frequency estimates are summarized and compared with the predictions for model 1066A *(Gilbert and Dziewonski, 1975)* in table 4.4. The measured b values are less than one standard deviation lower than predicted for 1066A and are thus consistent with the predictions for a rotating Earth in hydrostatic equilibrium.

Figures 4.6 and 4.7 show perspective plots of the singlet strips of ${}_0T_5$ and ${}_0T_6$. The multiplets ${}_0T_6$ and ${}_0T_8$ are well isolated whereas ${}_0T_5$ is close to ${}_1S_3$ and ${}_0T_7$ is close to ${}_0S_7$. In any case, we do not expect these toroidal multiplets to be Coriolis coupled since the harmonic degrees of nearby spheroidal modes differ by more then unity *(Dahlen, 1969)*. It is therefore consistent with our working hypothesis to strip simultaneously for all the singlets of the overlapping multiplets. The low signal-to-noise ratio for the singlet strips of ${}_0T_5$ is due both to the generally low signal-to-noise ratio in the original spectra and the small number of records available (see table 4.3). Attempts to strip for toroidal modes at frequencies lower than ${}_0T_5$ failed due to lack of signal.

In the light of the results of the previous chapter, we try to see if we can use the splitting of the fundamental toroidal modes to constrain the location of the structure responsible for anomalous splitting.

In order to quantify the sensitivity of the low-order fundamental toroidal modes to structure at the base of the mantle we have calculated the effect of changing the ellipticity of the CMB on the c_2^0 structure coefficient. Doubling the ellipticity of the CMB leads to a 1.8 μHz perturbation in c_2^0 for ${}_0T_2$ but only a 0.3 μHz perturbation for ${}_0T_6$. This perturbation is much smaller than both the estimated c_2^0 coefficients and the associated errors given in table 4.2. We are therefore led to conclude that the fundamental toroidal modes studied in this chapter are not sensitive enough to the structure of the CMB and of the lowermost mantle to allow useful bounds to be placed on the location of the structure responsible for anomalous splitting.

Turning our attention to the problem of getting precise estimates of the complex multiplet degenerate frequency, we proceed by assuming that the dominant cause of splitting is rotation and hydrostatic ellipticity and that splitting parameters have the values predicted for model 1066A and solve only for the degenerate frequency. The results of this fit are given in the second column of table 4.4. The error estimates were obtained using a bootstrapping procedure *(Efron and Tibshirani, 1986)*. The degenerate frequencies obtained this way agree well with the results from the histogram analysis (table 4.1).

mode	f [μHz]	$1000/Q$	a [10^{-3}]	b [10^{-3}]	c [10^{-3}]
	929.70	4.16	0.917	0.416	−0.102
${}_0T_5$	928.45	3.89	0.689	0.383	−0.068
	0.24	0.25	0.269	0.079	0.026
	1080.40	4.37	0.923	0.256	−0.069
${}_0T_6$	1078.83	4.01	0.796	0.241	−0.056
	0.18	0.37	0.210	0.052	0.015
	1222.36	4.60	0.926	0.170	−0.051
${}_0T_7$	1220.81	4.66	1.360	0.118	−0.072
	0.24	0.52	0.359	0.052	0.019
	1357.86	4.81	0.961	0.119	−0.038
${}_0T_8$	1356.79	4.95	1.140	0.089	−0.047
	0.25	0.33	0.277	0.041	0.011

Table 4.4 Frequency, Q and splitting parameters of low-order fundamental toroidal modes. For every mode the three lines contain (from top to bottom) the predictions for model 1066A, the observed values and their associated errors. The predicted rotational and elliptical splitting parameters are taken from *Dahlen and Sailor, 1979* and include all terms through second order in rotation and first order in ellipticity. The Q prediction in the third column are based on the Q model by *Masters et al. (1983)*.

Q measurement of broadly split multiplets from single records exhibit large scatter due to the beating between the singlets. Singlet stripping turns out to be very successful in removing this source of scatter and we can reliably estimate the Q of the multiplet by averaging the Q values obtained from the singlet strips. The third column of Table 4.4 compares the observed Q values with the prediction of the Q model of *Masters et al. (1983)*.

4.5. Conclusion

With a scalar moment $m_o = 16 \pm 4 \times 10^{20}$ Nm, the Macquarie rise event was the largest earthquake of the last decade. The strike slip source mechanism means that this event was very efficient at exciting toroidal free oscillations. We have used very long-period recordings of the horizontal ground acceleration and strain in the wake of this earthquake to study the lowest order fundamental toroidal modes. Using the singlet stripping technique, we have resolved the splitting of the modes ${}_0T_5$ through ${}_0T_8$ and estimated the singlet frequencies. The large number of peak frequency measurements available for the modes ${}_0T_8$ through ${}_0T_{10}$ has allowed us to estimate degree $s = 2$ aspherical structure coefficients for these modes. We have estimated the degenerate frequency for all fundamental toroidal modes up to ${}_0T_{10}$. Our observations of the modes ${}_0T_3$ through ${}_0T_9$ are consistent with earlier observations by *Dziewonski and Gilbert (1972, 1973)* and our error estimates are between 1.5 and 4 times smaller.

The large Coriolis correction for the mode ${}_0T_{10}$ make our degenerate frequency estimate incompatible with earlier estimates. For ${}_0T_2$ our degenerate frequency estimates differs by 2 μHz or three standard deviations from the value given by *Derr, (1969)*. Our attempt to confirm earlier observations of the mode ${}_0T_2$ based on the Isabella strain meter recording have failed and we believe that the BFO invar strain meter recordings of the Macquarie rise event have led to the first unambiguous observations of this mode. The precision of the degenerate frequency estimates presented here make it necessary to correct for second order effects before they can be used as gross Earth data in an inversion for the spherically averaged Earth structure. We find no sign of anomalous splitting of the low order toroidal modes but their sensitivity to aspherical structural perturbations near the base of the mantle is too weak to rule out the possibility (based on these observations) that the structure responsible for anomalous splitting is on the mantle side of the CMB.

References

Backus, G.E., Interpreting the seismic glut moments of total degree two or less. *Geophys. J. R. Astron. Soc.*, **51**, 1–25, 1977.

Backus, G.E., and J.F. Gilbert, The rotational splitting of the free oscillations of the earth. *Proc. Natl. Acad. Sci.*, **47**, 362–371, 1961.

Backus, G.E., and M. Mulcahy, Moment tensors and other phenomenological descriptions of seismic sources I. Continuous displacements. *Geophys. J. R. Astron. Soc.*, **46**, 341–362, 1976.

Benioff, H., F. Press, and S.W. Smith, Excitation of the free oscillations of the earth by earthquakes. *J. Geophys. Res.*, **66**, 605–619, 1961.

Bolt, B. A., and A. Marussi, Eigenvibrations of the Earth observed at Trieste. *Geopys. J.*, **6**, 299–311, 1962.

Braunmiller, J., and J. Nábělek, Rupture Process of the Macquarie Ridge Earthquake of May23, 1989. *Geophys. Res. Lett.*, **17**, 1017–1020, 1990.

Buland, R., J. Berger, and F. Gilbert, Observations from the IDA network of attenuation and splitting during a recent earthquake. *Nature*, **277**, 358–362, 1979.

Dahlen, F.A., The normal modes of a rotating, elliptical earth. *Geophys. J. R. Astron. Soc.*, **16**, 329–367, 1968.

Dahlen, F.A., The normal modes of a rotating, elliptical earth-II, Near-resonance multiplet coupling. *Geophys. J. R. Astron. Soc.*, **18**, 397–436, 1969.

Dahlen, F.A., The effect of data windows on the estimation of free oscillation parameters. *Geophys. J. R. Astron. Soc.*, **69**, 537–549, 1982.

Dahlen, F.A., and R.V. Sailor, Rotational and elliptical splitting of the free oscillations of the earth. *Geophys. J. R. Astron. Soc.*, **58**, 609–623, 1979.

Derr, J. S., Free Oscillation Observation through 1968. *Bull. Seism. Soc. A.*, **59**, 2079–2099, 1969.

Dziewonski, A.M., T.A. Chou, and J.H. Woodhouse, Determination of earthquake source parameters from waveform data for studies of global and regional seismicity. *J. Geophys. Res.*, **36**, 2825–2831, 1981.

Dziewonski, A.M., and J.F. Gilbert, Observations of normal modes from 84 recordings of the Alaskan earthquake of 28 March 1964. *Geophys. J. R. Astron. Soc.*, **27**, 393–446, 1972.

Dziewonski, A.M., and J.F. Gilbert, Observations of normal modes from 84 recordings of the Alaskan earthquake of 28 March 1964 II. *Geophys. J. R. Astron. Soc.*, **35**, 401–437, 1973.

Efron, B., and R. Tibshirani, Bootstrap methods for standard errors, confidence intervals, and other measures of statistical accuracy. *Statistical Science*, **1**, 54–77, 1986.

Ekström, G., A very broad band inversion method for the recovery of earthquake source parameters. *Tectonophysics*, **166**, 73–100, 1989.

Ekström, G., and B. Romanowicz, The 23 May 1989 Macquarie Ridge Earthquake: A very Broed Band Analysis. *Geophys. Res. Lett.*, **17**, 993–996, 1990.

Gilbert, F., The diagonal sum rule and averaged eigenfrequencies. *Geophys. J. R. Astron. Soc.*, **23**, 119–123, 1971.

Gilbert, F., and A.M. Dziewonski, An application of normal mode theory to the retrieval of structural

parameters and source mechanisms from seismic spectra. *Phil. Trans. R. Soc. Lond.*, **A278**, 187–269, 1975.

IRIS (Incorporated Research Institutions for Seismology), *Science Plan for a New Global Seismographic Network*. Washington, D.C., 1984.

Jordan, T.H., A procedure for estimating lateral variations from low-frequency eigenspectra data. *Geophys. J. R. Astron. Soc.*, **52**, 441–455, 1978.

Lindberg, C.R., and J. Park, Multiple-taper spectral analysis of terrestrial free oscillations: Part II. *Geophys. J. R. Astron. Soc.*, **91**, 795–836, 1987.

Müller, T., and W. Zürn, Observation of Gravity Changes During the Passage of Cold Fronts. *J. Geophysics*, **53**, 155–162, 1983.

Masters, G., and F. Gilbert, Structure of the inner core inferred from observations of its spheroidal shear modes. *Geophys. Res. Lett.*, **8**, 569–571, 1981.

Masters, G., and F. Gilbert, Attenuation in the earth at low frequencies. *Phil. Trans. R. Soc. Lond.*, **A308**, 479–522, 1983.

Masters, G., J. Park, and F. Gilbert, Observations of coupled spheroidal and toroidal modes. *J. Geophys. Res.*, **88**, 10,285–10,298, 1983.

NEIC, Preliminary Determination of Epicenters. *US Geological Survey*, , 1989.

Park, J., C.R. Lindberg, and D. Thomson, Multiple-taper spectral analysis of terrestrial free oscillations: Part I. *Geophys. J. R. Astron. Soc.*, **91**, 755–794, 1987.

Ritzwoller, M., G. Masters, and F. Gilbert, Observations of anomalous splitting and their interpretation in terms of aspherical structure. *J. Geophys. Res.*, **91**, 10,203–10,228, 1986.

Romanowicz, B., and G. Ekström, Macquarie earthquake of May 23,1989. *EOS, Trans. Am. Geophys. Soc.*, **65**, 700, 1989.

Romanowicz, B., and P. Guillemant, An experiment in the retrieval of depth and source parameters of large earthquakes using very long-period Rayleigh wave data. *Bull. Seism. Soc. Am.*, **74**, 417–437, 1984.

Smith, M.F., and G. Masters, The effect of Coriolis coupling of free oscillation multiplets on the determination of aspherical earth structure. *Geophys. Res. Lett.*, **16**, 263–266, 1989.

Smith, M.F., and G. Masters, Aspherical structure constraints from free oscillation frequency and attenuation measurements. *J. Geophys. Res.*, **94**, 1953–1976, 1989.

Sorrells, G. G., A preliminary Investigation into the Relationship between Long-Period Seismic Noise and Local Fluctuations in the Atmospheric Pressure Field. *Geophys. J. R. astr. Soc.*, **26**, 71–82, 1971.

Tanimoto, T., Long-wavelength S-velocity structure throughout the mantle. *Geophys. J. Int.*, **100**, 327–336, 1990.

Thomson, D.J., Spectrum estimation and harmonic analysis. *IEEE Proc.*, **70**, 1055–1096, 1982.

Widmer, R., G. Masters, and F. Gilbert, Spherically symmetric attenuation within the Earth from normal mode data. *Geophys. J. Int.*, **104**, 541–553, 1991.

Wielandt, E., and G. Streckheisen, The leaf spring seismometer: design and performance. *Bull. Seismol. Soc. Am.*, **72**, 2349–2368, 1982.

Chapter 5

Spherically Symmetric Attenuation within the Earth from Normal Mode Data

Abstract

Observations of the attenuation of free oscillations after large earthquakes are used to determine the spherically symmetric dissipative structure within the Earth. We model intrinsic attenuation of seismic energy between 0.3 and 10 mHz with a frequency independent Q model. The resolving power of our data indicates that simple models of Q can explain our observations and that we do not have enough information to constrain detailed absorption band models.

The average shear Q is relatively well constrained for the mantle and is $250\pm2\%$. The shear Q in the inner core is mostly constrained by new observations of $PKIKP$ equivalent modes and is $110\pm25\%$. This is lower than in some previous models, which have used possibly erroneous observations of core modes, though the new models still predict too little attenuation to match the observations of strong differential attenuation of the BC and DF branches of PKP at frequencies of about 1 Hz. Agreement between the mode and body-wave datasets should probably not be expected since it now seems likely that the $PKIKP$ data sense an absorption band which is distinct from that sensed by the mode data.

The distribution of bulk attenuation in the Earth remains ill-constrained though bulk attenuation is required somewhere to explain the attenuation of the radial modes. Successful models tend to put significant bulk Q in the upper mantle.

5.1 Introduction

Accurate determination of modal attenuation is difficult for two reasons. *Dahlen (1976)* has shown that, if the complex frequency $\omega + i\alpha$ of a mode is measured with a least squares estimator, the relative standard deviation in the attenuation, α, is $2Q$ times larger than the relative standard deviation in frequency. Here, $Q = \omega/2\alpha$ is the quality factor of the mode. Since typical modal Q values lie between 10^2 and 10^3, we expect measured Q values to be between 200 and 2000 times less precise than the corresponding frequencies. Clearly, the elastic structure of the Earth will always be much better known than the anelastic structure.

The second difficulty is due to the effect of aspherical structure which produces beating between the singlets within a multiplet. This beating effect leads to a large scatter in frequency and apparent attenuation measurements though the average value of many measurements of apparent attenuation appears to be an unbiased estimate of the mean attenuation of the mode *(Davis, 1985)*. This means that aspherical structure can essentially be regarded as a source of noise in estimates of mean attenuation, though it must be emphasized that it is a source with large variance and attenuation values based on small numbers of measurements must be suspect.

Since fundamental modes generally constitute the largest signal in low-frequency spectra, they have been extensively studied and apparent shifts of the center frequencies of such modes have been used to constrain the large-scale lateral variation of the elastic structure in the upper mantle (*Masters et al. 1982*; *Davis 1987*; *Romanowicz et al. 1987*). *Smith and Masters (1989a)* have extended the analysis to model the interference effects of aspherical structure on the measured apparent attenuation and have simultaneously estimated the structure coefficients (*Ritzwoller et al. 1986*, equation 5b) for elastic and anelastic structure. A product of their analysis is a set of reliable estimates of the mean frequency and attenuation of the modes. An attempt to model the variation in the attenuation measurements of spheroidal fundamental modes has shown that by estimating degree 2 Q structure simultaneously with the elastic structure yields only a 2.1% variance reduction over models which do not allow for lateral variation of Q (*Smith and Masters, 1989a*). This is disappointing since degree 2 elastic structure is responsible for over 60% of the variance in the frequency shift observations.

Rather than trying to resolve higher degree lateral Q structure, the goal of this study is to use the relatively well-known mean attenuation rates to determine a new radially symmetric Q model. We begin by discussing a new mean modal attenuation dataset consisting of our own observations and

selected measurements from the literature. A resolving power analysis indicates that we still have very few independent constraints on attenuation structure and also suggests how best to parameterize our model. Finally we invert the observations using various techniques. Differences between the resulting models can be attributed to the particular choice of a model norm whereas similarities can be interpreted as features preferred by the data.

5.2 The Q dataset

We have collected the most reliable Q measurements from the literature and augmented this data set with many new measurements of our own. Most of our final Q values are based on the application of several measurement techniques to datasets of many hundreds of records. Such large-scale experiments are necessary to assess the often dramatic effects of aspherical structure on the apparent attenuation of a mode.

For the fundamental modes ${}_0S_7$-${}_0S_{52}$ and ${}_0T_{11}$-${}_0T_{37}$, we have chosen to use the results of *Smith and Masters (1989a, 1990)*. Their mean attenuation estimates are averages of between 600 and 1500 individual measurements per spheroidal mode and between 100 and 250 per toroidal mode. The basic measuring technique consists of fitting a synthetic resonance function to single data spectra in a narrow frequency band around the target mode *(Masters and Gilbert, 1983)*. The free parameters in this procedure are the complex initial amplitude and the complex frequency. No use is made of the source mechanism to predict the initial phase or amplitude. After interactively assigning a signal-to-noise level, the error in the measurement of the complex frequency is computed following *Dahlen (1982)*. Elastic and anelastic structure coefficients as well as the complex degenerate frequency of the mode can be simultaneously estimated from such observations. The resulting mean attenuation rates have been corrected for the effects of Coriolis coupling (*Masters et al. 1983; Smith and Masters, 1989b*). This correction is typically 10% but can be as large as 25%; the modes which have been corrected are noted in Appendix A. The approximations used in the analysis by *Smith and Masters (1989b)* are not valid for very-low frequency fundamental modes, and we resort to two different techniques. We either use singlet stripping (*Gilbert, 1971a*; *Buland et al. 1979*) and average the Q observations obtained from the singlet strips or we simply use a bootstrapping technique (*Efron and Tibshirani, 1986*) to estimate the mean Q value from the single record measurements.

In principle, we could use the measurements of Q of individual singlets retrieved by the singlet-stripping algorithm to constrain lateral variations in attenuation structure. Usually, the precision of the

measurements is insufficient to allow this to be done. In the case of ${}_0S_2$, the rotational splitting of the multiplet is large enough to completely separate the individual singlets in frequency. *Tanimoto (1990)* has used the apparent variation of the singlet Q values of this mode to infer large-scale aspherical anelastic structure in the lower mantle. Using the same data as Tanimoto, we find that the singlet Q values of this mode depend strongly on record length used in the analysis suggesting that an analysis in terms of aspherical Q structure may be premature. The average Q of the singlets of a multiplet does, however, seem to be robustly determined by the data thereby allowing retrieval of spherically-averaged Q structure.

Individual Q observations are difficult to make for fundamental modes with frequencies higher than about 6 mHz because of significant overlap with nearest neighbors and our estimates of the mean attenuation are correspondingly less precise. A few relatively high l overtones which can be observed on individual spectra can be treated using the same techniques as for fundamental modes and are included in the final dataset.

We use the measurements of *Riedesel et al. (1980)* for the radial modes ${}_0S_0$ and ${}_1S_0$. The modes ${}_2S_0$ through ${}_9S_0$ have been observed on individual spectra and by using multiplet stripping techniques (*Gilbert and Dziewonski, 1975*). The Payson (Arizona) recording of the 1970 Colombian Earthquake made by W.E. Farrell is a particularly rich source of radial mode measurements. Radial mode Q values show little scatter since there is no beating between singlets as with other modes. Some of the radial modes may be weakly coupled to nearby modes (*Park, 1990*) which may lead to a small bias in their Q values though this bias is hard to assess in the absence of a comprehensive 3-D model of the Earth.

At frequencies higher than about 6 mHz, the identification of individual modes on single record spectra becomes nearly impossible due to the large overlap between adjacent modes. The only exceptions are the high Q, $PKIKP$-equivalent modes since they are coarsely spaced in frequency and generally decay slower than neighboring modes. We find that all $PKIKP$ modes with l greater than one are observably split and we have made separate Q measurements of all distinct spectral peaks. The interference between the singlets of such a multiplet leads to a large scatter in such measurements yet our estimated mean Q values are in good agreement with our own singlet stripping results and the results of *Giardini et al. (1988)*. The latter use an iterative spectral fitting technique to model the shape of the spectrum taking both the effect of 3-D elastic and 1-D anelastic structure into account. Figure 5.1 shows a perspective view of a collection of amplitude spectra from which we have measured frequency and Q of the mode ${}_{18}S_4$ while Figure 5.2 illustrates the results of performing singlet stripping. Figure 5.3 (upper panel) shows a histogram of Q measurements for the same mode made from individual recordings. The mean Q value of these measurements is in excellent agreement with the mean of the Q's measured

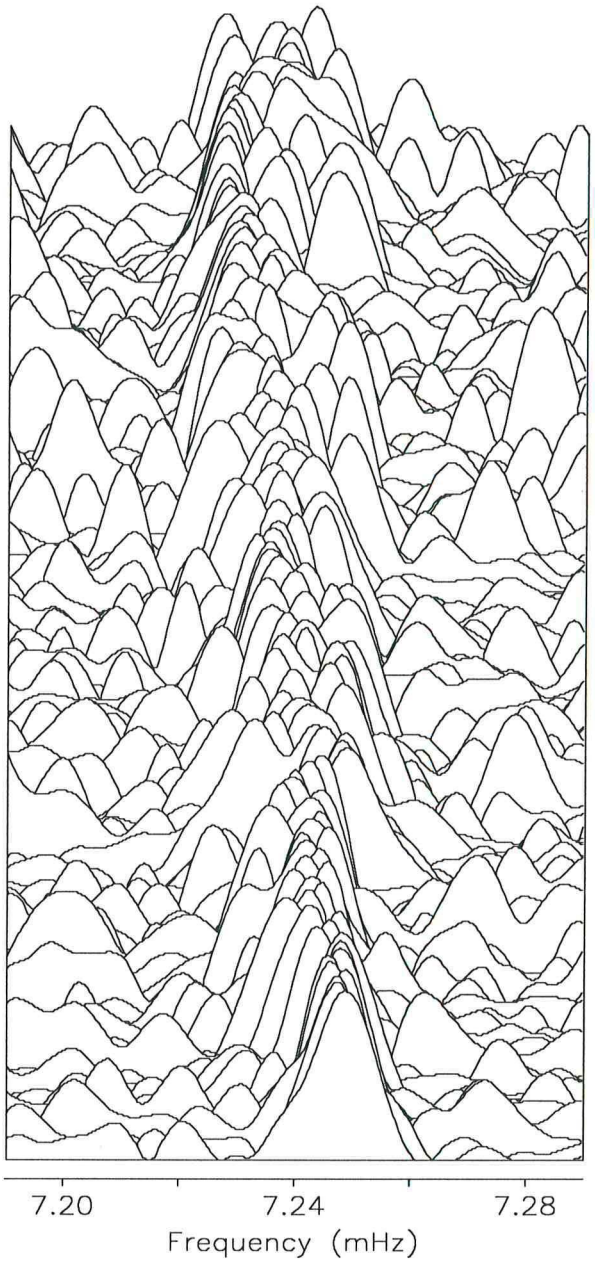

Figure 5.1 A perspective view of 140 amplitude spectra for the mode ${}_{18}S_4$. The spectra have been sorted according to the latitude of the recording stations: spectra recorded at polar stations are in front and spectra from equatorial stations are in the back. The fact that high-latitude stations show only one spectral peak at the high-frequency end of the multiplet is suggestive of splitting dominated by axisymmetric structure.

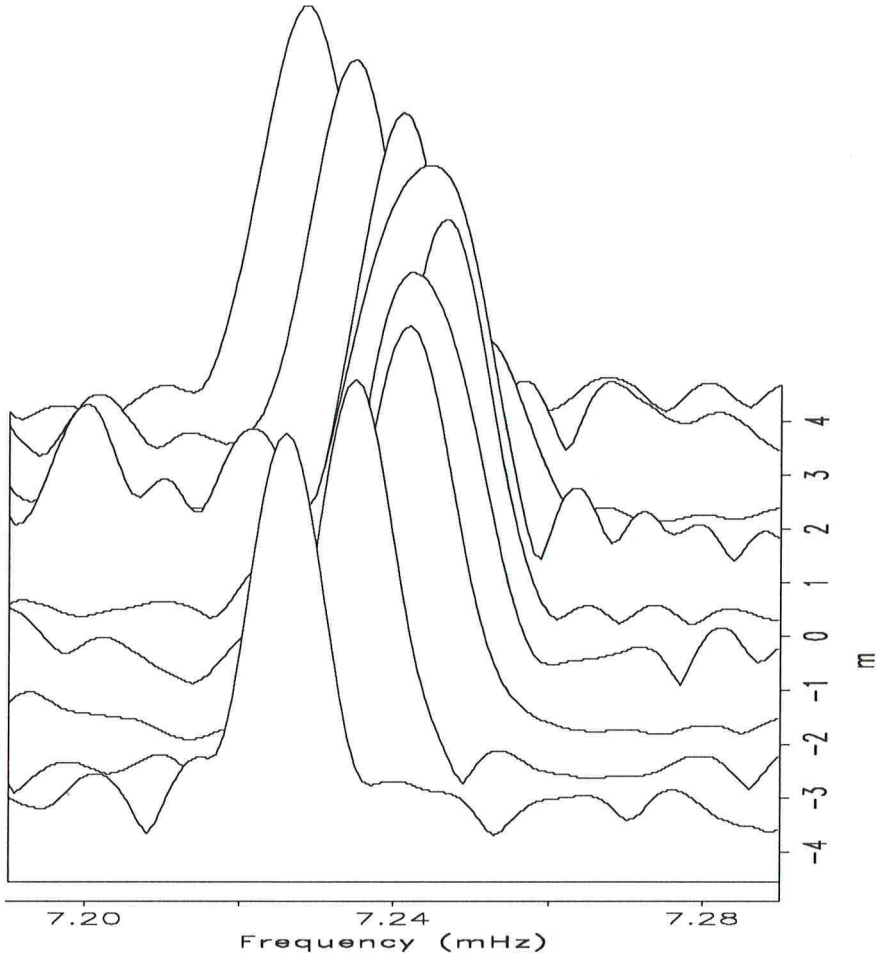

Figure 5.2 Amplitude spectra of the estimated singlet resonance functions of ${}_{18}S_4$.

from the singlet strips (lower panel) and gives us confidence in our results. In the case of high Q modes where we could not get enough observations from single records and singlet stripping failed, we used the results of *Giardini et al. (1988)*. Note that we have chosen to omit the modes ${}_{10}S_2$ and ${}_{12}S_8$ from the inversion experiments described in the next section since the eigenfunctions of these modes vary quite strongly with the choice of reference Earth model.

The use of multiple record techniques such as multiplet stripping and stacking *(Gilbert and Dziewonski, 1975)* is required to isolate most of the remaining modes below 10 mHz. These techniques have proven to be very successful in detecting modes that can not be unambiguously identified on single recordings. Unfortunately, Q measurements made from the resulting multiplet strips are biased low *(Dahlen, 1979)*. In an experiment with synthetic data, we have been able to show that the magnitude of this bias regularly exceeds the size of the measurement error. In the case of fundamental modes and

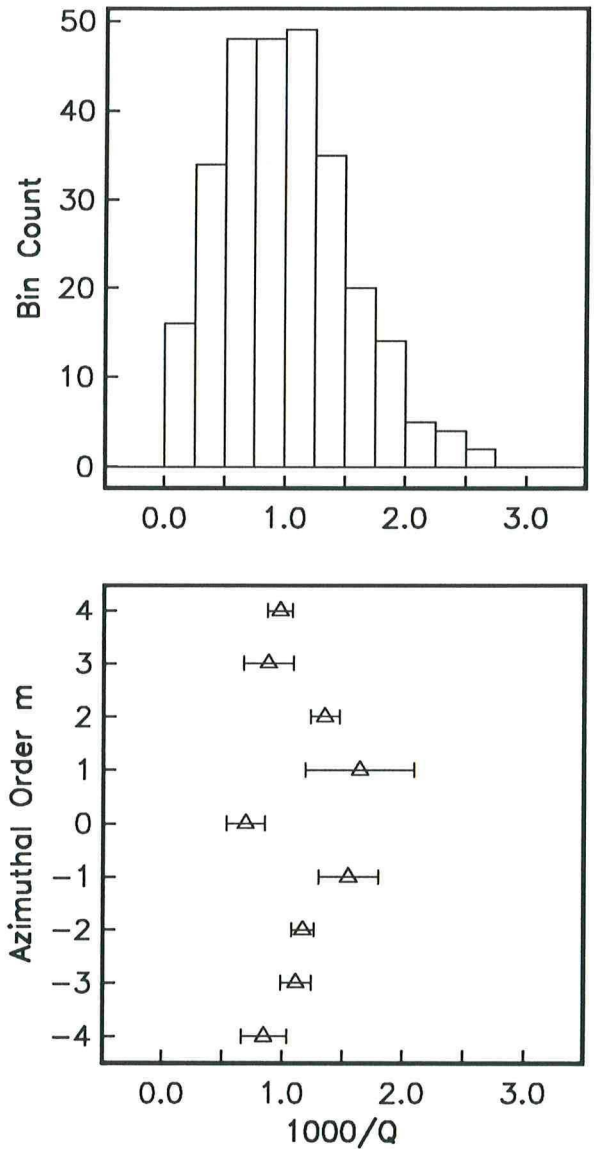

Figure 5.3 Histogram of the Q measurements (top panel) for the mode ${}_{18}S_4$. Mean and median are 1.044 ± 0.030 and 0.971 ± 0.032 respectively. The errors have been determined using the bootstrapping technique. The lower panel shows the scatter of the estimated attenuation and 1 σ errors for the singlets of the same mode. Averaging over all singlets we estimate the q of the multiplet to be 1.075 ± 0.062.

a small number of spheroidal overtones we are able to estimate the bias without the use of a synthetic experiment. We simply compare the Q measurements of the multiplet stripping technique with the (unbiased) means of single record measurements. This comparison shows that the bias towards low Q varies between 20% and 40%. These observations therefore place lower bounds on Q and could be incorporated as such into the inversions for Q structure. This bias is sufficiently large that little additional information is gained by using the multiplet strip measurements so they have not been included in the final

dataset. Indeed, the models presented in the next section are all consistent with bounds provided by the multiplet strip data. Some authors *(Okal and Jo, 1990)* have chosen to correct the bias in Q measurements from stacks by using the predictions of low-order models of the three-dimensional structure of the Earth. They estimate the bias to be about 12% for model M84A *(Woodhouse and Dziewonski, 1984)* which is much smaller than the bias that we observe for fundamental modes. This is probably due to the lack of short wavelength structure in the available mantle models. This suggests that correction of the bias in multiplet stack or strip Q measurements cannot be reliably done given the current status of knowledge of 3-D mantle structure.

It has recently been pointed out that, in the presence of anelasticity, the normal modes of a spherically-symmetric model can be coupled if they are of the same type and harmonic degree (*Lognonné, 1989*; *Tromp and Dahlen, 1990*). This can result in perturbations to the apparent attenuation rates though calculations show that none of the observed modes have their Q values significantly affected. The only current exception to this is the mode ${}_{12}S_8$ which has already been dropped from the dataset since its character is a strong function of inner-core structure.

Appendix A gives the center frequency and attenuation measurements used in our inversion experiments. The dataset consists of 9 radial modes, 55 fundamental spheroidal modes, 30 fundamental toroidal modes and 52 spheroidal overtones (30 of which are sensitive to the structure of the core). We have not included the core modes ${}_6S_2$ and ${}_7S_3$ which were first thought to be observed by *Masters and Gilbert (1981)* and, more recently, by *Fukao and Suda (1989)*. Masters and Gilbert originally felt sure of the identification of these observations because no other mode was known to exist at the frequencies at which these clear, high Q spectral lines were observed. It was later found that Coriolis coupling leads to energy on vertical component recordings at toroidal mode frequencies over a large frequency band (*Masters et al. 1983*). Unfortunately, both ${}_6S_2$ and ${}_7S_3$ are at potentially coupled toroidal mode frequencies and so may be misidentified. It might be argued that the high Q of the observations mitigates against them being dominantly fundamental toroidal mode energy but we have often observed "high Q" components of supposedly low Q modes. We illustrate this in Figure 5.4. This Figure shows a frequency band containing three fundamental spheroidal modes, a high Q radial mode and some high Q overtones. One of the fundamental modes is close to the possible frequency of the core mode ${}_{11}S_2$. Spectra of lagged time windows show many of the lines apparently growing relative to the radial mode ${}_4S_0$, which has a Q of about 1200. Naively, one would say that these lines must have a higher Q than 1200 but note that *all* the lines at fundamental spheroidal mode frequencies appear to grow relative to the radial mode. A measurement of Q gives a very uncertain value of about 3000 for these modes yet there are no high

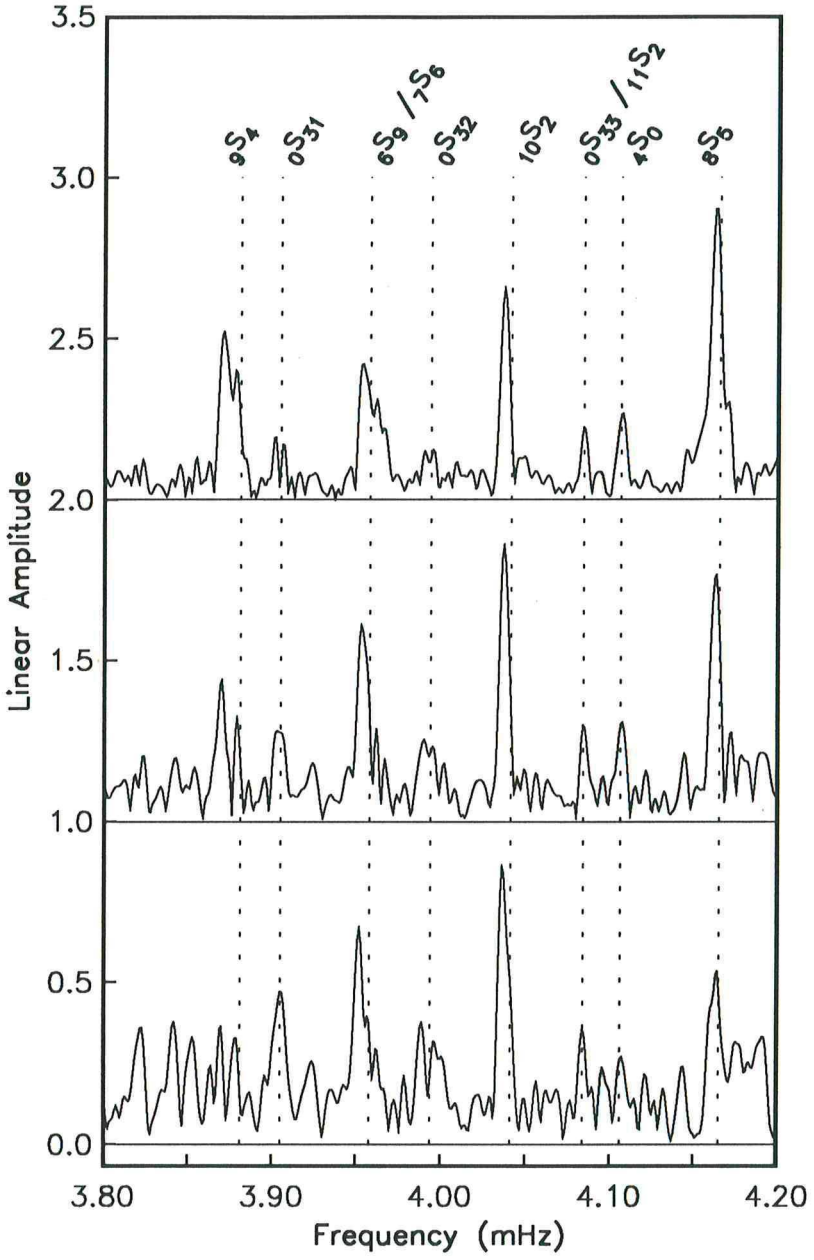

Figure 5.4 Linear amplitude spectra of 100 hours of data recorded at the IDA station SUR after the Tonga earthquake of June, 1977. The top panel is of a data segment starting 5 hours after the event, the middle panel starts 10 hours later while the lower panel starts 10 hours later yet. Note how lumps of energy persist at fundamental spheroidal mode peak frequencies and actually grow relative to the high Q radial mode ${}_4S_0$. This suggests that supposedly low Q modes can have weak apparently high Q components which can potentially be confused with "core modes" (such as ${}_{11}S_2$).

Q overtones at the frequencies of ${}_0S_{31}$ and ${}_0S_{32}$. At present, we do not have a completely satisfactory explanation of this behavior though it is possibly just an artifact of the extremely low signal levels with which we are working. These results do indicate that an identification of a core mode based on a Q argument must be treated with suspicion.

5.3 Inversion

It is convenient to work with inverse Q rather than Q itself and we follow *Masters and Gilbert, (1983)* and define as our datum $q_i = 1000/Q_i$. The model is defined as the pair of functions $q_\mu(r)$, $q_\kappa(r)$ where $q_\mu \equiv 1000/Q_\mu$ and similarly for q_κ . Under the assumption that the elastic structure is sufficiently well-known and that the elastic energy densities of the modes can be computed, we have a linear inverse problem to solve of the form:

$$q_i = \int_0^a [K_i(r)q_\kappa(r) + M_i(r)q_\mu(r)]\, dr. \tag{5.1}$$

The kernels K_i and M_i are proportional to the compressional and shear energy density of the i-th mode and can be computed for a given radially symmetric distribution of the density and elastic moduli within the Earth (*Backus and Gilbert, 1967*). We use model 1066A *(Gilbert and Dziewonski, 1975)* as a reference elastic model though the choice is unimportant for the vast majority of modes. (A few modes have characteristics which are a strong function of inner core structure but these have been elliminated from the data set.) The class of possible solutions to (5.1) is limited by the requirement that energy be dissipated at all depths which is equivalent to the condition

$$q_\kappa, q_\mu \geq 0. \tag{5.2}$$

The determination of the q_κ and q_μ structure from modal Q values is an extremely poorly conditioned inverse problem. The reason for this is that the relatively low precision of the data means that many of our observations do not place independent constraints on the model. This problem is further aggravated by the fact that most of the observations in our data set come from fundamental spheroidal and toroidal modes whose energy distribution is dominated by shear energy in the upper mantle and whose radial sensitivity is mainly confined to the upper mantle. Very few of our observations are at all sensitive to bulk attenuation, the only exception being the radial modes, and as a consequence q_κ is much more poorly constrained than q_μ. We use the ranking and winnowing procedure of *Gilbert, (1971b)* to determine the

number of independent constraints on the model provided by the dataset (we call these significant Earth data or "sEd"). We find that there are only six sEd with a relative error of less than 10% and 29 sEd with a relative error of less than 50%. With this number of independent constraints, it is hard to justify looking for complex models of dissipative structure and we have chosen to consider only those models where Q can be regarded as independent of frequency over the frequency range of our observations.

In a first experiment, we look for internal consistency in our dataset. To do this, we parameterize the model with a large number of layers of constant q. Given the small number of sEd, our problem is underdetermined as long as we do not impose any additional constraints on the model. If our data are consistent and our error estimates realistic we should be able to fit the observations on average to within one standard deviation. We discretize the model by

$$\left.\begin{aligned} q_\kappa(r) &= m_j \\ q_\mu(r) &= m_{j+L} \end{aligned}\right\} \quad r_{j-1} \le r < r_j, \qquad j = 1, \ldots, L \tag{5.3}$$

and define

$$G_{ij} = \int_{r_{j-1}}^{r_j} K_i(r)\, dr \quad \text{and} \quad G_{ij+L} = \int_{r_{j-1-L}}^{r_{j-L}} M_i(r)\, dr \qquad j = 1, \ldots, L \tag{5.4}$$

Taking our observed data as $q_i \pm \epsilon_i$ we have

$$\sum_{j=1}^{2L} G_{ij} m_j = q_i \pm \epsilon_i \qquad i = 1, \ldots, N \tag{5.5}$$

Normalizing every datum q_i and its corresponding row in G by the error ϵ_i we have

$$b_i = q_i/\epsilon_i \qquad H_{ij} = G_{ij}/\epsilon_i \tag{5.6}$$

$$\sum_{j=1}^{2L} H_{ij} m_j = b_i \quad \text{standard deviation} \quad 1 \tag{5.7}$$

In matrix notation, the problem to be solved is then

$$\text{minimize} \quad \|\mathbf{Hm} - \mathbf{b}\| \qquad \text{subject to} \quad \mathbf{m} \ge 0. \tag{5.8}$$

We use the FORTRAN procedure NNLS (*Lawson and Hanson, 1974)* to solve (5.8). We find that the scatter in the q measurements for the fundamental modes is too large to be fit by physically reasonable, spherically symmetric models. Detailed inspection of the fits of these modes suggests that coupling to

other modes may be weakly perturbing the observed q's. An increase in the errors on these measurements by a factor 2 is sufficient to allow an acceptable fit. We fit the entire dataset to within 1.4 standard deviations on average which indicates that our error estimates are still slightly too optimistic or that there are inconsistent observations left in the dataset. The final dataset which we use throughout the subsequent modeling is presented in Appendix A.

We now investigate the ability of the dataset to resolve the radially symmetric q_μ and q_κ structure. We try to answer the question of how well the average property within a layer is constrained by the data. In particular we would like to minimize simultaneously the variance of the estimated property and the bias of the estimate due to the influence of the q structure in the adjacent layers. This is a classical case of a trade-off calculation and we follow the procedure outlined by *Masters and Gilbert (1983)* to evaluate this trade-off. Boxcar-like averaging functions are constructed by forming linear combinations of the orthogonalized representers. Naturally, we start out by summing the representers associated with the most precise sEd. Our approximation to a boxcar improves as we increase the number of representers in the sum which means that increasingly less information from outside the interval of interest affects our estimate of the average property within the target interval. The price paid for improving our approximation to the boxcar, i.e. reducing the bias, is that we have to include representers whose associated data have increasingly large errors which means that the variance of the estimated mean is also increasing. We are thus faced with a trade-off between the variance in the estimated average property and the bias of this average due to leakage from neighboring regions. We show averaging functions for the inner core, the upper mantle and the whole mantle in Figure 5.5. While the average q_μ of the mantle can be determined to within 2%, the average q_μ for other regions is more poorly constrained. Figure 5.6 shows the trade-offs for q_μ.

If our approximation to a boxcar function leaks into a region of low q, we do not expect our estimate of q in the target layer to be strongly biased. On the other hand, our estimate can be severely biased if the boxcar approximation leaks only slightly into a high q region. The sign of the bias depends on the sign of the "spill-over" which is an integrated measure of how much our approximation to a boxcar leaks out of the layer of interest (see *Masters and Gilbert, 1983).* Consequently high q (low Q) zones are well constrained and low q (high Q) zones are ill constrained which is an especially serious problem for q_κ.

The results of the trade-off calculations are summarized in Table 5.1. As we expect, the error of the average shear q is large if we ask for the average in a thin layer such as D'' and, conversely, the errors are small if we look at the average over a large depth range. It is difficult to assess the effect of a

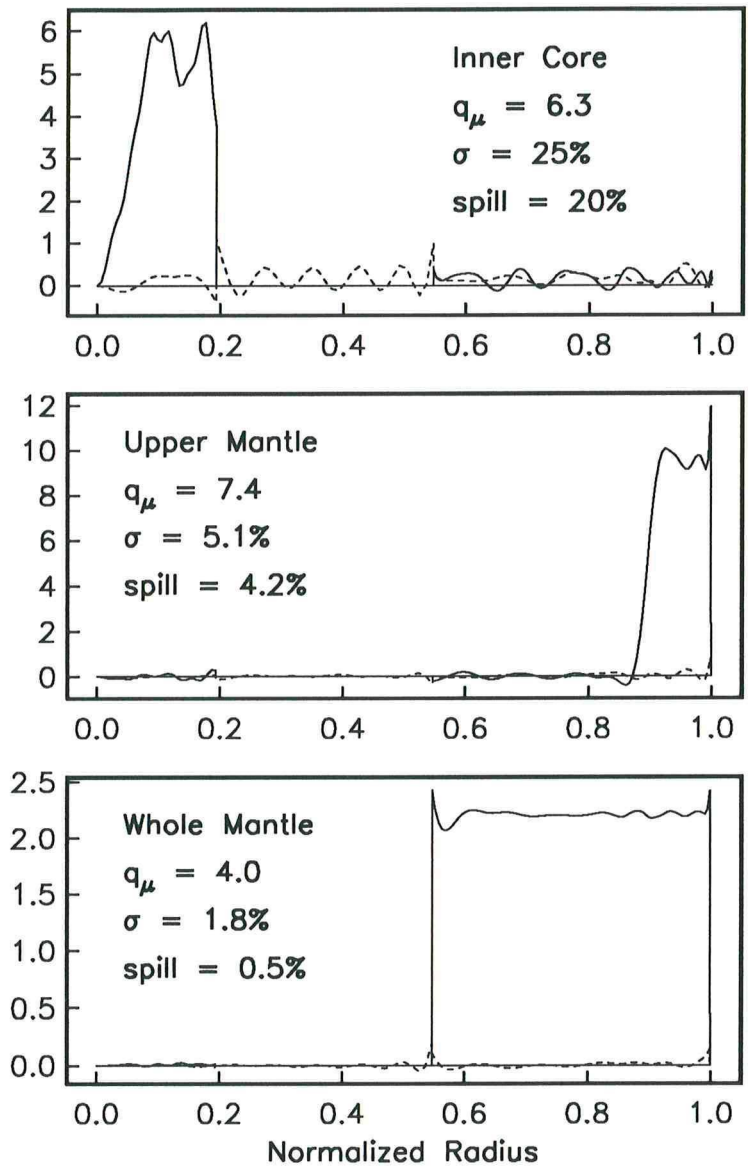

Figure 5.5 Averaging functions for the inner core, the upper mantle and the whole mantle. Dashed lines are for q_κ and solid lines are for q_μ

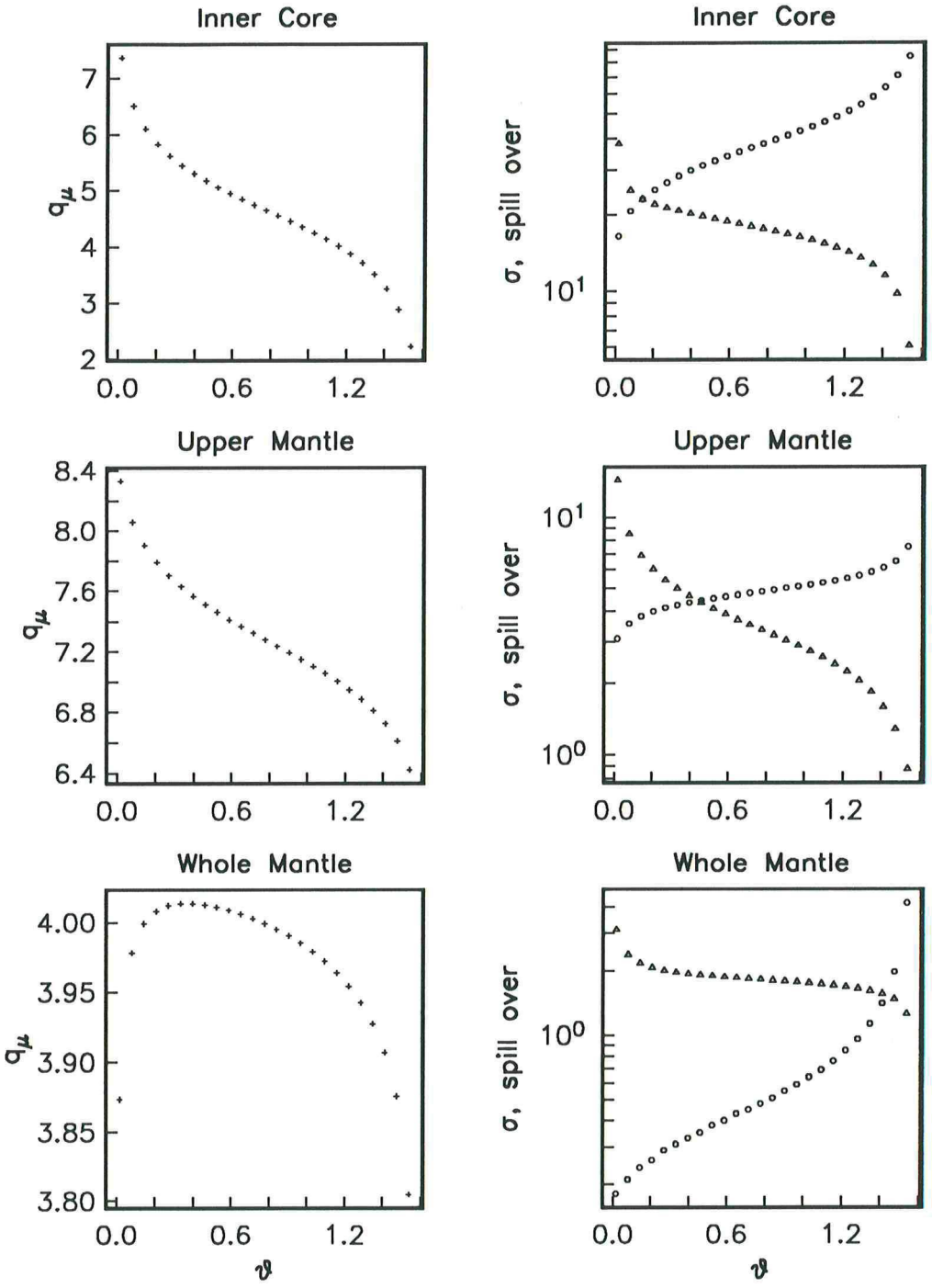

Figure 5.6 Trade-off curves for the inner core, the upper mantle, and the whole mantle. Shown are the average q_μ value (+), its 1σ error in per-cent (Δ) and the associated spill-over in per-cent ($\circ$) all as a function of the trade-off parameter ϑ. To give an example, taking $\vartheta = 0.2$ gives an average q_μ in the upper mantle of 7.8 with an error of 6% and a spill-over of 4%.

Region	$\bar{q}_\mu$	σ	χ^2/n
		(%)	(%)
Inner Core	7.0	30.	18.
D''^a	4.4	25.	18.
Lower Mantle^b	2.8	7.	4.
Upper Mantle	7.8	6.	4.
Whole Mantle	4.0	1.8	0.5

(a) taken to be the lowest 300km of the mantle
(b) excludes D''

Table 5.1 Results of the tradeoff calculations showing typical values for the average q in a layer, its error, and the corresponding spillover.

given spill-over but an indication of the severity of the bias may be obtained by looking at the trade-off diagrams (Figure 5.6). If the estimated average q does not vary with varying spill-over then our estimate is likely to be a robust one. This is certainly the case for q_μ in the mantle.

While a resolution analysis can help us to understand the ability of the data to constrain structure, it is not a very good way to construct actual models. In the following, we will take two different approaches to the construction of q-models, the reason being that we want to emphasize the difference between model features required by the data and features which are due to a particular inversion scheme.

In the first scheme, we simply look for the model with the minimum L_2 norm. The solution is straightforward and is perhaps the most frequently used approach to model construction. Let us write the forward problem in its simplest form

$$\mathbf{d} = \int_0^{2a} \mathbf{G}(r) m(r)\, dr. \tag{5.9}$$

This form can be obtained from (5.1) by making the variable substitutions

$$G_i(r) = K_i(r); \quad m(r) = q_\kappa(r) \quad \text{for} \quad 0 < r \leq a$$

$$G_i(r) = M_i(r-a); \quad m(r) = q_\mu(r-a) \quad \text{for} \quad a < r \leq 2a.$$

Let us assume that the representers $G_i(r)$ have been ranked and winnowed so that

$$\int_0^{2a} G_i(r) G_j(r)\, dr = \delta_{ij} \tag{5.10}$$

It is usually true that the representer associated with the most precise sEd are smooth functions of radius

and that the representers become increasingly oscillatory as the error of the sEd increases. This feature allows us to control the amount of structure in the model. Let

$$m(r) = \sum \alpha_i G_i(r) \tag{5.11}$$

then we can use (5.9) and the orthogonality relation (5.10) to find the expansion coefficients α_i:

$$d_j = \sum \alpha_i \int_0^{2a} G_i G_j \, dr = \sum \alpha_i \delta_{ij} = \alpha_j \tag{5.12}$$

Thus the minimum L_2 norm solution is

$$m(r) = \sum_{i=1}^{N^*} d_i G_i(r) \tag{5.13}$$

with the model norm

$$\|m(r)\|^2 = \sum_{i=1}^{N^*} d_i^2 \tag{5.14}$$

and the misfit

$$\chi^2 = \sum_{i=1}^{N^*} \left(\frac{d_i - d_i^{obs}}{\sigma_i} \right)^2 . \tag{5.15}$$

As we increase N^*, the number of sEd used to construct the model, the χ^2 misfit decreases but the model norm increases rapidly. We show the resulting models for three different χ^2 values in Figure 5.7. q_μ is positive for all three cases whereas q_κ oscillates between positive and negative values. Since we have not parameterized the model variables, we are unable to impose directly a positivity constraint with this particular model-construction technique. Inspection of the resulting models suggests that q_μ is quite well-determined throughout the mantle but, as expected, q_κ, is very poorly determined.

Since minimum L_2 norm models can be quite oscillatory, we seek an improved model construction technique which suppresses this behavior. One way to do this is to parameterize the model very coarsely. The effect of such a parameterization is to reduce the class of possible solutions though we must be careful that we still allow enough degrees of freedom of the right kind to allow models which are an adequate approximation to the true solution. A second and more satisfactory approach is to overparameterize the model and penalize the solution for roughness. This approach allows the data to dictate where structure is to occur in the model rather than the prejudices of the investigator. In

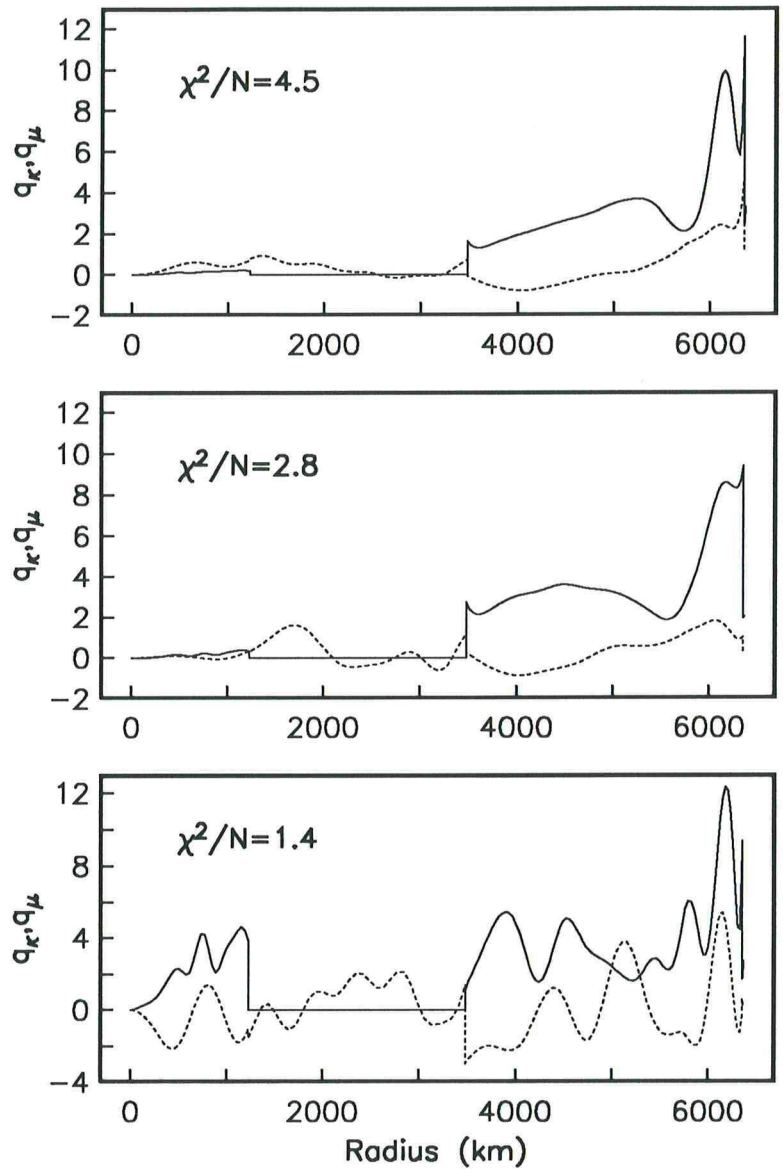

Figure 5.7 The minimum L_2 norm models obtained by summing up 6 (top), 11 (middle) and 30 (bottom) orthogonalized representers. The corresponding χ^2/N values for the three models are 4.5, 2.8 and 1.4 respectively. The solid line follows q_μ and the dashed line q_κ. While the first model exhibits little structure and has a small model norm it does a poor job fitting the observations. The third model fits the data very well but is too oscillatory to be physically reasonable. Furthermore, it has an excessively large model norm. The second model represents a reasonable compromise and q_μ is well behaved in the mantle. In the core q_κ oscillates strongly and at places exceeds the value of q_μ. There the model has to be rejected on physical grounds.

the following derivation, we follow closely the notation of *Constable et al. (1987)*. We use the same discretization as in (5.3) and as measure of roughness we choose both first and second differences

$$R_1 = \sum_{j=2}^{2L} (m_j - m_{j-1})^2 \tag{5.16}$$

and

$$R_2 = \sum_{j=2}^{2L-1} (m_{j+1} - 2m_j + m_{j-1})^2. \tag{5.17}$$

We modify these two measures of roughness to allow for step discontinuities at the inner core boundary (ICB) and core mantle boundary (CMB). This is achieved by dropping the terms in (5.16) which straddle the discontinuities. In matrix notation we can write our forward problem as

$$\mathbf{b} = \mathbf{Hm}, \tag{5.18}$$

the misfit to the data as

$$\chi^2 = \|\mathbf{b} - \mathbf{Hm}\|^2 \tag{5.19}$$

where we assume that the data and their associated representers have been normalized to unit variance as in (5.7). The roughness measures can be written as a matrix operation, e.g.

$$R_1 = \mathbf{m}^T \mathbf{D}^T \mathbf{D} \mathbf{m} \tag{5.20}$$

where $\mathbf{D}$ is a matrix which performs first differencing of the model vector. Smooth models which fit the data to within a prescribed misfit χ^2 are found by solving

$$\begin{bmatrix} \mathbf{b} \\ \mathbf{0} \end{bmatrix} = \begin{bmatrix} \mathbf{G} \\ \nu \mathbf{D} \end{bmatrix} \mathbf{m} \tag{5.21}$$

We again use the procedure NNLS to impose the constraint that $\mathbf{m}$ is positive. The parameter ν determines the amount of smoothing and, by solving (5.21) for a range of ν values, we can explore the trade-off between the norm of the model and the misfit. As noted above, the ratio of χ^2/N where N is the number of data is 1.4 for $\nu = 0$. Figure 5.8 shows the resulting models for a target χ^2/N of 2 using both R_1 and R_2 as a measure of roughness. We refer to these models as QM1 and QM2 respectively and the values for model QM1 are presented in Table 5.2. To confirm that no mode branches are systematically misfit,

Radius[a] (km)	Q_κ	Q_μ
192.0	∞	109.
422.4	∞	109.
652.8	∞	110.
883.2	∞	110.
1075.2	∞	111.
1229.4	∞	112.
3484.3	12000.	∞
3656.7	∞	266.
3829.9	∞	268.
4003.0	∞	271.
4176.2	∞	272.
4349.3	∞	274.
4522.5	∞	285.
4695.6	∞	311.
4868.8	∞	343.
5042.0	∞	360.
5215.1	∞	368.
5353.6	∞	379.
5492.2	∞	383.
5700.0	∞	362.
5825.0	2920.	286.
5950.0	2920.	210.
6052.5	2920.	152.
6180.6	2920.	121.
6283.1	2920.	116.
6371.0	2920.	120.

(a) The radii listed corespond to the radii of the top of a layer.

Table 5.2 Model QM1.

we have plotted the observed q values against the predictions of QM1 in Figure 5.9. In Appendix B we tabulate the model predictions and the misfit for the entire dataset.

The two models are nearly identical in the mantle which indicates that the structure is dictated by the data and not by the particular measure of roughness. Both QM1 and QM2 exhibit a positive q_μ gradient in the inner core but its magnitude is quite different for the two models. To see whether this gradient is a resolved feature, we look at the effect of the inner core q_μ structure on the total misfit to the data. We find that a model with a constant q_μ in the inner core with a value equal to the average inner core shear q of the above models has only a 0.03% effect on the total χ^2. A constant q_μ in the inner core increases χ^2 by 3.1% if we consider only those modes sensitive to inner core structure. We can thus conclude that the details of the q_μ structure in the inner core are not resolved by the data and a constant q_μ model is adequate. The average value of inner core q_μ in the two models is very similar and

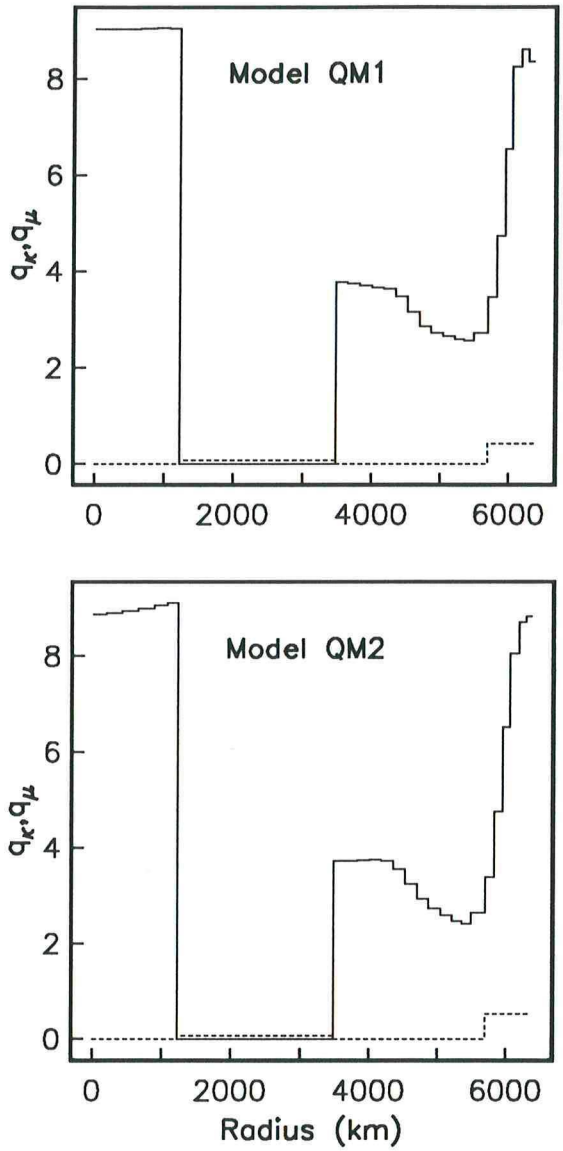

Figure 5.8 The smoothest models, QM1 and QM2, to fit our observations with $\chi^2/N = 2.0$. The measures of roughness used are first and second differences respectively. The discretization of q_κ is coarse reflecting our inability to constrain this parameter. Dashed lines are for q_κ and solid lines are for q_μ

Figure 5.10 shows the effect on the fit to the data of varying this parameter by ±30%. If q_μ is decreased to 7, the modes ${}_{27}S_2$, ${}_{13}S_3$, ${}_{11}S_5$ and ${}_{18}S_4$ are misfit by more than 2.5 standard deviations, while if q_μ is increased to 11 it is the modes ${}_{14}S_4$, ${}_{13}S_1$ and ${}_{9}S_4$ which are misfit by more than 2.5 standard deviations. It is thus reasonable to conclude that the average q_μ value for the inner core is $9 \pm 25\%$.

The shear Q of the minimum L_2 norm model (Figure 5.7 middle) compares well with both QM1 and QM2 down to the middle of the lower mantle. The q_μ models diverge below this depth due mainly to the physically unreasonable behavior of q_κ in the minimum L_2 norm model. This kind of

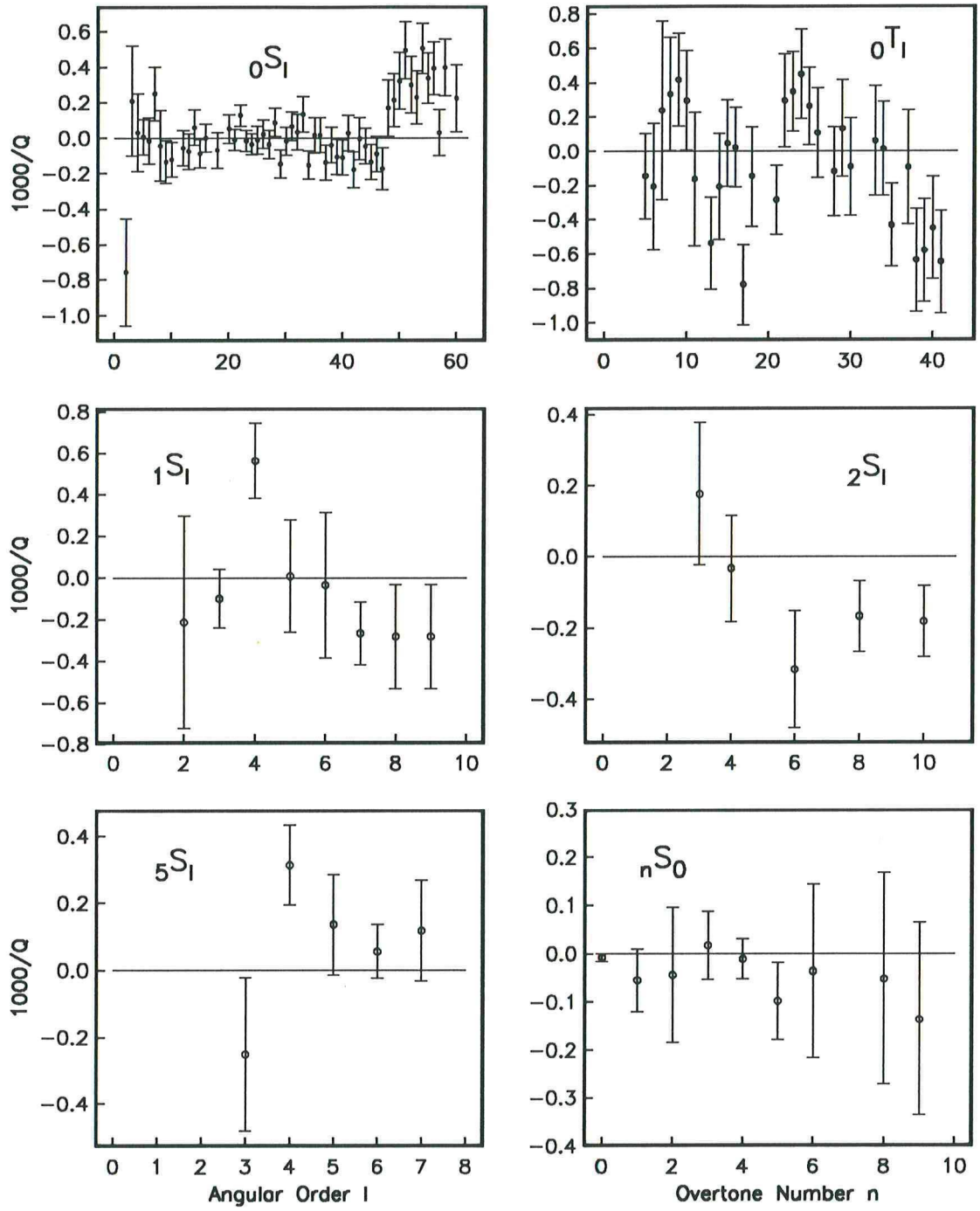

Figure 5.9 Residuals relative to model QM1 for selected mode branches.

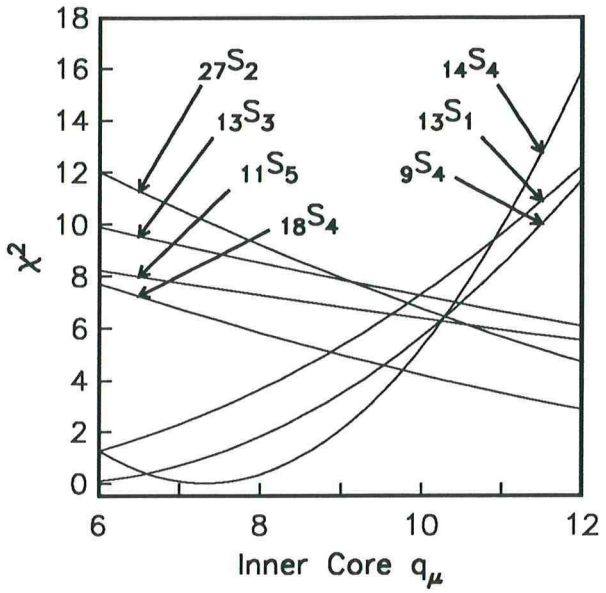

Figure 5.10 The misfit $\chi^2 = (q_{obs.} - q_{model})^2/\sigma^2$ of individual modes with significant shear energy in the inner core as a function of inner core shear q. The total χ^2 has a well-defined minimum at $q_\mu = 9$.

behavior is possible since q_κ was not constrained to be a smoothly varying, positive function. Clearly we have to discard the minimum L_2 norm model for inferences at the base of the mantle and in the core. The good agreement between the three models in the upper mantle is due to the fact that our most precise data come from observations of fundamental spheroidal modes.

Q model	χ^2/n
SL8 (Anderson and Hart, 1978)	43.0
PREM (Anderson and Dziewonski, 1981)	17.0
Masters, Park and Gilbert (1983)	4.7
QM1 (this study)	2.0

Table 5.3 Comparison of Q models from literature. The χ^2/n misfit for the data in Appendix A is given.

Models QM1 and QM2 look similar in shape to many models which have previously appeared in the literature though some of the older models must be rejected since they do not adequately fit the improved dataset. This is demonstrated in Table 5.3 where we show the fits of three older models to the data. Most of the misfit comes from small differences in shear Q structure in the upper mantle.

5.4 Conclusion

The dataset of mean attenuation values presented in this paper is probably the most comprehensive and precise to date. Many of these values are inferred from thousands of individual estimates to overcome the large signal from interference effects caused by aspherical structure. Despite this, our dataset covers too small a frequency bandwidth and is insufficiently precise for us to be able to constrain complex absorption models of attenuation. We therefore have chosen to assume that Q is independent of frequency - an assumption which seems to be in general agreement with the data though is certainly not mandated by them.

Our modeling indicates that shear Q is reasonably well-determined in the mantle with an average value of $250 \pm 2\%$. Our models indicate that attenuation is greatest in the upper mantle although the lower mantle also shows a systematic increase in attenuation as one goes deeper. Perhaps this is suggestive of the mantle geotherm approaching the solidus temperature with increasing depth. Details of shear Q in the inner core are not constrained by the mode data and is best determined near the ICB. We find that a value of 110 (precise to 25%) seems to be required by the data. This is in conflict with apparent observations of the attenuation of "core modes" but we feel that such observations are susceptible to misidentification and must be treated with caution. It is also true that shear q in the inner core is constrained by only a few modes and, since q observations are susceptible to bias, it is possible that expansion of the dataset will dictate a different value from that given here.

Comparisons between the waveforms of $PKP(DF)$ and $PKP(BC)$ have been used to estimate Q_α within the inner core (*e.g., Doornbos, 1974, 1983 Cormier, 1981*). These studies have generally indicated that P-wave attenuation is relatively strong in the outer inner core ($Q_\alpha \simeq 200$ with decreasing attenuation with depth in the inner core ($Q_\alpha = 1000$ at the center). Our new value for average inner core shear Q predicts attenuation of body waves which is in much better agreement with these observations though, if all attenuation is in shear, the body wave data suggest that the shear Q should be about 30 in the upper part of the inner core. Our data are inconsistent with such a value so, if all measurements are taken at face value, we must have strong frequency dependence of Q or there must be significant bulk attenuation in the inner core. In fact, there is some evidence that the body-waves are sensing an absorption band which is centered at frequencies higher than 1 Hz (*Doornbos, 1983*; *Bhattacharyya et al. 1990*). The existence of such an absorption band would not significantly affect the attenuation of low-frequency modes and seems the most likely explanation for the apparent discrepancy between modal

and body-wave attenuation measurements.

Finally, we note that the distribution of bulk attenuation in the Earth is still very poorly determined and we can say little beyond the well-known fact that it must exist to satisfy the Q observations of the radial modes.

References

Backus, G.E., and J.F. Gilbert, Numerical applications of a formalism for geophysical inverse problems. *Geophys. J. R. Astron. Soc.*, **13**, 247–276, 1967.

Bhattacharyya, J., P. Shearer, and G. Masters, Differential PKP waveform analysis of inner-core attenuation and absorption band models. *EOS, Trans AGU*, in press, 1990.

Buland, R., J. Berger, and F. Gilbert, Observations from the IDA network of attenuation and splitting during a recent earthquake. *Nature*, **277**, 358–362, 1979.

Constable, S.C., R.L. Parker, and C.G. Constable, Occam's Inversion: A practical algorithm for generating smooth models from electromagnetic sounding data. *Geophysics*, **52**, 289–300, 1987.

Cormier, V.F., Short-period PKP phases and the anelastic mechanism of the inner core. *Phys. Earth Planet. Inter.*, **24**, 291–301, 1981.

Dahlen, F.A., Models of the lateral heterogeneity of the earth consistent with eigenfrequency splitting data. *Geophys. J. R. Astron. Soc.*, **44**, 77–105, 1976.

Dahlen, F.A., The spectra of unresolved split normal mode multiplets. *Geophys. J. R. Astron. Soc.*, **58**, 1–33, 1979.

Dahlen, F.A., The effect of data windows on the estimation of free oscillation parameters. *Geophys. J. R. Astron. Soc.*, **69**, 537–549, 1982.

Davis, J.P., Variation in apparent attenuation of the earth's normal modes due to lateral heterogeneity. *Geophys. Res. Lett.*, **12**, 141–143, 1985.

Davis, J.P., Local eigenfrequency and its uncertainty inferred from fundamental spheroidal mode frequency shifts. *Geophys. J. R. Astron. Soc.*, **88**, 693–722, 1987.

Doornbos, D.J., The anelasticity of the inner core. *Geophys. J. R. Astron. Soc.*, **38**, 397–415, 1974.

Doornbos, D.J., Observable effects of the seismic absorption band in the Earth. *Geophys. J. R. Astron. Soc.*, **75**, 693–711, 1983.

Efron, B., and R. Tibshirani, Bootstrap methods for standard errors, confidence intervals, and other measures of statistical accuracy. *Statistical Science*, **1**, 54–77, 1986.

Fukao, Y., and N. Suda, Core modes of the Earth's free oscillations and structure of the inner core. *Geophys. Res. Lett.*, **16**, 401–404, 1989.

Giardini, D., X.-D. Li, and J.H. Woodhouse, Splitting functions of long period normal modes of the earth. *J. Geophys. Res.*, **93**, 13,716–13,742, 1988.

Gilbert, F., The diagonal sum rule and averaged eigenfrequencies. *Geophys. J. R. Astron. Soc.*, **23**, 119–123, 1971a.

Gilbert, F., Ranking and winnowing gross earth data for inversion and resolution. *Geophys. J. R. Astron. Soc.*, **23**, 125–128, 1971b.

Gilbert, F., and A.M. Dziewonski, An application of normal mode theory to the retrieval of structural parameters and source mechanisms from seismic spectra. *Phil. Trans. R. Soc. London*, **A278**, 187–269, 1975.

Lawson, C.L., and R.J. Hanson, *Solving Least Squares Problems.* Prentice-Hall, Englewood Cliffs, N.J., 1974.

Lognonné, P., *Modélisation des modes propres de vibration dans une Terre anélastique et hétérogène: Théorie et applications.* Ph. D. Thesis, Université de Paris VII, 1989.

Masters, G., and F. Gilbert, Structure of the inner core inferred from observations of its spheroidal shear modes. *Geophys. Res. Lett.*, **8**, 569–571, 1981.

Masters, G., T.H. Jordan, P.G. Silver, and F. Gilbert, Aspherical earth structure from fundamental spheroidal-mode data. *Nature*, **298**, 609–613, 1982.

Masters, G., and F. Gilbert, Attenuation in the earth at low frequencies. *Phil. Trans. R. Soc. London*, **A308**, 479–522, 1983.

Masters, G., J. Park, and F. Gilbert, Observations of coupled spheroidal and toroidal modes. *J. Geophys. Res.*, **88**, 10,285–10,298, 1983.

Okal, E. A. and Jo, B.-G., Q measurements for phase X overtones . *Pageoph*, **132**, 331–362, 1990.

Park, J., Radial mode observations from the 5/23/89 Macquarie Ridge earthquake. *Geophys. Res. Lett.*, **17**, 1005–1008, 1990.

Riedesel, M., D. Agnew, J. Berger, and F. Gilbert, Stacking for the frequencies and Q's of ${}_0S_0$ and ${}_1S_0$. *Geophys. J. R. Astron. Soc.*, **62**, 457–471, 1980.

Ritzwoller, M., G. Masters, and F. Gilbert, Observations of anomalous splitting and their interpretation in terms of aspherical structure. *J. Geophys. Res.*, **91**, 10,203–10,228, 1986.

Romanowicz, B., G. Roult, and T. Kohl, The upper mantle degree two pattern: constraints from GEOSCOPE fundamental spheroidal mode eigenfrequency and attenuation measurements. *Geophys. Res. Lett.*, **14**, 1219–1222, 1987.

Smith, M.F., and G. Masters, Aspherical structure constraints from free oscillation frequency and attenuation measurements. *J. Geophys. Res.*, **94**, 1953–1976, 1989a.

Smith, M.F., and G. Masters, The effect of Coriolis coupling of free oscillation multiplets on the determination of aspherical earth structure. *Geophys. Res. Lett.*, **16**, 263–266, 1989b.

Smith, M.F., and G. Masters, Aspherical mantle structure from spheroidal and toroidal free oscillation measurements. *J. Geophys. Res.*, accepted, 1990.

Tanimoto, T., Lateral variation of Q from singlet modal Q measurements of ${}_0S_2$. *Geophys. Res. Lett.*, **17**, 669–672, 1990.

Tromp, J., and F.A. Dahlen, Free oscillations of a spherical anelastic earth. *Geophys. J. Int.*, in press, 1990.

Woodhouse, J.H., and A.M. Dziewonski, Mapping of the upper mantle: three-dimensional modeling of earth structure by inversion of seismic waveforms. *J. Geophys. Res.*, **89**, 5953–5986, 1984.

Appendix A

Observed multiplet degenerate frequencies and mean attenuation values used in the inversions. The data in this table have been compiled from several investigators and we have indicated the source of the data in the last column. The sixth and eighth column list 1 σ errors for the frequency and q estimates. The fourth column contains the number of observations that were used to estimate degenerate frequency and q.

n		l	N_{obs}	f	df	q	dq	Remark
				[μHz]	[μHz]			
0	S	0		814.664	0.004	0.175	0.008	1
1	S	0		1631.51	0.03	0.541	0.065	1
2	S	0		2507.90	0.25	0.555	0.140	2
3	S	0		3272.30	0.13	0.709	0.071	2
4	S	0		4106.20	0.08	0.823	0.041	2
5	S	0		4889.10	0.20	0.800	0.080	2
6	S	0		5742.00	0.20	0.900	0.180	3
8	S	0		7429.27	0.80	0.900	0.220	3
9	S	0		8270.10	0.90	0.820	0.200	3
0	S	2	4	309.45	0.15	1.230	0.300	4
0	S	3		468.55	0.15	2.630	0.310	3
0	S	4		646.60	0.15	2.740	0.220	3
0	S	5		840.00	0.10	2.860	0.100	3
0	S	6		1037.50	0.10	2.910	0.130	3
0	S	7	209	1231.10	0.11	3.210	0.150	5
0	S	8	440	1412.69	0.07	2.918	0.200	6
0	S	9	598	1577.28	0.07	2.804	0.120	6
0	S	10	614	1725.21	0.07	2.787	0.100	6
0	S	12	700	1988.92	0.10	2.839	0.100	6
0	S	13	838	2111.58	0.10	2.841	0.100	6
0	S	14	925	2229.88	0.10	3.016	0.100	6
0	S	15	1003	2344.96	0.10	2.925	0.080	6
0	S	16	1039	2456.99	0.10	3.084	0.080	6
0	S	18	1079	2670.77	0.10	3.201	0.100	6
0	S	20	1151	2877.95	0.12	3.547	0.080	6
0	S	21	1317	2977.04	0.10	3.607	0.060	6
0	S	22	1314	3074.62	0.15	3.873	0.060	6
0	S	23	1500	3170.66	0.12	3.859	0.060	6
0	S	24	1133	3265.62	0.12	3.970	0.060	6
0	S	25	1251	3358.96	0.10	4.126	0.080	6
0	S	26	1280	3451.40	0.10	4.289	0.080	6
0	S	27	1401	3543.12	0.11	4.360	0.080	5
0	S	28	1448	3634.38	0.12	4.610	0.080	5
0	S	29	1522	3724.73	0.13	4.500	0.080	5
0	S	30	1309	3814.84	0.13	4.750	0.080	5
0	S	31	1244	3904.85	0.15	4.950	0.080	5
0	S	32	1213	3994.04	0.15	5.030	0.100	5
0	S	33	1518	4082.95	0.17	5.240	0.100	5
0	S	34	1222	4172.10	0.20	5.060	0.080	5

Appendix A continued.

n		l	N_{obs}	f	df	q	dq	Remark
				[μHz]	[μHz]			
0	S	35	1234	4261.45	0.20	5.330	0.100	5
0	S	36	1314	4351.15	0.25	5.430	0.100	5
0	S	37	1489	4440.70	0.25	5.370	0.100	5
0	S	38	1536	4529.20	0.20	5.560	0.100	5
0	S	39	1329	4618.65	0.22	5.580	0.100	5
0	S	40	1332	4707.70	0.22	5.660	0.100	5
0	S	41	1451	4798.10	0.30	5.880	0.100	5
0	S	42	1256	4887.70	0.25	5.750	0.100	5
0	S	43	1158	4977.35	0.35	6.000	0.120	5
0	S	44	1268	5068.40	0.35	6.030	0.100	5
0	S	45	1193	5157.00	0.35	6.010	0.100	5
0	S	46	1258	5247.90	0.25	6.120	0.100	5
0	S	47	1131	5338.10	0.30	6.100	0.120	5
0	S	48	1225	5428.46	0.22	6.503	0.160	7
0	S	49	1292	5518.77	0.22	6.606	0.150	7
0	S	50	1177	5609.44	0.22	6.768	0.160	7
0	S	51	1086	5701.03	0.22	6.993	0.160	7
0	S	52	1136	5792.27	0.24	6.851	0.160	7
0	S	53	1039	5884.98	0.47	6.829	0.150	4
0	S	54	929	5975.50	0.43	7.150	0.140	4
0	S	55	1135	6064.30	0.44	7.028	0.140	4
0	S	56	878	6158.79	0.51	7.125	0.150	4
0	S	57	1008	6246.27	0.42	6.803	0.130	4
0	S	58	1039	6340.96	0.45	7.210	0.160	4
0	S	60	849	6526.56	0.55	7.111	0.190	4
1	S	2		680.04	0.26	2.710	0.510	3
1	S	3		939.81	0.25	3.010	0.140	3
1	S	4		1172.56	0.15	3.760	0.180	3
1	S	5		1370.66	0.35	3.020	0.270	3
1	S	6		1521.16	0.30	2.640	0.350	9
1	S	7		1655.22	0.25	2.310	0.150	9
1	S	8		1798.27	0.26	2.310	0.250	3
1	S	9	43	1963.49	0.94	2.368	0.250	4
2	S	3		1243.43	0.20	2.530	0.200	3
2	S	4	98	1378.60	0.20	2.550	0.150	4
2	S	6	101	1681.99	0.47	3.375	0.164	4
2	S	8	535	2049.35	0.20	4.140	0.100	4
2	S	10	641	2404.00	0.50	4.510	0.100	4
3	S	1		944.26	0.20	1.250	0.120	9
3	S	2		1105.98	0.40	2.660	0.280	3
3	S	8		2819.50	0.30	3.330	0.170	9
4	S	3		2048.46	0.23	1.600	0.180	3

Appendix A continued.

n		l	N_{obs}	f	df	q	dq	Remark
				[μHz]	[μHz]			
5	S	3		2168.98	0.25	2.800	0.230	3
5	S	4		2379.19	0.23	2.110	0.120	3
5	S	5		2703.77	0.16	1.890	0.150	3
5	S	6		3011.85	0.40	1.800	0.080	3
5	S	7		3292.70	0.29	1.910	0.150	3
6	S	3		2821.71	0.35	2.230	0.160	3
8	S	1		2872.84	0.15	1.020	0.160	3
8	S	5		4165.71	0.23	1.630	0.150	3
9	S	3		3557.91	0.85	1.300	0.150	3
9	S	4		3880.03	1.25	1.620	0.240	3
10	S	2		4041.00	0.60	1.171	0.150	3
11	S	4		4765.97	0.35	1.350	0.110	3
11	S	5		5072.32	0.35	1.660	0.100	3
12	S	8		6132.42	0.55	2.012	0.110	3
13	S	1	18	4489.73	0.26	0.940	0.070	4
13	S	2		4843.97	0.50	1.000	0.050	3
13	S	3		5194.06	0.35	1.280	0.100	3
14	S	4		5544.94	0.79	1.230	0.060	3
15	S	3		6031.53	0.35	1.240	0.160	3
16	S	5		6829.84	1.44	1.860	0.150	3
16	S	6		7149.13	0.54	1.720	0.250	3
16	S	7		7470.08	1.00	1.500	0.150	3
18	S	3		6888.00	0.55	1.210	0.110	3
18	S	4		7238.40	0.60	1.080	0.060	3
20	S	1		6949.65	0.40	1.290	0.150	3
21	S	6		8848.53	0.72	1.600	0.200	3
21	S	7		9167.82	1.00	1.580	0.200	3
21	S	8		9489.88	1.20	1.500	0.090	3
22	S	1	41	7816.94	0.30	0.950	0.050	4
23	S	4		8934.36	0.70	1.340	0.150	3
23	S	5		9290.21	0.30	1.120	0.170	3

Appendix A continued.

n		l	N_{obs}	f	df	q	dq	Remark
				[μHz]	[μHz]			
25	S	1	50	8652.30	0.45	1.020	0.070	4
25	S	2		9026.51	0.69	1.220	0.110	3
27	S	1		9484.00	0.50	1.350	0.240	3
27	S	2		9870.60	1.10	1.320	0.100	3
0	T	5		928.36	0.21	3.890	0.250	3
0	T	6		1078.78	0.18	4.010	0.370	3
0	T	7		1220.79	0.26	4.650	0.520	3
0	T	8		1356.82	0.26	4.950	0.330	3
0	T	9	48	1487.26	0.30	5.240	0.270	4
0	T	10	123	1614.64	0.31	5.320	0.290	4
0	T	11	85	1737.35	0.38	5.057	0.390	8
0	T	13	101	1977.70	0.30	5.050	0.268	8
0	T	14	124	2094.98	0.34	5.548	0.310	8
0	T	15	164	2211.33	0.32	5.960	0.252	8
0	T	16	174	2325.38	0.30	6.083	0.232	8
0	T	17	161	2440.97	0.32	5.420	0.234	8
0	T	18	175	2552.17	0.40	6.178	0.290	8
0	T	21	235	2888.52	0.34	6.374	0.204	8
0	T	22	227	2998.51	0.44	7.050	0.272	8
0	T	23	273	3108.67	0.40	7.190	0.232	8
0	T	24	207	3221.56	0.46	7.374	0.260	8
0	T	25	240	3331.27	0.42	7.265	0.226	8
0	T	26	261	3441.49	0.50	7.180	0.262	8
0	T	28	215	3659.03	0.60	7.083	0.260	7
0	T	29	192	3768.39	0.64	7.394	0.284	7
0	T	30	217	3877.17	0.68	7.226	0.286	7
0	T	33	183	4207.42	0.84	7.523	0.322	7
0	T	34	221	4317.66	0.66	7.519	0.276	7
0	T	35	258	4428.45	0.64	7.113	0.242	7
0	T	37	144	4643.75	0.98	7.525	0.332	7
0	T	38	253	4759.15	1.06	7.016	0.300	4
0	T	39	350	4868.95	0.78	7.105	0.300	4
0	T	40	328	4979.47	0.82	7.266	0.300	4
0	T	41	217	5089.86	1.21	7.097	0.300	4

Remarks for Appendix A.
1.) Riedesel *et al.* , 1980
2.) Payson, Arizona
3.) Singlet stripping (this study)
4.) Histogram (this study)
5.) Smith and Masters, 1989a
6.) Smith and Masters, 1989a (Coriolis corrected)
7.) Smith and Masters, 1990
8.) Smith and Masters, 1990 (Coriolis corrected)
9.) Ritzwoller *et al.* , 1988; Giardini *et al.* , 1988

Appendix B

Fit of model QM1 to the data. Tabulated are the observed data q_{obs}, the observational uncertainty σ, the model prediction q_{QM1} and the relative misfit $\rho = (q_{obs} - q_{QM1})/\sigma$

n		l	q_{obs}	σ	q_{QM1}	ρ
0	S	0	0.175	0.008	0.182	-0.94
1	S	0	0.541	0.065	0.596	-0.84
2	S	0	0.555	0.140	0.599	-0.31
3	S	0	0.709	0.071	0.691	0.24
4	S	0	0.823	0.041	0.833	-0.26
5	S	0	0.800	0.080	0.897	-1.22
6	S	0	0.900	0.180	0.936	-0.20
8	S	0	0.900	0.220	0.952	-0.23
9	S	0	0.820	0.200	0.955	-0.67
0	S	2	1.230	0.300	1.986	-2.52
0	S	3	2.630	0.310	2.420	0.67
0	S	4	2.740	0.220	2.710	0.13
0	S	5	2.860	0.100	2.854	0.05
0	S	6	2.910	0.130	2.926	-0.12
0	S	7	3.210	0.150	2.959	1.66
0	S	8	2.918	0.200	2.961	-0.21
0	S	9	2.804	0.120	2.937	-1.11
0	S	10	2.787	0.100	2.908	-1.21
0	S	12	2.839	0.100	2.894	-0.55
0	S	13	2.841	0.100	2.916	-0.75
0	S	14	3.016	0.100	2.956	0.59
0	S	15	2.925	0.080	3.013	-1.10
0	S	16	3.084	0.080	3.085	-0.01
0	S	18	3.201	0.100	3.269	-0.68
0	S	20	3.547	0.080	3.494	0.65
0	S	21	3.607	0.060	3.617	-0.17
0	S	22	3.873	0.060	3.744	2.13
0	S	23	3.859	0.060	3.874	-0.26
0	S	24	3.970	0.060	4.006	-0.60
0	S	25	4.126	0.080	4.137	-0.14
0	S	26	4.289	0.080	4.267	0.26
0	S	27	4.360	0.080	4.396	-0.45
0	S	28	4.610	0.080	4.522	1.09
0	S	29	4.500	0.080	4.646	-1.82
0	S	30	4.750	0.080	4.766	-0.20
0	S	31	4.950	0.080	4.883	0.82
0	S	32	5.030	0.100	4.997	0.32
0	S	33	5.240	0.100	5.106	1.33
0	S	34	5.060	0.080	5.212	-1.90
0	S	35	5.330	0.100	5.315	0.14
0	S	36	5.430	0.100	5.413	0.16
0	S	37	5.370	0.100	5.508	-1.38
0	S	38	5.560	0.100	5.599	-0.39
0	S	39	5.580	0.100	5.687	-1.07

Appendix B continued.

n		l	q_{obs}	σ	q_{QM1}	ρ
0	S	40	5.660	0.100	5.771	-1.11
0	S	41	5.880	0.100	5.852	0.27
0	S	42	5.750	0.100	5.930	-1.80
0	S	43	6.000	0.120	6.004	-0.04
0	S	44	6.030	0.100	6.076	-0.46
0	S	45	6.010	0.100	6.144	-1.34
0	S	46	6.120	0.100	6.210	-0.90
0	S	47	6.100	0.120	6.273	-1.44
0	S	48	6.503	0.160	6.333	1.05
0	S	49	6.606	0.150	6.391	1.42
0	S	50	6.768	0.160	6.447	2.00
0	S	51	6.993	0.160	6.500	3.08
0	S	52	6.851	0.160	6.550	1.87
0	S	53	6.829	0.150	6.599	1.52
0	S	54	7.150	0.140	6.646	3.59
0	S	55	7.028	0.140	6.690	2.40
0	S	56	7.125	0.150	6.733	2.61
0	S	57	6.803	0.130	6.774	0.22
0	S	58	7.210	0.160	6.813	2.47
0	S	60	7.111	0.190	6.886	1.18
1	S	2	2.710	0.510	2.922	-0.41
1	S	3	3.010	0.140	3.109	-0.71
1	S	4	3.760	0.180	3.196	3.12
1	S	5	3.020	0.270	3.011	0.03
1	S	6	2.640	0.350	2.674	-0.09
1	S	7	2.310	0.150	2.576	-1.77
1	S	8	2.310	0.250	2.592	-1.12
1	S	9	2.368	0.250	2.650	-1.12
2	S	3	2.530	0.200	2.352	0.88
2	S	4	2.550	0.150	2.583	-0.21
2	S	6	3.375	0.164	3.692	-1.93
2	S	8	4.140	0.100	4.307	-1.67
2	S	10	4.510	0.100	4.692	-1.82
3	S	1	1.250	0.120	1.150	0.82
3	S	2	2.660	0.280	2.650	0.03
3	S	8	3.330	0.170	3.545	-1.26
4	S	3	1.600	0.180	1.795	-1.08
5	S	3	2.800	0.230	3.050	-1.09
5	S	4	2.110	0.120	1.796	2.61
5	S	5	1.890	0.150	1.754	0.90
5	S	6	1.800	0.080	1.743	0.70
5	S	7	1.910	0.150	1.792	0.78
6	S	3	2.230	0.160	2.033	1.22
8	S	1	1.020	0.160	0.907	0.70
8	S	5	1.630	0.150	1.362	1.78
9	S	3	1.300	0.150	1.158	0.94

Appendix B continued.

n		l	q_{obs}	σ	q_{QM1}	ρ
9	S	4	1.620	0.240	2.075	-1.89
11	S	4	1.350	0.110	1.327	0.20
11	S	5	1.660	0.100	1.397	2.62
13	S	1	0.940	0.070	1.107	-2.38
13	S	2	1.000	0.050	0.990	0.19
13	S	3	1.280	0.100	1.002	2.77
14	S	4	1.230	0.060	1.321	-1.51
15	S	3	1.240	0.160	1.078	1.00
16	S	5	1.860	0.150	1.534	2.16
16	S	6	1.720	0.250	1.230	1.95
16	S	7	1.500	0.150	1.171	2.18
18	S	3	1.210	0.110	1.022	1.70
18	S	4	1.080	0.060	0.946	2.22
20	S	1	1.290	0.150	0.958	2.20
21	S	6	1.600	0.200	1.246	1.76
21	S	7	1.580	0.200	1.150	2.14
21	S	8	1.500	0.090	1.547	-0.52
22	S	1	0.950	0.050	1.004	-1.08
23	S	4	1.340	0.150	1.066	1.82
23	S	5	1.120	0.170	0.983	0.80
25	S	1	1.020	0.070	0.987	0.46
25	S	2	1.220	0.110	1.058	1.46
27	S	1	1.350	0.240	1.499	-0.62
27	S	2	1.320	0.100	1.041	2.78
0	T	5	3.890	0.250	4.037	-0.58
0	T	6	4.010	0.370	4.217	-0.55
0	T	7	4.650	0.520	4.413	0.45
0	T	8	4.950	0.330	4.616	1.00
0	T	9	5.240	0.270	4.822	1.54
0	T	10	5.320	0.290	5.024	1.01
0	T	11	5.057	0.390	5.220	-0.41
0	T	13	5.050	0.268	5.587	-2.00
0	T	14	5.548	0.310	5.755	-0.66
0	T	15	5.960	0.252	5.913	0.18
0	T	16	6.083	0.232	6.060	0.09
0	T	17	5.420	0.234	6.198	-3.32
0	T	18	6.178	0.290	6.326	-0.51
0	T	21	6.374	0.204	6.658	-1.39
0	T	22	7.050	0.272	6.753	1.08
0	T	23	7.190	0.232	6.842	1.49
0	T	24	7.374	0.260	6.925	1.72
0	T	25	7.265	0.226	7.002	1.16
0	T	26	7.180	0.262	7.073	0.40
0	T	28	7.083	0.260	7.203	-0.46
0	T	29	7.394	0.284	7.262	0.46
0	T	30	7.226	0.286	7.316	-0.31

Appendix B continued.

n		l	q_{obs}	σ	q_{QM1}	ρ
0	T	33	7.523	0.322	7.462	0.18
0	T	34	7.519	0.276	7.504	0.05
0	T	35	7.113	0.242	7.545	-1.78
0	T	37	7.525	0.332	7.618	-0.28
0	T	38	7.016	0.300	7.652	-2.12
0	T	39	7.105	0.300	7.684	-1.93
0	T	40	7.266	0.300	7.715	-1.49
0	T	41	7.097	0.300	7.744	-2.15

Chapter 6

Toward a new Monopole Model: Summary and Outlook

The work presented in this thesis started out with the establishment of a large database of digital long-period recordings of large earthquakes. Though little has been said about it, the editing of several thousand records along with the attendant source mechanism analysis constitutes one of the major time sinks of this research.

In chapter 2 we use the multiplet stripping technique to analyze the dataset and make precise observations of multiplet degenerate frequencies. This is the first such experiment since the work of *Gilbert and Dziewonski (1975)* who analyzed manually digitized WWSSN recordings of the 1970 Columbian earthquake. The size of the dataset and the existence of analyses which incorporate the effects of 3-D structure for some modes allow us to remove many sources of bias in the current dataset of free oscillation frequencies.

An analysis of misfit showed that we can find models which have a PREM-like parameterization and fit the modes sensitive to structure in the mantle but that we are unable to find models which fit the core-sensitive modes. This observation was the motivation for the next two chapters in which we use techniques to observe the multiplet degenerate frequency which take the effect of aspherical structure into account. In chapter 3 we analyze 10 core-sensitive multiplets whose splitting characteristics have not been investigated previously. The observations presented in chapter 3 effectively double the number of observed anomalously split multiplets and, while spectral fitting was only successful in the case of three multiplets (${}_{15}S_3$, ${}_{18}S_4$ and ${}_{23}S_5$), we were able to estimate both the degenerate frequency and c_2^0 coefficients for all ten multiplets based on the singlet stripping results. While the c_2^0 structure coefficients allow us to constrain only axisymmetric structure of degree 2, it is this harmonic of structure which causes anomalous splitting. Currently, we do not have a model which satisfies these observations though

a large scale anomaly in compressional velocity in the outer core goes a long way to satisfying the data. Structure in the inner core appears to be incapable of explaining the observations.

In chapter 4, we apply the singlet stripping technique to the lowest order fundamental toroidal modes. This group of modes has been neglected since they were first observed in the wake of the 1960 Chilean earthquake and the 1964 Alaskan earthquake. The Macquarie rise event has provided us with the best opportunity to observe these modes since the advent of digital seismometry and we are able to report what we consider to be the first unambiguous observation of the gravest fundamental toroidal mode ${}_0T_2$.

Since attenuation of seismic energy in the Earth is weak, it can be treated by perturbation theory so that, if the elastic structure is known, recovery of anelastic structure is a linear inverse problem. In chapter 5, we use the Q values obtained from the singlet stripping in chapter 3 together with Q observations from single record observations of fundamental modes (*Smith and Masters, 1989*) to recover models of attenuation throughout the Earth. An analysis of the resolving power of this dataset shows that simple models of Q structure can fit the observations. The most notable feature of the resulting Q model (QM1) is the low Q_μ value in the inner core. Such a low Q value in the inner core puts into question previously reported observations of supposedly high-Q inner core shear modes.

Before we close the circle and go back to the inversion of the degenerate frequency dataset to obtain models of the sphericaly averaged Earth structure, we should critically assess the dataset and consider ways of augmenting the number of constraints in the inversion by including observations other than free oscillation degenerate frequencies.

Recent experiments with fundamental toroidal modes have shown that peak frequencies from single record measurements may be contaminated by nearby fundamental spheroidal modes and can not be reliably estimated above a frequency of about 4 mHz. For fundamental spheroidal modes, our observational techniques break down at around 7 mHz. The alternative to observing fundamental modes in the frequency domain is to study the dispersion of Rayleigh and Love waves in the time domain. While surface waves are strongly affected by shallow structure, the large number of records containing surface waves should make it possible to obtain unbiased estimates of the average dispersion. A project for the immediate future is to measure the dispersion of Love and Rayleigh waves between 90 and 250 seconds using a multi-taper transfer function technique (*Thomson and Chave, 1989*). These data will provide the strongest constraints of the existence and depth extent of transverse isotropy in the mantle.

Another dataset that could be included are observations of differential travel-times of long-period body waves. The global coverage of this dataset is sufficient to obtain unbiased global averages

(*Woodward and Masters, 1991*). Differential travel times of ScS-S, SS-S, PcP-P and PP-P are preferable to absolute travel time observations as they are practically unaffected by near source or near receiver structure. They are also unaffected by timing problems. ScS-S and PcP-P place constraints on structure of the lower mantle while SS-S and PP-P constrain upper mantle structure. Absolute times are more difficult to interpret since they depend more strongly on the poorly known dispersive properties of the Earth and thus on the frequency dependence of attenuation. Long-period body-waves have also been used in stacking experiments aimed at recovering the reflections from upper mantle discontinuities (*Revenaugh and Jordan, 1990*; *Shearer, 1990*) and the depth of the main discontinuities in the transition zone (410 km and 670 km) and the impedance contrast at these interfaces seem to be reasonably well-determined. Comparison of radial and transverse component stacks of SS, SSS and SSSS phases have also produced direct evidence for transverse isotropy in the upper mantle (*Shearer, 1991*) and new models should certainly incorporate this feature. Though the size of the signal generally agrees with that predicted by model PREM, the depth extent of anisotropy is poorly constrained (*Montagner and Anderson, 1989*). Incorporation of surface wave dispersion data should allow us to determine this parameter. Preliminary inversions of the mode dataset also indicate that significant transverse isotropy is required in the inner core though our current inability to fit the data adequately makes it dangerous to make too much of this.

The one other global dataset which can potentially provide us with constraints on the 1-D structure of the Earth is the ISC catalogue of travel-times of high-frequency (1Hz) seismic phases. This dataset has been used to derive summary travel-times for surface focus events at 1° intervals for both P- and S-waves (*Dziewonski and Anderson, 1981, 1983*; *Kennett and Engdahl, 1991*). The travel-times for these summary rays can be used to constrain the average upper and lower mantle structure but the difficulty in using these observations in conjunction with free oscillation degenerate frequencies lies in the need to account for the frequency dependence of the elastic moduli (physical dispersion). In the inversion for PREM, *Dziewonski and Anderson (1981)* chose to ignore the absolute travel-times of the summary rays and only use the shape of the travel-time curve which is much less affected by physical dispersion. Our resolution analysis in chapter 5 has shown that the frequency dependence of the Q structure in the mantle remains ill-constrained so that we cannot expect to be able to model adequately physical dispersion for rays turning in low-Q regions. Physical dispersion is a small effect for rays which are mostly sensitive to structure in the high-Q regions so that differential travel-times of PcP-P and ScS-S could be initially considered as data in the 1-D inversion.

Inversion techniques and strategies

In chapter two we performed a non-parametric inversion of a preliminary dataset looking for the smallest, smoothest perturbation to a pre-existing model which would fit the data. The procedure is computationaly very costly and it is not feasible to experiment with a large number of different starting models. Looking for the smallest possible perturbation to a given starting model is a sensible thing to do since it is an effective way to stabilize the highly non-linear inversion. The drawback of this strategy is that it constrains the final model to be close to the starting model. In particular, if we use two different starting models and iterate them to convergence we may find that the resulting two models are further apart in model space than they are from their respective starting model.

What is needed is a formulation of the inverse problem which allows large steps in model space. We would also like to reduce the number of parameters in the inversion so as to reduce the computational burden. The size of the problem can most easily be reduced if we specify the model in terms of polynomials and perform a parameter space inversion, solving for the polynomial coefficients. While we still have to recompute all eigenfunctions at every iteration, the modeling equation can be reduced from $n \times n$ to $m \times m$ where n is the number of data (typically 630) and m is the number of parameters (typically 100). Such models could then produce starting points for less-constrained inversions using the techniques described in chapter 2. Preliminary experiments indicate that a PREM or IASPEI type parametrization allows χ^2/N to be reduced to about 6 for a purely isotropic model. Introduction of transverse isotropy in the inner core and upper mantle reduces this number to less than 3. Allowing transverse isotropy in the lower mantle and outer core does not seem to improve the fit to the data. These experiments also indicate that the best fitting polynomial models have very small or non-existent discontinuities at the 400 km discontinuity (see also *Montagner and Anderson, 1989*) which is clearly at variance with the observation of long-period converted and reflected phases (*Shearer, 1991*). This may reflect a problem in the dataset or the parameterization may be too constrained. To avoid the latter possibility, we plan to explore other model construction techniques such as Occam's inversion (*Constable et al. 1987*). In the appendix we give an outline of our implementation of that technique.

Once we have settled on a dataset and constructed a model which we consider to have an acceptable fit to the data we plan to address several questions of broader geophysical interset. Linearization of the forward problem allows a Backus-Gilbert style resolution analysis so that the uncertainty of individual model parameters can be estimated. In particular we plan to address the question of the density jump at the ICB. This parameter determines the amount of gravitational energy which is released by the

accretion of the inner core. Estimates of density gradient in the outer core and in the lower mantle can be used to determine whether these regions are stably stratified (*Masters, 1979*) and so place constraints on the convective flow believed to exist in these regions.

References

Backus, G.E., and J.F. Gilbert, Numerical applications of a formalism for geophysical inverse problems. *Geophys. J. R. Astron. Soc.*, **13**, 247–276, 1967.

Constable, S.C., R.L. Parker, and C.G. Constable, Occam's Inversion: A practical algorithm for generating smooth models from electromagnetic sounding data. *Geophysics*, **52**, 289–300, 1987.

Dziewonski, A.M., and D.L. Anderson, Preliminary reference Earth model. *Phys. Earth Planet. Inter.*, **25**, 297–356, 1981.

Dziewonski, A.M., and D.L. Anderson, Travel times and station corrections for P-waves at teleseismic distances. *J. Geophys. Res.*, **88**, 3295–3314, 1983.

Gilbert, F., A.M. Dziewonski, and J.N. Brune, An informative solution to a seismological inverse problem. *Proc. Natl. Acad. Sci.*, **70**, 1410–1413, 1973.

Gilbert, F., and A.M. Dziewonski, An application of normal mode theory to the retrieval of structural parameters and source mechanisms from seismic spectra. *Phil. Trans. R. Soc. Lond.*, **A278**, 187–269, 1975.

Kennett, B. N. L., and E. R. Engdahl, Traveltimes for global earthquake location and phase identification. *Geophys. J. Int.*, **105**, 429–465, 1991.

Masters, G., Observational constraints on the chemical and thermal structure of the earth's deep interior. *Geophys. J. R. Astron. Soc.*, **57**, 507–534, 1979.

Montagner, J-P., and D.L. Anderson, Constrained reference mantle model. *Phys. Earth Planet. Inter.*, **58**, 205–227, 1989.

Parker, R.L., Understanding inverse theory. *Ann. Rev. Earth Planet. Sci.*, **5**, 35–64, 1977.

Revenaugh, J.S., and T.H. Jordan, Mantle layering from *ScS* reverberations: 1. Waveform inversion of zeroth-order reverberations. *J. Geophys. Res.*, submitted, 1990.

Shearer, P.M., Seismic imaging of upper-mantle structure with new evidence for a 520-km discontinuity. *Nature*, **344**, 121–126, 1990.

Shearer, P., Constraints on upper-mantle discontinuities from observations of long-period reflected and converted phases. *J. Geophys. Res.*, submitted, 1991.

Smith, M.F., and G. Masters, Aspherical structure constraints from free oscillation frequency and attenuation measurements. *J. Geophys. Res.*, **94**, 1953–1976, 1989.

Thomson, D.J., and A.D. Chave, Jackknife error estimates for spectra, coherences and transfer functions. In: *Advances in spectral analysis and array processing, ed. by S. Haykin, Prentice Hall, NJ*, pp., 1989.

Woodhouse, J.H., and F.A. Dahlen, The effect of a general aspherical perturbation on the free oscillations of the earth. *Geophys. J. R. Astron. Soc.*, **53**, 335–354, 1978.

Woodward, R. L., and G. Masters, Global Upper Mantle Structure From Long-Period Differential Travel Times. *J. Geophys. Res.*, **96**, 6351–6377, 1991.

Appendix: A recipe for the construction of smooth 1-D models

The problem of constructing a spherically symmetric Earth model from a set of observed degenerate frequencies has received considerable attention in the geophysical literature (*Gilbert et al. 1973*; *Parker 1977*). The proposed strategy of *Gilbert et al. (1973)* is to look for smooth perturbations $\delta m(r)$ to a given starting model. This is achieved by minimizing the square of the integrated second derivative of the model perturbation $E = \int [d^2\delta m/dx^2]^2 dx$. Here we adopt a slightly different strategy and seek a perturbation $\delta m(r)$ to a given starting model m_o and penalize the perturbed model $m_o + \delta m$ for roughness. Let $\gamma_i \pm \sigma_i$ be the observed degenerate frequency of the ith mode and m_o be a given starting model such as 1066A or PREM. Furthermore let ω_i be the degenerate frequency of the ith mode calculated for the model m_o and $\mu_i = \gamma_i - \omega_i$ be the difference between the observed and predicted degenerate frequency. We define the penalty function

$$E = \lambda \left\| \frac{\mu_i}{\sigma_i} - \frac{1}{\sigma_i} \int_0^a g_i(r)\delta m(r) dr \right\|^2 + \int_0^a R^2(m(r)) dr \tag{6.1}$$

where λ is a Lagrange multiplier, R is an nth derivative roughening operator and $g_i(r)$ is the ith data kernel (*Backus and Gilbert, 1967*; *Woodhouse and Dahlen, 1978*). (6.1) is based on a linearization of the forward problem and is only applicable for small perturbations δm. We seek a perturbation to the model which is a linear combination of the representers (data kernels):

$$\delta m(r) = \sum a_i \frac{g_i(r)}{\sigma_i} \tag{6.2}$$

and we assume that the representers have been orthogonalized so that

$$\int_0^a \frac{g_i(r)}{\sigma_i} \frac{g_j(r)}{\sigma_j} dr = \delta_{ij}. \tag{6.3}$$

With these definitions the perturbation to the ith eigenfrequency produced by the perturbation $\delta m(r)$ is

$$\hat{\mu}_i = \int_0^a g_i(r)\delta m(r) dr = \sum a_i \sigma_i \int_0^a \frac{g_i(r)}{\sigma_i} \frac{g_j(r)}{\sigma_j} dr = \sigma_i a_i \tag{6.4}$$

so that the first term on the right side of (6.1) becomes

$$\lambda\left(\frac{\mu_i}{\sigma_i}-\frac{\hat{\mu}_i}{\sigma_i}\right)^2=\lambda\sum_i\left(\frac{\mu_i^2}{\sigma_i^2}-2a_i\frac{\mu_i}{\sigma_i}+a_i^2\right). \tag{6.5}$$

The second term on the right side of (6.1) is a measure of the model roughness. Define the roughened initial model as

$$\tilde{m}_o(r)=R(m_o(r)) \tag{6.6}$$

and the roughened kernel as

$$\tilde{g}_i(r)=R(g_i(r)) \tag{6.7}$$

so, by (6.2) the roughened model perturbation is

$$R(\delta m(r))=\sum a_i\frac{\tilde{g}_i(r)}{\sigma_i} \tag{6.8}$$

Thus our measure of roughness can be written as

$$\int_0^a R^2(m(r))dr=\int_0^a\tilde{m}_o^2(r)dr+2\sum_i a_i\int_0^a\tilde{m}_o(r)\frac{\tilde{g}_i(r)}{\sigma_i}dr+\sum_{i,j}a_ia_j\int_0^a\frac{\tilde{g}_i(r)}{\sigma_i}\frac{\tilde{g}_j(r)}{\sigma_j}dr \tag{6.9}$$

Substituting (6.5) and (6.9) into (6.1) and letting $\partial E/\partial a_i=0$ gives the following system of equations for the expansion coefficients a_i

$$\sum_i\left[\int_0^a dr\frac{\tilde{g}_i(r)}{\sigma_i}\frac{\tilde{g}_j(r)}{\sigma_j}+\lambda\delta_{ij}\right]a_i=\lambda\xi_i-c_i \tag{6.10}$$

where we have defined $\xi_i=\mu_i/\sigma_i$ and

$$c_i=\int_0^a dr\tilde{m}_o(r)\frac{\tilde{g}_i(r)}{\sigma_i}. \tag{6.11}$$

Diagonalization of the inner product matrix of the roughened kernels in (6.10) leads to an efficient algorithm for the exploration of the trade-off between data misfit and model roughness. Let

$$\int_0^a dr\frac{\tilde{g}_i}{\sigma_i}\frac{\tilde{g}_j}{\sigma_j}=B_{ij}=\mathbf{B}=\mathbf{U}\mathbf{\Lambda}\mathbf{U}^{\mathbf{T}} \tag{6.12}$$

then we can rewrite (6.10)

$$\left[\mathbf{\Lambda}+\lambda\mathbf{I}\right]\mathbf{U}^{\mathbf{T}}\mathbf{a}=\lambda\mathbf{U}^{\mathbf{T}}\boldsymbol{\xi}-\mathbf{U}^{\mathbf{T}}\mathbf{c}. \tag{6.13}$$

If we now introduce the rotated vectors $\mathbf{a}' = \mathbf{U}^T\mathbf{a}$, $\boldsymbol{\xi}' = \mathbf{U}^T\boldsymbol{\xi}$ and $\mathbf{c}' = \mathbf{U}^T\mathbf{c}$ we get

$$\mathbf{a}' = \left[\boldsymbol{\Lambda} + \lambda\mathbf{I}\right]^{-1}\left(\lambda\boldsymbol{\xi}' - \mathbf{c}'\right). \tag{6.14}$$

Equation (6.14) can be evaluated for a range of λ values. Given the solution vector, $\mathbf{a}'$, we can use (6.5) to compute the χ^2 misfit of the perturbed model

$$\chi^2 = \left(\frac{\mu_i}{\sigma_i} - \frac{\hat{\mu}_i}{\sigma_i}\right)^2 = \left(\boldsymbol{\xi} - \mathbf{a}\right)^T\left(\boldsymbol{\xi} - \mathbf{a}\right) = \left(\boldsymbol{\xi}' - \mathbf{a}'\right)^T\left(\boldsymbol{\xi}' - \mathbf{a}'\right) \tag{6.15}$$

and (6.9) to compute its roughness:

$$\int_0^a R^2(m(r))dr = \int_0^a \tilde{m}_o^2(r)dr + 2\mathbf{a}^T\mathbf{c} + \mathbf{a}^T\mathbf{B}\mathbf{a} = \int_0^a \tilde{m}_o^2(r)dr + 2\mathbf{a}'^T\mathbf{c}' + \mathbf{a}'^T\boldsymbol{\Lambda}\mathbf{a}' \tag{6.16}$$

Evaluating these expressions involves only vector dot products and thus is very efficient. Since the forward problem is non-linear and (6.1) is based on the linearization of it, (6.15) and (6.16) are only valid for small perturbations. To calculate the misfit exactly, one has to compute the eigenfrequencies and eigenfunctions of the perturbed model. This does not add to the computational burden since the eigenfunctions and eigenfrequencies are needed to start the next iteration.